Competing Phases in Iron-Based Superconductors Studied by High-Resolution Thermal-Expansion and Shear-Modulus Measurements

Zur Erlangung des akademischen Grades eines
DOKTORS DER NATURWISSENSCHAFTEN
der Fakultät für Physik des
Karlsruher Institut für Technologie (KIT)
genehmigte

DISSERTATION

von

Dipl.-Phys. Anna Elisabeth Böhmer
aus Trier

Tag der mündlichen Prüfung: 16.05.2014

Referent: Prof. Dr. H. v. Löhneysen
Korreferent: Prof. Dr. J. Schmalian

Contents

1. Introduction

Iron-based superconductors have enjoyed enormous attention since their discovery as a new class of high-temperature superconductors in 2008 [1]. With superconducting transition temperatures up to 55 K, high critical fields and moderate anisotropy of their superconducting properties, they offer a potential for applications [2–4]. As to fundamental research, their rich phase diagrams with several competing or cooperative order parameters have attracted particular attention [5–7]. A structurally distorted (orthorhombic with respect to a high-temperature tetragonal phase), an itinerant stripe-type antiferromagnetic and a superconducting phase are found in close proximity to each other. The proximity of superconductivity and magnetism is reminiscent of heavy-fermion and cuprate superconductors [8]. Furthermore, the multiband nature of the iron-based compounds, which are for the most part moderately correlated electron systems, adds to their complexity. There are various families of iron-based superconductors, which are termed according to their crystal structure. Their central, common, structural element are tetrahedrally coordinated Fe-As(Se) layers. Most of these systems become superconducting under chemical substitution of various elements or under the application of hydrostatic pressure.

On the road to understanding how superconductivity emerges in the iron-based systems, the interrelationship of the various phases and tuning parameters is of great interest. In particular, structural distortion and antiferromagnetism usually appear very close to each other in the phase diagrams. Superconductivity arises close to the point where structural distortion and magnetism are suppressed by substitution or pressure and seems to compete with these phases. Their fluctuations, on the other hand, are promising candidates for the superconducting pairing glue and quantum criticality possibly plays a role. Whether the structural or the magnetic instability is the primary driving force, is, however, still an open question [9]. In this context, the picture of a "spin-nematic" phase, in which magnetic fluctuations spontaneously break the four-fold rotational symmetry of the lattice, has been invoked [10]. Further, the study of how all these phases can be tuned is very important. These questions will be addressed in this work using thermodynamic measurements in a variety of materials.

Thermal expansion probes the pressure dependence of the entropy and is therefore an extremely sensitive bulk probe of phase transitions. The close proxim-

ity of different ground states, the three-dimensional nature of the fundamental structural element, and the availability of a large variety of systems and substitutions make the iron-based systems a very promising class of materials for thermal-expansion studies. In particular, the questions of phase competition and quantum criticality, as well as the relationship of different tuning parameters to (uniaxial) pressure can be naturally addressed. The shear modulus, which is the soft mode of the structural phase transition, is well suited to study the question of nematicity and possible structural quantum criticality.

In this thesis, $BaFe_2As_2$ (the archetypal representative of the 122 family of iron-based superconductors) substituted with K is in special focus. It is compared to Co-, P- and Ni-substituted $BaFe_2As_2$. FeSe is studied as a contrasting material, which undergoes a structural and a superconducting transition, but no magnetic transition.

This thesis is structured as follows. In chapter 2, a few general properties of the iron-based systems and their phase diagrams are presented and fundamental thermodynamic relations are recapitulated. As an example, the specific heat and thermal expansion of a BCS-type superconductor within the alpha-model is presented. The capacitance dilatometer employed for most measurements is briefly introduced and an overview of the single-crystalline samples is given.

Chapter 3 presents our investigation of the thermal expansion of $(Ba,K)Fe_2As_2$ and a comparison with $Ba(Fe,Co)_2As_2$, $Ba(Fe,Ni)_2As_2$ and $BaFe_2(As,P)_2$ [11, 12]. All systems show evidence for competition between magnetism and superconductivity. The data in the superconducting state are analyzed by extending the two-band alpha-model [13] to the thermal-expansion coefficient. We find that K substitution is qualitatively different from applying pressure, but confirm the equivalence of Co substitution to uniaxial pressure proposed previously [11]. The determined uniaxial pressure effects motivate the representation of substituted $BaFe_2As_2$ in a phase diagram with two distinct superconducting domes.

The fourth and largest chapter of this thesis is concerned with the study of the elastic shear modulus of $(Ba,K)Fe_2As_2$ and $Ba(Fe,Co)_2As_2$. The novel technique of high-resolution three-point bending in a capacitance dilatometer is developed and the calibration of the setup is presented. The technique is much easier to apply and less demanding in terms of sample size and quality than conventional ultrasound measurements. As a result, we obtain the temperature dependence of the soft elastic mode of $Ba(Fe,Co)_2As_2$, which agrees very well with previous ultrasound data—and of K-Ba122, where no data has been reported previously. The softening of the shear modulus is shown to be related to a "nematic susceptibility", whatever be its nature. The nematic susceptibility shows quantum-critical-like behavior only in the $Ba(Fe,Co)_2As_2$ system, but suggests a first-order transition between orthorhombic and tetragonal ground states in $(Ba,K)Fe_2As_2$

instead. Further, we find a scaling relation between magnetic fluctuations and lattice softening which provides evidence for a magnetic origin of the nematic susceptibility and for the presence of a spin-nematic phase in $Ba(Fe,Co)_2As_2$.

Chapter 5 is concerned with FeSe, the structurally simplest iron-based superconductor, which possibly displays an extended nematic region in the phase diagram. Thermal expansion shows, however, no evidence for competition between "nematicity" and superconductivity, in strong contrast to $BaFe_2As_2$-based systems. The lattice softening in FeSe is found to be identical to underdoped $Ba(Fe,Co)_2As_2$. We have also measured magnetic fluctuations using nuclear magnetic resonance of single crystals of FeSe and find no clear evidence for their relation to the structural transition. This suggests that the structural transition is likely not driven by magnetic fluctuations and that the orthorhombic phase of FeSe should probably not be associated with a spin-nematic phase.

Chapters 3 and 4 are largely self-contained and independent of each other. Chapter 5, being concerned with a new material, frequently resorts to comparisons with results of the previous two chapters. Concluding remarks in chapter 6 summarize the findings and their relation to each other.

2. Background

In this thesis, the phase interplay in iron-based superconductors is investigated by means of high-resolution thermal-expansion and shear-modulus measurements in an existing capacitance dilatometer. This chapter provides the background, starting with a short general introduction into the iron-based superconductors and their thermodynamic phases. Then, the relevant thermodynamic quantities and the capacitance dilatometer, which is used to measure them, are introduced. Finally, an overview over the studied single-crystalline samples is given.

2.1. Phase interplay in iron-based superconductors

Several families of iron-based superconductors have been discovered since 2008. Their common structural element are Fe-As layers, in which the Fe atoms are arranged on a square layer with As atoms in (slightly distorted) tetrahedral coordination around them. The families differ in spacer layers, which results in different crystal structures (see Fig. 2.1). The structurally simplest system is the '11' family [14] (represented by FeSe), which contains no spacer layer at all. LiFeAs [15] is a typical member of the '111' family, in which one Li (or Na) atom per Fe lies between the Fe-As layers. The very diverse '122' family contains an alkali or alkaline earth atom per two Fe atoms. A representative and widely studied member is $BaFe_2As_2$ [16]. In the '1111'-type oxyarsenides, layers of rare-earth and oxygen atoms alternate with Fe-As layers, as, e.g., in LaFeAsO [1]. Several systems with larger unit cells, such as $(CaFeAs)_{10}Pt_4As_8$ [17] with a '1048' structure or $(Fe_2As_2)(Ca_4(Mg,Ti)_3O_y)$ [18] with a '22438' structure, have also been reported.

The iron-based systems have in common rich phase diagrams which contain strongly interacting structurally distorted, antiferromagnetic and superconducting phases. They can be tuned by hydrostatic or uniaxial pressure and by a large variety of chemical substitutions. Together with the variety of starting materials, this leads to a great number of systems, whose similarities and differences are an interesting and very wide field of study. Examples for substitutions in $BaFe_2As_2$ are hole doping with K on the Ba site [16], electron doping with Co or Ni on the

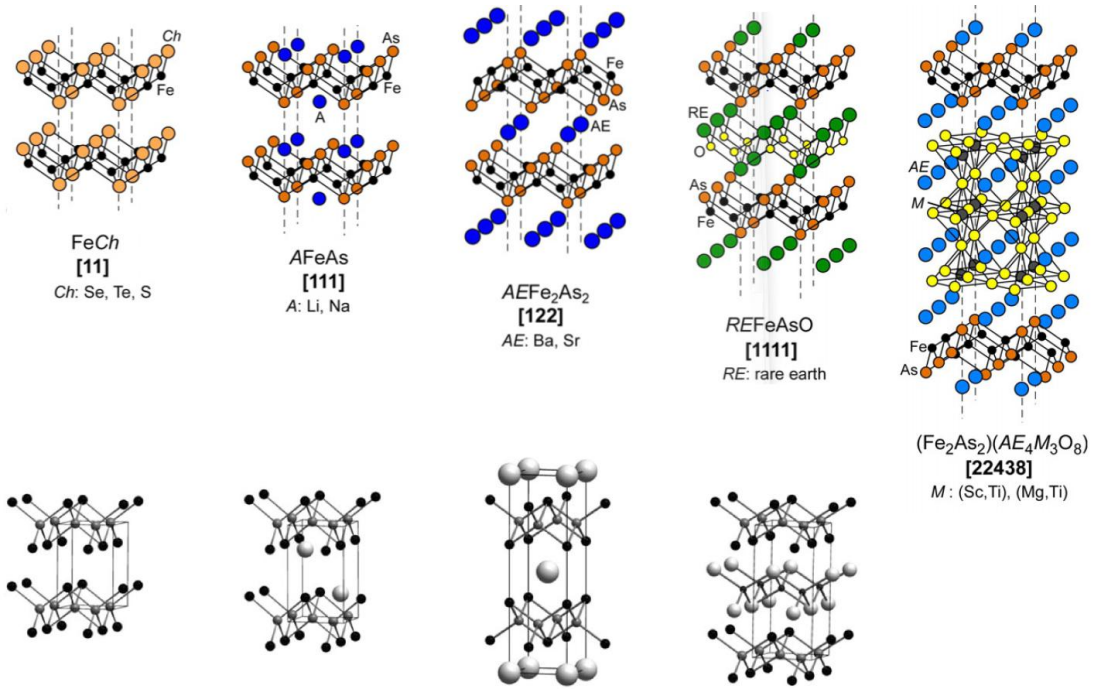

Figure 2.1.: Crystal structure of the four most common families of the iron-based superconductors, and one example of a system with a more complex structure. The tetragonal unit cell is indicated in the lower row. The common structural element of the systems are Fe-X layers (X=As, Se, Te, S or P), in which the Fe atoms are arranged on a square lattice with a pnictogen or chalcogen atom in tetrahedral coordination around them. Figure adapted from [4, 24].

Fe site [1] [20, 21], or isoelectronic substitution with Ru on the Fe site, or P on the As site [22, 23].

Fig. 2.1 shows schematically the phase diagram of Co-substituted $BaFe_2As_2$, which is representative of the iron-based systems. The undoped parent compound $BaFe_2As_2$ undergoes a magneto-structural phase transition at $\sim$ 140 K from a tetragonal and paramagnetic high-temperature phase to an orthorhombic and antiferromagnetic low-temperature phase with a stripe-type spin arrangement [25]. The tetragonal unit cell is defined with axes along next-nearest neighbor iron atoms. The structural distortion amounts to a shear distortion between the tetragonal in-plane axes. The unit cell in the antiferromagnetic state is orthorhombic;

1. The simple "doping" picture has, however, been challenged [19] and is under intense debate, in particular for Co and Ni. In principle, on should use the more neutral term "substitution" as done predominantly in this work.

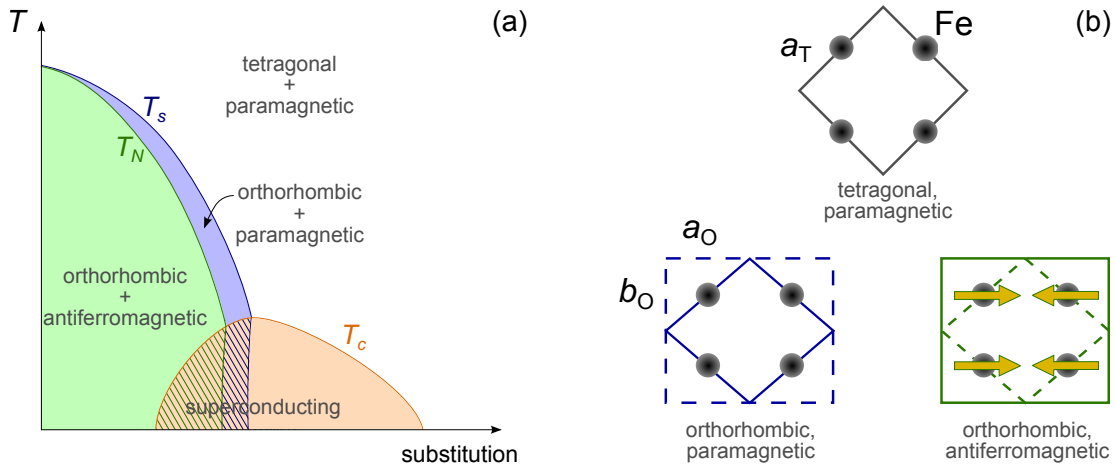

Figure 2.2.: (a) Schematic phase diagram of $Ba(Fe,Co)_2As_2$ as an example of a typical iron-based system, with six different phases indicated. Orthorhombic distortion and antiferromagnetism coexist with superconductivity within a part of the phase diagram. (b) Pattern of the structural distortion and the antiferromagnetic order within the iron plane. Fe atoms are represented by black disks, static magnetic moments by yellow arrows, and the unit cell is indicated by continuous lines.

it is twice as large as the tetragonal one and rotated by 45° with respect to it (Fig. 2.1). The iron moments order antiferromagnetically along the orthorhombic a_o axis and ferromagnetically along the shorter b_o axis. The structural order parameter, the orthorhombic distortion, is defined as $\delta = (a_o - b_o)/(a_o + b_o)$.

The orthorhombic distortion and the stripe-type antiferromagnetism are closely connected by symmetry [10, 26]. They (nearly [27]) coincide in the parent compound $BaFe_2As_2$, but they split upon Co substitution [28]. The structural transition precedes the magnetic one in this case, which raises the question whether the magnetic or the structural instability is the primary one [9]. However, the transitions still track each other closely in most phase diagrams, which suggests their intimate connection. The structural order parameter is enhanced at the magnetic transition [27], which demonstrates the cooperative coupling of the two phases. A dome of superconductivity with maximum $T_c \approx 25$ K emerges close to the point where the structural and magnetic phase transitions are suppressed. In many systems, there is a coexistence region in which superconducting, magnetic and structural order parameters are simultaneously finite but compete. This is clearly seen from the reduction of the magnetic moment [29] and the orthorhombic order parameter [30] below T_c. Within the narrow region of structural distortion without magnetic order, superconductivity competes with the distortion alone.

Another sign of this competition is the hardening of the elastic shear modulus [10] below T_c even within the tetragonal phase on the overdoped side.

2.2. Thermodynamic probes

It is well known that materials undergo a length, or volume, change under a temperature change. The thermodynamic quantity that quantifies this change is the fractional length change

$$\xi_i = L_i(T)/L_i(T_0), \tag{2.1}$$

where the subscript i stands for the direction. Similarly, the relative length change $\Delta L_i/L_i \approx (L_i(T) - L_i(T_0))/L_i(T_0) = \xi_i - 1$ is frequently considered. T_0 usually corresponds to room temperature. The linear thermal-expansion coefficient α_i is defined as the relative length change with temperature T, i.e., the logarithmic derivative of ξ_i,

$$\alpha_i = \frac{1}{L_i}\frac{dL_i}{dT} = \frac{d\ln\xi_i}{dT}. \tag{2.2}$$

α_i can be shown to be equal to the uniaxial pressure derivative of the entropy using the Maxwell relation for the Gibbs free energy G,

$$\alpha_i = \frac{1}{L_i}\frac{\partial L_i}{\partial T} = \frac{1}{V}\frac{\partial^2 G}{\partial T \partial p_i} = -\frac{1}{V}\frac{dS}{dp_i}. \tag{2.3}$$

Here, L_i is the sample length, V its volume and S its entropy. The measurement of α_i allows to map out exactly any structural changes of a compound. More generally, however, signatures of any pressure-dependent physical quantity that contributes to the entropy are observed in the thermal expansion.

Entropy and specific heat C_p are related via

$$\frac{C_p}{T} = \frac{dS}{dT}. \tag{2.4}$$

The entropy of a Fermi liquid well below its Fermi temperature is linear in temperature, $S = \gamma T$, where γ is the Sommerfeld coefficient. As a consequence, the electronic specific heat and the electronic thermal expansion of a Fermi liquid are both proportional to temperature,

$$C_p^{el} = T dS^{el}/dT = \gamma T, \tag{2.5}$$

$$\alpha_i^{el} = -\frac{1}{V}\frac{dS^{el}}{dp_i} = -\frac{1}{V}\frac{d\gamma}{dp_i}T. \tag{2.6}$$

Since γ is proportional to the density of states per spin at the Fermi level N_0, $\gamma = \frac{2\pi^2}{3} k_B^2 N_0$, one can directly obtain the pressure dependence of the density of states from the electronic thermal-expansion coefficient, and "γ" and "density of states" are sometimes used synonymously.

A phase transition at a critical temperature T_c is marked by an anomaly in the entropy and, in consequence, by anomalies in the specific heat and thermal expansion. At a first-order transition, the entropy increases discontinuously on increasing T, which corresponds to a latent heat $T\Delta S$, and the sample lengths change abruptly. Specific heat and thermal expansion show a peak, accordingly. The pressure derivative of the transition temperature is given by the Clausius-Clapeyron relation

$$\frac{dT_c}{dp_i} = V \frac{\Delta L_i / L_i}{\Delta S}. \tag{2.7}$$

At a mean-field second-order phase transition, the entropy shows a kink, which corresponds to a discontinuous jump of its derivatives, ΔC_p and $\Delta \alpha_i$. In this case, the pressure dependence of T_c is given by the Ehrenfest relation

$$\frac{dT_c}{dp_i} = V_m \frac{\Delta \alpha_i}{\Delta C_p / T_c}. \tag{2.8}$$

Here, C_p is the molar heat capacity and V_m the molar volume of the material. The signs are chosen such that ΔC_p and $\Delta \alpha_i$ are positive (negative), if the respective quantity increases (decreases) on decreasing T through the transition. Then, $\Delta C_p > 0$, and dT_c/dp_i has the same sign as the thermal-expansion anomaly.

The Young modulus Y_i is defined as the ratio between the amount of applied uniaxial stress σ_i and induced strain ε_i along direction i, i.e., it is the elastic modulus for uniaxial tension and related to the elastic compliance (see appendix B). Y_i shows a step-like decrease at a second-order phase transition, similar to the step-like increase of the specific heat. An Ehrenfest-type relation may also be found for Y_i, or, more precisely, for the respective component of the elastic compliance $-(1/V)\,(d^2G/d\sigma_i^2) = S_{ii} = Y_i^{-1}$,

$$\frac{dT_c}{dp_i} = \frac{\Delta S_{ii}}{\Delta \alpha_i} = -\frac{\Delta Y_i}{Y_i^2 \Delta \alpha_i}. \tag{2.9}$$

2.2.1. Specific heat and thermal expansion of a superconductor

As explained above, specific heat and thermal expansion are derivatives of the entropy. In consequence, both can be computed once the entropy and its pressure derivative are known in a specific model. As an example for a mean-field

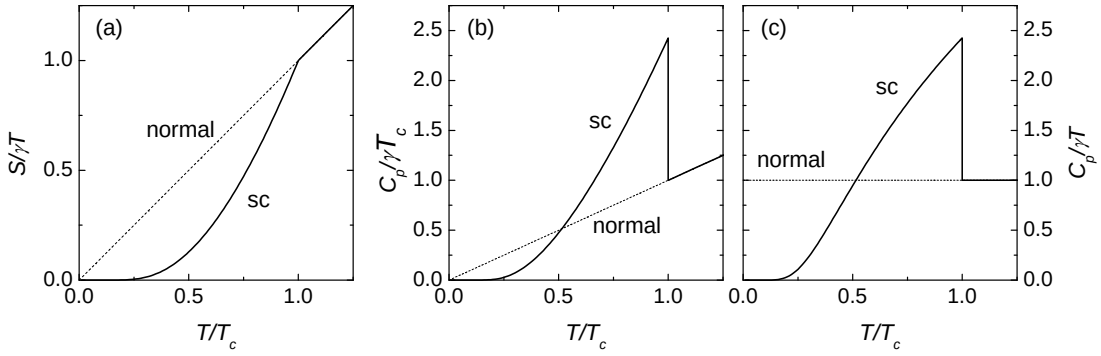

Figure 2.3.: Normalized (a) entropy, (b) specific heat and (c) specific heat divided by temperature as a function of reduced temperature T/T_c calculated for a normal-conducting Fermi liquid ("normal") and a superconductor within the BCS theory in the weak-coupling limit ("sc").

second-order phase transition, these thermodynamic quantities are shown here for a single-band BCS superconductor.

The electronic entropy of a superconductor can be calculated as the entropy of an independent set of fermions with dispersion $E = \sqrt{\epsilon^2 + \Delta^2}$,

$$S^{el} = -2N_0 \int_{-\infty}^{\infty} d\epsilon J(\sqrt{\epsilon^2 + \Delta^2}/T) \tag{2.10}$$

where $\Delta(T)$ is the superconducting energy gap (in units of temperature), N_0 the density of states per spin at the Fermi level, and the function J is defined by

$$J(z) = [1 - f(z)] \ln [1 - f(z)] + f(z) \ln f(z) \tag{2.11}$$

with f the Fermi function, $f(z) = (\exp(-z) + 1)^{-1}$ [31].

Fig. 2.3 shows the so computed electronic entropy S^{el} of a BCS superconductor and the resulting electronic specific heat C^{el} and specific-heat divided by temperature C^{el}/T in normalized units. The BCS superconductor is defined here by the fact that $\Delta(T)$ is determined by the BCS gap equation in the weak coupling limit [32]

$$0 = \int_0^{\infty} d\xi \left[\frac{\tanh\left(\frac{1}{2T/T_c}\sqrt{\xi^2 + (\Delta_{BCS}/T_c)^2}\right)}{\sqrt{\xi^2 + (\Delta_{BCS}/T_c)^2}} - \frac{1}{\xi} \tanh\left(\frac{\xi}{2}\right) \right], \tag{2.12}$$

which implies a universal ratio $\Delta_{BCS}(0) = 1.764 T_c$ and a universal value of the discontinuity $\Delta C_p = 1.43 \gamma T_c$. Various effects, such as strong-coupling or multi-band superconductivity, can increase or decrease this ratio. They can be described

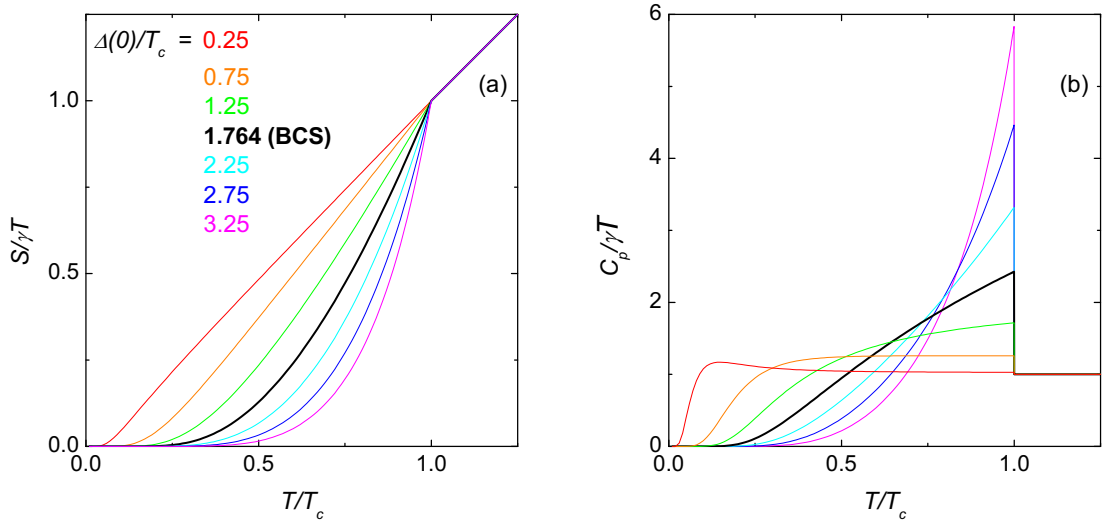

Figure 2.4.: Normalized (a) entropy and (b) specific heat divided by temperature of a superconductor with varying gap ratio $\Delta(0)/T_c$ (see panel (a)) calculated for a superconductor within the alpha-model.

within the widely-used phenomenological alpha-model [31]. It basically consists of treating the zero-temperature value $\Delta(0)/T_c$, the "coupling strength", as an adjustable parameter, while maintaining the temperature dependence of the BCS gap $\Delta(T) = \Delta(0)\frac{\Delta_{BCS}(T)}{\Delta_{BCS}(0)}$. Fig. 2.4 shows the entropy and specific-heat coefficient divided by temperature for a single-band superconductor with different values of $\Delta(0)/T_c$.

A change of variables in equation 2.10 shows that $S^{el}/\gamma T$ is a function of $\Delta/T \equiv D$ (not Δ/T_c!) only,

$$\frac{S_{es}}{\gamma T} = -\frac{6}{\pi^2}\int_{-\infty}^{\infty} d\zeta J\left(\sqrt{\zeta^2 + D^2}\right) = -\frac{6}{\pi^2}\Sigma(D). \tag{2.13}$$

Here, $\zeta = \epsilon/T$ and the function $\Sigma(D)$ has been defined in the second step. This form is advantageous for the calculation of the thermal-expansion coefficient and has been introduced for this purpose in Ref. [33]. The electronic entropy of a superconductor is determined by three parameters within the alpha-model: the Sommerfeld coefficient γ, the transition temperature T_c and the gap at zero temperature $\Delta(0)/T_c$. The thermal expansion coefficient is obtained by taking the pressure derivative of the entropy, which in this formalism contains three terms (three types of contribution) [33, 34], related to the pressure derivative of one of

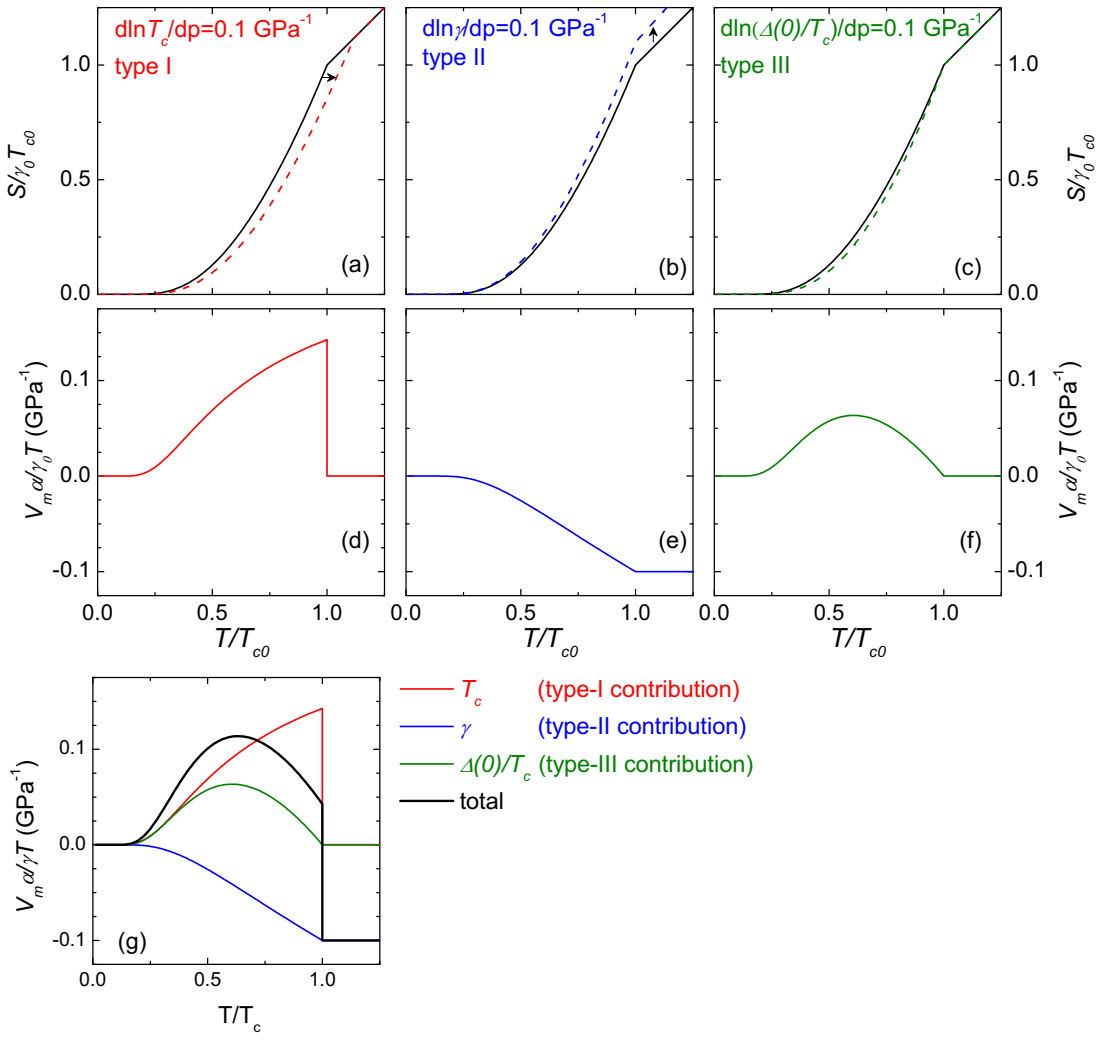

Figure 2.5.: Illustration of the origin of three types of contribution to the thermal expansion of a BCS superconductor. Panels (a)-(c) illustrate how the entropy changes if one of the parameters T_c, γ, and $\Delta(0)/T_c$, respectively, changes with pressure: solid curves are calculated with $T_{c,0}$, γ_0 and $\Delta(0)/T_c = 1.764$ while dashed lines are calculated with the respective parameter increased by 10%. Panels (d)-(f) present the corresponding thermal-expansion coefficient $\alpha/T = -d(S/T)/dp$ normalized by V_m/γ to units of GPa^{-1}. Panel (g) shows the sum of the curves in (d)-(f), i.e., the thermal expansion of a superconductor with $d\ln T_c/dp = d\ln\gamma/dp = d\ln(\Delta(0)/T_c)/dp = 0.1$ GPa^{-1}.

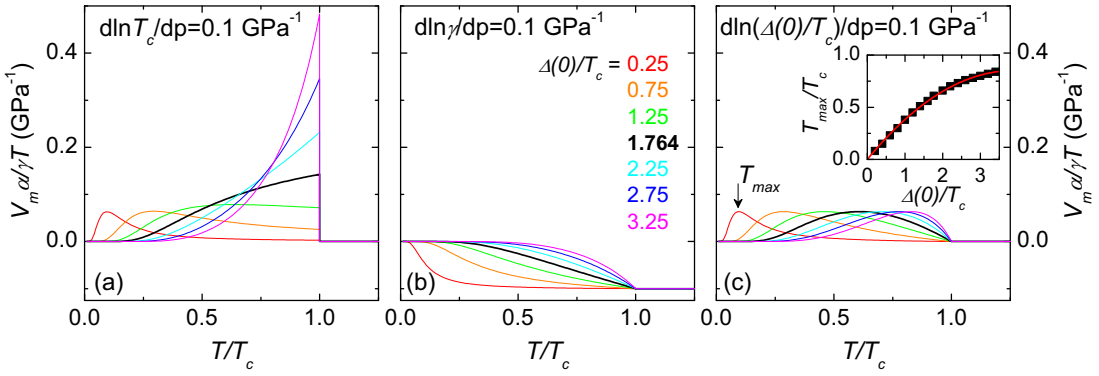

Figure 2.6.: Variation of the three types of contribution to the thermal expansion of a superconductor with varying coupling strength $\Delta(0)/T_c$ within the alpha-model. Curves are calculated with fixed logarithmic pressure derivative of (a) T_c, (b) γ, and (c) $\Delta(0)/T_c$ (the other two being zero), while $\Delta(0)/T_c$ is varied as indicated in panel (b). The inset in (c) shows the position of the maximum of the type-III contribution as a function of $\Delta/T_c(0)$. The solid line represents is a second order polynomial fit $T_{max}/T_c = 0.44\,(\Delta(0)/T_c) - 0.057\,(\Delta(0)/T_c)^2$.

the three variables T_c (type I), γ (type II), and $\Delta(0)/T_c$ (type III), when the other two are kept constant, respectively,

$$\frac{V_m\alpha}{\gamma T} = \frac{6}{\pi^2}\left(-\frac{d\ln T_c}{dp_i}\frac{d\Sigma(D)}{dD}\frac{dD}{dt}t + \frac{d\ln\gamma}{dp_i}\Sigma(D) + \frac{d\ln\left(\Delta(0)/T_c\right)}{dp_i}\frac{d\Sigma(D)}{dD}D\right). \tag{2.14}$$

Fig. 2.5 visualizes these contributions to the thermal expansion as the entropy difference resulting from a variation of the parameters T_c, γ and $\Delta(0)/T_c$. The contribution of type I is proportional to $d\ln T_c/dp$. It results in a discontinuity $\Delta\alpha$ at T_c which has the same sign as $\frac{d\ln T_c}{dp_i}$ and whose magnitude is, in agreement with the Ehrenfest relation 2.8, given by $\Delta\alpha = V_m\Delta C_p d(\ln T_c)/dp$. It is largest at $T \lesssim T_c$. The contribution of type II arises from the pressure dependence of γ. Its sign is opposite to the sign of $d\ln\gamma/dp$. Naturally, it is the only contribution to be finite in the normal state and grows smaller as the number of excited quasiparticles is reduced in the superconducting state. The contribution of type III comes from the pressure dependence of the ratio $\Delta(0)/T_c$, i.e., the coupling strength within the alpha-model. It goes through an maximum (minimum) at $0 < T_{max} < T_c$ if $\frac{d\ln(\Delta(0)/T_c)}{dp}$ is positive (negative). The thermal expansion of a real material will of course be a sum of contributions of these three types and can therefore display a variety of shapes.

How the shape of the different types of contribution to the thermal expansion varies with the coupling strength $\Delta(0)/T_c$ is shown in Fig. 2.6. The type-I contribution resembles the specific heat, while the type-II contribution changes curvature on increasing $\Delta(0)/T_c$. It is larger when the gap amplitude is small because more quasiparticles are excited at low temperatures in this case. The type-III contribution has a maximum whose position T_{max}/T_c depends monotonically on the coupling strength (inset of Fig. 2.6(c)). From an analysis of specific heat and thermal expansion one can thus hope to learn about the coupling strength $\Delta(0)/T_c$, and the uniaxial pressure derivatives of T_c, γ and $\Delta(0)$. For multiband systems, each band contributes individually to the entropy and the analysis becomes more complex. It will be shown in detail in chapter 3.3.3 for (Ba,K)Fe_2As_2.

2.3. The capacitance dilatometer

The capacitance dilatometer, with which most results of this thesis were obtained, measures changes in sample length with high resolution by measuring the change of the capacitance of a plate-type capacitor [35, 36]. For this, one capacitor plate is moveably attached to the frame of the dilatometer via a set of parallel springs, while the second plate is fixed to the frame and electrically isolated from it. The sample is pressed with a small force (~ 0.2 N) against the movable plate by a screw (Fig. 2.7). Any change in sample length therefore leads to a change of the capacitor gap and, hence, the capacitance. Capacitance changes are read out using a capacitance bridge by the company *Eichhorn und Hausmann*. An absolute length resolution of $0.1 - 0.01$ Å is achieved. Samples between 100 μm and 8 mm length have been measured, so that the relative resolution is $10^{-7} - 10^{-10}$. The dilatometer is installed in a He-flow cryostat and data is typically taken on heating between $5 - 300$ K at a rate of 15 mK/s.

The raw data are immediately corrected for the thermal expansion of the capacitor plates in the data acquisition program, hence the "output" of the dilatometer is the change of the size of the capacitor gap with respect to an initially set reference value. A correction for the thermal expansion of the cell (made entirely of Cu:Be) and other reproducible effects has to be made by using a calibration measurement with a Cu sample. The procedure has been explained in Ref. [37] and yields the relation between measured capacitor gap d and sample length L

$$\begin{aligned} L_x(T) =& L_{Cu}(T_0)\xi_{Cu}(T) + \left(d_x(T_0) + L_x(T_0) - d_{Cu}(T_0) - L_{Cu}(T_0)\right)\xi_{Cu:Be}(T) \\ &+ d_{Cu}(T) - d_x(T). \end{aligned} \tag{2.15}$$

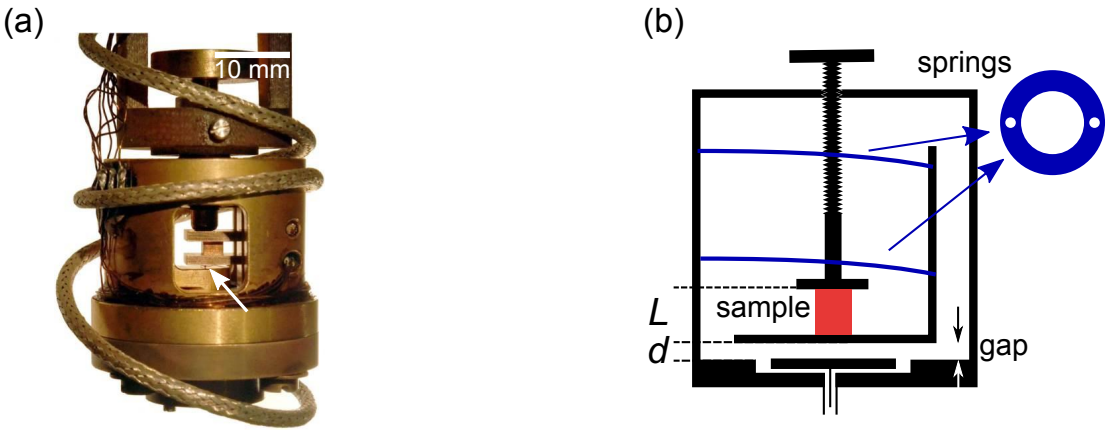

Figure 2.7.: (a) Photograph of the dilatometer with which most of the measurements were performed. The (here very small) sample is fitted into the middle part marked by an arrow; the capacitor plates are located in the lower part of the dilatometer. (b) Schematic drawing of the cross section of the dilatometer with the length of a sample L, the capacitor gap d and the set of parallel springs indicated. A top view of one of the springs is also shown.

Here, the subscript x refers to the actual measurement while the index Cu corresponds to the calibration measurement with a Cu sample; ξ is defined in equation 2.1. Note that only the last two terms are the size of the capacitor gap as a function of temperature, i.e., the output of the dilatometer. The other terms contain the room temperature (T_0) value of sample length and capacitor gap. $L(T_0)$ is measured with a micrometer and $d(T_0)$ can be estimated from the value at which the capacitance bridge is balanced. The thermal expansion coefficient of Cu is taken from Ref. [38] and of Cu:Be from measurements by C. Meingast.

The iron-based superconductors undergo a shear deformation of their in-plane axes at the structural phase transition (see Fig. 2.2). This leads to the formation of structural twins, i.e., domains in which the orthorhombic a and b axis are interchanged with respect to each other [39]. Measurements of the in-plane thermal-expansion thus yield (ideally) the average of a and b axis. However, the dilatometer intrinsically applies a small uniaxial force to the samples in order to transfer the sample length change to the capacitor. If this force is directed along [110], i.e., the diagonal of the tetragonal unit cell, then domains with their (shorter) orthorhombic b axis along the measured direction are favored and, ideally, the thermal expansion of the b axis alone is obtained [12] (see also [40]). Thermal expansion in the twinned state can only be measured if the force of the

dilatometer is directed along the [100] direction, the tetragonal a axis, so that no domain type is favored. An example of such measurements is shown in Fig. 3.3.

2.4. Samples

A large number of samples from a variety of iron-based materials has been investigated in this work. A nearly exhaustive list is provided in the appendix C, and only a brief description of preparation techniques and characterization is given here [2].

Single crystals of K-substituted $Ba_{1-x}K_xFe_2As_2$ were grown from self-flux in alumina crucibles sealed in a steel container. FeAs flux was used for lower K contents (up to $\sim 60\%$) [41] while samples with high K content ($\sim 80-100\%$) were grown out of a K-As flux [42]. Typical cooling rates were $0.2-0.4$ °C/h. At the end of the growth, the flux was decanted by tilting the crucible inside the furnace. Most batches were annealed *in situ* by slow cooling with further holding steps in the range of $350-450$ °C. As in other 122 systems, the obtained single crystals have a plate-like shape. Typical dimensions are $5 \times 5 \times 0.2$ mm^3 with the shortest direction along the c axis. However, samples with thickness of up to 1 mm and in-plane dimensions in excess of 1 cm could sometimes be obtained. Samples were characterized by energy-dispersive x-ray spectroscopy (EDX) and structural refinement with a 4-circle diffractometer using Mo-radiation [3]. With these techniques, the K content $x = 0-1$ could be determined with a typical error of 0.005. Uniaxial thermal expansion measurements were conducted on many of these samples (chapter 3). Only measurements with sharp transitions, which fit well into the phase diagram, were retained for further analysis. Moreover, only samples from batches whose thermal expansion fits well into the established systematics were used for Young's modulus measurements (chapter 4).

Co- and Ni- substituted $BaFe_2As_2$ samples were grown out of FeAs self-flux [43]. Some samples were codoped with Mn by adding MnAs to the starting composition. The substitution level was determined by EDX and 4-circle x-ray refinement. For this work, measurements of the Young's modulus of $Ba(Fe,Co)_2As_2$ from batches previously checked by thermal expansion [11] were conducted.

FeSe single crystals used in this work were grown out of the vapor phase using $AlCl_3$ as a transport agent [44]. Fe and Se powders were mixed in a ratio 1.1:1 together with a eutectic mixture of KCl and $AlCl_3$. The charge was sealed

2. All samples were grown by Thomas Wolf, Doris Ernst and Peter Adelmann at the Institute of Solid State Physics (IFP) at the Karlsruhe Institute of Technology.

3. These measurements were performed by R. Fromknecht and P. Schweiss, respectively, at the Institute of Solid State Physics (IFP) at the Karlsruhe Institute of Technology.

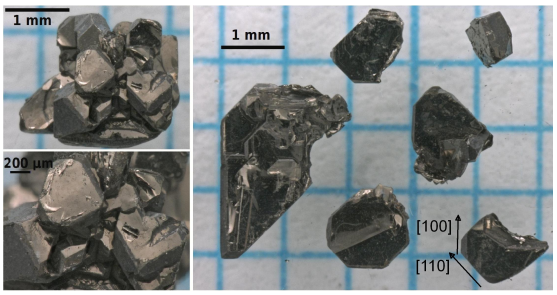

Figure 2.8.: Photograph of vapor-grown single crystals of FeSe used in this study. In the lower right hand corner, crystallographic directions with respect to the crystal facets are indicated.

in an evacuated SiO_2 ampule and heated to 390°C on one end while the other end of the ampule was kept below 240°C. After approximately one month, FeSe crystals of tetragonal morphology were extracted at the colder end. At such low temperatures, samples form directly in the tetragonal state. At higher temperatures, FeSe would form in a hexagonal phase and transform into the tetragonal structure on decreasing T [45], which would introduce internal stresses. Typical sample dimensions were $2 \times 2 \times 0.2$ mm^3, with some samples exceeding 5 mm in length or 500 μm in thickness. Wavelength dispersive x-ray spectroscopy revealed an impurity level below 500 ppm, in particular there is no evidence for Cl, Si, K or Al impurities. x-ray powder diffraction confirms the tetragonal structure with lattice constants $a = 3.7707(12)$ Å and $c = 5.521(3)$ Å. 4-circle x-ray refinement yielded a composition of Fe:Se=0.995(4):1, (i.e., stoichiometric within the error bar) and a structural z parameter of $z = 0.26668(9)$. No indications for interstitial atoms were found. The growth procedure (initial composition and temperatures) was slightly varied for different batches. This resulted in a variation of the predominant morphology (aspect ratio) of the crystals, however, no variation of their composition or lattice parameters was found within the error bar. The thermal expansion of samples from 5 different batches was measured and found to be reproducible, even though transition temperatures vary slightly between different samples, even within one batch (see Fig. 5.3 (b)).

3. Thermal expansion of $BaFe_2As_2$-based iron-arsenide superconductors

$BaFe_2As_2$ is one of the most widely studied iron-based systems not least because of the large variety of chemical substitutions which can induce superconductivity. The first of these 122-superconductors to be discovered was (Ba,K)Fe_2As_2 [16]. This system still exhibits the highest known $T_c \approx 38$ K in the 122 family (at $\sim 40\%$ K content) and a large superconducting dome extending up to 100% K content. Studies of bulk properties of single-crystalline (Ba,K)Fe_2As_2 are relatively rare, presumably because of the difficulty in crystal growth. In this chapter, an extensive study of the thermal expansion of single-crystalline (Ba,K)Fe_2As_2 is presented; its phase diagram, uniaxial pressure effects, and the relationship between uniaxial pressure and different kinds of substitution are studied. As an introduction to the thermal-expansion of 122-type iron-based superconductors, previous studies of the Ba(Fe,Co)$_2As_2$ system [11, 43] are reviewed. Then, experimental results on the uniaxial thermal expansion of the (Ba,K)Fe_2As_2 system covering a wide doping range are presented. The phase diagram and the normal-state thermal expansion are discussed first. Using the alpha-model for the thermal expansion of multigap superconductors, the pressure dependence of T_c, the density of states and the superconducting gaps are determined. The chapter concludes with a comparison of Co-, Ni-, P- and K-substituted $BaFe_2As_2$.

3.1. Previous work on Ba(Fe,Co)$_2As_2$

The main results of previous thermal-expansion studies of Ba(Fe,Co)$_2As_2$ [11, 46], namely the signatures of the structural, magnetic and superconducting phase transitions, structural tuning parameters and their relationship to Co substitution, and competition between structural distortion and superconductivity are summarized here.

Thermal expansion is a very sensitive probe of phase transitions. Fig. 3.1 presents the length change $\Delta L_i/L_i$ and the uniaxial thermal-expansion coefficient

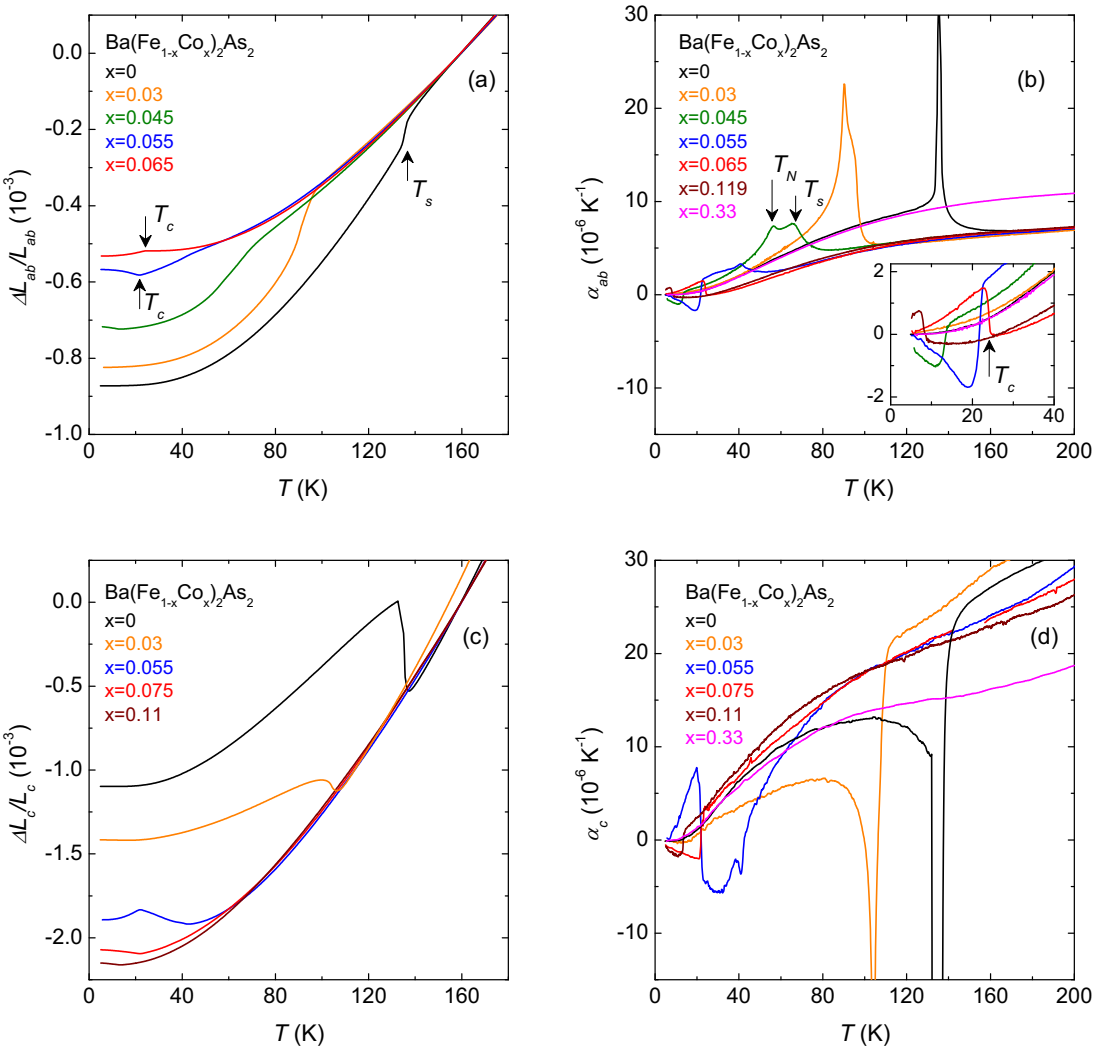

Figure 3.1.: (a) Relative in-plane length change $\Delta L_{ab}/L_{ab}$ and (b) in-plane thermal expansion coefficient α_{ab} of $Ba(Fe,Co)_2As_2$ in the twinned state. The inset in (b) shows the low-temperature data on an expanded scale. Examples of the structural (T_s), magnetic (T_N) and superconducting (T_c) transitions are indicated by arrows. (c) and (d) show similar data along the c axis. Data are taken from Ref. [11]

α_i for in-plane measurements on twinned samples ($i = ab$, average a and b axis length) and along the c axis ($i = c$) in the $Ba(Fe,Co)_2As_2$ system. On decreasing T through the magneto-structural phase transition of $BaFe_2As_2$ (see Fig. 2.1), the in-plane length L_{ab} decreases and the c-axis length L_c increases abruptly. This corresponds to a positive peak in α_{ab} and a negative peak in α_c. The results directly show that the orthorhombic antiferromagnetic state favors a longer c axis and a compressed ab plane.

The peak in α_{ab} splits upon Co substitution, revealing a difference of the structural transition temperature T_s and the magnetic transition temperature T_N of a few K. The structural transition appears to be weakly first order for the undoped and second order for doped samples with $> 2\%$ Co content. The onset of superconductivity at T_c on the underdoped side is signaled by a negative step-like anomaly in α_{ab}, i.e. an anomaly in which α_{ab} decreases with respect to its value extrapolated from the high-temperature phase. It corresponds to a kink in L_{ab}. A similar, but positive, anomaly at T_c is observed in α_c. Such step-like anomalies in α are naturally expected for second-order phase transitions. The orthorhombic, magnetic and superconducting order parameters coexist on the underdoped side. On the overdoped side, there is no longer any structural transition and the anomaly of α_{ab} (α_c) at T_c is positive (negative). This sign change of $\Delta\alpha$ with doping can be used to unambiguously determine whether a sample is underdoped or overdoped.

Thermal-expansion anomalies at a phase transition are related to the pressure derivative of the transition temperature dT_c/dp via the Clausius-Clapeyron (Eq. 2.7) and the Ehrenfest (Eq. 2.8) relation, for first-order and second-order phase transitions, respectively. In particular, the sign of dT_c/dp is given by the sign of the respective thermal-expansion anomaly. For example, measurements of a slightly overdoped $Ba(Fe_{0.92}Co_{0.08})_2As_2$ sample [43] yield uniaxial pressure derivatives of the superconducting transition temperature $dT_c/dp_a = 3.1(1)$ K/GPa and $dT_c/dp_c = -7.0(2)$ K/GPa. They cancel largely in the volume average, which results in a small hydrostatic pressure effect $dT_c/dp_{vol} = 2dT_c/dp_a + dT_c/dp_c = -0.9(3)$ K/GPa, a value which agrees well with direct pressure measurements [47]. On the underdoped side, the dT_c/dp_i's are clearly of opposite sign and larger in magnitude than those of the overdoped samples.

It is evident from the sign of the thermal-expansion anomalies of underdoped samples that the uniaxial-pressure derivatives of T_s and T_N have the opposite sign with respect to the derivatives of T_c for all directions. This is consistent with competition between the magnetic-orthorhombic phase and superconductivity, since uniaxial pressure will always favor one phase at the expense of the other [48]. Importantly, the fact that in-plane and c-axis pressure derivatives have opposite sign establishes the c/a ratio (the ratio $c/\frac{a+b}{2}$ in the case of underdoped samples)

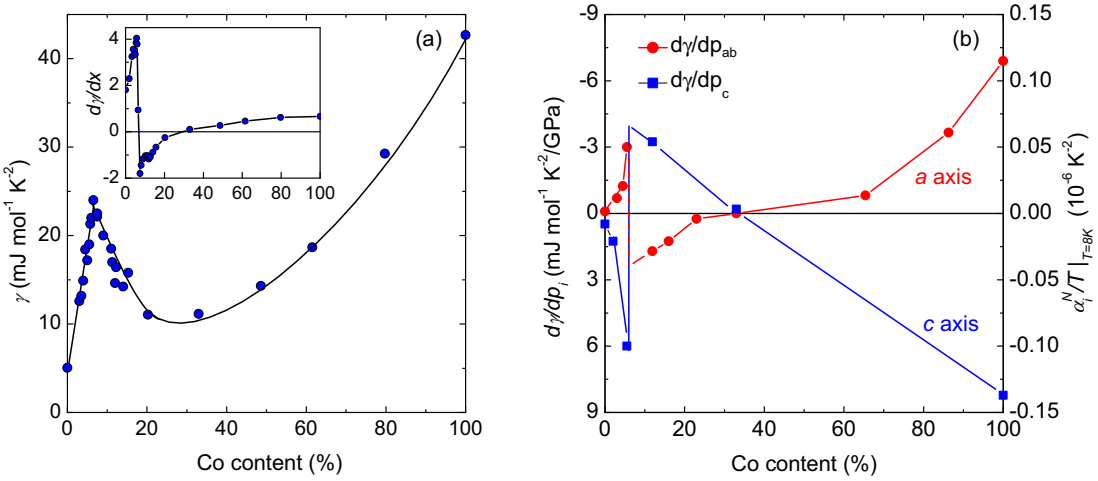

Figure 3.2.: (a) Sommerfeld coefficient γ (in the magnetic state for $\leq 6\%$ Co content) as a function of Co content. (b) Low-temperature limit of α_i/T (in-plane and c-axis expansion, respectively, $i = ab$ (red circles), $i = c$ (blue squares)), proportional to the uniaxial pressure derivative $d\gamma/dp_i$. Lines are a guide to the eye. The inset in (a) shows the Co-content derivative $d\gamma/dx$ which closely resembles $d\gamma/dp_i$ suggesting the equivalence of Co substitution and uniaxial pressure. Figure adapted from Refs. [49] and [11].

as an important structural tuning parameter of these systems. In contrast, all effects cancel largely in the volume average, which is thus shown to be not as good a tuning parameter.

The relation between Co doping and uniaxial pressure as tuning parameters was studied in Ref. [11] by considering the pressure and the doping derivative of the electronic density of states γ. The pressure derivative of γ is obtained from the low-temperature intercept of α_i/T (see eq. 2.6), shown in Fig. 3.2 [11]. The comparison with specific-heat data [49] reveals that $d\gamma/dp_i$ resembles the derivative of γ with respect to Co doping, $d\gamma/dx$. This demonstrates the direct relation between uniaxial pressure and Co doping. Namely, for each Co concentration the effect of uniaxial pressure is directly proportional to additional doping: an increase in doping level by 1 at%Co is approximately equivalent to -1.4 GPa (+0.6 GPa) of uniaxial pressure applied along the a axis (c axis) [11]. Consistently, the sign of all uniaxial pressure derivatives of T_s, T_N and T_c can be accounted for by identifying uniaxial pressure with a shift in the Co content: uniaxial pressure along the c axis mimics an increased substitution level while in-plane pressure mimics a decreased substitution level.

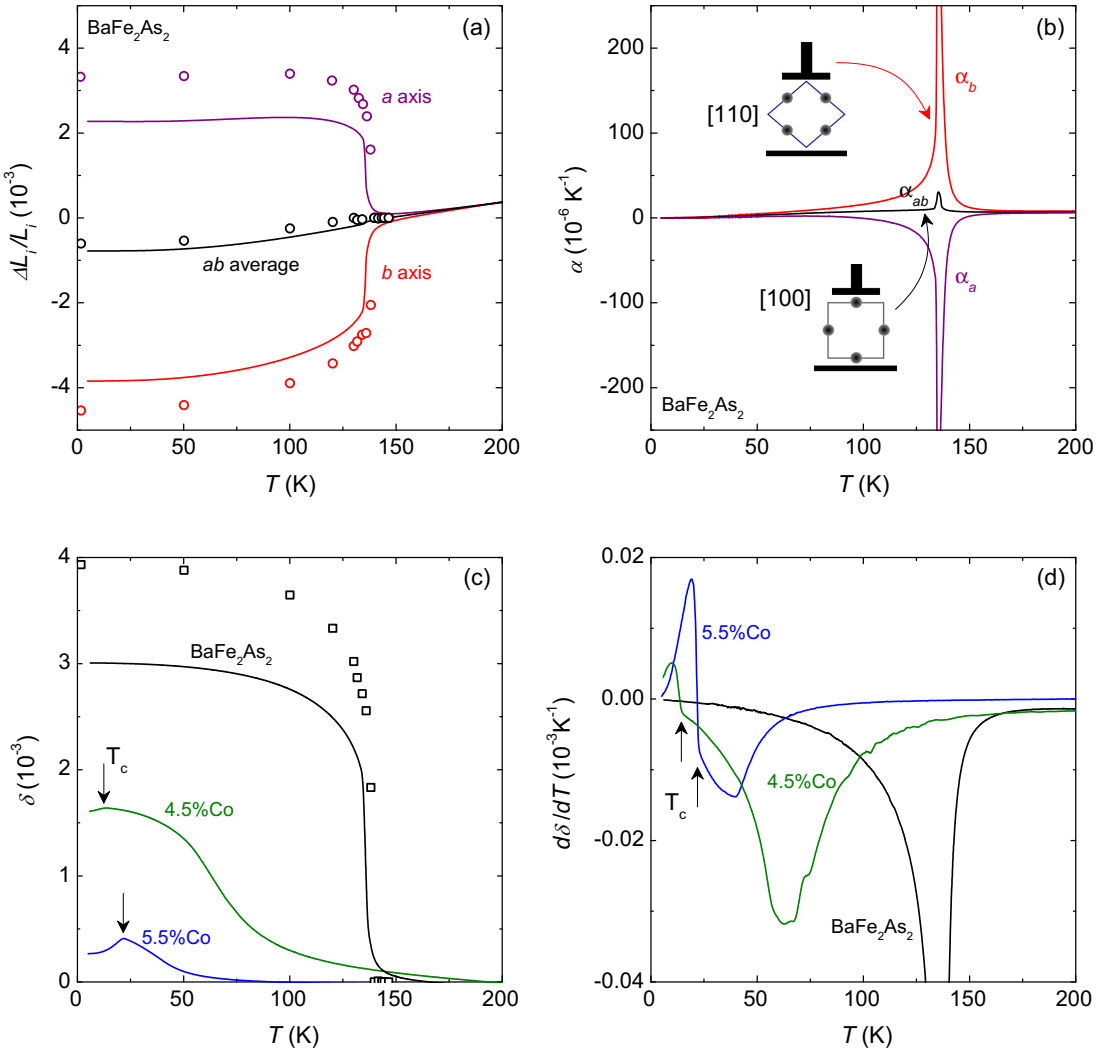

Figure 3.3.: (a) In-plane length changes and (b) thermal-expansion coefficients of $BaFe_2As_2$ [11, 50]. Scetches in (b) illustrate the orientation of the sample within the dilatometer for the measurements of α_{ab} and α_b. α_a was inferred from these results as $\alpha_a = 2\alpha_{ab} - \alpha_b$. (c) and (d) show the orthorhombic order parameter and its temperature derivative, respectively, calculated from the data in (a). Continuous lines show thermal-expansion data, while symbols show results of neutron powder diffraction of undoped $BaFe_2As_2$ from Ref. [51]

The $Ba(Fe_{0.67}Co_{0.33})_2As_2$ sample is special in that α_a/T and α_c/T have a negligible intercept at low T, which means that the electronic $d\gamma/dp$ contribution to its thermal expansion vanishes for both a and c direction. This is fortunate, because data of $Ba(Fe_{0.67}Co_{0.33})_2As_2$ can then be used as a phonon background in various contexts [11]. Note that the phonon background is expected to depend only weakly on Co content since Fe and Co atoms have very similar mass [49].

At the tetragonal-to-orthorhombic phase transition, naturally, the in-plane lattice constants become inequivalent. As explained in chapter 2.3, we can selectively measure the shorter orthorhombic b axis (samples are *in situ* detwinned) by controlling the in-plane orientation of samples inserted into the dilatometer. In combination with data in the twinned state, the temperature dependence of the orthorhombic a axis can also be calculated. Fig. 3.3 shows the relative length changes of the in-plane axes of $BaFe_2As_2$ and the corresponding thermal expansion coefficients. The comparison to neutron scattering data [51] reveals reasonable, if not perfect, detwinning. The peak at T_s is naturally much larger in α_b than in α_{ab}. Fig. 3.3 (c) presents the orthorhombic order parameter $\delta = (a-b)/(a+b)$ computed from the thermal-expansion data of $Ba(Fe,Co)_2As_2$ [4], and a comparison with the neutron diffraction data of the undoped compound. The value of $\delta(T=0) \approx 3 \times 10^{-3}$ is slightly lower than determined by diffraction (4×10^{-3}) due to the incomplete detwinning. $\delta(T=0)$ decreases with doping and is approximately proportional to T_s. At finite Co doping, a marked high-temperature tail to the transition emerges, which is presumably due to the finite in-plane pressure applied for detwinning. Also, the structural transition might be broadened by impurities or the sample might exhibit a distribution of T_s. The dramatic reduction of δ below T_c, previously reported in Ref. [30], is evident from this data, too. It is manifest as a discontinuity in the temperature derivative $d\delta/dT$ and demonstrates the competition between orthorhombic distortion and superconductivity, which we have previously inferred from the pressure derivatives.

4. When calculating δ from thermal expansion data, one effectively evaluates the integral $\int (\alpha_{\text{“}twinned''} - \alpha_{\text{“}detwinned''})dT$. In ideal measurements this yields $(\Delta a/a_0 + \Delta b/a_0)/2 - \Delta b/a_0 = \frac{a-b}{2a_0}$, which is equal to the orthorhombic order parameter $\delta = (a-b)/(a+b)$ within 0.1%. If, however, a sample is not completely detwinned or, conversely, partly detwinned even in the “twinned” measurement, the anomaly in $\alpha_{\text{“}twinned''}$ ($\alpha_{\text{“}detwinned''}$) will increase (decrease) and the value of the integral will be smaller than the real δ.

3.2. Experimental results for the (Ba,K)Fe_2As_2 system

The uniaxial thermal expansion of more than 70 samples of (Ba,K)Fe_2As_2 (see appendix C) was measured for this work. The a-axis, (twinned ab average for the underdoped samples), and c-axis length changes of a small selection of them are shown in Fig. 3.4 as an overview. Anomalies at T_s or T_c are very small in comparison to the total length change. Especially striking is that the total a-axis length change is strongly enhanced by K substitution. On the other hand, K substitution has only little effect on the total c-axis length change.

Anomalies at the phase transitions can be seen much clearer in the temperature derivative of these data, i.e., the thermal-expansion coefficients. Fig. 3.5 shows the in-plane thermal-expansion coefficient α_a of the samples from Fig. 3.4. Anomalies at T_s and T_c are very sharp. The anomaly at T_s changes sign from positive to negative between 0% and 22% K content. Note again that a positive (negative) anomaly is defined as an increase (a decrease) on decreasing T through the transition. The step-like anomaly at T_c has the opposite sign to the anomaly at T_s, which signals the competition between the orthorhombic phase and superconductivity, same as in Ba(Fe,Co)$_2$As$_2$. However, all signs are inverted with respect to Ba(Fe,Co)$_2$As$_2$, a result which will be discussed below.

To establish the systematic evolution of the thermal expansion, Fig. 3.6 presents a larger selection of in-plane measurements. The anomaly at T_s changes sign between 0% and 17% K content and shows a rather complicated structure at 22% and 25%, see below. However, no distinct two transitions, which would indicate a splitting of the magneto-structural transition, can be identified. We conclude therefore that the magnetic and structural transition remain coincident upon K substitution with $T_s = T_N = T_{s,N}$. The thermal expansion of samples with $22\% - 25\%$ K content is negative between $T_{s,N}$ and T_c, while the anomaly at T_c is positive and rather large. Samples that do not undergo the structural transition ($x \geq 0.28$), on the other hand, show a sharp negative step at T_c. It is worth noting that a few samples were found (e.g., with 28% K content and $T_c = 33$ K) that were underdoped, i.e., their T_c was below the optimal value of 38.3 K, but did not undergo the structural phase transition. The value of the normal-state thermal expansion increases significantly with K substitution on the overdoped side in accord with the lengths changes.

Figures 3.6 (c), (d) show our c-axis data. The morphology of the samples (thin platelets) made reliable measurements of the c-axis thermal expansion rather difficult, a problem already encountered in the Ba(Fe,Co)$_2$As$_2$ system [11]. Therefore, only a very limited number of reliable measurements were successful and

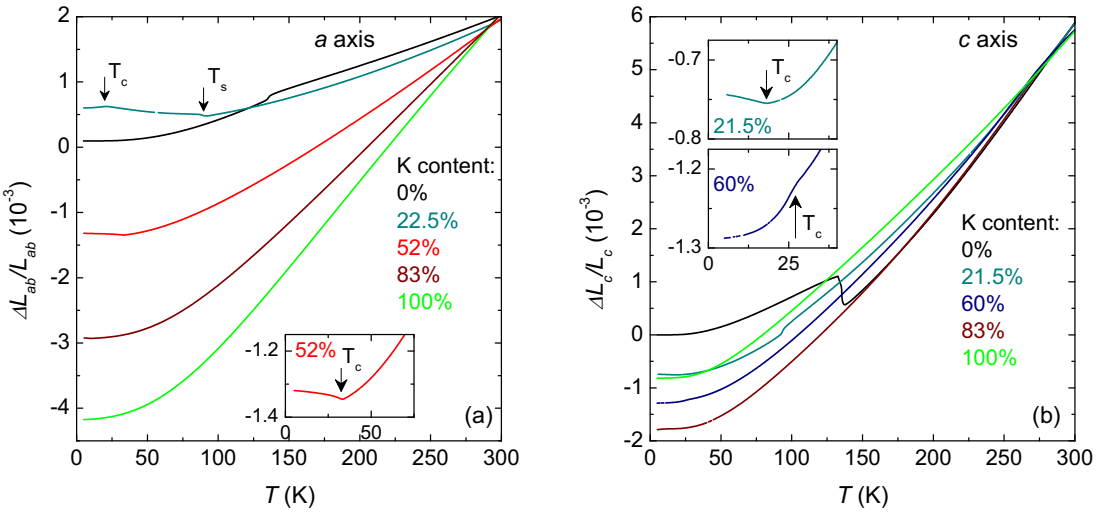

Figure 3.4.: Relative in-plane (a) and c-axis (b) length change of a selection of (Ba,K)Fe_2As_2 single crystals across the phase diagram. The twinned ab average is shown for the underdoped samples. Insets show data close to T_c on an expanded vertical scale.

are shown. The sharp peak at T_s changes sign between 0% and 21.5% K content and the step-like anomaly at T_c changes sign between 21.5% and 36% K content. All anomalies have opposite sign and similar shape as compared to the average in-plane measurements.

The thermal expansion of the orthorhombic b axis, α_b, measured on *in-situ* detwinned samples, shows a sharp positive peak at T_s and a negative, step-like anomaly at T_c (Fig. 3.7). This is identical to what was observed in $Ba(Fe,Co)_2As_2$ and to be expected for the shorter orthorhombic axis. The jump in the relative length changes $\Delta L_b/L_b$ establishes the structural transition as a first-order transition, which is emphasized by the extremely sharp peaks at the transition (Fig. 3.7(d)). The marked increase of $\Delta L_b/L_b$ below T_c indicates that the orthorhombic distortion is reduced by the onset of superconductivity also in (Ba,K)Fe_2As_2. On the other hand, only very small effects are seen at $T_{s,N}$ and T_c in the twinned average $\Delta L_{ab}/L_{ab}$ (Fig. 3.7 (c)).

$T_{s,N}$ manifests itself as a predominantly negative anomaly in α_{ab}, which usually consists of several sharp negative and positive peaks over a certain temperature interval. Even the smallest (presumably most homogeneous) and best-aligned

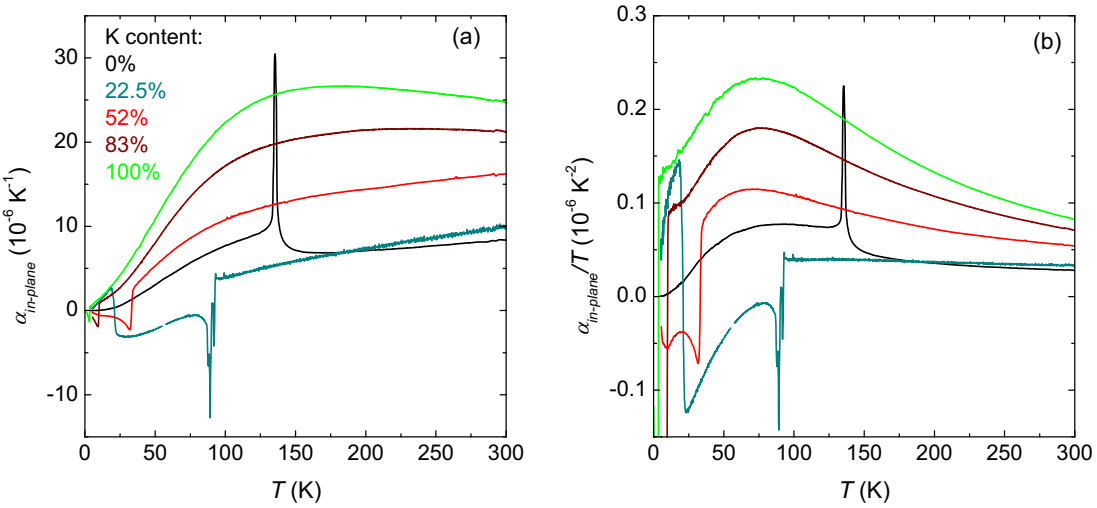

Figure 3.5.: In-plane thermal expansion coefficient α_a (a) and α_a divided by T (b) of the selection of (Ba,K)Fe_2As_2 single crystals from Fig. 3.4. The twinned ab average is shown for the underdoped samples.

samples show such a structure of the transition. Fig. 3.7(d) shows a comparison of the data in twinned and detwinned state. Note that the measurements of α_{ab} and α_b at $\approx 22\%$ K content were not performed on the identical sample. $T_{s,N}$ is clearly defined only in α_b, while the structure associated with $T_{s,N}$ extends over a much larger temperature interval in α_{ab}. We attribute it to a domain effect at the first-order transition. Within a region close to T_s, structural domains easily switch orientation, which results in the peaks in α_{ab}. By detwinning, one type of domains is favored and no such switching can occur.

Shortly before the end of this work, samples with 26%-28% K content, i.e., close to the endpoint of the magneto-structural transition line became available (see Fig. 3.8). Several samples show a surprising sequence of four phase transitions, which are very sharp for the sample with 26.2(3)% K content (see, e.g., Fig. 3.8). On decreasing T, the familiar magneto-structural phase transition with $T_{s,N} = 56$ K is crossed first. Then, another first-order phase transition at $T_1 = 31.5$ K, which presumably brings the sample back to a tetragonal state, is signaled by a negative peak in α_b. Within this new phase, there is a superconducting transition with $T_c = 25.8$ K, which was confirmed by magnetization and specific-heat measurements. No anomaly at T_c is visible in α_b due to its strong temperature dependence and the step-like anomaly in α_{ab} at T_c is about three times smaller than for "normal" tetragonal samples (e.g. 28.3%). Finally,

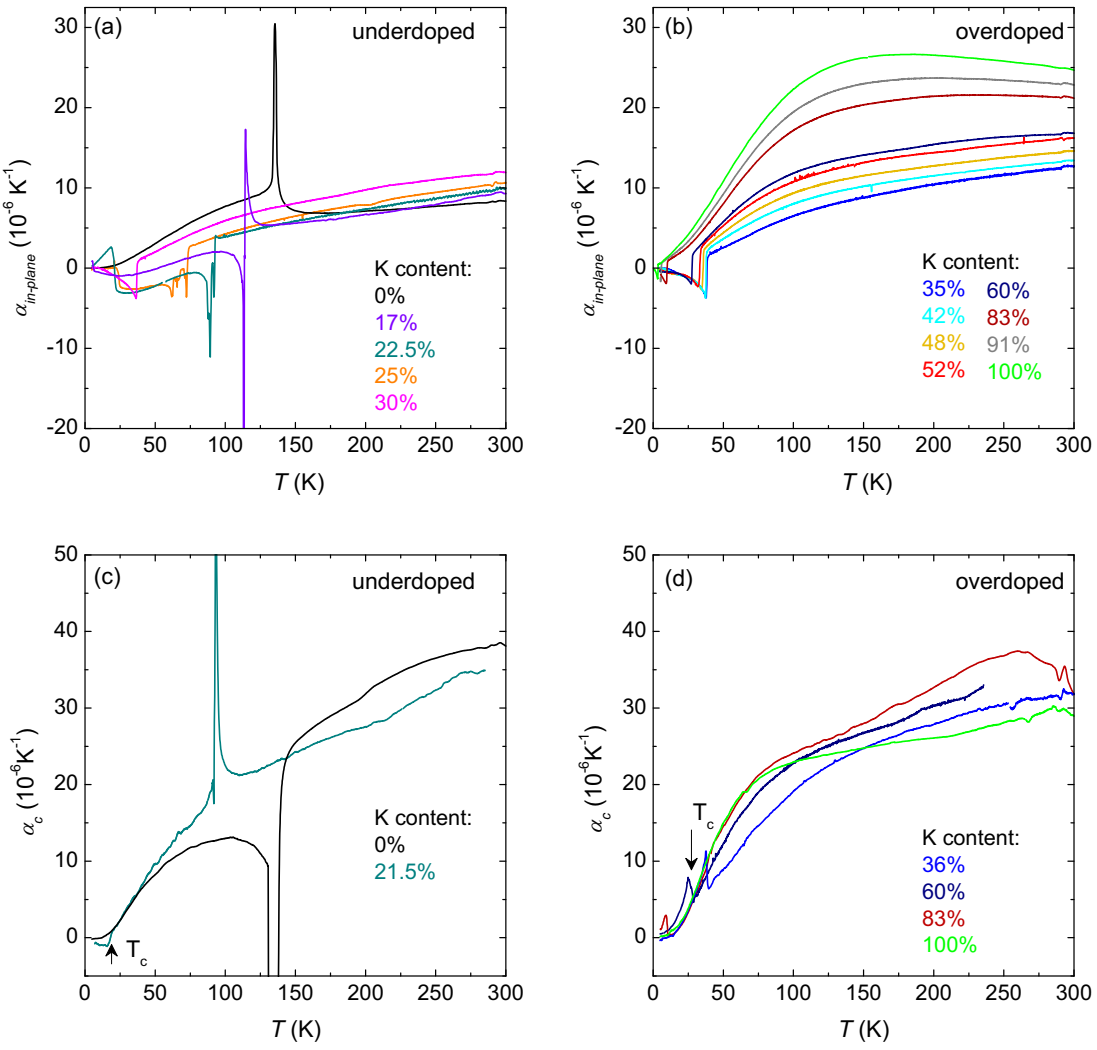

Figure 3.6.: (a), (b) In-plane thermal-expansion coefficients of underdoped and overdoped (Ba,K)Fe_2As_2, respectively. The *ab* average is shown for samples which have an orthorhombic ground state. (c), (d) *c*-axis thermal-expansion coefficients of underdoped and overdoped (Ba,K)Fe_2As_2, respectively.

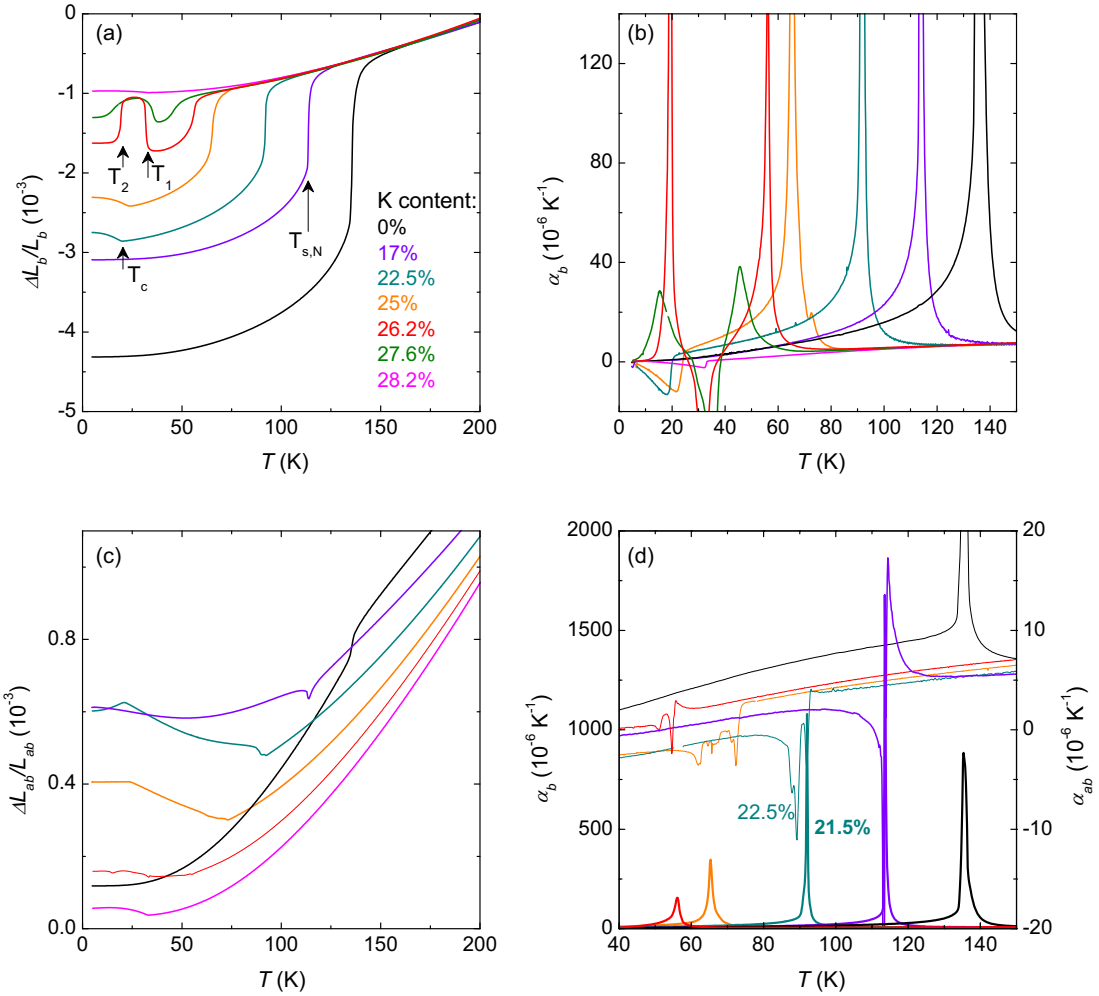

Figure 3.7.: (a) *b*-axis length change and (b) thermal-expansion coefficients of underdoped (Ba,K)Fe_2As_2, obtained via *in-situ* detwinning in the dilatometer. (c) shows the average in-plane length change L_{ab} and (d) contrasts the anomalies at $T_{s,N}$ observed in the thermal-expansion coefficient α_{ab} with the much sharper anomalies in α_b. The measurements at $\approx 22\%$ K content were conducted on two different samples, the other ones on the identical sample.

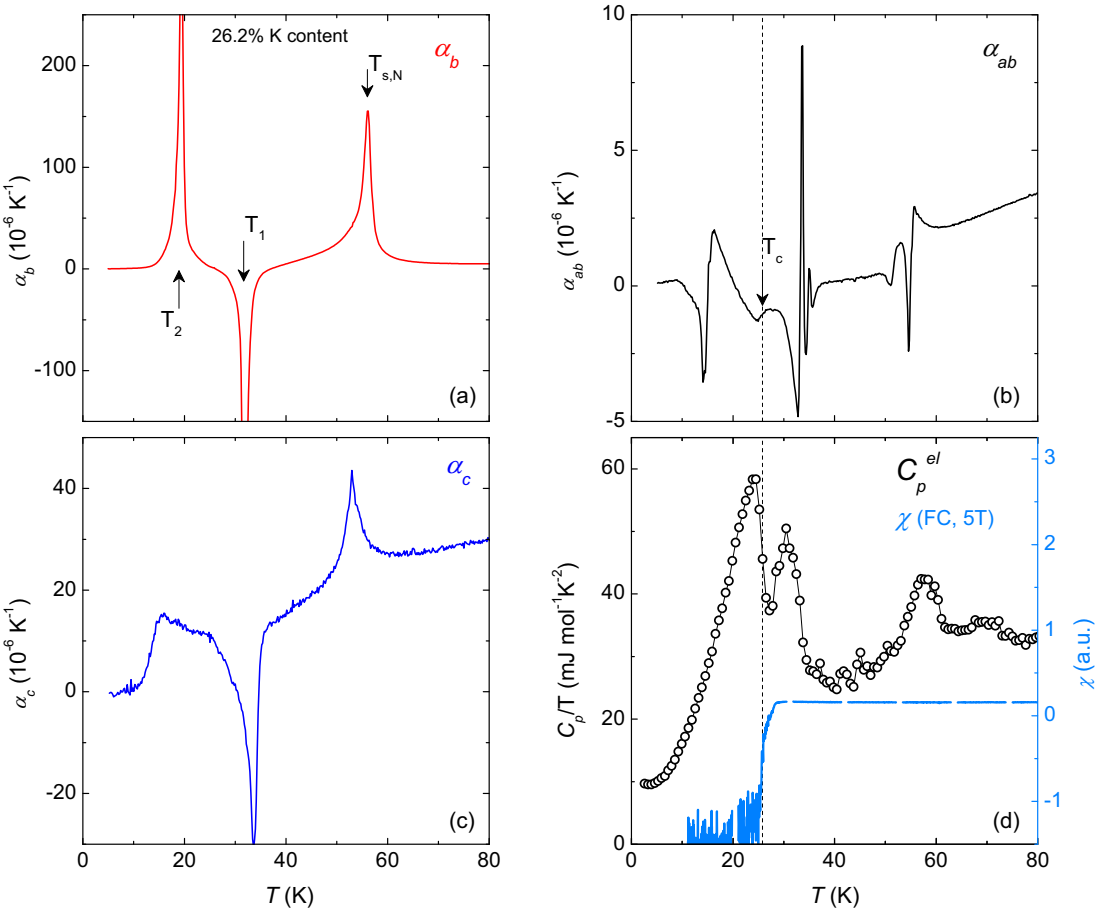

Figure 3.8.: Thermodynamic data of samples (Ba,K)Fe_2As_2 samples exhibiting the new phase. (a) b-axis thermal expansion, clearly revealing three structural phase transitions. An anomaly at T_c is presumably hidden by the huge temperature dependence of the background (compare the vertical scale of (a) and (b)). (b) Average in-plane thermal expansion, measured in the twinned state, showing complicated structures at $T_{s,N}$, T_1 and T_2 and a slightly broadened step-like anomaly at T_c. (c) c-axis thermal expansion showing clearly $T_{s,N}$, T_1 and T_2 and a kink which can be associated with T_c. (d) Electronic specific heat and magnetic susceptibility (measured in 5 T under field-cooled conditions). The specific heat clearly shows all transitions except for the lower structural one. A possible residual density of states at low T may suggest phase separation. The susceptibility clearly shows diamagnetic shielding, however, with a possible two-step transition at an onset higher than the bulk T_c from C_p and α_{ab}. α_{ab}, α_b, C_p and χ were measured on (pieces of) the same sample, while α_c was measured on another one.

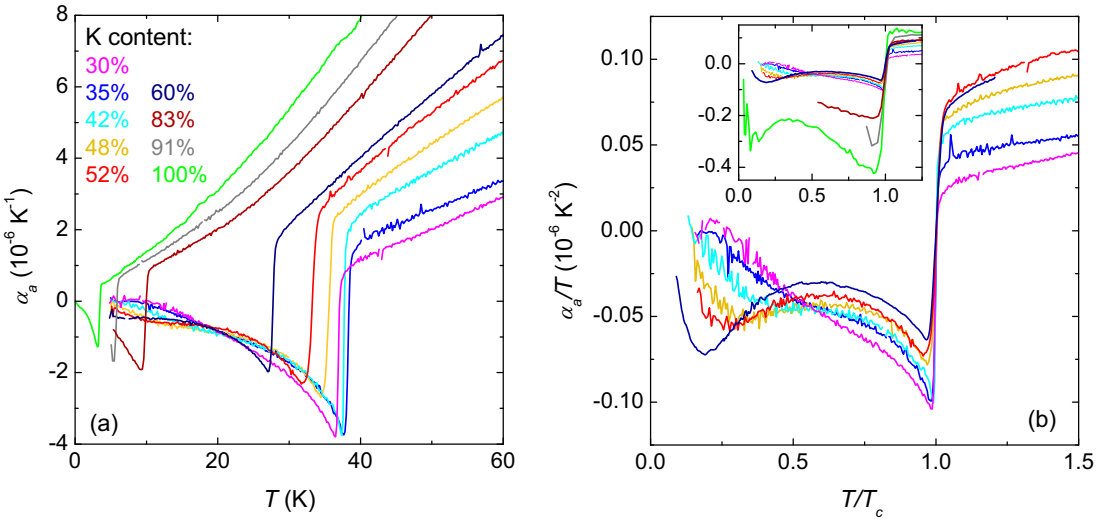

Figure 3.9.: (a) The superconducting transition in α_a of (Ba,K)Fe_2As_2 samples with tetragonal ground state. (b) Thermal-expansion coefficients divided by temperature plotted vs. reduced temperature T/T_c revealing a structure and its continuous evolution with K substitution below T_c. The inset shows the same data on an enhanced vertical scale to comprise also the samples with high K content. Low-temperature data of KFe_2As_2 were kindly provided by D. Zocco [52], and data on the sample with 60% K content in panel (b) by P. Burger.

another, presumably tetragonal-to-orthorhombic, transition occurs at $T_2 \sim 19$ K, well inside the superconducting phase. This last transition has a very small signature in the specific-heat data which indicates a tiny entropy change at this transition. Consistently, the transition seems to be extremely sensitive to uniaxial pressure. Finally, the specific heat seems to indicate a residual density of states in the superconducting state at low temperature. This may be a sign of phase separation or of a very small superconducting gap and needs to be studied further. Another sample with slightly higher K content (27.6(3)%) shows similar, but slightly broader transitions, while a sample with 28.2(3)% K content only undergoes the superconducting transition and has a tetragonal ground state.

The superconducting transition of samples with tetragonal ground state (i.e., $\geq 28.3\%$ K content) is presented in Fig 3.9 in more detail. The low-temperature data of pure KFe_2As_2 sample were provided by D. Zocco, [52], and additional data on a sample with 60% K content by P. Burger. The negative anomalies at T_c are all very sharp (less than 1 K in width). A rich structure of the curves below T_c and its continuous evolution with K substitution is seen more clearly in α/T

(panel (b)). The normal-state value of α/T increases with K substitution, while the discontinuity $\Delta\alpha/T_c$ stays approximately constant between 30% and 60% K content. A hump at $\sim 0.2 - 0.25T/T_c$ changes sign from positive to negative and shifts slightly to lower reduced temperature T/T_c with increasing K content. α_a/T below T_c starts to become increasingly more negative between 60% and 80% K, while the curves retain their general shape up to 100% K content (see inset). In section 3.3.3 these curves will be analyzed in detail and it will be shown that the structure arises from the multiband nature of the compounds.

3.3. Discussion

The discussion of our extensive thermal-expansion data on the $(Ba,K)Fe_2As_2$ system is structured as follows. First, the phase diagram is mapped out from thermal expansion. We find a new, very narrow, phase close to the end point of the magneto-structural phase-transition line and discuss the interplay between the orthorhombic-magnetic state and superconductivity. Then, the electronic thermal expansion in the normal state, which is related to the electronic density of states, is considered. Next, the pressure derivatives of the parameters related to superconductivity, namely the transition temperature T_c, the electronic density of states γ and the gap $\Delta(0)/T_c$, are obtained from analysis of the thermal expansion in the superconducting state within the two-band alpha-model. Using these results, the relationship between K substitution and uniaxial pressure is discussed. Finally, we discuss the proposed relation [53] between ideal tetrahedral Fe-As-Fe angle and optimal T_c in the $(Ba,K)Fe_2As_2$ system.

3.3.1. Phase diagram and interplay of magnetism and superconductivity

The orthorhombic order parameter was computed from data on twinned and detwinned samples of underdoped $(Ba,K)Fe_2As_2$ as $\delta = \int (\alpha_{ab} - \alpha_b)\, dT$ (see note 4 on page 24) and is shown in Fig. 3.10. Naturally, this formula is only valid if the distortion really is a shear strain between the tetragonal in-plane axes, as it is the case for $BaFe_2As_2$. The orthorhombic order parameter $\delta(T)$ jumps discontinuously at $T_{s,N}$, demonstrating the first-order character of the structural transition, at least down to $T_{s,N} \sim 70$ K at 25% K content. A high-temperature tail presumably arises from the finite stress applied during the measurement. δ is significantly reduced below T_c, which is also shown by the large jump in $d\delta/dT$ at T_c. Surprisingly, we observe a pocket of a possible tetragonal phase between $\sim 20 - 30$ K, at $\sim 26\% - 28\%$ K content. In a first-order-like transition at

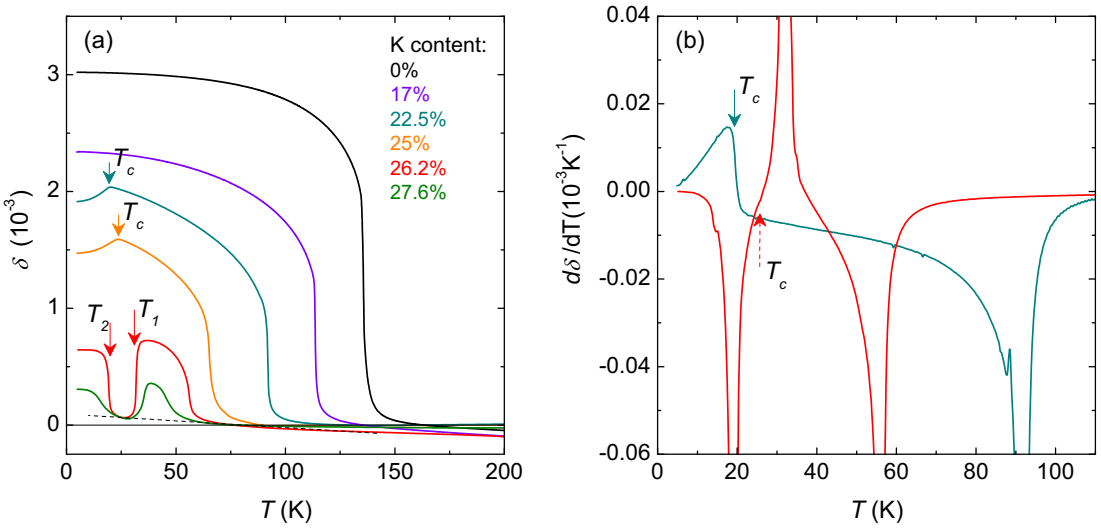

Figure 3.10.: (a) Orthorhombic order parameter δ of underdoped (Ba,K)Fe_2As_2 computed from thermal expansion. The finite distortion above T_s is due to uncertainties in the experiment and the stress applied for detwinning the sample. A clear reduction of δ below T_c (marked by arrows) is visible at 22% and 25% K content. For 26.2% and 27.6% K content, δ is presumably reduced to zero below T_1 (see dashed line). (b) shows the temperature derivative $d\delta/dT$ of two superconducting samples. While a large anomaly marks $T_c \approx 20$ K within the orthorhombic state, no anomaly is seen at $T_c = 25.8$ K (dashed arrow, determined from C_p, see Fig. 3.8) within the new phase.

$T_1 < T_{s,N}$, δ is strongly reduced, presumably to zero. Upon decreasing T within this "new phase", the sample undergoes the superconducting transition, however, no anomaly could be resolved in the temperature derivative $d\delta/dT$ at T_c. Within the superconducting phase, δ increases in a step-like fashion again, suggesting another, first-order-like, tetragonal-to-orthorhombic phase transition.

The strong reduction of δ below T_c between 17% and 25% K content demonstrates that superconductivity and the orthorhombic-magnetic state compete. Such a behavior was previously reported for polycrystalline (Ba,K)Fe_2As_2 [54] and for single crystals of, e.g., $Ba(Fe,Co)_2As_2$ [30] and $BaFe_2(As,P)_2$ [12]. It is taken as indication that magnetism and superconductivity coexist homogeneously [29, 30, 55]. In strong contrast, no anomaly in δ (or $d\delta/dT$) is observed at T_c within the new phase. This is expected if this phase has tetragonal symmetry, because the pressure derivatives of T_c along [100] and [110] are identical in a tetragonal system.

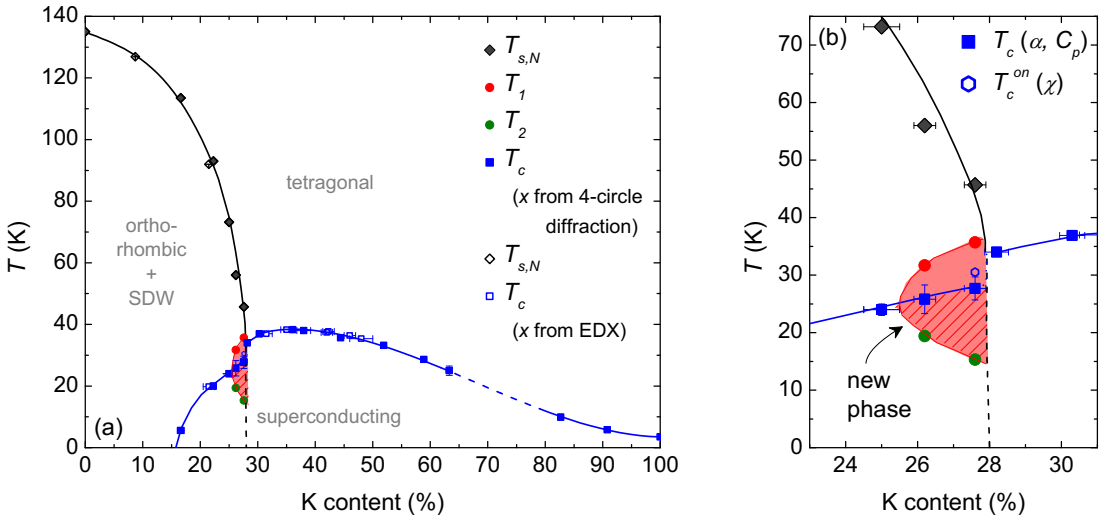

Figure 3.11.: Phase diagram of (Ba,K)Fe_2As_2 determined from our thermal-expansion measurements. The K content was determined by 4-circle x-ray refinement or energy-dispersive x-ray spectroscopy on the same samples. A pocket of a new, presumably tetragonal, phase is tentatively indicated. (b) enlarged view of the region in which the new phase is observed. T_c was determined by the bulk probes C_p or α_{ab}. The onset of the superconducting transition of the sample 27.6% K content in dc magnetization (zero-field cooled, 50 Oe) is also shown.

The phase diagram of (Ba,K)Fe_2As_2 has been compiled from the anomalies at $T_{s,N}$ and T_c in the thermal expansion coefficients and electronic specific heat, and is shown in Fig. 3.11. For the structural transitions, data on detwinned samples, which show sharp peaks, have been used. The K content $x = 0 - 1$ was determined by 4-circle x-ray refinement or energy dispersive x-ray analysis on the same samples on which the thermal expansion was performed. Batches in which thermal-expansion anomalies were unusually broad, had an anomalous shape or samples with double transitions were discarded (see appendix C).

$T_{s,N}$ is found to be suppressed by K substitution initially at a relatively slow rate. For example, $T_{s,N}$ decreases only from 135 K to 118 K under the substitution of 17% K. The suppression becomes more rapid beyond this value and the magneto-structural phase-transition line becomes very steep around 26% K content. $T_{s,N}$ remains first order at least up to 25% K content and there is no evidence for a splitting between T_s and T_N. Very close to the end point of the $T_{s,N}$-line, we find a possible very narrow pocket of a new phase, which seems to coexist with superconductivity. Within this new phase, the orthorhombic or-

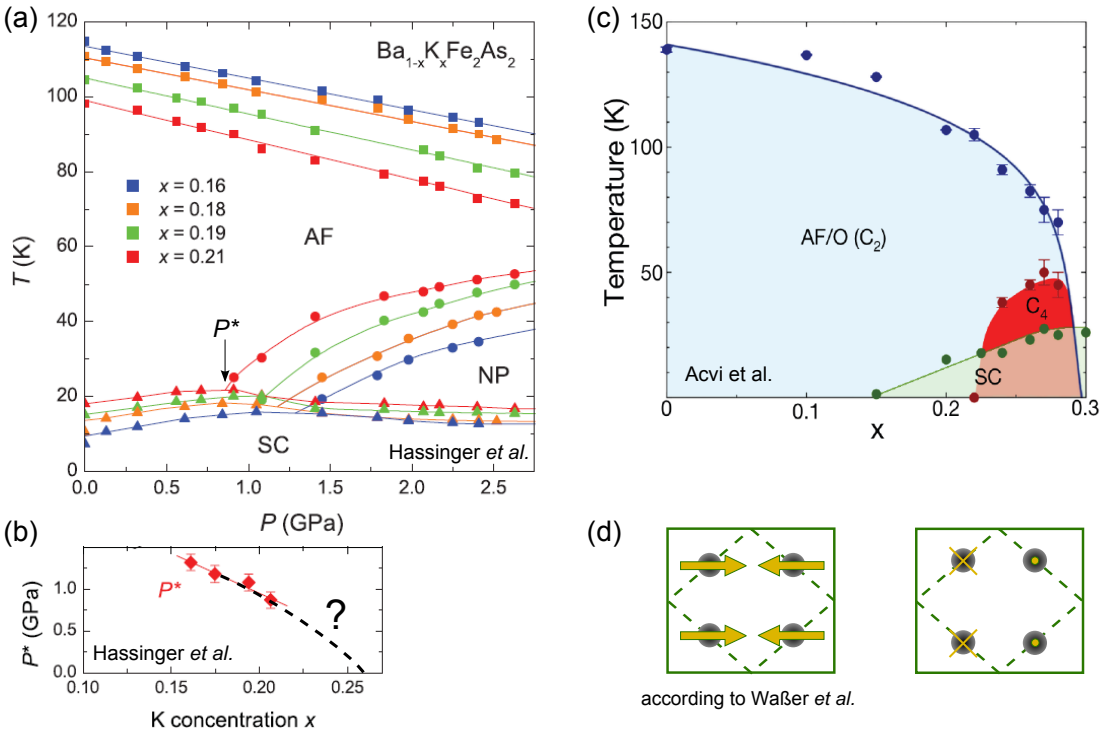

Figure 3.12.: (a) Pressure-temperature phase diagram of underdoped (Ba,K)Fe_2As_2, featuring a "new phase" above a critical pressure P^*, within the magnetic phase, from Ref. [56] (b) P^* as a function of K content. The dashed line is a tentative extrapolation, suggesting that we may observe the same phase at ambient pressure. (c) Phase diagram of (Ba,Na)Fe_2As_2 showing a second magnetic phase, claimed to have C_4 symmetry, from Ref. [57]. (d) Schematic drawing of the usual magnetic structure of the pnictides (left, see Fig. 2.2 (b)), and a proposed structure of the second magnetic phase in (Ba,Na)Fe_2As_2, in which magnetic moments are aligned along the c axis but keep the stripe-type C_2 symmetry (right), from [58].

der parameter presumably vanishes. Neutron scattering studies show a similar phase transition to a possible C_4 magnetic phase [57] between T_s and T_c in Na substituted $BaFe_2As_2$ with $24\% - 28\%$ Na content (see Fig. 3.12). In another study on (Ba,Na)Fe_2As_2, it has been proposed [58] that the iron moments rotate and align along the c axis in a way that preserves the stripe-type structure at this transition. Also, a significant reduction of the magnetic moment below T_c has been observed, possibly indicating competition between the new magnetic phase and superconductivity[58]. However, reentrance of the original orthorhom-

bic phase coexisting with superconductivity, as seemingly observed here, has not been reported to date.

Resistivity data under hydrostatic pressure in underdoped (Ba,K)Fe_2As_2 (16%−21% K content) also show a new phase that sets in between $T_{s,N}$ and T_c and competes with superconductivity [56]. It was suggested that this phase is a second spin-density wave. We may conjecture that the same phase is observed here at 26%-27% K content under ambient pressure conditions, since the critical pressure above which the new phase is observed, possibly extrapolates to zero at this value (see Fig. 3.12). The reentrance of an orthorhombic structure below T_c can, naturally, not be observed by resistivity measurements. However, additional measurements are necessary to uncover the nature of the new phase reported here, and the possibility of electronic phase separation needs to be investigated.

A close look at the phase diagram determined by bulk probes reveals a step-like increase of T_c as a function of K content at the point where $T_{s,N}$ vanishes. This indicates that T_c is reduced by the competition with the other phases. The orthorhombic-magnetic phase is suppressed by K substitution in a first-order-like fashion (see results of chapter 4) at $\approx 28\%$ K content, which is presumably the cause of the abrupt increase of T_c. The maximum T_c of 38.3 K is, however, reached only around 35% K content, which is beyond the point where the structural transition vanishes. The superconducting dome is very wide and extends to 100% K substitution. Despite considerable effort, sample growth did not succeed in the range between 63% and 83%, suggesting a possible miscibility gap at high temperature in the composition-temperature phase diagram.

A detailed phase diagram of (Ba,K)Fe_2As_2 has also been reported in Refs. [51, 59], determined from neutron and x-ray diffraction and SQUID magnetization measurements. The results are for the most part consistent with ours. In particular, the diffraction experiments provide clear evidence that the magneto-structural transition remains coincident and first-order at least down to $T_{s,N} = 100$ K. No structural transition with $T_s \lesssim 75$ K has been reported, which is presumably the reason why the narrow pocket of the new phase was not found. However, T_c was found to increase linearly on the underdoped side, at odds with our results. Yet, T_c was determined using SQUID magnetization measurements on powder samples, which is presumably less accurate than our bulk measurements of single crystals. A comparison between phase diagrams obtained by different kinds of substitution in $BaFe_2As_2$ will be shown in the concluding section of this chapter.

3.3.2. Normal-state thermal expansion and the electronic density of states

Thermal-expansion coefficients divided by temperature are of interest because, apart from a phonon contribution, they are given by the pressure derivative of the density of states of a Fermi liquid (see eq. 2.6). Fig. 3.13 shows the in-plane thermal expansion divided by temperature in the normal state of (Ba,K)Fe_2As_2. Also plotted are values at 50 K and 200 K as a function of K content. A kink between 25% and 28% K content is evident even at 200 K. Such a behavior is suggestive of a Lifshitz transition, i.e., a topological change of the Fermi surface upon substitution. It is curious that such a transition would occur just at the concentration at which the ground state changes from orthorhombic-magnetic to tetragonal. α/T at 50 K shows a discontinuous increase in this concentration range which is a consequence of the reduced the density of states in the orthorhombic-magnetic phase and indicative of a first-order transition on increasing K content. Above 28% K content, α/T increases linearly as a function of substitution, indicating an increasingly pressure-sensitive density of states.

In order to study how the density of states, or the electronic entropy, responds to uniaxial pressure in more detail, one needs to subtract the phonon contribution α^{ph} from the thermal expansion. The phonon background of the Ba(Fe,Co)$_2As_2$ system, namely data of a Ba($Fe_{0.67}Co_{0.33}$)$_2As_2$ sample [11], is presumably also appropriate for the low-K-content part of the (Ba,K)Fe_2As_2 system. As in Ref. [60], we assume that it is indeed appropriate for the whole (Ba,K)Fe_2As_2 series. One needs to keep in mind that this is a rather crude approximation. In fact, the average mass of the K ion (39 g/mol) is significantly smaller than that of a Ba ion (137 g/mol), which may change the phonon spectrum and hence the lattice thermal expansion. Yet, the electronic contribution is rather large at high K content, so that an accurate determination of α^{ph} is less crucial. Here, mainly the a-axis data is analyzed, because the electronic contribution to the c-axis expansion is relatively small and therefore hard to determine. The very narrow region of the new phase will not be considered.

Fig. 3.14 shows the electronic thermal expansion $\alpha_a^{el}/T = \alpha_a/T - \alpha_a^{ph}/T$ of the (Ba,K)Fe_2As_2 series. Several points are worth notice. First, α_a^{el}/T of pure $BaFe_2As_2$ is vanishingly small below T_s (interpreted as a result of quenched electronic degrees of freedom [11]). Yet, a negative contribution below T_s evolves with K substitution, which shows pronounced non-Fermi-liquid behavior at 22.5% K content. A similar contribution emerging under Co substitution is positive [11]. Samples with $\geq$ 28% K content remain tetragonal down to the lowest temperatures. α_a^{el}/T in the normal state of the sample with 30% K content is nearly constant as a function of temperature at a rather small negative value. On in-

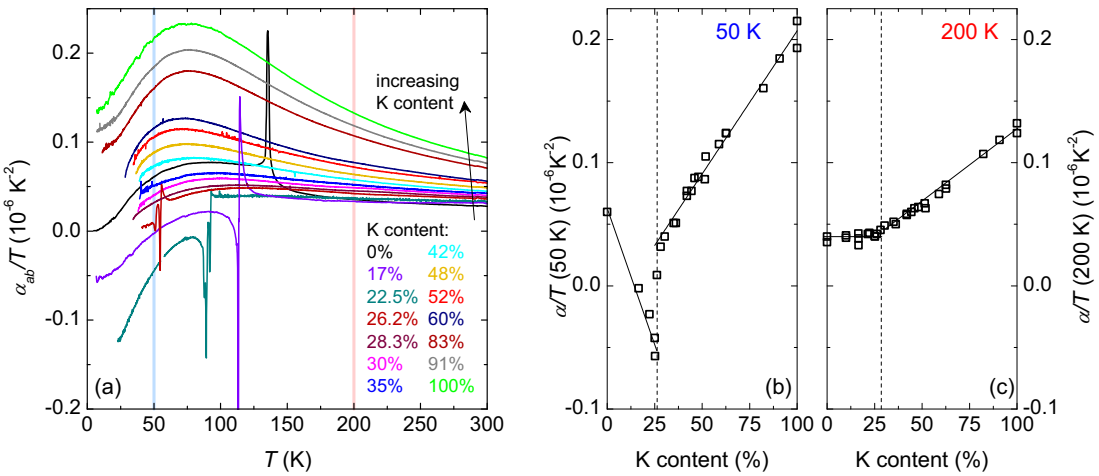

Figure 3.13.: (a) In-plane thermal-expansion coefficients α_a/T of (Ba,K)Fe_2As_2 divided by temperature (twinned ab average for samples with a structural phase transition). (b), (c) Values of $\alpha_{in-plane}/T$ at 50 K and 200 K, respectively, as a function of K content.

creasing the K substitution, α_a^{el}/T increases and starts to develop a hump-like feature around $\sim 50-75$ K. This is most pronounced for highly overdoped samples ($80-100\%$ K content), where clearly α_a^{el}/T passes through a broad maximum on decreasing T and is constant with relatively elevated values at low temperatures.

The magnetic susceptibility of pure KFe_2As_2 has a very similar temperature dependence as its electronic thermal expansion [60]. Its behavior is analyzed in detail in Ref. [60] and shown to reflect a temperature-driven incoherence-coherence crossover into a strongly correlated state at low temperatures. This low-temperature state, out of which superconductivity arises, is a heavy Fermi-liquid state as demonstrated by the T^2 temperature dependence of the electrical resistivity, and the strongly enhanced Sommerfeld coefficient ($\gamma = 102$ mJ/mol/K^2) and Pauli susceptibility ($\chi = 4 \times 10^{-4}$) [60]. The strong correlations have been shown to be well described by close proximity of KFe_2As_2 to an orbital selective Mott transition [60, 62].

The uniaxial pressure derivative $d\gamma/dp_a$ can be simply read off the flat Fermi-liquid-like part of α_a^{el}/T for samples with $> 80\%$ K content. At lower K content, such a Fermi-liquid-like state is not reached above T_c. Therefore, we scale α_a^{el}/T of samples with $> 40\%$ K content onto α_a^{el}/T of pure KFe_2As_2 (see Fig. 3.15 (a)) in order to obtain $d\gamma/dp_a$ of the hypothetical low-temperature Fermi-liquid

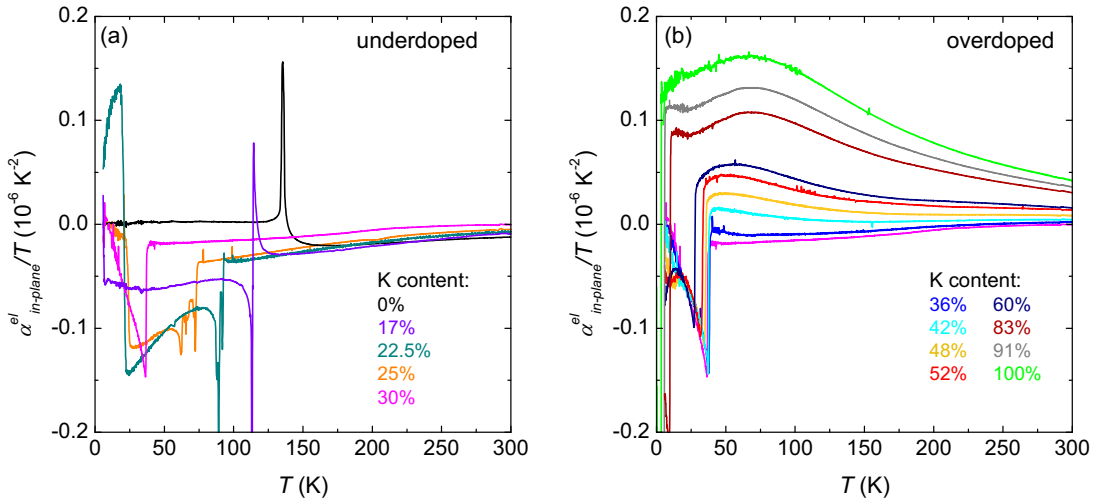

Figure 3.14.: Electronic in-plane thermal expansion of (a) underdoped and (b) overdoped (Ba,K)Fe_2As_2 divided by temperature. As an approximate lattice background the data of $Ba(Fe_{0.67}Co_{0.33})_2As_2$ have been subtracted. The *ab* average is shown for samples which undergo the magneto-structural transition.

state of these samples. For even lower K contents, a linear extrapolation of α_a^{el}/T to low temperature is used [5]. Note that most of these samples, except for $Ba_{0.775}K_{0.225}Fe_2As_2$, are nearly Fermi-liquid-like. Fig. 3.15 (b) presents the doping evolution of γ [61] and $d\gamma/dp_a$. γ increases on K substitution between $0\% - 24\%$, when magnetism is weakened. It then seems to reach a plateau of ~ 50 mJ/mol/K^2 between 30% and 60% K content and finally increases to 102 mJ/mol/K^2 for pure KFe_2As_2. No indication for non-Fermi-liquid behavior was found in C_p [61]. However, specific heat is expected to be less sensitive to it than thermal expansion. $d\gamma/dp_a$ is positive for low K content with a peak just below the point of disappearance of magnetism. It decreases linearly upon further K substitution with a sign change around 35% K content and reaches $d\gamma/dp_a = -8.7$ mJ mol^{-1}K^{-2}/GPa for KFe_2As_2. This linear decrease was found to be so robust that a simple linear interpolation of the value of, e.g., $\alpha/T(100\text{ K})$ is a reliable and easy way to determine the K content of a new sample. It is also an indication that the normal-state electronic structure does not change significantly between 60% and 80% K content, the range in which no samples are available.

5. We consider the density of states out of which superconductivity arises, i.e., in the orthorhombic-magnetic state for underdoped samples.

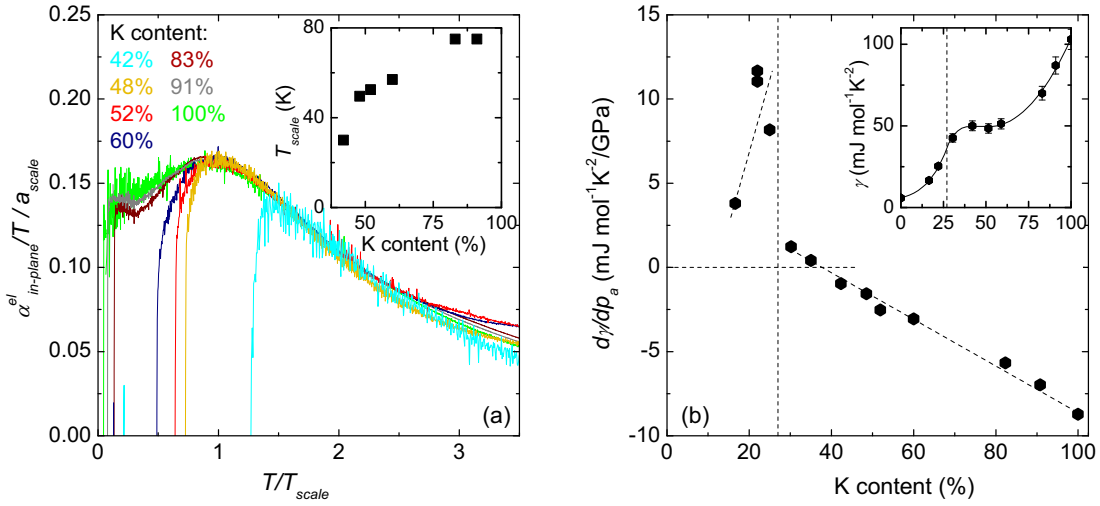

Figure 3.15.: (a) Electronic thermal expansion α_a^{el}/T of samples with $> 40\%$ K content scaled onto the data of KFe_2As_2. The inset presents the temperature T_{scale}. (b) The in-plane pressure derivative $d\gamma/dp_a$, obtained from the zero-temperature intercept of α_a^{el}/T for $x < 0.4$ and from scaling α_a^{el}/T to the curve of pure KFe_2As_2 for samples with $> 40\%$ K content in (a). The inset shows the Sommerfeld coefficient γ of (Ba,K)Fe_2As_2 [61]. Lines are a guide to the eye.

It is interesting to compare the pure KFe_2As_2 with its isovalent compounds $RbFe_2As_2$ and $CsFe_2As_2$. The Sommerfeld coefficient of KFe_2As_2 is quite large with 102 mJ mol^{-1}K^{-2}. It increases to $\gamma = 127$ mJ mol^{-1}K^{-2} for $RbFe_2As_2$ [63] and reaches 176 mJ mol^{-1}K^{-2} in $CsFe_2As_2$ [61]. These values reach the order of magnitude of light heavy-Fermion systems and motivate the comparative study of these three compounds, because they are expected to display the same physics with the largest electronic effects in $CsFe_2As_2$.

Fig. 3.16 presents the uniaxial thermal expansion of KFe_2As_2, $RbFe_2As_2$, and $CsFe_2As_2$. The thermal expansion of the Rb- and Cs-based compounds is much larger than the thermal expansion of KFe_2As_2, but with qualitatively the same temperature dependence. α_a/T is constant at low temperatures and passes through a maximum on increasing T. The low-temperature value of α/T is very large with 0.33×10^{-6} K^{-2} and 1×10^{-6} K^{-2} for $RbFe_2As_2$ and $CsFe_2As_2$ respectively, as compared to 0.14×10^{-6} K^{-2} in KFe_2As_2. The lattice contribution to α is expected to be of similar magnitude as for the other 122 compounds, hence the measured thermal expansion of $RbFe_2As_2$ and, especially, $CsFe_2As_2$ is largely dominated by the electronic contribution. Its temperature dependence,

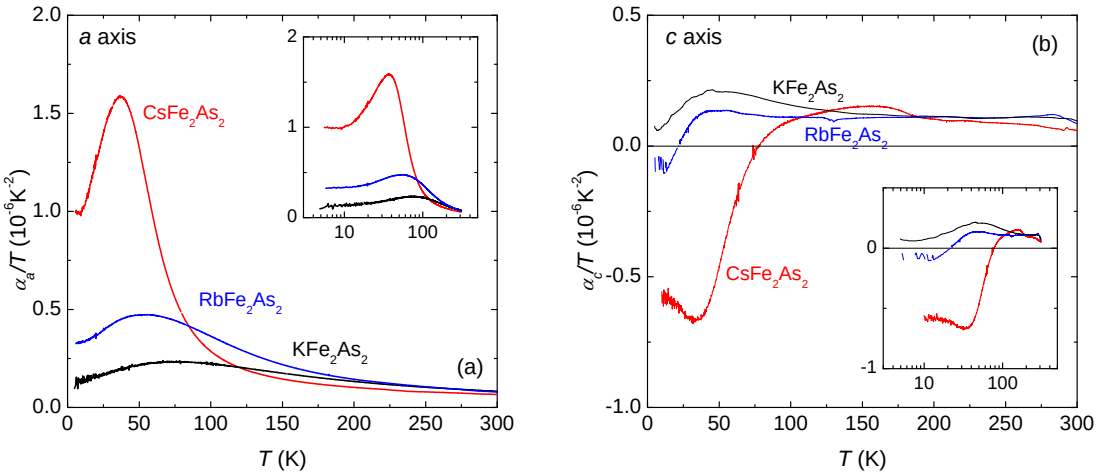

Figure 3.16.: (a) a-axis and (b) c-axis thermal-expansion coefficients divided by T of KFe_2As_2, $RbFe_2As_2$ and $CsFe_2As_2$. Insets show the same data on a logarithmic temperature scale. α_a/T of $RbFe_2As_2$ and $CsFe_2As_2$ shows qualitatively the same temperature dependence as α_a^{el}/T of KFe_2As_2, however, values are much larger. The constant α/T at low temperatures demonstrates the formation of a Fermi-liquid-like state.

which closely resembles α_a^{el} obtained for KFe_2As_2, confirms that the background subtraction in the (Ba,K)Fe_2As_2 system is essentially correct. The fact that the electronic contribution dominates the thermal expansion of $CsFe_2As_2$ offers also the possibility to study α^{el}/T along the c axis. The data in Fig. 3.16 show that the α_i/T have very little anisotropy at high temperature. However, α_c/T decreases on lowering the temperature, changes sign and eventually becomes nearly constant at the rather large, negative value of -0.6×10^{-6} K^{-2} for $CsFe_2As_2$.

The data show that not only γ increases on passing from KFe_2As_2 to $RbFe_2As_2$ and $CsFe_2As_2$, but also $d\gamma/dp_a$ and the relative pressure derivative $(1/\gamma)(d\gamma/dp_a)$ (Fig. 3.17), which amounts to -0.086 GPa^{-1}, -0.19 GPa^{-1} and -0.40 GPa^{-1} for KFe_2As_2, $RbFe_2As_2$ and $CsFe_2As_2$, respectively (see Fig. 3.17). The fact that γ of $CsFe_2As_2$ is more stress sensitive than γ of KFe_2As_2 points to the close proximity of $CsFe_2As_2$ to an instability. Plausibly, $CsFe_2As_2$ is simply closer to an orbital selective Mott transition than KFe_2As_2 [60].

As to the anisotropy of the uniaxial-pressure derivatives of the density of states, one obtains $d\gamma/dp_a \approx -70$ mJ $mol^{-1}K^{-2}$/GPa and $d\gamma/dp_c \approx 40$ mJ $mol^{-1}K^{-2}$/GPa in $CsFe_2As_2$. The compound thus displays the sign change between a-axis and c-axis pressure derivative, which is familiar from the study

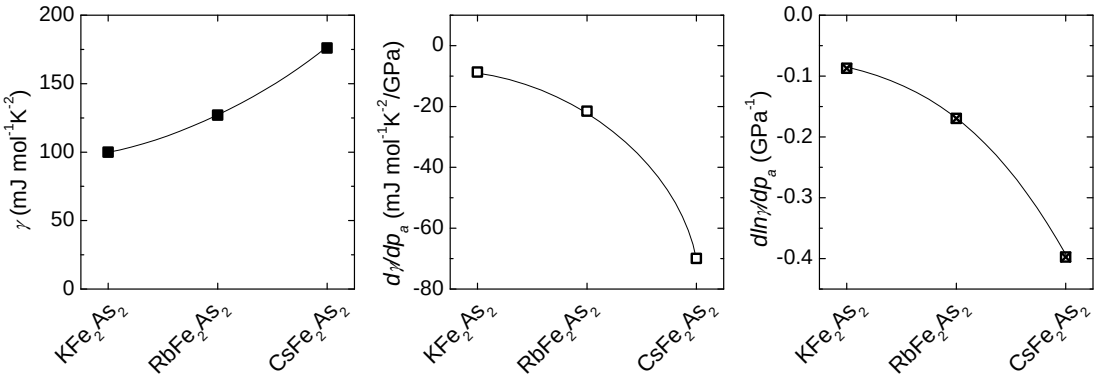

Figure 3.17.: (a) Sommerfeld coefficient γ, (b) its in-plane pressure derivative $d\gamma/dp_a$, and (c) its logarithmic derivative $d\ln\gamma/dp_a$ of KFe_2As_2 (c), $RbFe_2As_2$ and $CsFe_2As_2$. Compounds become significantly more pressure sensitive from KFe_2As_2 to $RbFe_2As_2$ and $CsFe_2As_2$.

of $Ba(Fe,Co)_2As_2$ [11, 43]. However, in contrast to $Ba(Fe,Co)_2As_2$, the volume derivative $d\gamma/dp_{vol} = 2d\gamma/dp_a + d\gamma/dp_c \approx -100$ mJ mol^{-1}K^{-2} is of similar magnitude as the uniaxial derivatives, which indicates that volume, or hydrostatic pressure, is also a relatively good tuning parameter od γ in $CsFe_2As_2$.

3.3.3. Pressure derivatives from multiband analysis of the thermal expansion in the superconducting state

In multiband systems, one frequently encounters multiple superconducting gaps of different size $\Delta(0)/T_c$. A well-known example is MgB_2. To describe the specific heat of such a superconductor, the two-band alpha-model has been introduced by Bouquet *et al.* [13]. In the iron-based superconductors, this model has for example been applied in a detailed analysis of the specific heat of $Ba(Fe,Co)_2As_2$ [46, 49]. Here, we extend the analysis to the thermal expansion (see the introduction 2.2.1) and apply it to the $(Ba,K)Fe_2As_2$ system. The pressure dependence of the parameters that characterize the superconducting state within the alpha-model are obtained, considering isotropic *s*-wave gaps.

The starting point for the multiband analysis is to note that the entropy of different bands is additive. In particular, each band i contributes with a weight proportional to its density of states γ_i to the entropy, and thus also to the specific heat and thermal expansion. In such a two-band model, the normalized specific heat $C/\gamma_{tot}T$ ($\gamma_{tot} = \gamma_1 + \gamma_2$) is thus given by a sum of the specific heat of

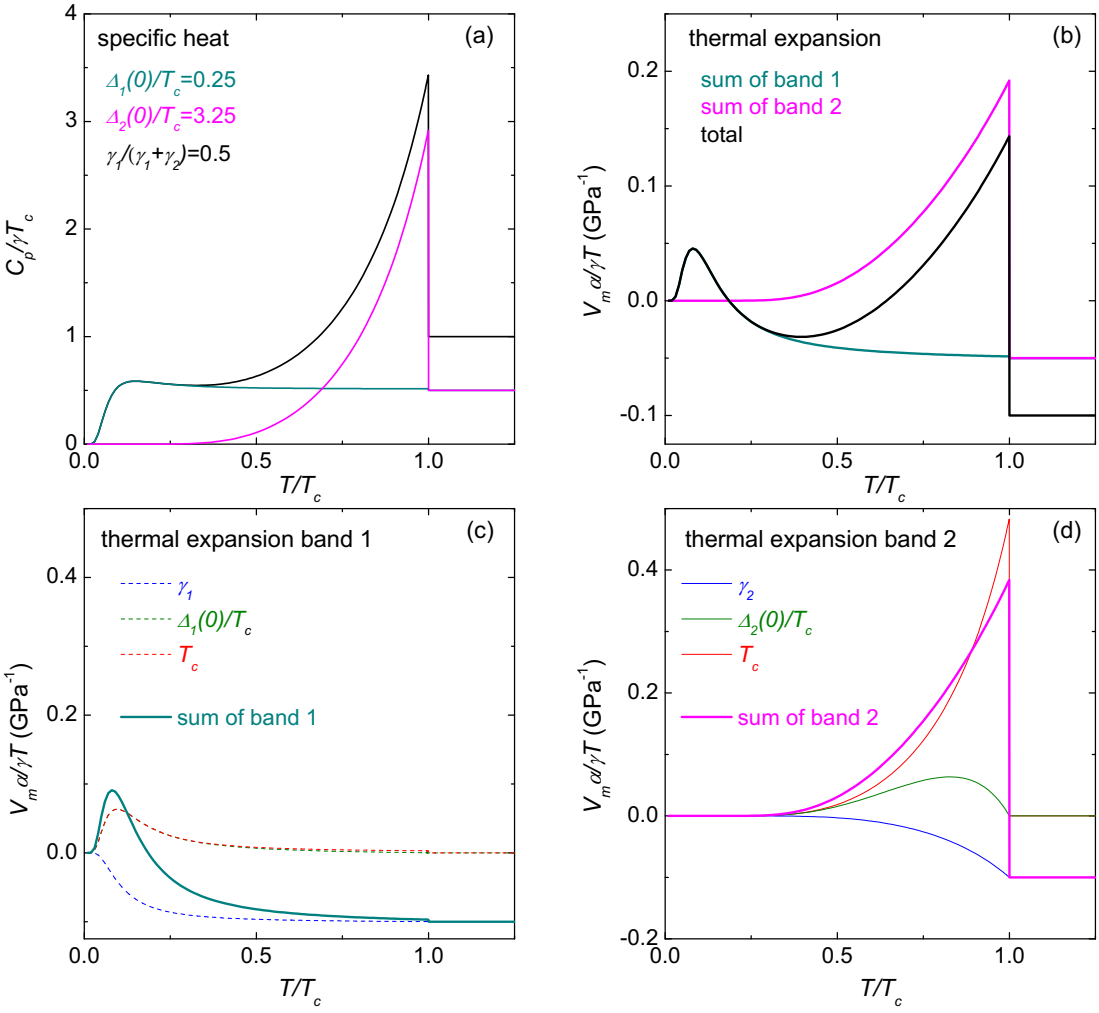

Figure 3.18.: Example of the specific heat (a) and thermal expansion (b) of an extreme two-band superconductor within the alpha-model. Parameters $\Delta_1(0)/T_c = 0.25$, $\Delta_2(0)/T_c = 3.25$ and $\gamma_1 = \gamma_2$ have been used for the calculation. Further, $d\ln T_c/dp = d\ln\gamma_{1,2}/dp = d\ln\left(\Delta(0)_{1,2}/T_c\right)/dp = 0.1$ GPa^{-1} has been assumed for the calculation of the thermal expansion. Panel (c) and (d) show the thermal expansion of the band with the small and the large gap, respectively, split into the three types of contribution of Fig. 2.5.

each band, as calculated in section 2.2, weighted by the density of states. In consequence, it is described by three parameters: $\Delta_1(0)/T_c$, $\Delta_2(0)/T_c$ and γ_1/γ_{tot} instead of only one (namely, $\Delta(0)/T_c$) for the single-band alpha-model. Fig. 3.18(a) shows for example the specific heat divided by temperature of a two-band superconductor in which the small gap amounts to $\Delta_1(0) = 0.25T_c$ and the large gap to $\Delta_2(0) = 3.25T_c$, and both bands have equal density of states. The index 1 is arbitrarily assigned to the smaller gap. Incidentally, such an extreme case is approximately realized in KFe_2As_2 [64].

An analogous approach for the thermal-expansion coefficient is developed here. Fig. 2.5 has shown that there are three contributions to the thermal expansion of a single-band superconductor within the alpha-model and Fig. 2.6 how these three contributions change with varying $\Delta(0)/T_c$. The thermal expansion of a two-band superconductor is, hence, expected to be a sum of six contributions—three per band—which are weighted by their density of states. One condition is that, as T_c [65], the pressure derivative dT_c/dp has to be identical for coupled bands. Thermal-expansion curves with a large variety of shapes are evidently possible. Interestingly, thermal expansion in the superconducting state allows to distinguish the pressure derivative of the density of states of the individual bands γ_1 and γ_2, while in the normal state only their sum is of importance. Fig. 3.18 visualizes the contributions to the thermal expansion for the case of the above specific-heat example. The parameters $d\ln T_c/dp = d\ln\gamma_{1,2}/dp = d\ln(\Delta(0)_{1,2}/T_c)/dp = 0.1$ GPa^{-1} have been assumed for the purpose of demonstration. Panel (c) and (d) show the thermal-expansion deriving from the small and the large gap, respectively, split into their three contributions. The small gap manifests itself extremely clearly in the total thermal-expansion curve (panel (b)) at low T/T_c, which makes thermal expansion an ideal probe to study multigap superconductivity.

The specific heat of a selection of the $(Ba,K)Fe_2As_2$ samples from thermal expansion has been measured and a lattice background subtracted by F. Hardy [61]. In a first step, input parameters for the thermal-expansion analysis, namely γ_{tot}, γ_1/γ_{tot}, $\Delta_1(0)/T_c$ and $\Delta_2(0)/T_c$, are determined from a fit of C^{el}/T to the two-band alpha-model (Fig. 3.19) and resulting parameters are plotted in Fig. 3.20. The gaps $\Delta_{1,2}(0)/T_c$ are largest around optimal doping, where $\Delta_2(0)/T_c$ is nearly two times higher than the BCS value and $(Ba,K)Fe_2As_2$ is clearly in the strong-coupling regime. Further, Δ_2 is approximately three times larger than Δ_1 with nearly equal density of states associated with the two gaps. Thus, $(Ba,K)Fe_2As_2$ is a rather extreme case of multiband superconductivity and a promising candidate to analyze its thermal expansion. One needs to caution, however, that the two-band description is less satisfactory than for $Ba(Fe,Co)_2As_2$ [49], especially for the samples with K content $\geq 59\%$. Instead, three or four bands may be necessary for a perfect fit. For example, a detailed analysis of KFe_2As_2 shows that four gaps,

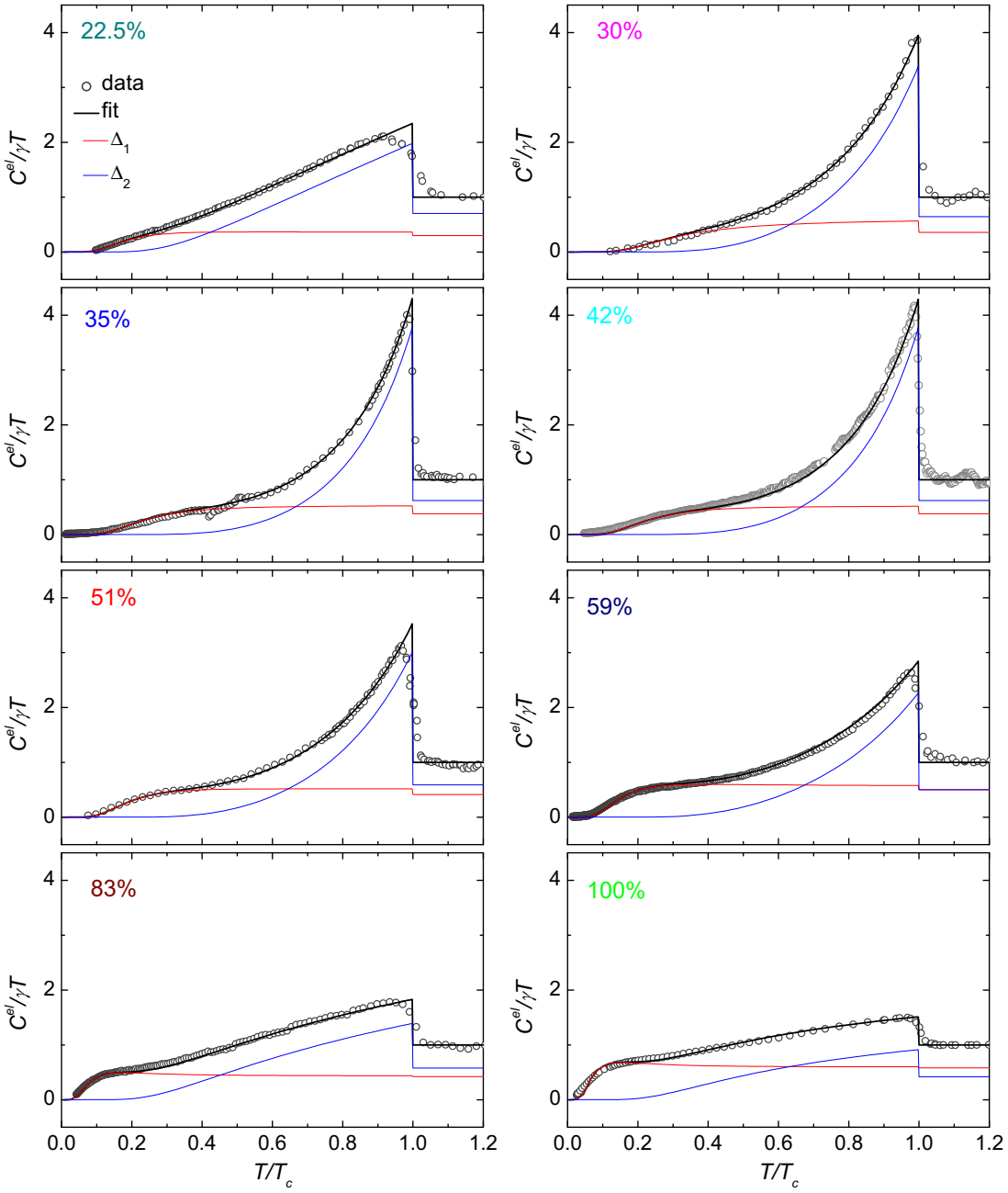

Figure 3.19.: Analysis of the electronic specific heat C^{el}/T of (Ba,K)Fe_2As_2 within the two-band alpha-model. The two-band model provides a reasonable description of the data. However, three or even four bands would be necessary for a perfect fit at high K content. Data are a courtesy of F. Hardy [61].

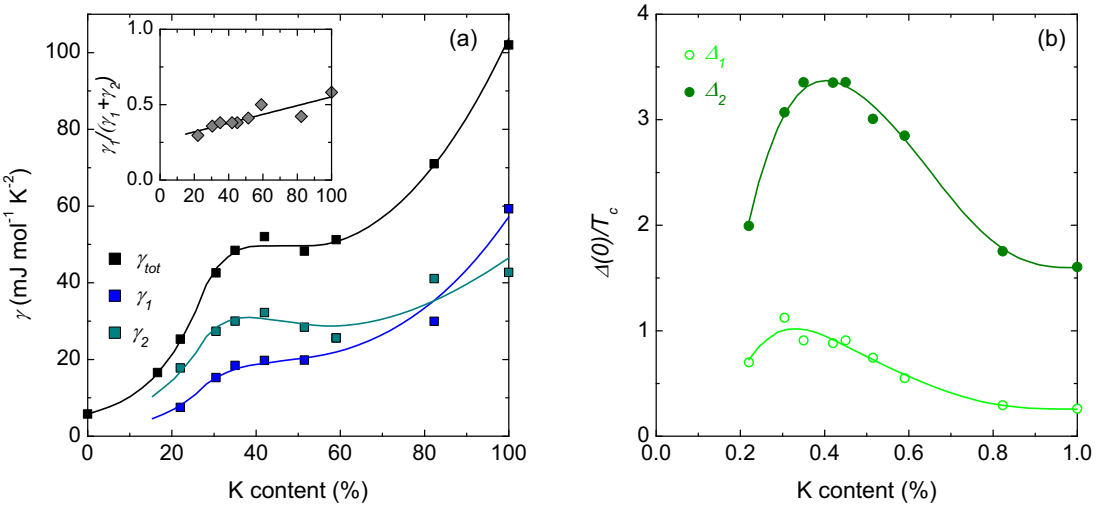

Figure 3.20.: Parameters obtained from the two-band analysis of the specific heat of (Ba,K)Fe_2As_2 in Fig. 3.19. (a) shows the total and the individual densities of states of the two bands (black squares: total, blue squares: band 1, cyan squares: band 2) and (b) the gaps (open light green circles: $\Delta_1(0)/T_c$, full dark green circles: $\Delta_1(0)/T_c$). The inset in (a) shows the weight of the band with the small gap. Lines are a guide to the eye.

which furthermore do not follow the BCS temperature dependence contrary to the alpha-model, are necessary to describe the specific heat [64]. Bearing in mind that a description of the thermal expansion needs twice as many parameters as a description of the specific heat, we content ourselves with an effective two-band model in the following.

Fig. 3.21 shows the electronic thermal-expansion coefficients of (Ba,K)Fe_2As_2 normalized by molar volume V_m and by γ. $V_m\alpha^{el}/\gamma T$ is plotted because it has the same units (GPa^{-1}) as the logarithmic pressure derivatives, which are the parameters to be adjusted (see eq. 2.14) [6]. Fig. 3.22 presents the curves adjusted to the data of Fig. 3.21. Having fixed $\Delta_{1,2}(0)/T_c$ and γ_1/γ_{tot} from the analysis of the specific heat, five parameters ($d\ln T_c/dp$, $d\ln\gamma_{1,2}/dp$ and $d\ln(\Delta_{1,2}(0)/T_c)/dp$) remain. The shape of the curves fortunately makes a nearly unique determination of these parameters possible. $d\ln T_c/dp$ can be determined reliably, because it exclusively determines the discontinuity of $\Delta\alpha$ at T_c, as expected from the Ehrenfest relation 2.8. The hump at low reduced temperature, which is negative and

6. The logarithmic pressure derivatives are identical to Grüneisen parameters except for a compressibility factor and indicate the pressure dependence of the respective energy scale.

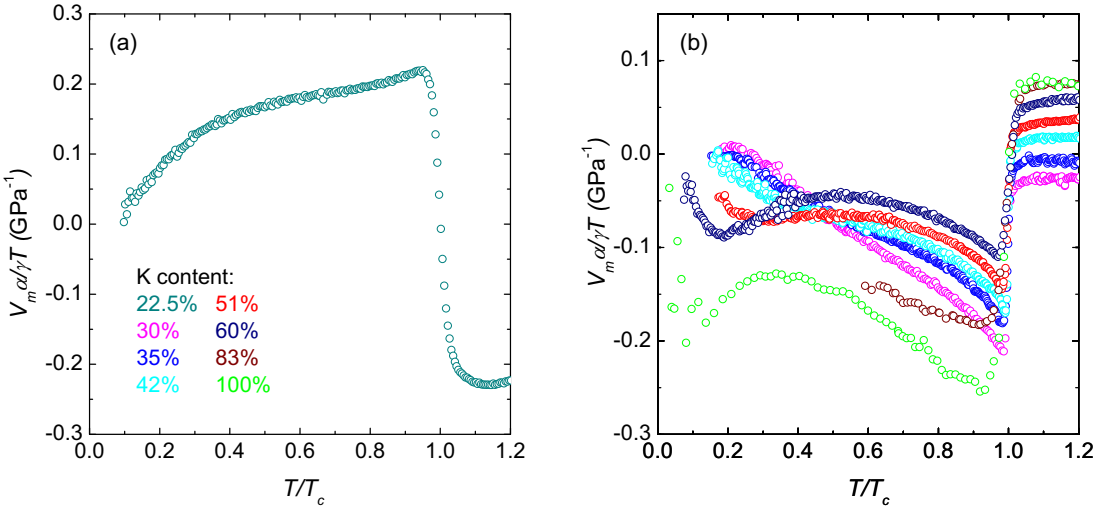

Figure 3.21.: Electronic thermal expansion of (Ba,K)Fe_2As_2, normalized by γ_{tot}/V_m to units of GPa^{-1} in the superconducting state. (a) shows data of an orthorhombic sample (*ab* average) and (b) data from tetragonal samples, compare Fig. 3.9

especially pronounced at 60% K content and clearly positive at 30% K content (see Fig. 3.21), is predominantly determined by the small gap $d\ln(\Delta_1(0)/T_c)/dp$ and $d\ln T_c/dp$. Hence, also the former of these parameters can be extracted with relative confidence. The condition on the normal state value of α^{el}/T

$$\frac{V_m\alpha_N^{el}}{\gamma_{tot}T_c} = \frac{d\ln\gamma}{dp} = \frac{d\ln\gamma_1}{dp} + \frac{d\ln\gamma_2}{dp} \tag{3.1}$$

links the parameters $d\ln\gamma_1/dp$ and $d\ln\gamma_2/dp$. They dominate the calculated curves in the intermediate temperature regime. The pressure derivative of the large gap $d\ln(\Delta_2(0)/T_c)/dp$ contributes mainly to the slope of α^{el}/T just below T_c. In practice, a matlab® code was written to produce a least-squares fit with four parameters (having imposed condition 3.1) to the data and the results were checked to reproduce all the essential features of the experimental curves. Fig. 3.22 shows that they are indeed very satisfactory.

Fig. 3.24 presents the logarithmic pressure derivatives that were obtained from the thermal-expansion analysis. Several points are of interest. $d\ln T_c/dp_a$ is positive at 22% K content (where superconductivity emerges within the orthorhombic-magnetic state) and negative at $\geq 30\%$ K content. $d\ln T_c/dp_a \approx -0.07$ GPa^{-1} is nearly constant between 30% and 60% K content and increases to ≈ -0.7 GPa^{-1} for pure KFe_2As_2. While $d\ln\gamma_{tot}/dp$ is rather small, the pressure derivatives of the

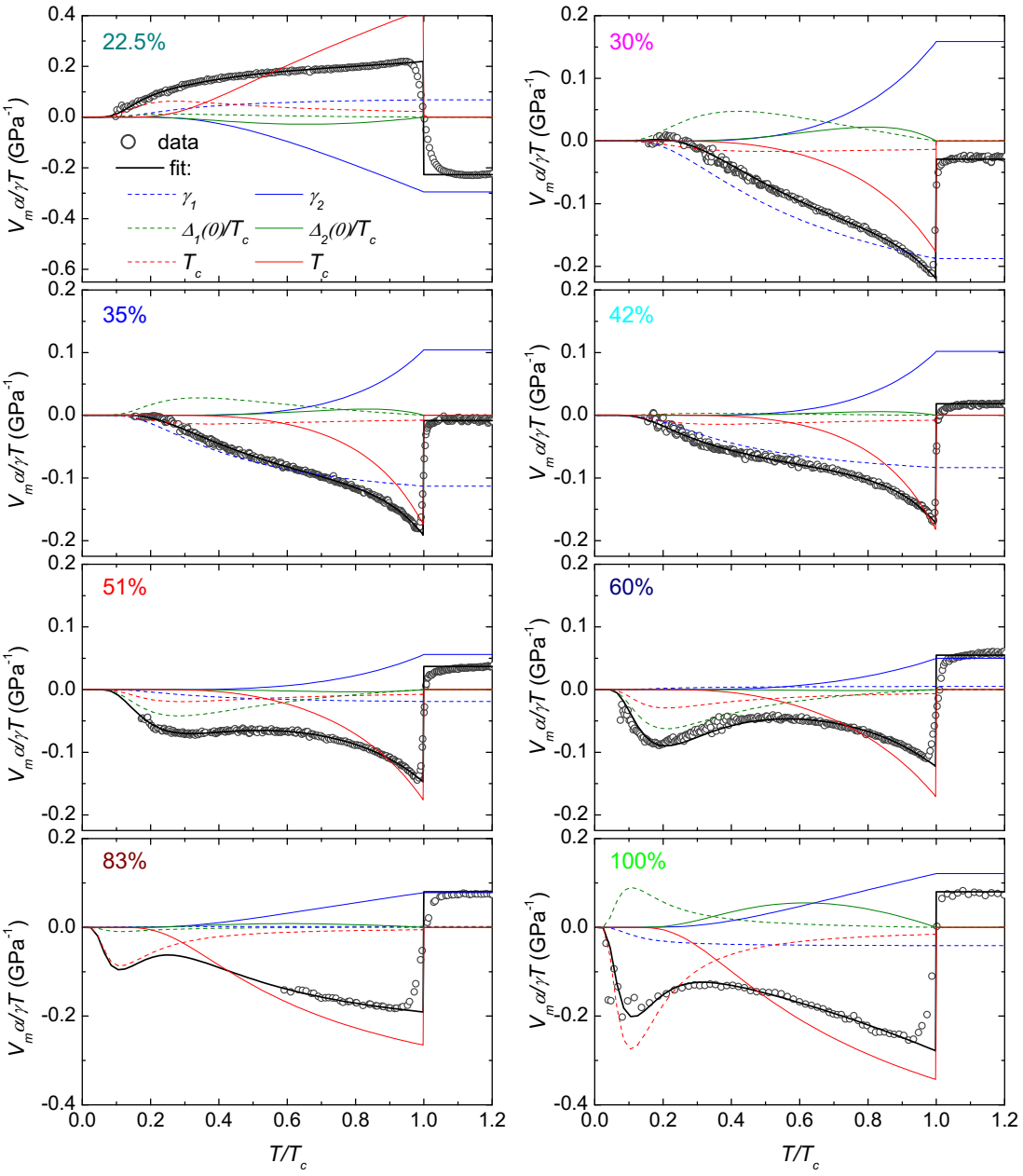

Figure 3.22.: Two-band analysis of α_a of (Ba,K)Fe_2As_2 in the superconducting state. The parameters $\Delta_{1,2}(0)/T_c$ and γ_1/γ_{tot} are taken from Fig. 3.20. Logarithmic pressure derivatives are proportional to the calculated contributions (colored lines, see Fig. 3.18) and were adjusted. The results are shown in Fig. 3.24. Only panels for samples with $30\% - 60\%$ K content are on the same vertical scale.

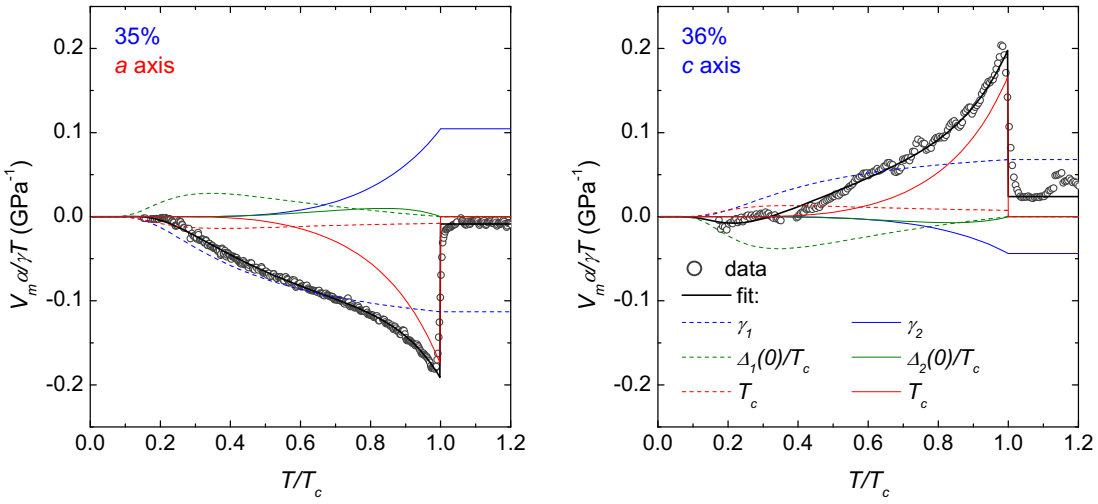

Figure 3.23.: Two-band analysis of the a- and c-axis thermal expansion, respectively, of optimally doped (Ba,K)Fe_2As_2, analogous to Fig. 3.22.

individual γ_1 and γ_2 turn to be rather large (with opposite sign) below 50% K content. Except for 30% and 100% K content, $d\ln(\Delta_2(0)/T_c)/dp$ is rather small. This means that the coupling strength hardly changes with pressure and $\Delta_2(0) \propto T_c$. On the other hand, $d\ln(\Delta_1(0)/T_c)/dp$ is quite large and manifests itself clearly in the data. Namely, the change of curvature and a small positive hump at low temperatures at 30% K content indicates a large positive pressure derivative of $\Delta_1(0)/T_c$. Upon further substitution, this contribution grows smaller and changes sign to become again very pronounced at 51% and 60% K content. Note that the data are a clear prove of multiband superconductivity in (Ba,K)Fe_2As_2.

The pure KFe_2As_2 compound shows a qualitatively very similar thermal expansion to $Ba_{0.4}K_{0.6}Fe_2As_2$. However, the parameter $d(\Delta_1(0)/T_c)/dp$ has opposite sign for the two samples. This is because of the combined effect of very small $\Delta_1(0)/T_c$ and large $d\ln T_c/dp_a$ in KFe_2As_2. The value of $d\ln T_c/dp_a$ results in a large negative type-I contribution from the small gap at low temperatures, which is indeed larger than the experimentally observed negative hump, so that $d\ln(\Delta_1(0)/T_c)/dp$ has to be positive in order for the type-III contribution to balance it. It is hard to say whether this sign change of $d(\Delta_1(0)/T_c)/dp$ between 60% and 100% K content reflects an intrinsic change of the pressure effect on the gap structure or whether it is an artifact of the effective two-band description that works less well at high K content.

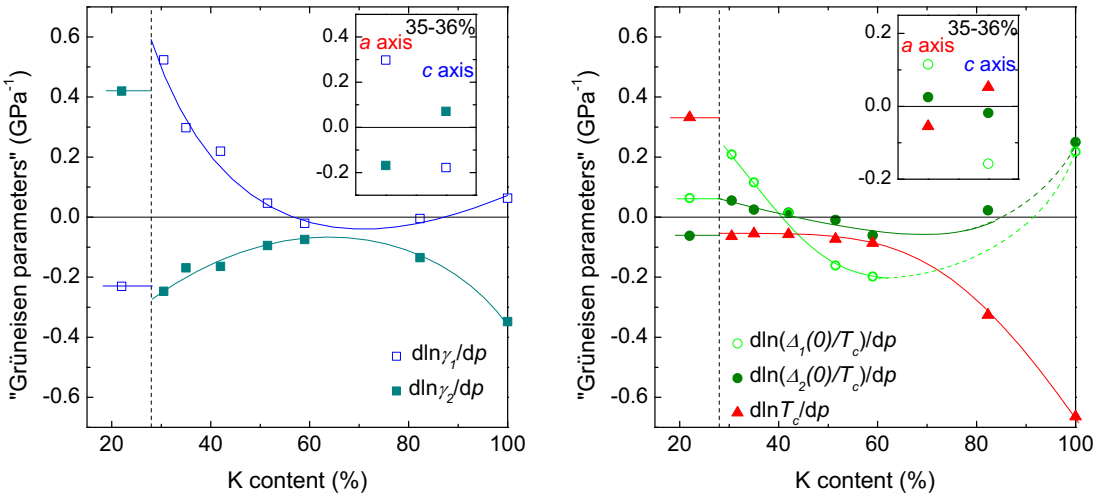

Figure 3.24.: Logarithmic a-axis pressure derivatives (i.e., Grüneisen parameters except for a compressibility factor) of (a) γ_1 (blue open squares), γ_2 (cyan full squares), (b) T_c (red triangles), $\Delta_1(0)/T_c$ (light green open circles) and $\Delta_2(0)/T_c$ (dark green full circles), resulting from the two-band analysis of the thermal expansion of (Ba,K)Fe_2As_2. Lines are a guide to the eye. Insets show the comparison between a-axis and c-axis pressure derivatives of optimally doped (Ba,K)Fe_2As_2.

The c-axis thermal expansion data of the optimally doped sample (36% K content) is exceptionally good, so that the multiband analysis can be performed. By subtracting α_c of $Ba(Fe_{0.67}Co_{0.33})_2As_2$ as a phonon background, the electronic contribution α_c^{el} has been obtained. Fig. 3.23 presents the analysis and compares with the a-axis data. All contributions have very similar magnitude but change sign between the directions (see also insets in Fig. 3.24). This demonstrates nicely that the c/a ratio is an important tuning parameter of all quantities related to the superconducting state in optimally doped (Ba,K)Fe_2As_2.

Having obtained the detailed pressure dependence of the superconducting state, we discuss in the following how uniaxial pressure may be related to K substitution. For this, K-substitution derivatives are determined by differentiating the smooth lines through $T_c(x)$ (Fig. 3.11), $\gamma(x)$ (Fig. 3.15), $\gamma_1/\gamma_{tot}(x)$ and $\Delta_{1,2}(0)/T_c(x)$ (Fig. 3.20). The procedure is illustrated in Fig. 3.25, which shows T_c, γ_{tot} and their derivatives with respect to substitution and a-axis pressure. A scaling between pressure and substitution derivatives in which 1 at% K content, x, corresponds to 0.25 GPa a-axis pressure, p_a, is attempted. Indeed, dT_c/dp_a and dT_c/dx scale approximately, except for the region around $\sim 25\% - 35\%$ K content. The same scaling for the derivatives of γ works approximately below $\sim 40\%$ K content.

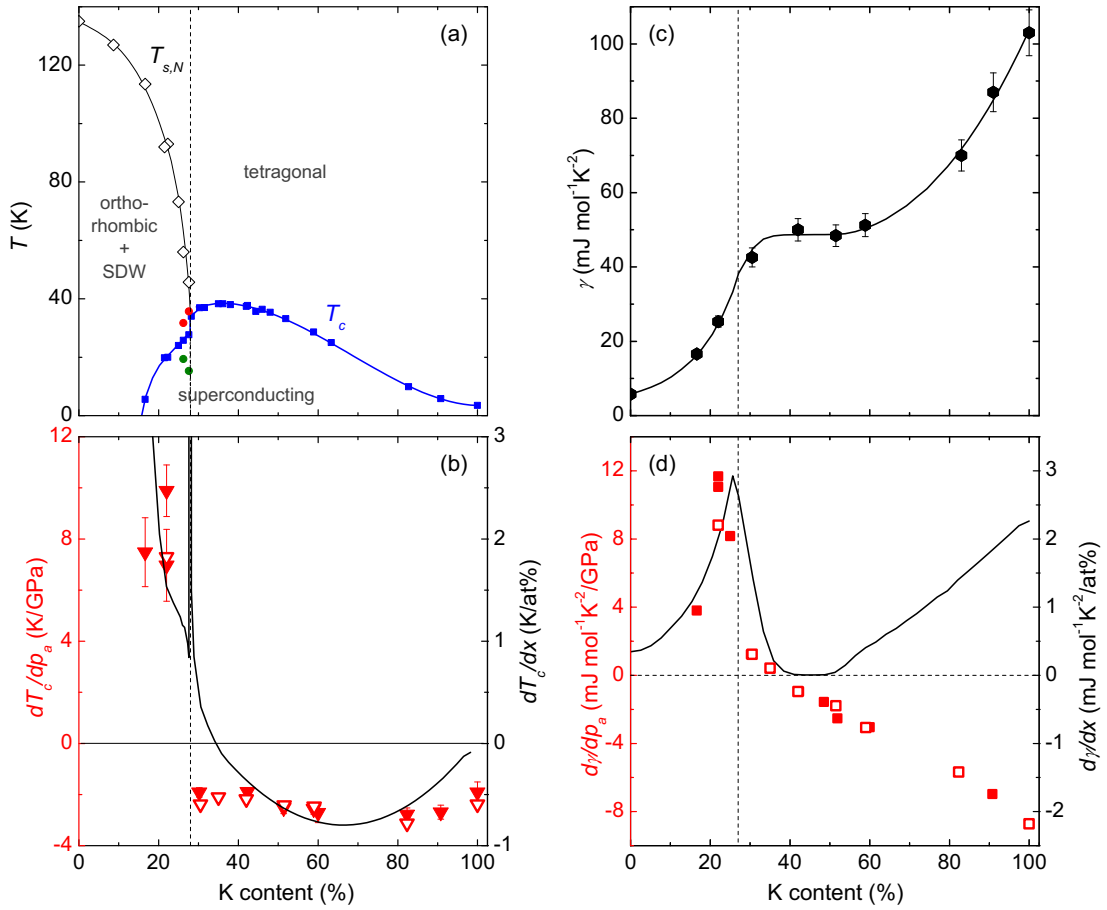

Figure 3.25.: (a) Phase diagram and (c) Sommerfeld coefficient γ of (Ba,K)Fe_2As_2. (b) in-plane pressure derivative dT_c/dp_a (left scale) obtained from multiband analysis (open symbols) and from application of the Ehrenfest relation (closed symbols); and derivative with respect to K content dT_c/dx (right scale) obtained from differentiating the smooth line in panel (a). The two derivatives scale approximately according to 1 at% K = 0.25 GPa, except for the region around optimal doping. (d) same scaling of $d\gamma/dp_a$ (full symbols from Fig. 3.15 (b) and open symbols from Fig. 3.24) and $d\gamma/dx$, obtained from differentiating the smooth line in (c). This scaling fails dramatically above 40% K content.

It fails, however, dramatically in the overdoped part of the phase diagram, where $d\gamma/dx$ and $d\gamma/dp$ have opposite sign. Namely, both additional K substitution and p_a decrease T_c in this region, whereas additional K substitution enhances γ, while p_a *decreases* γ. This establishes, firstly, that γ does not decisively determine T_c and, secondly, it demonstrates that K substitution is not simply equivalent to uniaxial pressure.

In Fig. 3.26, the comparison between pressure and substitution derivatives is extended to comprise also the individual densities of state $\gamma_{1,2}$ and gaps $\Delta_{1,2}(0)/T_c$. Here, logarithmic pressure and doping derivatives are shown. The logarithmic derivatives of T_c and γ_{tot} exhibit the partial scaling discussed above. Further, it is interesting to note that $d\ln\gamma_{tot}/dp_a$ seems to saturate above 80% K content, which indicates a doping-independent Grüneisen parameter. On the other hand, $d\ln T_c/dp_a$ increases markedly in this region (result of decreasing T_c and constant dT_c/dp_a). This shows again that γ is not directly linked to T_c. One of the central results of the two-band analysis is the opposite pressure derivative of γ_1 and γ_2 below 50% K content. Fig. 3.26(c) shows that the doping derivatives of γ_1 and γ_2 do not show this behavior. Thus, no relation between pressure and doping can be found for the partial densities of states in any part of the phase diagram. This can be quite naturally explained in that K substitution adds charge carriers, in addition to a possible chemical-pressure effect [66]. Concerning the gap size, doping and pressure derivatives of $\Delta_2(0)/T_c$ indeed seem to scale in most of the phase diagram, which means that the coupling strength for the large gap is affected by doping and by pressure in a similar way. Furthermore, the small gap $\Delta_1(0)/T_c$ is found to be extremely pressure and doping sensitive. However, it is curious that $d\ln T_c/dp_a$ hardly changes with doping in the large range between 30% and 60% K content, in which all other pressure derivatives, in particular those of the coupling strength, change dramatically. The parameters which affect T_c in this complicated multiband system thus remain elusive.

In contrast to K substitution, Co substitution was found not to add carriers [66] and to be equivalent to uniaxial pressure on the basis of the similarity between pressure and doping derivatives of γ [11] (see introduction 3.1). The same multiband analysis of the thermal expansion as for $(Ba,K)Fe_2As_2$ has been applied here to the a-axis data from Ref. [11] and is shown in the appendix A. Using the obtained logarithmic pressure derivatives, we check the relationship between pressure and Co substitution also for the individual densities of states $\gamma_{1,2}$ and for $\Delta_{1,2}(0)/T_c$. A particularity of the $Ba(Fe,Co)_2As_2$ system is that there is also a residual density of states γ_r at low temperatures in the superconducting state [49]. Fig. 3.27 shows the scaling of logarithmic pressure derivatives from thermal-expansion analysis (Fig. A.2) together with logarithmic Co-doping derivatives of the respective quantities obtained from differentiating smooth lines through the

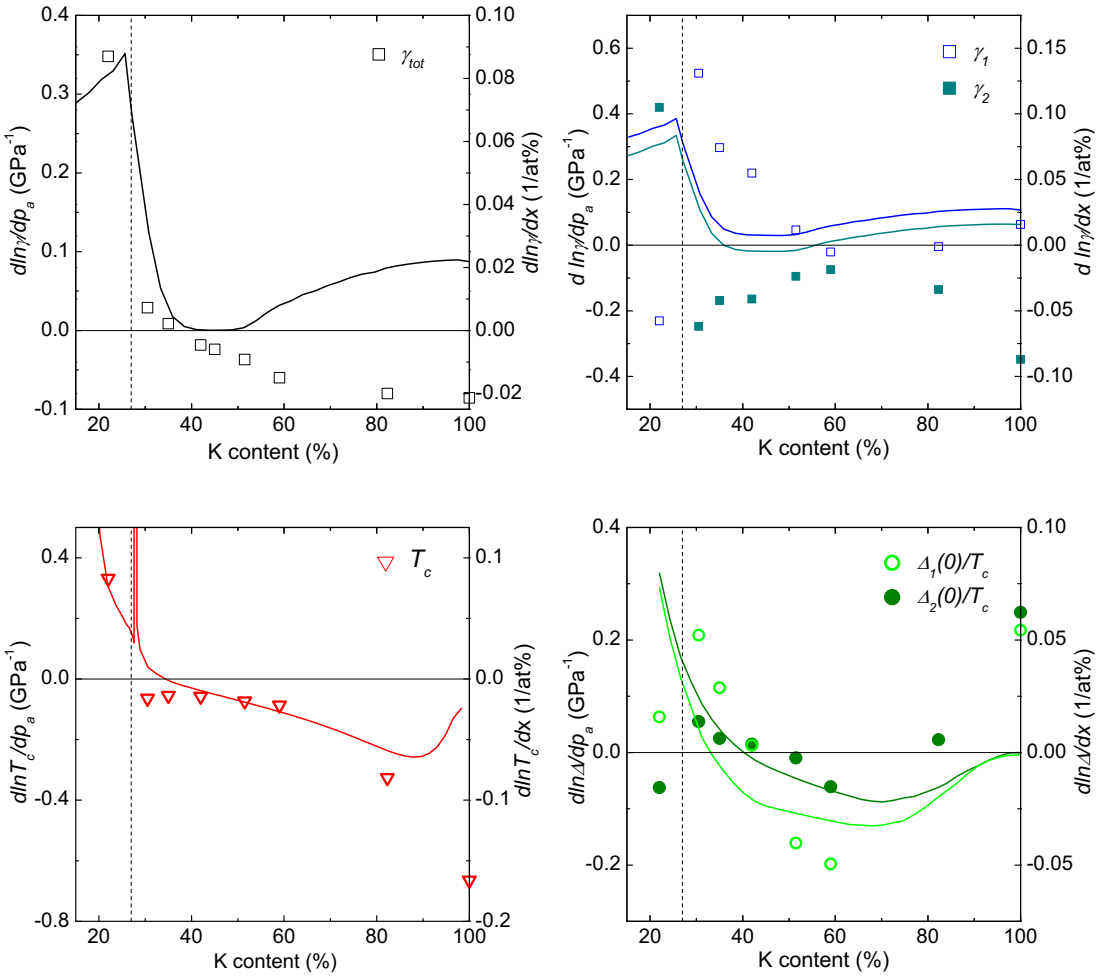

Figure 3.26.: Comparison of logarithmic pressure and doping derivatives of (a) γ_{tot}, (b) $\gamma_{1,2}$, (c) T_c, and (d) $\Delta_{1,2}(0)/T_c$. Symbols (as in Fig. 3.24) are logarithmic in-plane pressure derivatives obtained from the analysis of the thermal-expansion data (left scale) and solid lines are derived from the doping dependence of the respective parameters (right scale). A scaling relation 1 at%K = 0.25 GPa is tested in all panels. Very few quantities seem to correlate.

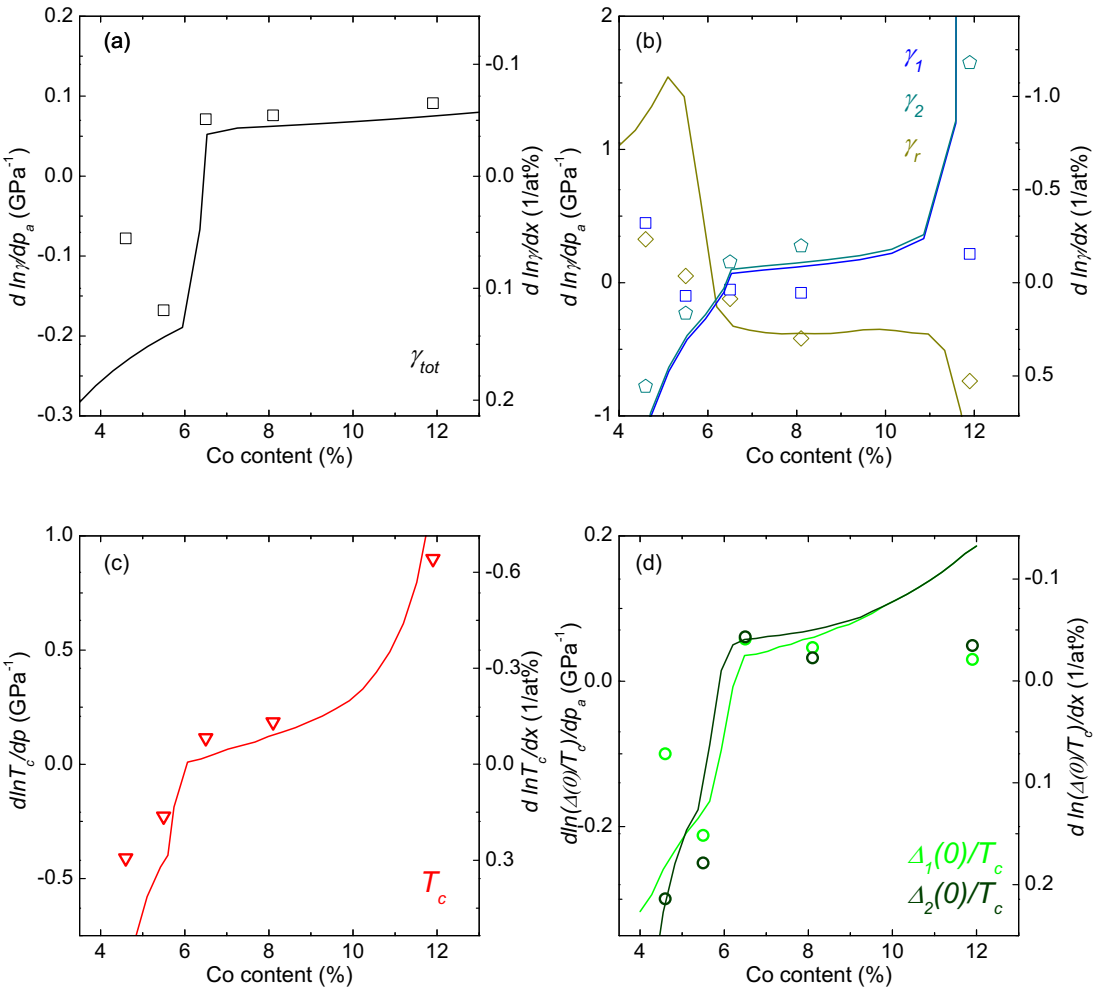

Figure 3.27.: Comparison of logarithmic pressure and doping derivatives of (a) γ_{tot}, (b) $\gamma_{1,2}$ and γ_r, (c) T_c, and (d) $\Delta_{1,2}(0)/T_c$ of $Ba(Fe,Co)_2As_2$. Open symbols are logarithmic in-plane pressure derivatives derived from analysis of the thermal-expansion data (Fig. A.2) and solid lines are derived from the doping-dependence of the respective parameters (Fig. A.1), using the conversion factor $\frac{dp_a}{dx} = -1.4$ GPa/at%. The good agreement confirms the direct relation between Co substitution and uniaxial pressure. The consistency also supports the validity of the thermal-expansion analysis.

data (Fig. A.1). The same scaling factor $dp_a/dx = -1.4$ GPa/at% as in Ref. [11] was used. There is indeed very good or reasonably good agreement between pressure and doping derivatives with the same scaling factor for γ_{tot}, γ_2, γ_r, T_c, $\Delta_1(0)/T_c$ and $\Delta_2(0)/T_c$. A deviation occurs for γ_1 for very low and very high Co content. The condition $\gamma_1 + \gamma_2 + \gamma_r = \gamma_{tot}$ has been enforced for both doping and pressure derivatives. All in all, the equivalence between a-axis pressure and Co doping is well confirmed. This consistency also supports the validity of the thermal-expansion analysis.

3.3.4. Do ideal Fe-As tetrahedra result in optimal T_c?

Very early in the study of the iron-pnictides, it was suggested that T_c in the iron-based systems reaches its optimum value when the Fe and As atoms form regular tetrahedra [67, 68]. In the (Ba,K)Fe_2As_2 system in particular, the maximum T_c was found to coincide with the point at which the Fe-As tetrahedra become regular, both when the phase diagram is tuned by K substitution and by hydrostatic pressure [53]. Based on these findings, the equivalence of pressure and K substitution was also suggested. Further, it was suggested in Ref. [69] that pressure scales with K substitution up to 70% K content from comparing direct measurements of the hydrostatic pressure derivative dT_c/dp_{vol} with the slope of $T_c(x)$ in the phase diagram. The here obtained uniaxial pressure derivatives of T_c shed light on these proposed relations.

Fig. 3.28 presents the Fe-As-Fe tetrahedral angles, determined by 4-circle x-ray refinement of our samples at room temperature, together with their T_c. In a perfect tetrahedron both angles equal 109.5°. The data show that, indeed, the maximum T_c (at $x_{opt} = 0.36$) nearly coincides with the point where the Fe-As tetrahedra are regular. Panel (b) shows the uniaxial pressure derivatives dT_c/dp_a and dT_c/dp_c, determined from α and C_p. Note that the maximum T_c of (Ba,K)Fe_2As_2 lies well inside the tetragonal phase, so that T_c and its derivatives are not influenced by the competition with the orthorhombic, magnetic phase. This competition very likely causes the sign change of dT_c/dp_a and dT_c/dp_c between 25% and 28% K content, where $T_{s,N}$ crosses the superconducting dome. Importantly here, the pressure derivatives of T_c do not change sign at the point where the FeAs tetrahedra are regular. This shows that no causal relationship between optimal T_c and ideal tetrahedral angles exists. Specifically, uniaxial pressure should push the angles closer to their optimal value on one side of x_{opt} and farther away from their optimal value on the other side. If (Ba,K)Fe_2As_2 was tuned through a maximum of T_c by a change of the tetrahedral angle, one would expect a sign change of the uniaxial pressure derivatives of T_c at x_{opt}, at variance with the results. In fact, the uniaxial pressure derivatives show no anomaly at

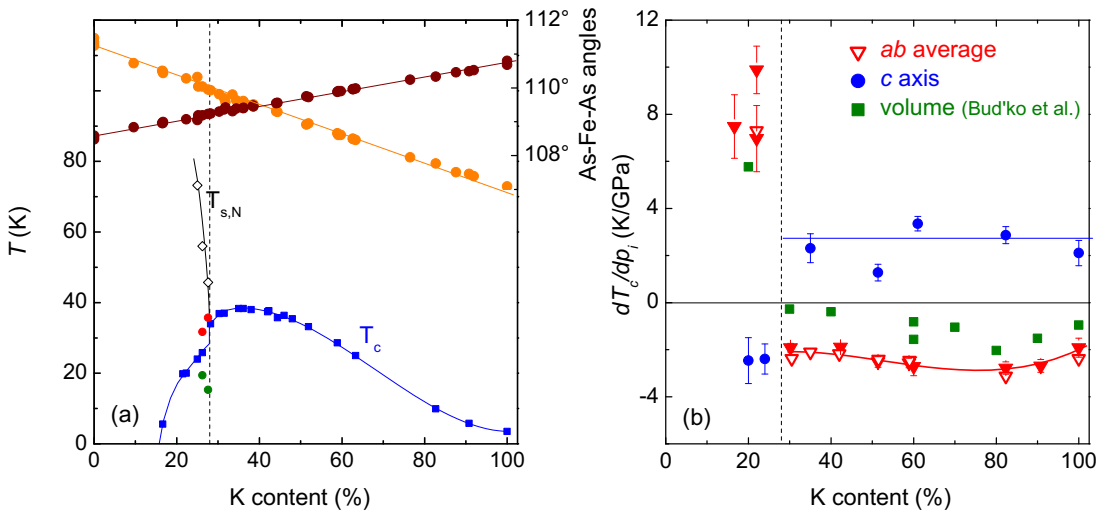

Figure 3.28.: (a) Tetrahedral angles of (Ba,K)Fe_2As_2 (right scale; orange and brown circles) and T_c (left scale; blue squares) showing that the optimal T_c coincides with a regular Fe-As tetrahedra. $T_{s,N}$ (diamonds), T_1 and T_2 (small red and green circles, respectively) are also indicated for illustration. (b) Uniaxial pressure derivatives of T_c. Open triangles are from the analysis in section 3.3.3, full triangles from evaluation of the Ehrenfest relation for the in-plane derivative. The c-axis derivative (from the Ehrenfest relation) is indicated by blue circles. The hydrostatic pressure derivative from direct measurements [69] is shown for comparison (green squares). Lines are a guide to the eye. The structural data are a courtesy of P. Schweiss. The absence of a sign change of the dT_c/dp_i at the K-content at which the Fe-As tetrahedra become regular, demonstrates that there is not causal relation to optimal T_c.

all at x_{opt} which demonstrates that T_c in (Ba,K)Fe_2As_2 is not mainly tuned by structural changes or pressure.

Even though the hydrostatic pressure derivative was reported to be nearly zero at optimal doping [69], the uniaxial pressure derivatives are significant there ($dT_c/dp_a = -1.9(2)$ K/GPa, $dT_c/dp_c = 2.3(6)$ K/GPa). This is a clear sign that T_c may be increased beyond the ambient-pressure limit of ~ 38.3 K by anisotropic strain or stress, as might be realized, e.g., in thin films or by chemical pressure.

3.4. Summary: comparison of various kinds of substitution in $BaFe_2As_2$

In summary, the uniaxial thermal expansion of (Ba,K)Fe_2As_2 was studied in detail in this chapter. A narrow pocket of a new, likely tetragonal, phase was found in the phase diagram. The electronic thermal expansion of overdoped (Ba,K)Fe_2As_2 shows evidence for a coherence-incoherence crossover, which gradually develops above $\sim 40-50\%$ K content. A multiband analysis of the thermal expansion in the superconducting state establishes pronounced multigap behavior. The pressure dependence of the parameters describing the superconducting state within the alpha-model has been obtained. The comparison of pressure and K substitution derivatives shows that these two ways of tuning the system are qualitatively different. In contrast, uniaxial pressure and Co substitution are found to be essentially equivalent. Finally, uniaxial pressure derivatives show that no causal relation between ideal tetrahedral angle in the Fe-As layers and optimal T_c exists.

To compare different kinds of substitution in $BaFe_2As_2$, Fig. 3.29 presents the uniaxial thermal-expansion coefficients of Co-, Ni-, P- and K-substituted $BaFe_2As_2$ for representative substitution levels. While Co, Ni and P substitution have a very similar effect on the thermal expansion coefficients—and by inference on the entropy of the system—K substitution is qualitatively different from the others. The sign change between a-axis and c-axis pressure derivatives (i.e., thermal-expansion anomalies) shows that the c/a ratio is a good structural tuning parameter in all the studied systems. However, there is a sign change between Ba(Fe,Co)$_2As_2$, Ba(Fe,Ni)$_2As_2$ and $BaFe_2$(As,P)$_2$, on one side, and (Ba,K)Fe_2As_2 on the other side. For example, while an increase of c/a enhances T_c in overdoped Ba(Fe,Co)$_2As_2$, superconductivity in overdoped (Ba,K)Fe_2As_2 favors a decrease of c/a. This motivates us to draw a two-sided phase diagram of substituted $BaFe_2As_2$, featuring two domes of superconductivity (Fig. 3.30). A study of codoping with K and Co in $BaFe_2As_2$ also provides clear evidence for such a two-dome phase diagram [70], namely, it demonstrates that two superconducting domes can be traced by increasing the K content in $Ba_{1-x}K_x(Fe_{0.925}Co_{0.075})_2As_2$.

In section 3.3.3, it was suggested that 1at% Co corresponds to -1.4 GPa in-plane pressure and a scaling of 1at% K substitution with 0.25 GPa in-plane pressure (note the sign change with respect to Co substitution) was attempted. Incidentally, this also means that 1at% Co should have a similar effect on the phase diagram as $(-1.4/0.25 =) -5.6$ at%K. The effect of Co and K substitution and a-axis pressure on the phase diagram is summarized and compared in Fig. 3.30. The horizontal axes are scaled such that 1 at%Co corresponds to -5.6 at%K.

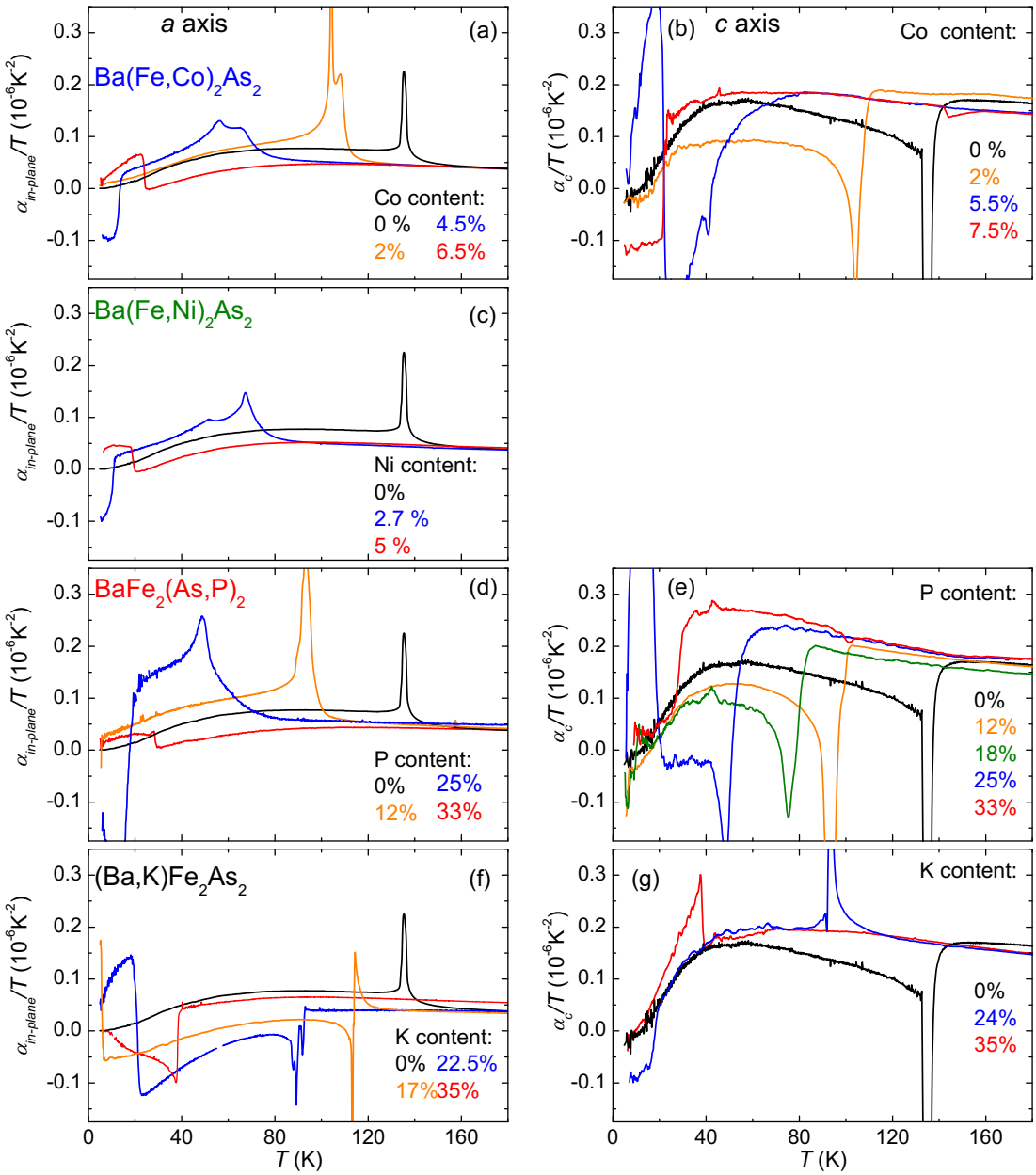

Figure 3.29.: Thermal expansion coefficients divided by temperature of $Ba(Fe,Co)_2As_2$ [11] (a),(b); $Ba(Fe,Ni)_2As_2$ (c); $BaFe_2(As,P)_2$ [12] (d),(e) and $(Ba,K)Fe_2As_2$ (f),(g). Representative compositions have been selected for each system. (a),(c),(d) and (f) show the in-plane; (b),(e) and (g) the c-axis thermal-expansion coefficients. K-substituted $BaFe_2As_2$ is clearly different from the other three systems, which are very similar among themselves.

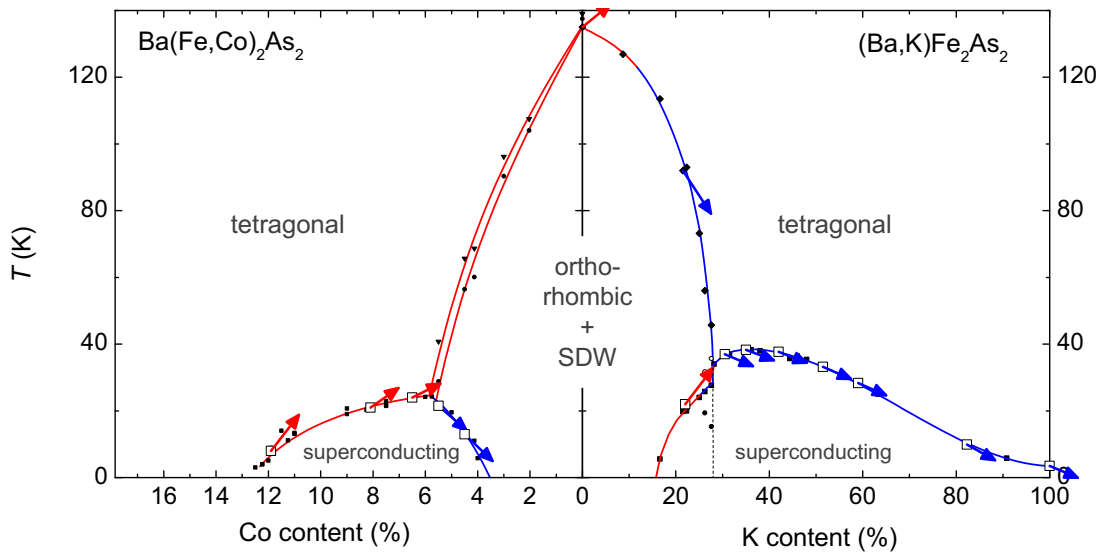

Figure 3.30.: Visualization of the a-axis pressure effect on the transition temperatures of $Ba(Fe,Co)_2As_2$ and $(Ba,K)Fe_2As_2$. Colored arrows indicate the pressure derivatives. They point to the value of T_c ($T_{s,N}$) expected at $p_a = 1.5$ GPa and their slope is determined by the relation between doping and pressure (1at%Co= -1.4 GPa, 1at%K= 0.25 GPa). See text for a more detailed explanation. Red (blue) lines indicate a positive (negative) pressure effect.

Arrows visualize the in-plane pressure derivative of $T_{s,N}$ and T_c. Namely, they point to the value of T_c ($T_{s,N}$) expected under the application of $p_a = 1.5$ GPa and the substitution level corresponding to this pressure if 1at% Co $= -1.4$ GPa and 1at% K $= 0.25$ GPa. Broadly, application of p_a corresponds to "right shift" of the whole two-dome phase diagram. The sign of the anomalies in thermal-expansion shows that p_c, on the other hand, would correspond to a "left shift". On closer inspection, however, this assignment does not work for the magneto-structural transition at low K doping nor for most of the superconducting dome of $(Ba,K)Fe_2As_2$. In particular, uniaxial pressure does not only shift the superconducting dome of $(Ba,K)Fe_2As_2$, but also changes its height.

Fig. 3.31 shows the phase diagrams of Co-, Ni-, P- and K-substituted $BaFe_2As_2$, with substitution level normalized to 1 at optimal doping. From Ni, over Co, to P substitution, the size of the splitting between T_s and T_N decreases and the maximum T_c increases systematically. It may be conjectured that these effects arise from impurity scattering with Ni acting as the strongest scatterer, followed by Co and P. This is because Ni, with a nominal charge of 2^+, should act as a stronger

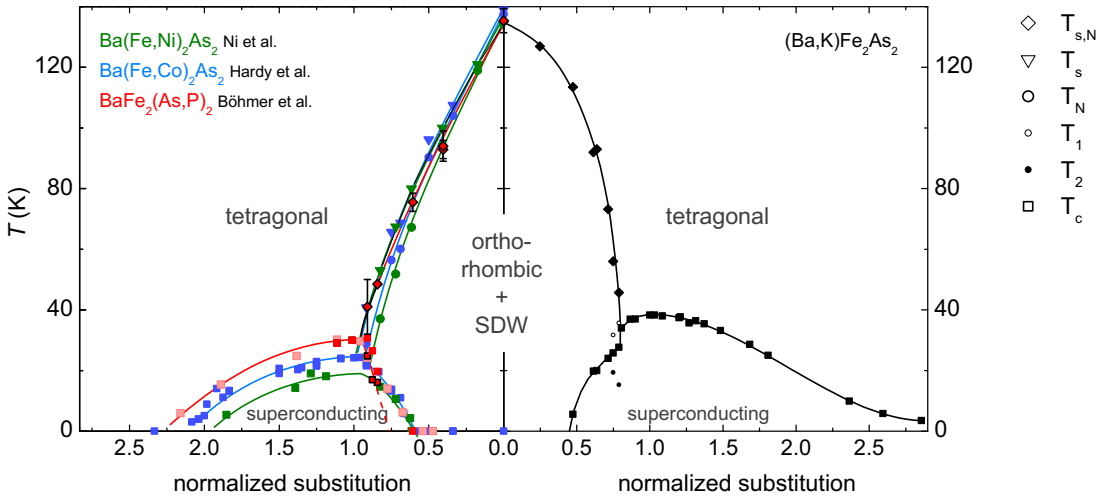

Figure 3.31.: Phase diagram of $Ba(Fe,Co)_2As_2$ [49] (blue symbols), $Ba(Fe,Ni)_2As_2$ [71] (green symbols), $BaFe_2(As,P)_2$ [12] (red symbols) and $(Ba,K)Fe_2As_2$ (this work, black symbols). The composition was normalized at optimal doping. The opposite uniaxial-pressure effects, as determined from thermal expansion (Fig. 3.29), motivate us to draw the phase diagram of $(Ba,K)Fe_2As_2$ to the opposite side of the others. Which symbols correspond to the various transition temperatures is indicated on the right.

scatterer than Co with a nominal charge of 1^+ (see [19]). These two ions are substituted in the Fe-layer, while P substitution is out of the iron plane. Such a sequence (without considering Ni) was, for example, inferred from resistivity and optical measurements [72]. Aside from these putative disorder effects, the phase diagrams of the three systems $Ba(Fe,Co)_2As_2$, $Ba(Fe,Ni)_2As_2$ and $BaFe_2(As,P)_2$ are very similar. However, some clear differences between, e.g., $Ba(Fe,Co)_2As_2$ and $(Ba,K)Fe_2As_2$ can be noted. The magneto-structural transition stays concomitant and first-order upon K substitution, while the transitions split and become more second-order-like upon Co substitution. Further, the $T_{s,N}$-line falls much steeper towards its end point in $(Ba,K)Fe_2As_2$ than in $Ba(Fe,Co)_2As_2$. Also, the maximum T_c is reached right at the point where the structural phase transition crosses the superconducting dome in $Ba(Fe,Co)_2As_2$, but the maximum T_c in $(Ba,K)Fe_2As_2$ lies well beyond this point.

In conclusion, many kinds of substitution in $BaFe_2As_2$ lead to similar phase diagrams. However, K substitution seems to be qualitatively different from Co-, Ni-, or P-substitution, which all produce much the same effects. Thus, a complete

picture of the physics of the $BaFe_2As_2$ system can only be obtained if properties of both $Ba(Fe,Co)_2As_2$ and $(Ba,K)Fe_2As_2$, at least, are studied and compared.

4. Nematic susceptibility of Co- and K-substituted $BaFe_2As_2$

"Nematic" originally refers to a liquid-crystal phase in which rotational symmetry is broken while translational symmetry is preserved. The term has been borrowed from its original context for the orthorhombic state of the iron pnictides in order to underline the idea that an anisotropy of the correlated electron system underlies the tetragonal-to-orthorhombic lattice distortion. Which electronic degrees of freedom (e.g., spin or orbital) drive this transition, if this is indeed the case, is still a subject of intensive debate [9, 73, 74]. In this chapter, first, a brief account on previous work concerning the nematic state in iron-based superconductors is given. Then, we present a novel setup, based on a capacitance dilatometer, which is well suited to measure the soft elastic mode of the structural phase transition of iron-based materials. Results on Co- and K-substituted $BaFe_2As_2$ superconductors are presented. The influence of uniaxial, conjugate, stress on the magneto-structural transition of $BaFe_2As_2$ is discussed first of all. Then, the susceptibility of the nematic order parameter is extracted from the presented data using a Landau model, and its doping and temperature dependence is analyzed. Finally, we attempt to identify the electronic degrees of freedom that drive the structural transition by comparing shear-modulus softening and spin-lattice relaxation rate of $Ba(Fe,Co)_2As_2$.

4.1. Introduction and motivation

In the stripe-type antiferromagnetic phase, which occurs in proximity to superconductivity in the iron-based systems, the two in-plane directions are inequivalent. This naturally results in an orthorhombic distortion of the high-temperature tetragonal lattice so that the antiferromagnetic transition always entails the structural one [26]. Such simultaneous magnetic and structural phase transition are, for example, observed in $(Ba,K)Fe_2As_2$ (see section 3.2 and Ref. [51]). Hence, it is a natural idea that the magnetic order causes the lattice distortion. However, it was observed early on that the (nearly [27]) concomitant magneto-structural phase transition of the parent compound $BaFe_2As_2$ splits into two well-defined

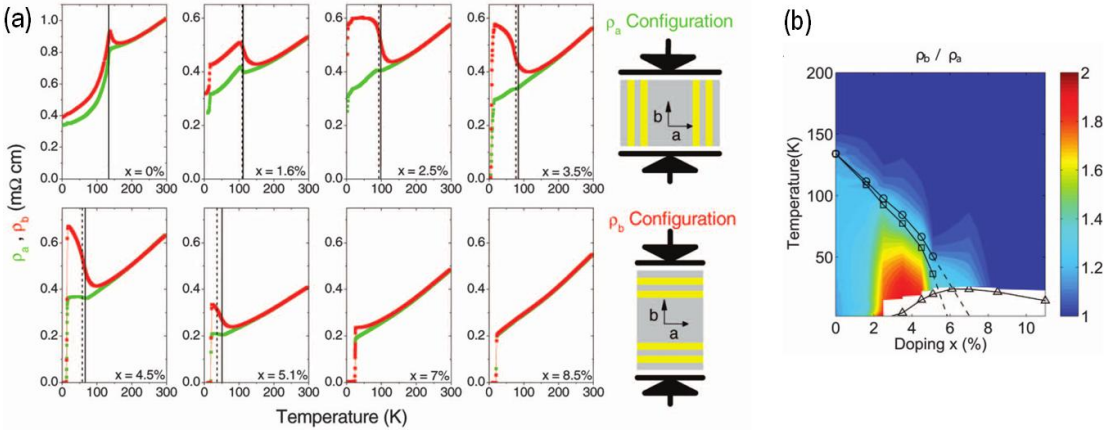

Figure 4.1.: (a) Resistivity along the orthorhombic a and b direction measured in stress-detwinned single crystals of $Ba(Fe,Co)_2As_2$ over a wide substitution range [80]. (b) shows the same data as a color plot in the temperature-composition phase diagram. The large a-b anisotropy in presence of a small lattice distortion $< 0.4\%$ is taken as indication for electronic nematicity. Figure adapted from Ref. [80]

transitions upon Co substitution [28, 75]. Neutron diffraction studies demonstrated that the structural transition temperature is several K higher than the magnetic one [76, 77]. Hence, there is a small region of an orthorhombic—i.e., "nematic"—but paramagnetic phase in $Ba(Fe,Co)_2As_2$, which is also observed in other transition-metal doped 122-systems [71], in F-doped 1111-compounds [78] and in Co-doped NaFeAs [79]. Intuitively, $T_s > T_N$ suggests that the structural instability is the primary one. It certainly puts the simple picture of the orthorhombic distortion as a mere consequence of antiferromagnetism into question and has started an intensive debate about the origin of the structural phase transition in the iron-based materials [9, 73, 74].

In order to experimentally study the in-plane anisotropy of various physical quantities, the formation of twins, i.e., structural domains in which the inequivalent a and b axis are exchanged relative to each other [39], has to be prevented. Therefore, many experiments have been carried out under uniaxial stress along the tetragonal direction [110], $\sigma_{[110]}$, which detwins the samples because it favors the domains with the (shorter) b axis along the direction of the applied stress [40].

One of the first observations was a large in-plane anisotropy of the resistivity in $Ba(Fe,Co)_2As_2$ (nearly a factor of 2) which grows with Co content [80], see Fig. 4.1. However, only very weak resistivity anisotropy is observed in $(Ba,K)Fe_2As_2$ [82], and, subsequently, disorder was shown experimentally to play an important

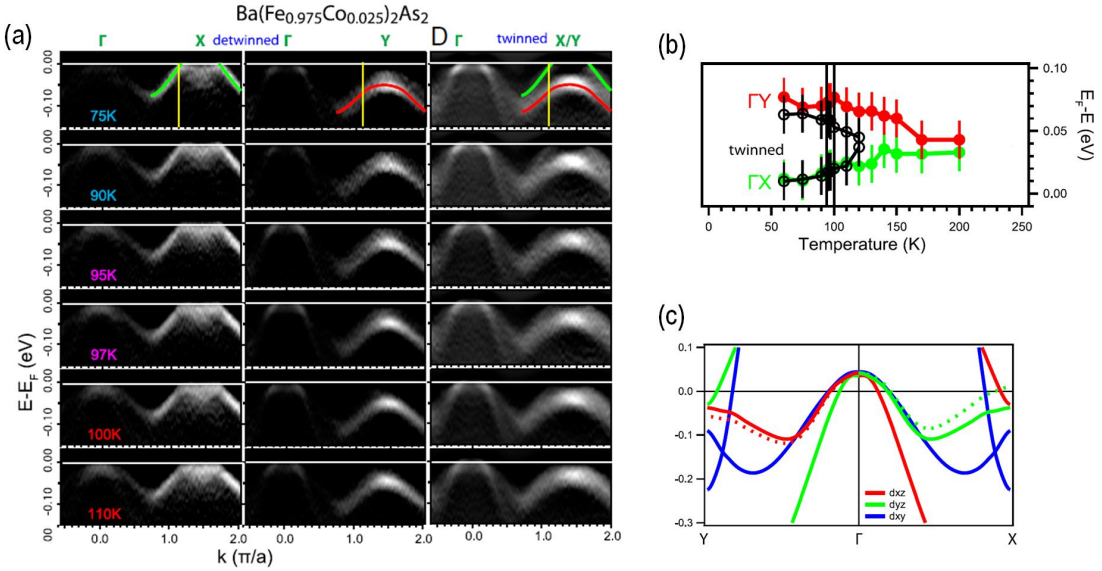

Figure 4.2.: (a) Evolution of the band structure of lightly doped $Ba(Fe,Co)_2As_2$ upon increasing T. The measurement of detwinned crystals allows to distinguish the energy shift of different orbitals. (b) Energy of the top of the hole bands with respect to the Fermi level, revealing that the d_{xz} (d_{yz}) band shifts to lower (higher) energies approximately at T_s. (c) Schematic drawing of the dispersion. Continuous lines represent the bandstructure in the high-temperature tetragonal phase and broken lines the shifted bandstructure in the orthorhombic phase. Figure adapted from Ref. [81].

role in creating this resistivity anisotropy [83, 84]. Angular resolved photo emission spectroscopy (ARPES) in detwinned samples was also measured early [81] and the d_{xz} (d_{yz}) orbital was found to shift to lower (higher) energies below T_s (Fig. 4.2). Various optical conductivity studies also stress the importance of orbital anisotropy [83, 85] and scattering rates [85]. A nuclear magnetic resonance [86] and an inelastic neutron scattering study [87] show significant anisotropy of the spin dynamics even at $T_s > T > T_N$. Altogether, the observed large electronic anisotropy in the presence of a rather small lattice distortion of $< 0.4\%$ has been interpreted as evidence for an electronic order parameter driving the lattice distortion. The existence of such an electronic order parameter has been claimed to be demonstrated in a measurement of the resistivity anisotropy as a function of strain, applied via a piezo stack to a sample [88]. The experiment is briefly reviewed in section 4.4.1. Because this electronic order parameter necessarily breaks the four-fold rotational symmetry of the tetragonal lattice, it is termed

"nematic". It became evident that the small uniaxial stress needed for detwinning significantly smears out the structural transition and induces some anisotropy of electronic properties even above T_s [80, 89–91]. This clearly demonstrates a large sensitivity of the system to $\sigma_{[110]}$, i.e., a large nematic susceptibility.

As to the nature of the nematic order parameter, two competing (families of) models have been proposed. The first one places emphasis on orbital degrees of freedom [73, 92]. In the high-symmetry tetragonal phase, the iron d_{xz} and d_{yz} orbitals are degenerate. In a simple picture, the system may lower its total energy by distorting such that the two degenerate orbitals become inequivalent (see Fig. 4.3), in analogy to a Jahn-Teller distortion. The "nematic" order parameter is then given by the difference in orbital occupation. Orbital order can induce changes in the magnetic correlation length, which may induce magnetism. This model naturally explains why the structural transition occurs above the magnetic transition, yet the magnetic transition does not necessarily follow the structural one within the orbital scenario.

The second model, the spin-nematic scenario, is based on spin fluctuations as the driving force for the structural transition. In this model, the primary instability is that of the stripe-type magnetic phase. However, this state has an additional degree of freedom with respect to common checkerboard antiferromagnetism. Namely, the symmetry of the magnetic order parameter is $O(3) \times Z_2$, where $O(3)$ is the spin-rotational symmetry (broken in any magnetic state) and Z_2 is a discrete, two-fold (i.e., Ising-type) symmetry that describes the orientation of the ferromagnetic stripes. The stripe-type magnetic state may be visualized by dividing the square iron-lattice into two imaginary sublattices, characterized by the Néel vectors $\mathbf{m}_1$ and $\mathbf{m}_2$ (see Fig. 4.4). Their relative orientation is then another, scalar order parameter $\varphi = \mathbf{m}_1 \cdot \mathbf{m}_2$. φ is the "spin-nematic" order parameter, which determines whether stripes are oriented along the 'horizontal' or the 'vertical' in Fig. 4.4. Flipping the spins on only one sublattice changes the orientation of the stripes and the sign of φ. The calculation of Ref. [10] has shown that the Z_2 symmetry may be broken by spin fluctuations (which induces the orthorhombic distortion) at a higher temperature than the temperature at which the spin-rotational symmetry is broken and the individual magnetic sublattices order. This can explain why the structural transition may precede the magnetic one, even if both are driven by magnetic fluctuations.

A central issue for unconventional superconductors is the search for a "pairing glue", a boson which mediates attractive interaction between electrons. In case of the iron-based superconductors, spin fluctuations have been an obvious candidate because of the proximity between superconductivity and antiferromagnetism. They were shown to lead to a sign-changing s_{+-} superconducting order parameter [94–96]. On the other hand, orbital fluctuations have also been con-

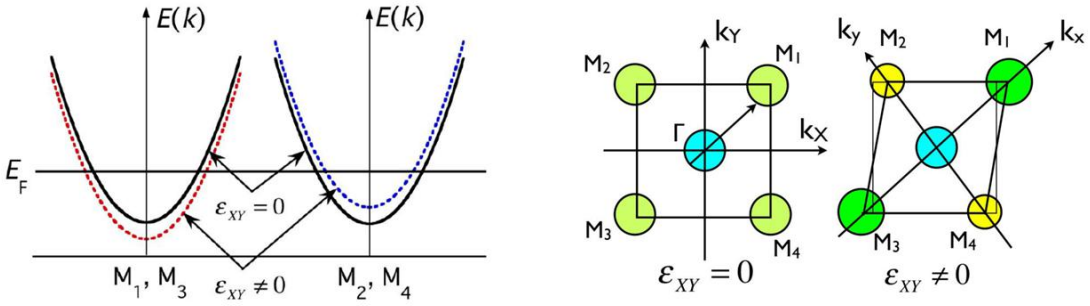

Figure 4.3.: Schematic representation of how an orthorhombic distortion, ε_{XY}, lifts the degeneracy of the electronic dispersion near the M points of the Brillouin zone and induces anisotropic orbital occupation. Figure taken from Ref. [92].

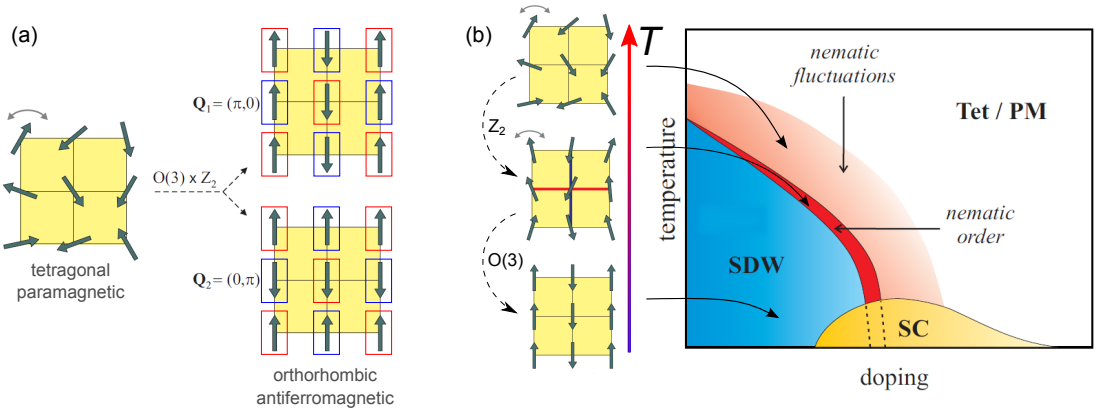

Figure 4.4.: Schematic drawing showing how the structural transition arises from spin fluctuations. A likely spin configuration of the iron atoms is shown for each state. (a) The magnetic state of the iron-arsenides with two possible orientations of the ferromagnetic stripes. It is determined by the relative orientation of the Néel vectors of the 'red' and the 'blue' sublattices. (b) Upon decreasing T, the direction of the ferromagnetic stripes is defined (nematic/structural phase transition, Z_2 broken) before the individual spins order (magnetic phase transition, $O(3)$ broken). Arrows in (b) indicate which regions of the phase diagram of, e.g., $Ba(Fe,Co)_2As_2$ are associated with these states. Figure adapted from Ref. [93].

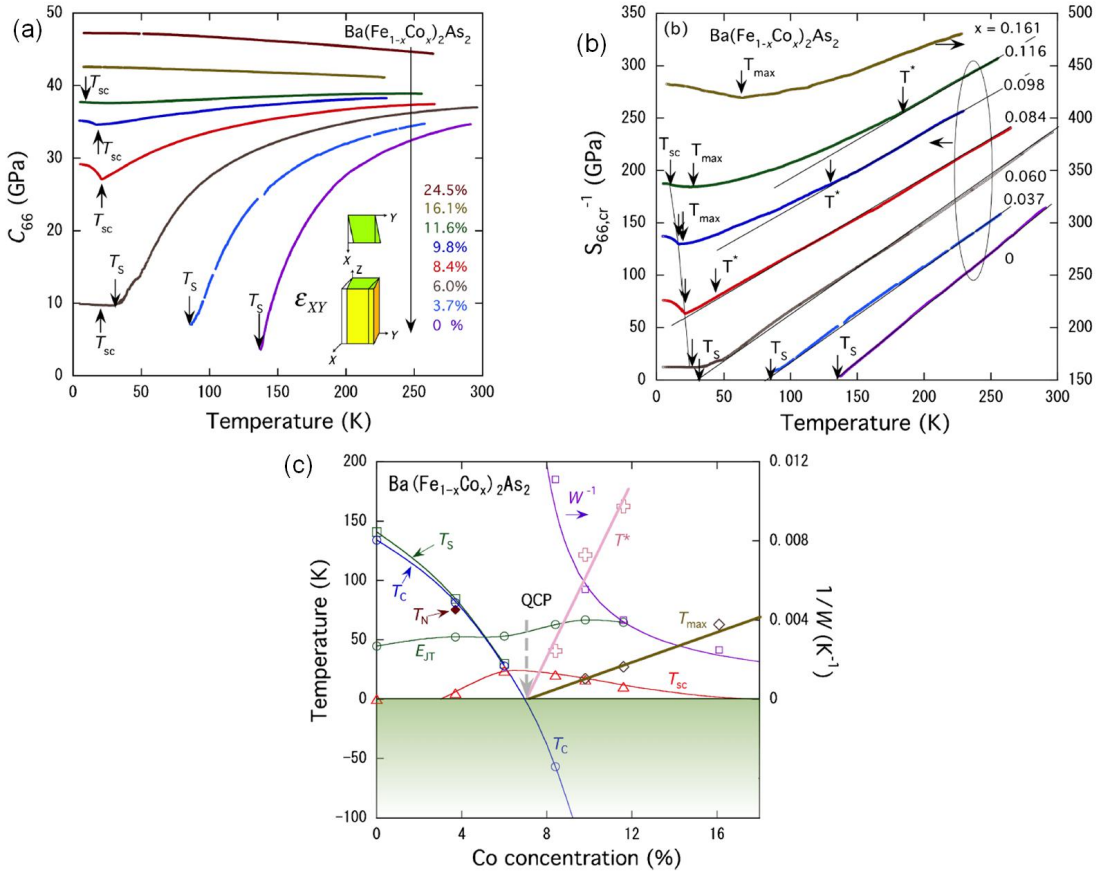

Figure 4.5.: (a) Elastic shear modulus C_{66} for a wide substitution range of $Ba(Fe,Co)_2As_2$, measured using ultrasound. C_{66} is clearly shown to be the "soft mode" of the structural phase transition. (b) The temperature and doping dependence of its inverse, the structural susceptibility. (c) shows characteristic temperatures from (b) in a phase diagram, suggesting a "structural quantum critical point" at optimal doping. Figures taken from Ref. [98].

sidered and superconductivity of sign-conserving s_{++} kind was suggested on this basis [73, 97]. This relation with the superconducting gap structure clearly raises the stakes for finding the driving force—orbital or spin physics—of the structural phase transition in the iron-based compounds.

It is clear that once a material undergoes the structural transition, all properties (e.g., lattice constants, orbital occupation or spin fluctuations) will be anisotropic, which makes it difficult to distinguish between the two scenarios. As an alternative, the study of the susceptibility of the various quantities above the structural

transition has been suggested [9, 99]. The structural susceptibility is given by the inverse elastic stiffness and was studied extensively in the $Ba(Fe,Co)_2As_2$ system using ultrasound [10, 92, 98, 100]. These measurements clearly establish the shear mode C_{66} as the soft mode of the structural transition, as expected from the symmetry of the lattice distortion. Further, signatures of a behavior which was termed "structural quantum criticality" were found around optimal doping. Namely, the temperature and doping dependence of the structural susceptibility $S_{66} = C_{66}^{-1}$ was found to resemble closely the magnetic susceptibility in proximity to a magnetic quantum critical point (Fig. 4.5) [98]. The elastic softening persists over a large part of the superconducting dome on the overdoped side which makes the associated fluctuations a promising candidate for the pairing glue in the iron-based systems [98].

As pointed out in the conclusion of chapter 3, the hole-doped $(Ba,K)Fe_2As_2$ system is different from the electron doped one in many respects. In particular, there is no separate orthorhombic-paramagnetic, i.e., nematic phase and $T_s = T_N = T_{s,N}$ for all doping levels. Furthermore, $T_{s,N}(x)$ falls more steeply at the endpoint of the magnetically ordered phase and the superconducting dome is wider. It is therefore of great interest to also examine the elastic shear modulus of $(Ba,K)Fe_2As_2$ and to clarify whether an elastic softening may be related to superconductivity and whether structural quantum criticality is a universal feature of the iron arsenides. The experimental study is, however, complicated by the fact that single crystals of $(Ba,K)Fe_2As_2$ of sufficient quality for ultrasound studies have not yet become available. Instead, we have developed the novel technique of high-resolution three-point bending in the capacitance dilatometer, which allows to measure the elastic shear modulus of both $(Ba,K)Fe_2As_2$ and $Ba(Fe,Co)_2As_2$.

4.2. Three-point bending in a capacitance dilatometer

Three-point bending is a long-standing and extremely widely used mechanical test to study elastic properties. Applications range from material engineering to food industry. The technique is particularly appealing by its simplicity. A platelet- or beam-shaped sample is supported along two lines, while a force F is applied at a third, middle, line and the deflection u is measured (see Fig.4.6) yielding the stiffness $k_s = F/u$. Since rather small forces result in sizable deflections, a high resolution can be achieved.

4.2.1. Basics of three-point bending

The stiffness k_s of a sample in three-point bending is given by the following combination of geometric parameters and material constants [101] (see Fig. 4.6)

$$k_s = 4w \left(\frac{h}{l}\right)^3 Y_{\vec{\mu}} \left[1 + \frac{3}{2}\left(\frac{h}{l}\right)^2 \frac{Y_{\vec{\mu}}}{G_{\vec{\mu},\vec{\nu}}}\right]^{-1} \tag{4.1}$$

Here, l, w and h are the span, the width and the thickness of the sample, respectively, and $\vec{\mu}$ is directed along l while $\vec{\nu}$ is directed along h. $Y_{\vec{\mu}}$ is the Young modulus for a uniaxial tensile experiment along $\vec{\mu}$ and $G_{\vec{\mu},\vec{\nu}}$ is the shear modulus for shear deformation between the directions $\vec{\mu}$ and $\vec{\nu}$.

Typical dimensions of our samples are $l \times w \times h = 3\text{mm} \times 1\text{ mm} \times 0.1\text{ mm}$ with the shortest dimension parallel to the crystal c axis. When $h/l \ll 1$, the shear term proportional to $(h/l)^2$ may the neglected, given that the ratio Y/G is not too large. Thus, for our thin samples, three-point bending is essentially equivalent to a uniaxial-tension experiment, and the stiffness k_s is proportional to the Young modulus of the material. The uniaxial stress to which the sample is subjected is highly inhomogeneous. The maximum tensile stress is reached at the lower surface and amounts to [101]

$$\sigma_{max} = \frac{3Fl}{2wh^2} \tag{4.2}$$

The Young modulus is related to components of the elastic stiffness tensor. For example, $Y_{[100]}$ (in a coordinate system oriented along the symmetry directions of a tetragonal sample) is given by

$$Y_{[100]} = \frac{1}{S_{11}} = C_{11} + \frac{2C_{12}C_{13}^2 - C_{11}C_{13}^2 - C_{12}^2C_{33}}{C_{11}C_{33} - C_{13}^2} \tag{4.3}$$

Physically, the second term arises from transverse contractions (analogous to the Poisson effect). In order to compute the equivalent expression for $Y_{[110]}$, which is in the focus here, one has to rotate the reference frame by 45° around the principal 3 axis before taking the '11' component of the compliance tensor. Care has to be

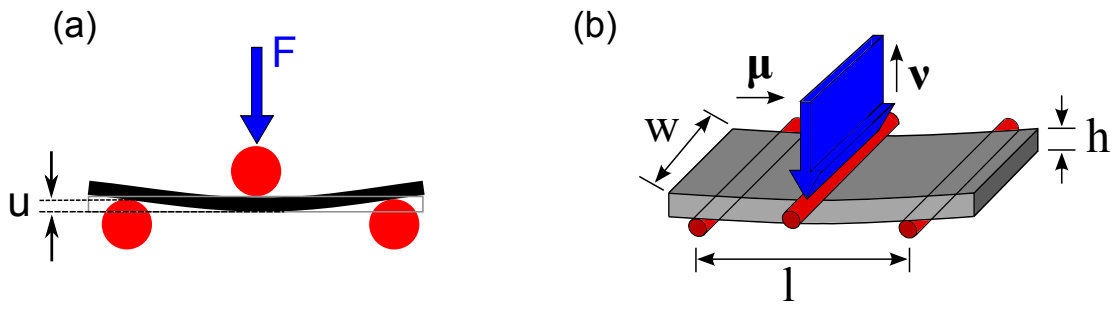

Figure 4.6.: (a) Force F and deflection u in a three point bending setup. (b) Definition of sample dimensions and directions in equation 4.1.

taken because S_{ij} is not a "real" matrix and transforms in a specific way under rotations: $S' = T_\varepsilon S T_\sigma^{-1}$ [102]. The Young modulus in this case[7] is given by

$$Y_{[110]} = 1/S'_{11} = 4\left(\frac{1}{C_{66}} + \frac{1}{\gamma}\right)^{-1} \quad \text{with } \gamma = \frac{C_{11}}{2} + \frac{C_{12}}{2} - \frac{C_{13}^2}{C_{33}}. \tag{4.4}$$

It turns out to be fortunate for the present work, that this is dominated by C_{66} as long as C_{66} is smaller than the combination γ. In particular, C_{66} is expected to be small close to the structural phase transition of the iron-based materials.

7. The rotation by 45° around the '3' axis is translated by

$$T_\varepsilon = \begin{pmatrix} 1/2 & 1/2 & 0 & 0 & 0 & 1/2 \\ 1/2 & 1/2 & 0 & 0 & 0 & -1/2 \\ 0 & 0 & 1 & 0 & 0 & 0 \\ 0 & 0 & 0 & 1/\sqrt{2} & -1/\sqrt{2} & 0 \\ 0 & 0 & 0 & 1/\sqrt{2} & 1/\sqrt{2} & 0 \\ -1 & 1 & 0 & 0 & 0 & 0 \end{pmatrix}$$

and

$$T_\sigma^{-1} = \begin{pmatrix} 1/2 & 1/2 & 0 & 0 & 0 & -1 \\ 1/2 & 1/2 & 0 & 0 & 0 & 1 \\ 0 & 0 & 1 & 0 & 0 & 0 \\ 0 & 0 & 0 & 1/\sqrt{2} & 1/\sqrt{2} & 0 \\ 0 & 0 & 0 & -1/\sqrt{2} & 1/\sqrt{2} & 0 \\ 12 & -1/2 & 0 & 0 & 0 & 0 \end{pmatrix}$$

which yields for the '11' component of S'

$$S'_{11} = \frac{2C_{33}C_{66} + C_{11}C_{33} + C_{12}C_{33} - 2C_{13}^2}{4\left(C_{11}C_{33}C_{66} + C_{12}C_{33}C_{66} - 2C_{13}^2C_{66}\right)}.$$

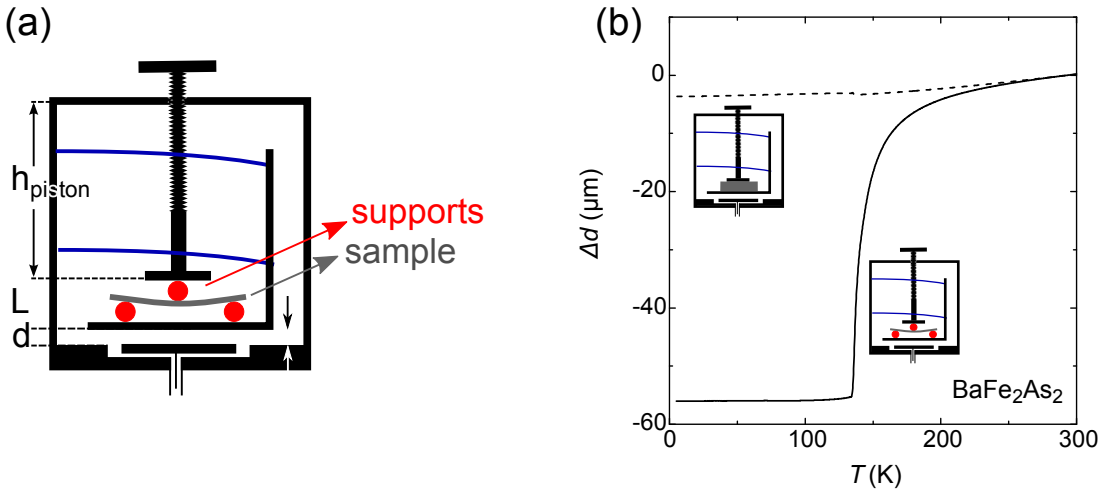

Figure 4.7.: (a) Schematic drawing of how a sample is placed into the dilatometer in a three-point bending configuration using wire supports. The lengths L, d, and h_{piston}, see 4.2.2, have been indicated. (b) Measured change of the capacitor gap $\Delta d = d(T) - d(300\ \mathrm{K})$ for a bending experiment along [110] using a $BaFe_2As_2$ sample with $l \times w \times h = 3.3\ \mathrm{mm} \times 1\ \mathrm{mm} \times 0.1\ \mathrm{mm}$ (solid line). A huge effect on approaching T_s from above is observed. Shown for comparison is the much smaller change of the capacitor gap, when the c-axis thermal expansion of a 0.887 mm long sample of $BaFe_2As_2$ is measured (dashed line), see sketch.

Our newly-developed setup employs a capacitance dilatometer to measure $Y_{[110]}$ using a three-point bending setup. Figure 4.7 shows an example of the huge effect observed when a $BaFe_2As_2$ sample is inserted in the dilatometer in three-point bending configuration as compared to a regular thermal-expansion measurement of a similar sample. In the bending experiment, the capacitor gap increases dramatically on decreasing T from room temperature to $T_s = 135$ K. The next section details the quantitative analysis of these data.

4.2.2. Derivation of a method for quantitative analysis

In general in the dilatometer, a sample of length L is squeezed between piston and movable plate of the plate-type capacitor by fixing the piston length h_{Piston} (see Fig. 2.7), so that sample-length changes lead to a change of the capacitor gap d. Capacitance changes are read out using a capacitance bridge which is initially balanced for a certain value of d. When a sample that is mounted in three-point bending configuration (Fig. 2.7) grows soft, its flection increases and

its effective length L decreases. Note that L is the total length of the sample and the supports along the dilatometer axis, as shown in Fig. 4.7. This length change can be measured with very high accuracy ($\sim 10^{-11}$ m). For the quantitative analysis, however, both length and force measurements are required. It turns out that both quantities can be evaluated from the measured capacitor gap $d(T)$ if the sample stiffness at room temperature $k_s(RT)$ is known, which can be determined *in situ*.

To derive the formulas for quantitative evaluation we consider the temperature dependence of the capacitor gap during a normal measurement [superscript (1)] compared to a reference "zero-force" state [superscript (0)]. In this hypothetical state, a sample is mounted but no force is applied via the piston. The stiffness of the combined two dilatometer springs k_d has been determined (see below) and will be considered as given, while the sample stiffness k_s is to be determined. Both k_d and k_s as well as the zero-force lengths $L^{(0)}$, $d^{(0)}$ and $h^{(0)}_{Piston}$ are temperature dependent. In the derivation of the evaluation formulas, we refer to an arbitrary temperature T as compared to room temperature RT.

The stiffness of the sample at a given temperature is given by Hooke's law from the force applied to it via the piston and its length change under this force. However, the same force is also responsible for the change of the capacitor gap, so that

$$k_s(T) = \frac{F_{piston}(T)}{L^{(0)}(T) - L^{(1)}(T)} \tag{4.5}$$

$$= \frac{k_d(T)\left(d^{(0)}(T) - d^{(1)}(T)\right)}{L^{(0)}(RT)\xi_s - L^{(1)}(T)} \tag{4.6}$$

Here, $\xi_s = L(T)/L(RT)$ accounts for the thermal expansion of the sample between RT and T. The length change with temperature of the sample in the dilatometer $L^{(1)}(T) - L^{(1)}(RT)$ is obtained from the measured capacitor gap using a calibration measurement with a copper sample (index "Cu") and the formula for the relation between capacitor gap and sample-length change from Ref. [37] (see eq. 2.15 in the introduction 2.3). In the notation of this chapter, it is written as

$$L^{(1)}(T) = L_{Cu}(RT)\xi_{Cu} + (d^{(1)}(RT) + L^{(1)}(RT) - d_{Cu}(RT) - L_{Cu}(RT))\xi_{Cu:Be} + d_{Cu}(T) - d^{(1)}(T). \tag{4.7}$$

By using this procedure, results are corrected for thermal expansion of the cell and the sample. The relationship between $L^{(1)}(RT)$ and $L^{(0)}(RT)$ is again given

by Hooke's law $L^{(1)}(RT) = L^{(0)}(RT) - \frac{F_{piston}}{k_s(RT)}$. Inserting these two equations and rearranging leads to

$$\begin{aligned} k_s(T) &= \frac{k_d(T)\left(d^{(0)}(T) - d^{(1)}(T)\right)}{A + B - (d_{Cu}(T) - d^{(1)}(T))} \quad \text{with} \\ A &= \frac{k_d(RT)}{k_s(RT)}\left(d^{(0)}(RT) - d^{(1)}(RT)\right)\xi_{Cu:Be} + \left(d_{Cu}(RT) - d^{(1)}(RT)\right)\xi_{Cu:Be} \\ B &= L^{(0)}(RT)\left(\xi_s - \xi_{Cu:Be}\right) - L_{Cu}(RT)\left(\xi_{Cu} - \xi_{Cu:Be}\right). \end{aligned} \tag{4.8}$$

The temperature dependence of k_s, proportional to the Young modulus of the sample, can therefore, finally, be obtained as,

$$\frac{k_s(T)}{k_s(RT)} = \frac{k_d(RT)}{k_s(RT)}\frac{k_d(T)}{k_d(RT)} \times \frac{d^{(0)}(T) - d^{(1)}(T)}{A + B - (d_{Cu}(T) - d^{(1)}(T))} \tag{4.9}$$

In particular, the room-temperature value $k_s(RT)$ is needed. It can be determined by making use of the effect of gravity on the dilatometer (see Fig. 4.8). Namely, we measure the difference of the capacitor gap d when the dilatometer is horizontal versus vertical. The effect is easily understood by considering the empty dilatometer. When no sample in inserted and the dilatometer is horizontal the capacitor gap is

$$d_{hor} \equiv d_{0,0}. \tag{4.10}$$

When the dilatometer is brought into a vertical position, the weight of the internal parts of the dilatometer acts with a force $F_{internal}$ on the dilatometer springs. Thus, according to Hooke's law,

$$\Delta d_{hor-vert} = d_{hor} - d_{vert} = \frac{F_{internal}}{k_d} \tag{4.11}$$

When a sample is mounted and the dilatometer is turned from horizontal to vertical in this state, a gap change occurs if k_s is finite. This is because the stiffness of the combined system when the sample is squeezed against the movable capacitor plate with a force $F_{piston} > F_{internal}$ is given by $k_d + k_s$ and, hence,

$$\Delta d_{hor-vert} = \frac{F_{internal}}{k_s + k_d}. \tag{4.12}$$

In this way, $k_s(RT)$ can be obtained from $\Delta d_{hor-vert}$. Note that $\Delta d_{hor-vert}$ vanishes for a regular sample with $k_s \to \infty$, which is why the effect of gravity is not normally observed.

Equations 4.9 and 4.12, together with the calibration measurements, were implemented in a small matlab® code that is used to evaluate the data.

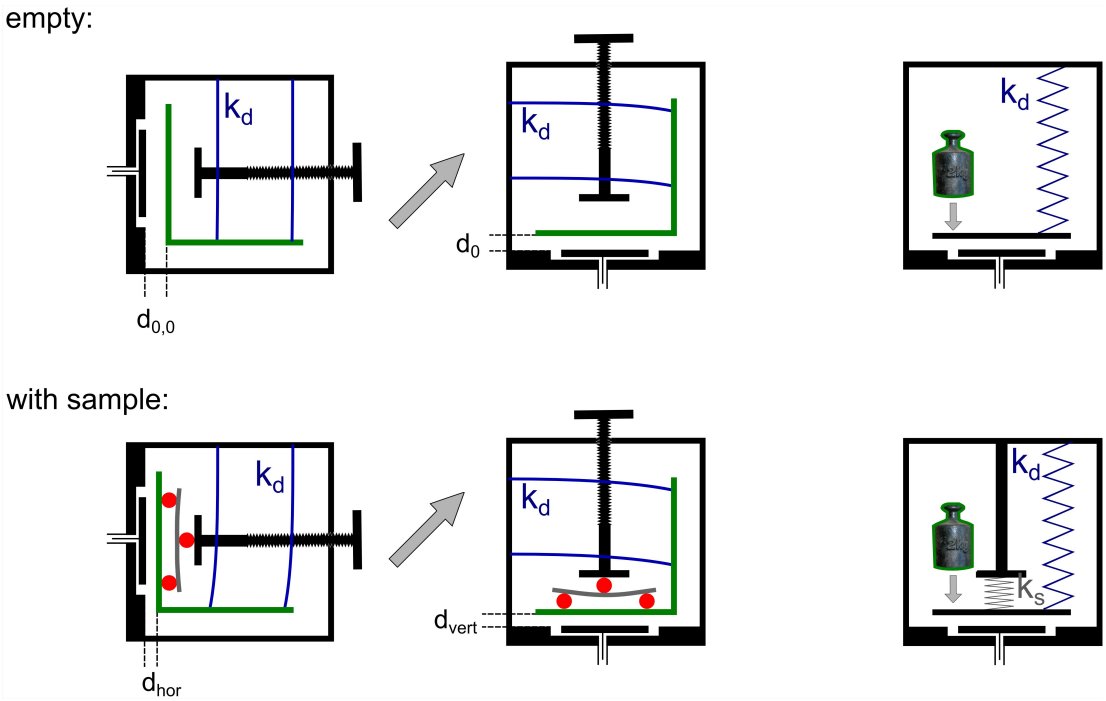

Figure 4.8.: Effect of gravity on the capacitor gap, used to determine the sample stiffness k_s at room temperature. The empty dilatometer (dilatometer with a sample of finite stiffness) is shown in the top (bottom) row. The movable part of the dilatometer, whose weight $F_{internal}$ is decisive for the procedure to work, is sketched in green, the dilatometer springs are in blue. The capacitor gap d changes according to equations 4.11 and 4.12 when the dilatometer is turned from 'horizontal' to 'vertical'. On the right side, the equivalent of the turning experiment, i.e., adding the weight $F_{internal}$ is illustrated.

4.2.3. Calibration of the dilatometer

In order to use the evaluation formulas 4.9 and 4.12 the following quantities need to be determined:

- the stiffness of the dilatometer springs k_d at room temperature
- the mass of the internal parts of the dilatometer $F_{internal}$
- the capacitor gap in zero-force state $d^{(0)}$ at room temperature
- the temperature dependence of $d^{(0)}$ and k_d
- a calibration measurement of the thermal expansion of a copper sample $d_{Cu}(T)$, whose length L_{Cu} is comparable to the length $L^{(1)}$ of the samples measured in bending

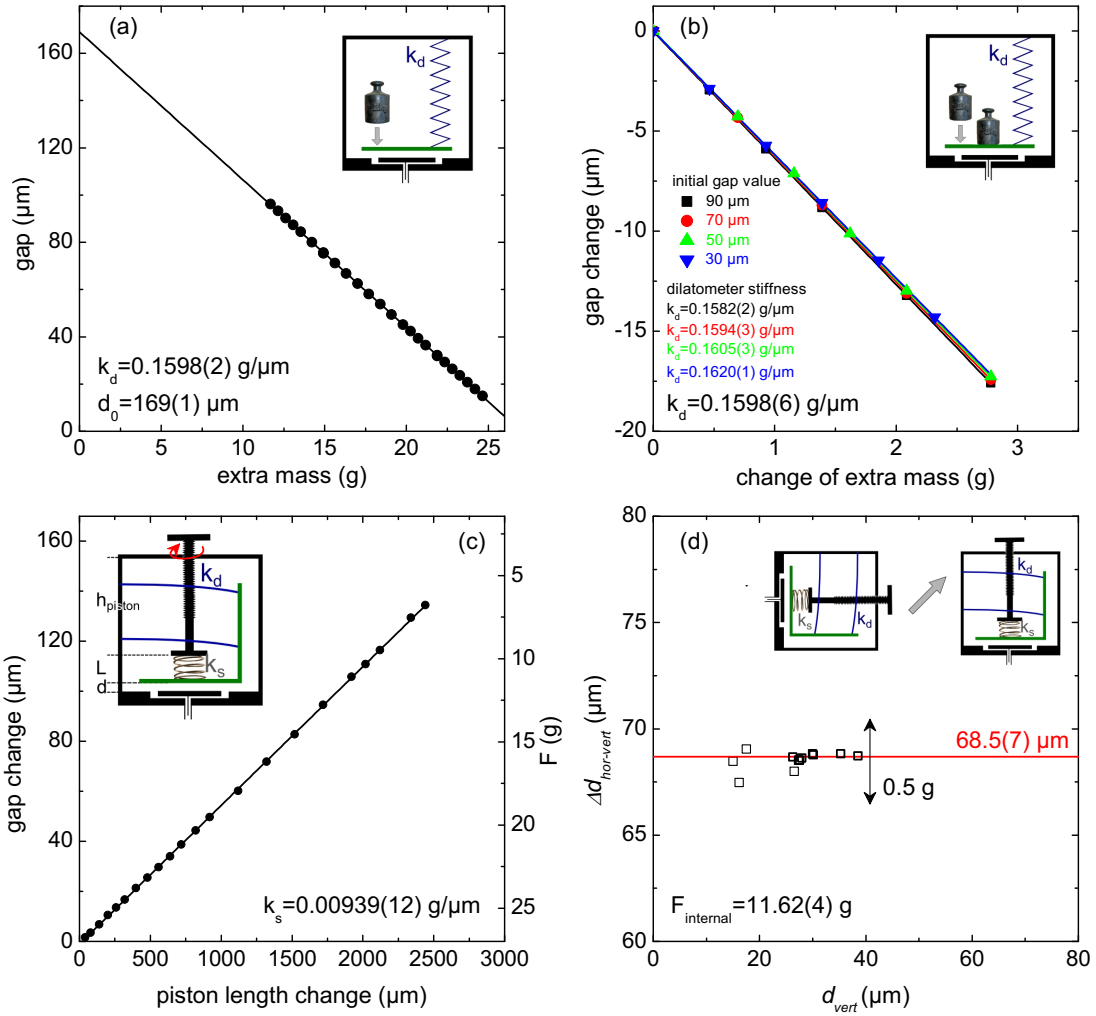

Figure 4.9.: (a) Determination of the spring constant k_d and the zero-force gap $d^{(0)}(RT) = d_0$ by evaluating the gap change due to weights placed onto the movable part of the dilatometer. Below 14 μm, the capacitor plates are too close and no measurement is possible, above 100 μm the preamplifier is out of range. (b) shows a similar experiment using different initial gap values. (c) Determination of the stiffness of a steel compression spring used as a calibration sample. (d) Determination of $F_{internal}$ from turning the dilatometer with the same steel spring inserted. Schematic drawings illustrate each experiment.

The room-temperature quantities $k_d(RT)$, $d^{(0)}(RT)$ and $F_{internal}$ can be determined with a simple set of experiments (see Fig. 4.9). First, the empty dilatometer is brought into a vertical position and additional weights are attached to the movable part. The capacitance bridge is rebalanced each time a weight is added and the amount by which its reference value had to be changed is converted into μm so that the whole gap vs. weight curve is obtained, which yields

$$\begin{aligned} k_d(RT) &= 0.1598(2)\ \text{g}/\mu\text{m} = 1.598(2)\text{mN}/\mu\text{m}, \\ d^{(0)}(RT) &= d_0 = 169(1)\ \mu\text{m}. \end{aligned} \tag{4.13}$$

Note that we choose to measure forces due to gravitation in g, i.e., in equivalent mass for clarity. In order to check the linearity of the gap vs. mass relation, data are taken with different initial gap values and the gap difference arising from additional masses is recorded. A fit to all data points yields an average $k_d(RT) = 0.1598(6)$ g/μm. There is indeed a very small dependence of $k_d(RT)$ on the gap value, i.e., the relationship is slightly non-linear. Fortunately, the variation of k_d over the whole maximally relevant gap interval (20 μm-80 μm) is of only 2% and will be neglected.

In order to determine $F_{internal}$, we first calibrate the stiffness of a steel compression spring. The spring is inserted into the dilatometer and the piston length h_{piston} is changed by turning the dilatometer screw (pitch 500 μm) by a fraction of 360° while recording the gap change (Fig. 4.9). h_{piston} and Δd are related via [8]

$$\Delta d = \frac{k_s}{k_s + k_d} \Delta h_{piston}. \tag{4.14}$$

The experiment yields a value of $k_s = 0.00939(12)\text{g}/\mu\text{m} = 0.0939(12)\text{mN}/\mu\text{m}$. for our steel spring. We can now use the procedure of turning the dilatometer from the horizontal into the vertical and record $\Delta d_{hor-vert}$ to obtain $F_{internal}$ via equation 4.12. The procedure is repeated several times (Fig. 4.9 (d)) and the average yields,

$$\Delta d_{hor-vert} = 68.5(7)\ \mu\text{m} \tag{4.15}$$

$$F_{internal} = 11.6(2)\ \text{g}. \tag{4.16}$$

The temperature dependence of the gap value with no applied force except for the mass $F_{internal}$, $d^{(0)}(T) - d^{(0)}(RT)$, was measured by cooling down the empty

8. The relation follows by considering two states, (k) and (l), that differ by the force F applied to the dilatometer spring and the sample $F^{(k)} - F^{(l)} = k_s \left(L^{(k)} - L^{(l)}\right) = k_d \left(d^{(k)} - d^{(l)}\right)$. The total length is constant, *i.e.* $h^{(k)}_{piston} + L^{(k)} + d^{(k)} = h^{(l)}_{piston} + L^{(l)} + d^{(l)}$, which yields relation 4.14 for the differential quantities $\Delta L = L^{(k)} - L^{(l)}$ and $\Delta h_{piston} = h^{(k)} - h^{(l)}$.

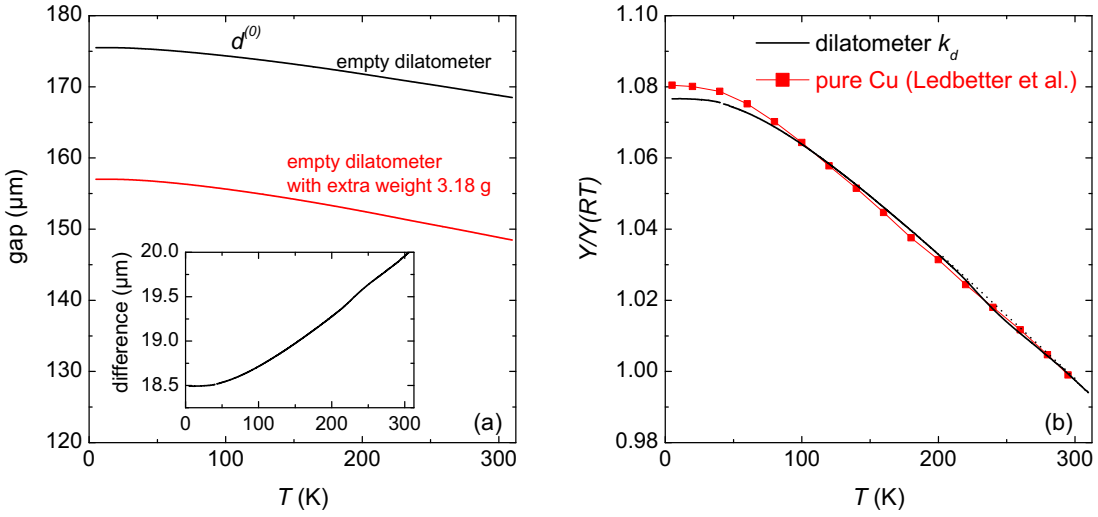

Figure 4.10.: (a) Temperature dependence of the gap value of the empty dilatometer $d^{(0)}(T)$ and of the dilatometer with extra mass inserted. A small offset of the data has been corrected to match results 4.13. The inset shows the difference between the two measurements, which is proportional to the inverse of the dilatometer stiffness $\left(d^{(0)} - d\right) = F_{extra}/k_d$. (b) Comparison between the obtained $k_d(T)$ and the Young modulus of polycrystalline Cu [103], normalized at room temperature. The agreement is very good.

dilatometer and is shown in Fig. 4.10. The temperature dependence of k_d is determined by inserting a mass ($F_{extra} = 3.1817$ g) into the dilatometer, i.e., increasing $F_{internal}$ and measuring the capacitor gap change upon cooling again (Fig. 4.10). At any temperature, the gap difference between the measurement with this extra weight and without it, is proportional to the inverse of the dilatometer spring constant, from which $k_d(T)$ is obtained. Fig. 4.10 shows the resulting $k_d(T)$ normalized by its room temperature value. It hardens by $\sim 8\%$ between room temperature and zero temperature. A small non-reversible anomaly, presumably arising from effects within the dilatometer cell, is detected above 200 K. The temperature dependence of k_d is in principle given by the temperature dependence of the Young modulus of Cu:Be. Cu:Be contains a small amount of Be which serves to pin dislocations and therefore increase the yield strength (i.e., the limit for plastic deformation), but the Young modulus of Cu:Be is expected to be very similar to pure copper. Indeed, our overall result compares very well to the Young modulus of polycrystalline copper from literature [103]. We use the literature result in the evaluation procedure. Finally, a calibration measurement with a small

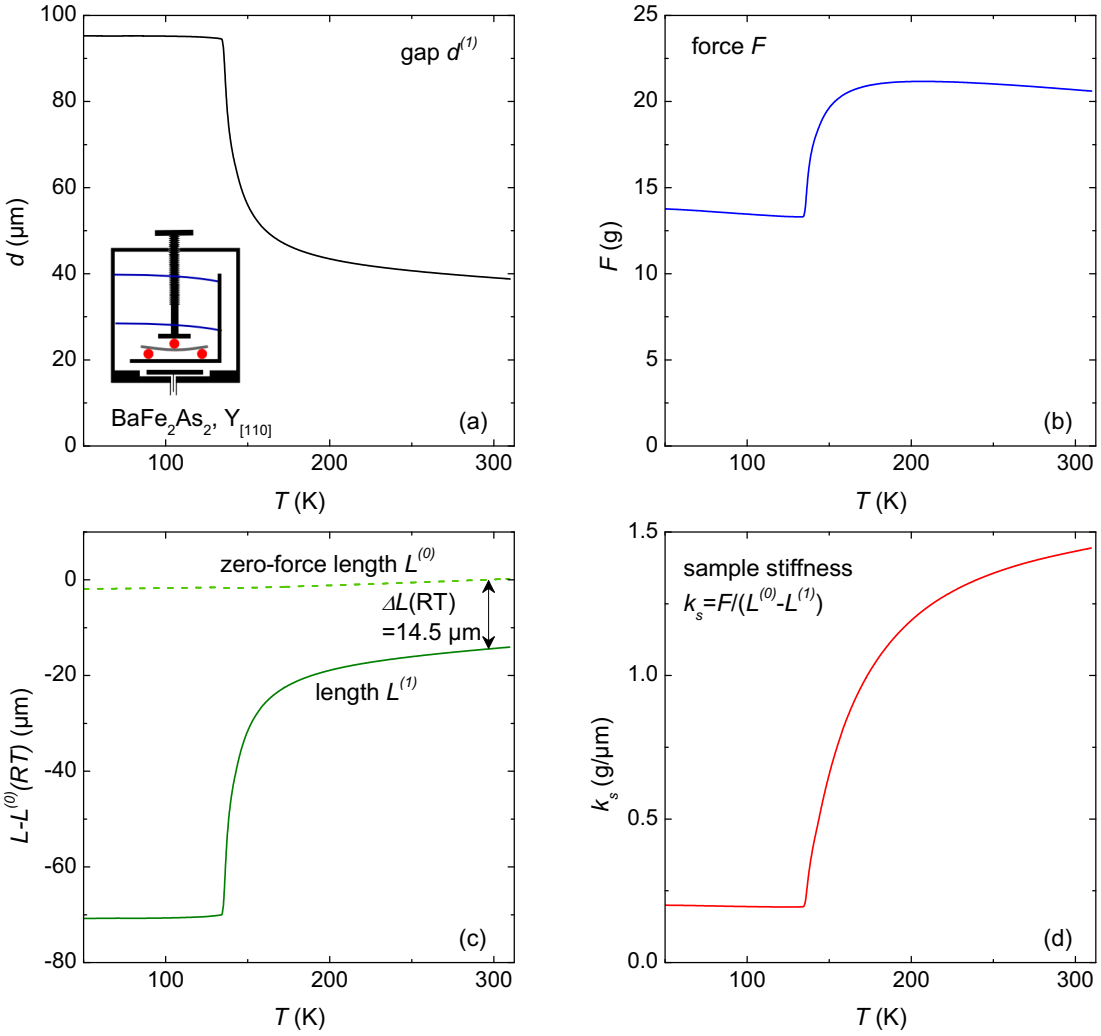

Figure 4.11.: Example of quantitative evaluation of the three-point bending data from Fig. 4.7. The measured gap change between holding the dilatometer horizontal and vertical with this sample is $\Delta d_{hor-vert} = 7.3$ μm, which yields $k_s(RT) = 1.42$ g/μm. (a) shows the capacitor gap and (b) the force acting on the sample $F(T) = k_d(T)\left(d^{(0)}(T) - d^{(1)(T)}\right)$, while panel (c) shows the temperature-dependent length change of the unbent sample $L^{(0)}(T) - L^{(0)}(RT)$ (dashed line; from a separate thermal-expansion measurement) and the sample-length change due to bending $L^{(1)}(T) - L^{(0)}(RT)$, inferred from the measurement of $d^{(1)}(T)$ using $k_s(RT) = 1.42$ g/μm (solid line). Finally, (d) shows the resulting sample stiffness in three-point bending $k_s(T) = \frac{F(T)}{d^{(0)}(T)-d^{(1)}(T)}$, proportional to the Young modulus $Y_{[110]}$.

piece of copper ($L_{Cu} = 0.527$ mm) has been carried out in order to obtain d_{Cu} in equation 4.7.

Figure 4.11 shows the evaluation of the three-point bending measurement of $Y_{[110]}$ of $BaFe_2As_2$ ($T_s = 135$ K) as an example. The capacitor gap, which amounts to $\sim$ 40 μm at room temperature increases strongly upon cooling, when the flection of the sample increases. The force F acting on the sample is determined by the increasing gap d and the increasing dilatometer stiffness k_d on decreasing T. The two effects compete and result in a non-monotonic temperature dependence of F. The fractional length change of the unbent sample $L^{(0)}(T)/L^{(0)}(RT)$ is obtained by a separate c-axis thermal-expansion measurement. The length change of the bent sample with respect to $L^{(0)}(RT)$ is calculated from the gap change correcting for the thermal expansion of the cell (eq. 4.7) and from the result of turning the dilatometer from the horizontal into the vertical with the same sample inserted (eq. 4.12). Finally, the resulting sample stiffness in three-point bending $k_s(T) = \frac{F(T)}{d^{(0)}(T) - d^{(1)}(T)}$, proportional to the Young modulus $Y_{[110]}$, is obtained.

4.3. Experimental Young modulus of K- and Co-substituted $BaFe_2As_2$

In a first step, undoped $BaFe_2As_2$ was investigated. Fig. 4.12 shows the Young modulus of $BaFe_2As_2$ along the in-plane [110] and [100] directions measured in a three-point bending setup in the capacitance dilatometer. Data have been normalized at room temperature, because absolute values are poor due to their high sensitivity to geometrical parameters (eq. 4.1). The structural phase transition at $T_s = 135$ K is clearly visible as a sharp kink. The Young modulus along [110], $Y_{[110]}$ shows a softening of 85% upon decreasing T between room temperature and T_s, while $Y_{[100]}$ only shows a softening of $\sim$ 10%. Both have an essentially flat temperature dependence below T_s. The extensive softening of $Y_{[110]}$ above T_s is expected from equation 4.4 for a system in which C_{66} is the soft elastic mode. $Y_{[100]}$, on the other hand, is not expected to contain any contribution from C_{66} (equation 4.3), consequently it should not soften upon cooling. The observed small softening may be explained by a small sample misalignment. The constant soft Young modulus below T_s contrasts with the expected hardening of the soft mode (see Fig. 4.16).

Measurements of $Y_{[110]}$ in dynamic mode were conducted in collaboration with the group of W. Schranz at the Physics Institute of the University of Vienna using a Diamond DMA (dynamical mechanical analyzer) from PerkinElmer® [104]. Samples were mounted in three-point bending configuration and submitted to a

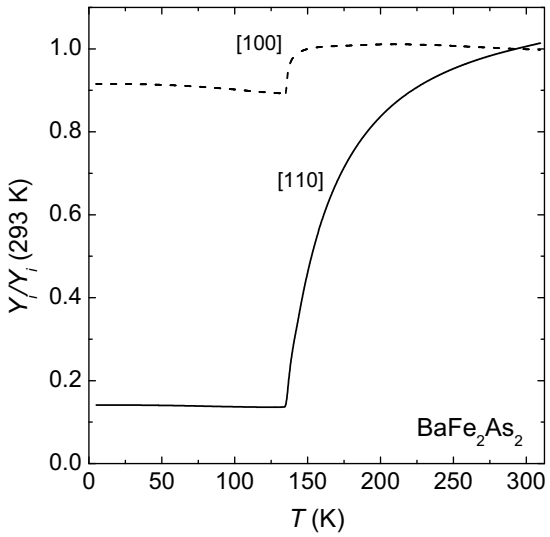

Figure 4.12.: Young modulus of $BaFe_2As_2$ along the two inequivalent in-plane directions [100] (dashed line) and [110] (solid line), measured in a three-point bending configuration in the capacitance dilatometer. A large softening is only observed in $Y_{[110]}$ which is dominated by the shear mode C_{66}.

force $F = F_S + F_D \exp(i\omega t)$, with the dynamic force $F_D \sim (0.7 - 0.8)F_s$, at a frequency of 1 Hz (see Fig. 4.13). The setup was cooled with liquid nitrogen. From the displacement response $u = u_S + u_D \exp(i(\omega t - \delta))$, the amplitude u_D and the phase lag δ were recorded. The dynamic stiffness $k_s = F_D/u_D \exp(i\delta) \propto Y_{[110]}$ is complex in the presence of dissipation. Fig. 4.13 shows the real part of the Young modulus Y', which is equivalent to the result of static measurements, and $\tan(\delta)$, which is proportional to the dissipated energy per cycle. Measurements were conducted on several samples under varying applied force F_S by keeping the ratio F_D/F_S approximately constant (Fig. 4.13). The maximal uniaxial stress at the sample surface arising from F_S, $\sigma_{max,S} = \frac{3F_S l}{2wh^2}$ is given as characteristic parameter. The two measurements with the lowest force were conducted in "constant amplitude" mode which increases the resolution. In this mode, the applied force is smaller in the temperature region in which the sample is soft and increases when the sample becomes harder. The other measurements were conducted at constant force.

A smooth softening of $Y_{[110]}$ upon cooling is also observed in the dynamical measurements. At the lowest stress, a kink and a small, sharp, minimum may be ascribed to the structural and magnetic transition, respectively (see inset in Fig. 4.13(a)). $Y_{[110]}$ has no strong temperature dependence below T_N. With

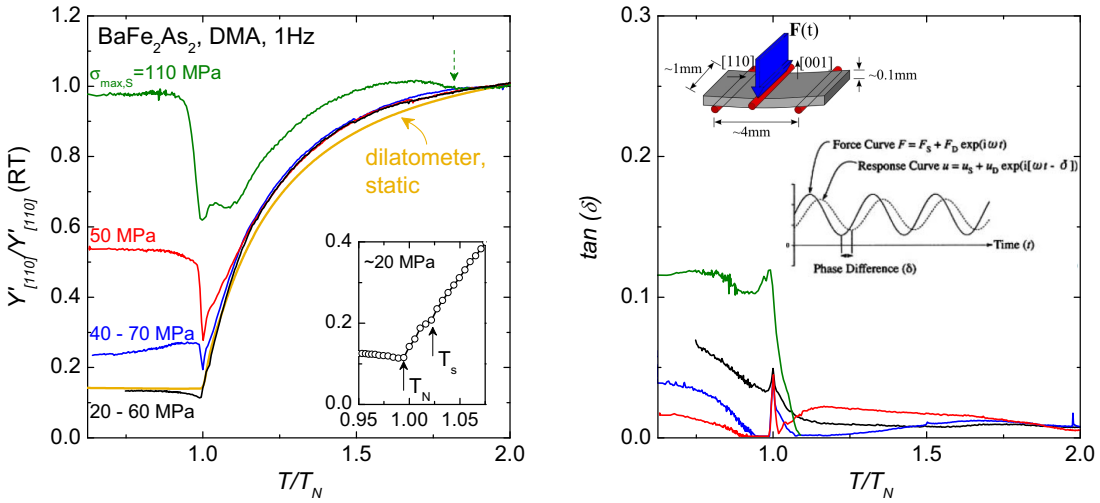

Figure 4.13.: Young modulus of $BaFe_2As_2$ along [110], measured at 1 Hz in a dynamical mechanical analyzer at different bending stress σ. The two measurements with the lowest stress were conducted in constant-amplitude mode, in which the applied force is larger when the sample is stiffer, the other two under constant force F_S. Temperature is normalized at the magnetic transition T_N (minimum of $Y_{[110]}$). (a) shows the real part of the Young modulus and the result of the static measurement in the capacitance dilatometer for comparison. The dashed arrow indicates the onset of a spurious contribution to the high-stress data. The inset in (a) shows the low-stress DMA data around T_s and T_N on a magnified scale. (b) shows the dissipative loss function $\tan(\delta)$ for the same measurements. The insets in (b) illustrate the experiment schematically [104].

increasing stress, the temperature dependence of the Young modulus deviates from the low-stress behavior below some $T > T_s$ and the magnitude of softening decreases. The structural transition is smeared out, while the magnetic transition is affected much less. Furthermore, the splitting between "effective" T_s and T_N seems to increase. Interestingly, a discontinuous hardening of the Young modulus on cooling below T_N emerges with increasing stress. At the highest applied stress, $\sigma_S = 110$ MPa, $Y_{[110]}$ indeed recovers its initial high-temperature value at $\sim 0.9T_N$. Note that this curve also contains a spurious contribution, presumably arising from sample degradation. Results from static measurement in the capacitance dilatometer closely resemble the low-stress DMA experiment, even though the static stress applied within the dilatometer is in the range of $\sim 50 - 100$ MPa. A slight deviation between results from the two techniques presumably arises from poor temperature control in the Diamond DMA, which is not optimized for low-

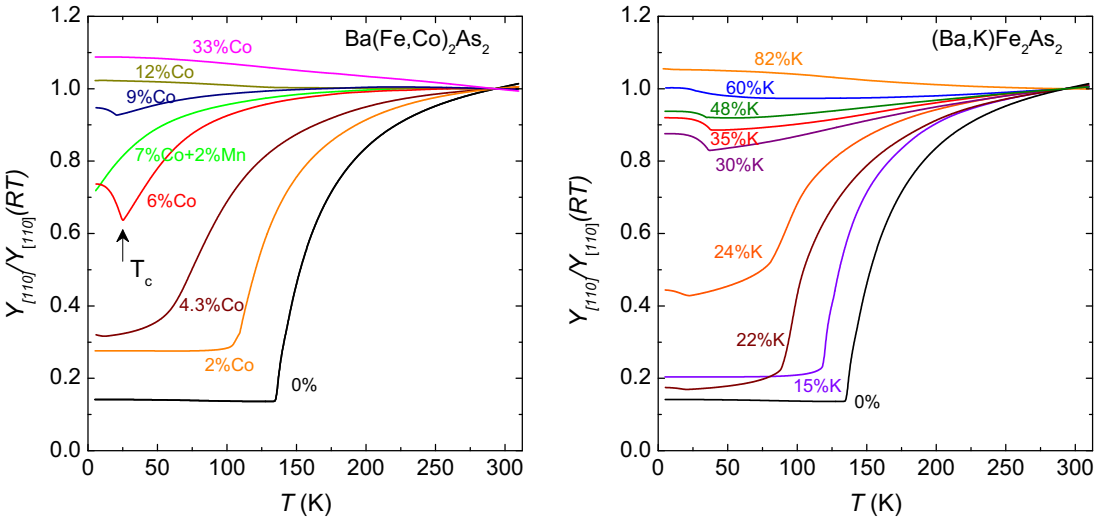

Figure 4.14.: Young's modulus $Y_{[110]}$ of (a) $Ba(Fe,Co)_2As_2$ and (b) $(Ba,K)Fe_2As_2$ over a wide range of substitution obtained from static three-point bending in the capacitance dilatometer. Data are normalized at room temperature.

temperature measurements. The dissipative loss $\tan(\delta)$ is nearly constant with temperature above the transition, has a peak close to T_s and increases again on decreasing T in the ordered state.

Fig. 4.14 shows the Young modulus $Y_{[110]}$ of electron-doped $Ba(Fe,Co)_2As_2$ and hole-doped $(Ba,K)Fe_2As_2$ over a wide doping range measured by static three-point bending in the capacitance dilatometer. Samples in the narrow region of the "new phase" of section 3.3.1 are not studied here. The softening of $Y_{[110]}$ on approaching T_s from above is clearly observed for all underdoped and moderately overdoped compounds. Its magnitude decreases with substitution. A significant hardening is observed at T_c of most samples, e.g., at 25 K for $Ba(Fe_{0.94}Co_{0.06})_2As_2$. The effect is huge, compared to the typical response of an elastic stiffness to superconductivity. One sample in which the superconducting transition was suppressed by adding 2% Mn impurities was also investigated. Strongly overdoped samples show only tiny anomalies at T_c and hardly any softening upon cooling.

Despite their overall similarity, the shear modulus of hole- and electron-doped $BaFe_2As_2$ shows somewhat different temperature dependences. For example, optimally doped $Ba(Fe,Co)_2As_2$ displays critical softening down to T_c, however, the softening of optimally doped $(Ba,K)Fe_2As_2$ appears to be cut off at some higher temperature. In fact, in the $Ba(Fe,Co)_2As_2$ system, the $Y_{[110]}(T)$ curves evolve continuously from underdoped to strongly overdoped. In contrast, the curves for

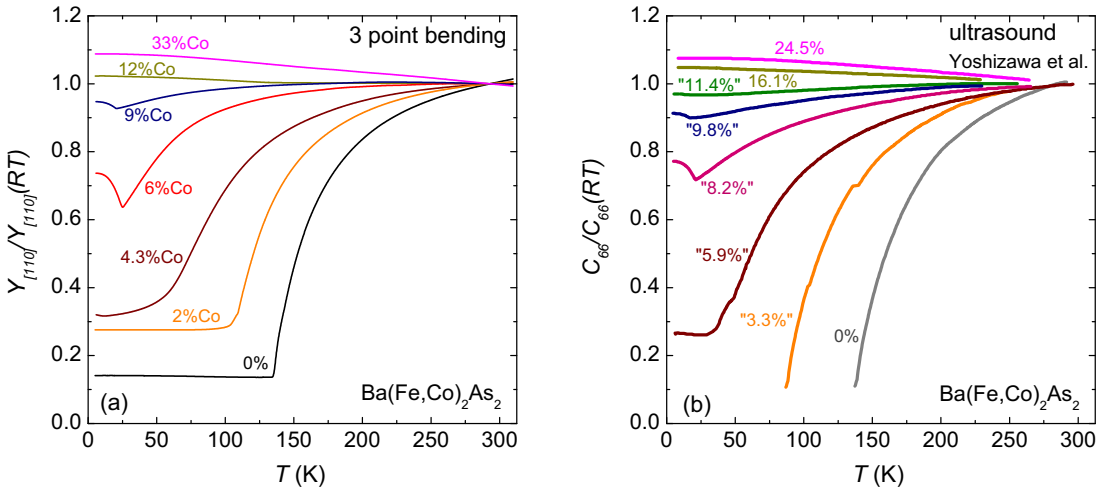

Figure 4.15.: Comparison between (a) $Y_{[110]}$ obtained from three-point bending in the dilatometer and (b) C_{66} from ultrasound velocity measurement [98] of $Ba(Fe,Co)_2As_2$. Both quantities have been normalized at room temperature. The good agreement confirms the reliability our technique to determine the temperature dependence of the shear modulus of iron-based materials.

$(Ba,K)Fe_2As_2$ seem to fall into two categories: Samples which actually undergo the structural phase transition show critical softening, while the others show a moderate softening with a different temperature dependence (Fig. 4.14). This behavior will be in the focus of the analysis in section 4.4.3.

The shear modulus C_{66} of $Ba(Fe,Co)_2As_2$ has been previously measured by Yoshizawa *et al.* using ultrasound velocity [98]. In Fig. 4.15 these data are compared with the present results on $Ba(Fe,Co)_2As_2$. Note that the ultrasound signal is lost in the twinned state below T_s. Since the determination of the Co content varies between different groups, an effective Co content "x" has been determined for the ultrasound samples by comparing their available transition temperatures with the phase diagram of Ref. [28]. $Y_{[110]}(T)$ from bending in the dilatometer essentially reproduces the temperature dependence of C_{66} from ultrasound for all doping levels, which confirms the reliability of our novel technique to determine the shear modulus of iron-based materials.

4.4. Analysis and Discussion

In a Landau model of a structural phase transition induced by bilinear strain-order parameter coupling, the temperature dependence of the soft elastic mode is determined by the susceptibility of the order parameter that drives the transition. Presuming that a "nematic" order parameter—whatever be its nature—drives the structural transition of the 122 iron-arsenides, we derive the nematic susceptibility from the bending results and analyze its temperature and doping dependence. For the discussion of the shear-modulus data, the Landau model is first introduced. Then, the effect of conjugate uniaxial stress on the structural transition of $BaFe_2As_2$ is considered. Subsequently, we show in detail how the nematic susceptibility is obtained from the bending data. The analysis of its doping and temperature dependence focuses on a possible structural or nematic quantum critical point and its relationship to superconductivity in Co- and K-doped $BaFe_2As_2$. Finally, we show how the nematic susceptibility obtained here can be related to the spin-lattice relaxation rate from nuclear magnetic resonance measurements, within the spin-nematic model. The comparison of experimental data on $Ba(Fe,Co)_2As_2$ provides evidence that the nematic order parameter has a magnetic nature.

4.4.1. Landau theory of bilinear strain-order parameter coupling

The order parameter of the structural transition of the 122 iron-based systems is the spontaneous shear strain (the orthorhombic distortion) ε_6 (see appendix B). The stress-strain relation $\varepsilon_6 = (C_{66})^{-1} \sigma_6$ implies that a spontaneous orthorhombic distortion can occur in a second-order phase transition if $C_{66} \to 0$, which is why C_{66} is called the "soft mode" of the transition.

We presume that this structural phase transition is induced by the coupling of ε_6 to another, electronic, order parameter φ that has an instability at a bare transition temperature T_0. The results of Ref. [88] justify this assumption, as explained below. φ and ε_6 are allowed to couple bilinearly in the Landau expansion of the free energy if they have the same symmetry (i.e., if they transform under the same irreducible representation of the lattice point group). Because of this symmetry property, φ can be called "nematic". The Landau expansion of the free energy is thus given by

$$F = F_0 + \frac{1}{2} C_{66,0} \varepsilon_6^2 - \lambda \varepsilon_6 \varphi + \frac{1}{2} (\chi_\varphi)^{-1} \varphi^2 + \frac{B}{4} \varphi^4. \tag{4.17}$$

C_0 is the bare (i.e., without the coupling λ) elastic constant which has no strong temperature dependence, and χ_φ is the bare (again signifying $\lambda = 0$) linear susceptibility of φ assumed to diverge on approaching T_0. $B(> 0)$ is the usual quartic coefficient of the Landau expansion and λ the electron-lattice coupling constant. Any other strain ε_Γ that does not break the tetragonal lattice symmetry (e.g., ε_3) may couple linear-quadratically ($g\varepsilon_\Gamma\varphi^2$) in the free energy, which leads to a step-like anomaly of C_Γ at T_s. Γ is a symmetry index. However, we only consider the order parameter ε_6 and the elastic constant C_{66} here, and omit all indices "6" for simplicity.

Generally, the effective elastic constant C is given by thermodynamics (see B.4) [105],

$$C = \frac{d^2F}{d\varepsilon^2} = \frac{\partial^2 F}{\partial\varepsilon^2} - \left(\frac{\partial^2 F}{\partial\varepsilon\partial\varphi}\right)^2 \left(\frac{\partial^2 F}{\partial\varphi^2}\right)^{-1} \tag{4.18}$$

With the free energy 4.17 this reduces to

$$C = C_0 - \frac{\lambda^2}{(\chi_\varphi)^{-1} + 3B\varphi^2}. \tag{4.19}$$

which contains the order parameter φ. Its temperature dependence is obtained from minimizing the free energy, which leads to

$$\frac{\partial F}{\partial\varphi} = (\chi_\varphi)^{-1}\varphi + B\varphi^3 - \lambda\epsilon = 0 \tag{4.20}$$

$$\frac{\partial F}{\partial\varepsilon} = -\lambda\varphi + C_0\varepsilon = 0, \tag{4.21}$$

showing that ε is proportional to φ. Solving equation 4.21 and inserting into equation 4.20 yields an expression containing φ only,

$$\left((\chi_\varphi)^{-1} - \frac{\lambda^2}{C_0}\right)\varphi + B\varphi^3 = 0. \tag{4.22}$$

In this, $\left((\chi_\varphi)^{-1} - \lambda^2/C_0\right)^{-1} = \tilde{\chi}_\varphi$ is the nematic susceptibility renormalized by the electron-lattice coupling λ, as considered, e.g., in Ref. [10]. The solution of eq. 4.22 is given by,

$$\varphi = 0, \text{ for } T \text{ such that } \chi_\varphi < \frac{C_0}{\lambda^2} \tag{4.23}$$

$$\varphi^2 = -\left((\chi_\varphi)^{-1} - \frac{\lambda^2}{C_0}\right)/B, \text{ for } T \text{ such that } \chi_\varphi > \frac{C_0}{\lambda^2}. \tag{4.24}$$

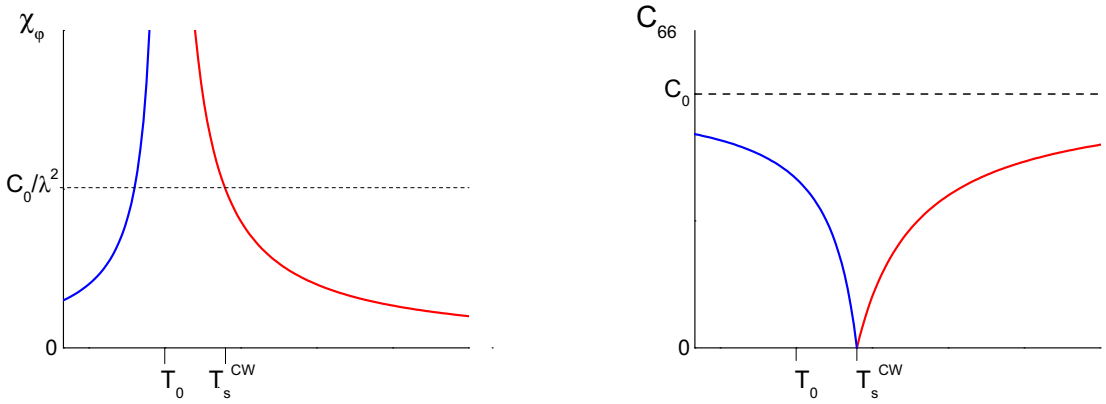

Figure 4.16.: Temperature dependence of (a) the bare nematic susceptibility χ_φ, and (b) the effective elastic modulus C in the Landau model 4.17, assuming a mean-field-like temperature dependence of χ_φ, eq. 4.27. The structural transition occurs at $T_s^{\mathrm{CW}} = T_0 + \frac{\lambda^2}{AC_{66,0}}$ when $\chi_\varphi = \frac{C_0}{\lambda^2}$ and $C = 0$. Red lines show the high-temperature branch (as in Eq. 4.28) and blue lines the low-temperature branch (Eq. 4.29).

It is evident that the transition temperature of the coupled system is higher than the bare nematic transition temperature T_0: Without the coupling λ to the elastic system, the nematic transition would occur when χ_φ reaches infinity. By introducing the coupling, however, a finite threshold value $\chi_\varphi = C_0/\lambda^2$ is sufficient to trigger off the transition.

From the temperature dependence of φ^2 follows the temperature dependence of the renormalized elastic modulus,

$$C = C_0 - \lambda^2 \chi_\varphi \text{ for } T \text{ such that } \chi_\varphi < \frac{C_0}{\lambda^2} \tag{4.25}$$

$$C = C_0 - \frac{\lambda^2}{3\lambda^2/C_0 - 2\left(\chi_\varphi\right)^{-1}} \text{ for } T \text{ such that } \chi_\varphi < \frac{C_0}{\lambda^2}. \tag{4.26}$$

Finally, by assuming a Curie-Weiss mean-field temperature dependence

$$\left(\chi_\varphi\right)^{-1} = A(T - T_0), \tag{4.27}$$

the explicit expression for the temperature dependence of the soft mode $C(T)$,

$$\frac{C}{C_0} = \left(1 - \frac{\epsilon}{T - T_0}\right) = \left(\frac{T - T_s^{\mathrm{CW}}}{T - T_0}\right) \text{ for } T > T_s^{\mathrm{CW}} \tag{4.28}$$

$$\frac{C}{C_0} = \left(\frac{2(T_s^{\mathrm{CW}} - T)}{2(T_0 - T) + 3\epsilon}\right) = \left(\frac{2(T_s^{\mathrm{CW}} - T)}{3T_s^{\mathrm{CW}} - T_0 - 2T}\right) \text{ for } T < T_s^{\mathrm{CW}}, \tag{4.29}$$

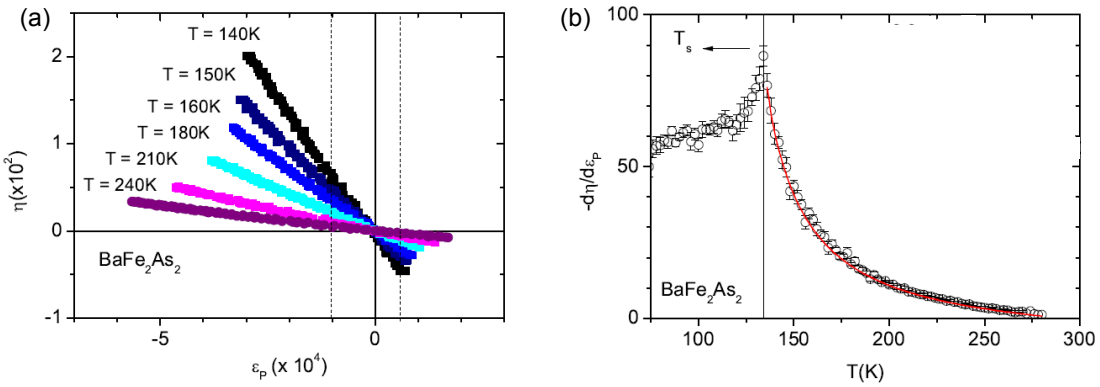

Figure 4.17.: (a) Resistivity anisotropy $\eta \propto \varphi$ in $BaFe_2As_2$ as a function of strain applied along [110] at various temperatures. (b) Temperature dependence of the nematic susceptibility $-d\eta/d\varepsilon_P \propto \lambda\chi_\varphi$ from the data in (a). The strong temperature dependence is evidence that an electronic instability underlies the lattice distortion in $BaFe_2As_2$. Figures taken from Ref. [88].

is obtained (see Fig. 4.16). The new transition temperature is $T_s^{\mathrm{CW}} = T_0 + \frac{\lambda^2}{AC_0}$. $\epsilon = T_s^{\mathrm{CW}} - T_0$ (the "Jahn-Teller energy" of Refs. [98, 100]) is an energy scale characteristic of the coupling λ between ε and φ.

In principle, the structural transition may arise either from diverging χ_φ, as an electronically-driven transition (assumed here), or from vanishing C_0, as a bare lattice instability. The assumption of an electronically-driven transition is strongly supported by the results of Ref. [88], where the resistivity anisotropy (assumed to be proportional to φ) was measured as a function of strain ε_6, externally applied to the sample via a piezo stack. From eq. 4.17, this yields $d\varphi/d\varepsilon_6 \propto \lambda\chi_\varphi$ [88], which is independent of the bare shear modulus $C_{66,0}$. If the lattice (i.e., vanishing $C_{66,0}$) caused the transition, then $\lambda^2\chi_\varphi/C_{66,0}$ would diverge, but $\lambda\chi_\varphi$ would show no strong temperature dependence. The experiment [88] showed that, however, $\lambda\chi_\varphi$ also diverges, which means that φ drives the transition and the lattice would remain undistorted without its coupling to φ.

4.4.2. Influence of uniaxial stress on the magneto-structural phase transition of $BaFe_2As_2$

An elastic modulus, analogous to a magnetic susceptibility, is probed by applying the conjugate field. We therefore investigate first of all the effect of applied uniaxial stress along [110], $\sigma_{[110]}$, on the magneto-structural transition of $BaFe_2As_2$

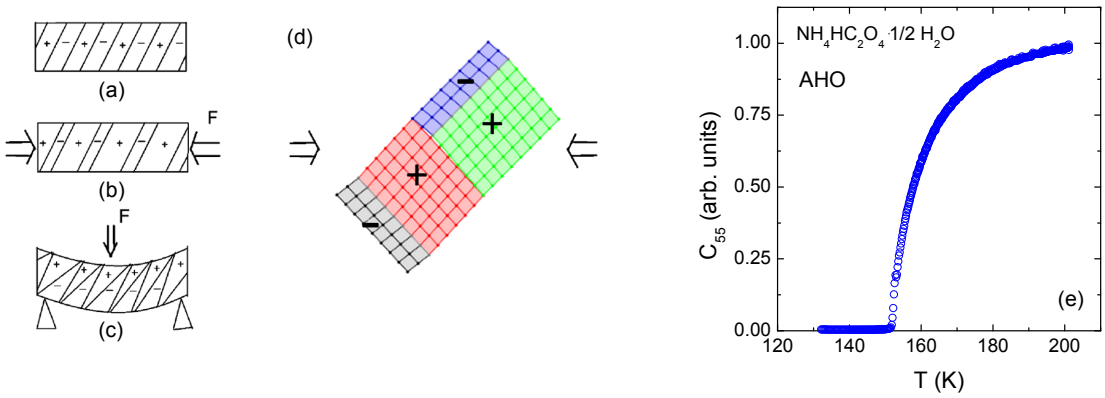

Figure 4.18.: On the domain-wall contribution to the low-frequency elastic modulus. (a) Schematic drawing of a twinned sample showing two domain types (elongated or shortened along the direction of applied stress). (b), (c) Domain wall motion as response to uniaxial stress and to bending stress, respectively. (d) assignment of the two domain types to the domain structure of the pnictides. (e) Soft mode C_{55} of the organic compound AHO, measured in three-point bending configuration. It also shows a huge domain wall contribution below T_s, similar to $BaFe_2As_2$. Figures taken from Ref. [106] (a)-(c) and Ref. [39] (d). Data in (e) are a courtesy of W. Schranz, see [107].

in this section. In principle, $\sigma_{[110]}$ has two effects on the structure. First, it detwins samples by favoring one kind of orthorhombic domains [40] and second, it acts as the conjugate field to the structural order parameter, analogously to a magnetic field for a ferromagnet. Consequently, $\sigma_{[110]}$ smears out the transition and induces some orthorhombicity even above the stress-free T_s. In fact, a structural transition temperature T_s in this field can no longer be strictly defined (because the tetragonal symmetry is broken at any temperature) and the transition turns into a crossover. The effect is most pronounced when the nematic susceptibility is large and the shear modulus is soft.

In the dynamical three-point bending experiment at the lowest stress, a kink and a minimum of $Y_{[110]}$ can be associated with the structural and magnetic transition respectively, while the Young modulus is essentially temperature independent below T_N (Fig. 4.13). The observations contrast with the expected hardening below the transition (Fig. 4.16) and are very likely a consequence of the formation of structural domains. Namely, there are two kinds of domains, $'-'$-type domains in which the lattice constants are elongated along [110] and $'+'$-type type domains in which they are shortened along this direction (see Fig. 4.18). Application of a small compressive stress $\sigma_{[110]}$ increases the fraction of

$'+'$-type domains at the expense of the $'-'$-type domains, so that the total sample length decreases through domain wall motion, an effect which dominates elastic properties at low frequencies. A relatively small applied force can thus induce significant length changes, which means that the elastic modulus appears very soft ("superelasticity") [106–108]. However, monodomain material properties are not probed. This kind of behavior was, for example, reported for the soft elastic mode of the organic compound AHO [107] (see Fig. 4.18 (e)).

In the three-point bending experiment, samples are subjected mainly to stress along the [110] direction. Increasing the applied force is therefore expected to suppress domain formation. This is clearly observed in the evolution of the Young modulus below T_s with increasing stress, Fig. 4.19. A discontinuous hardening below T_N emerges, and $Y_{[110]}$ indeed recovers its high-temperature value at low temperature under the highest applied stress. Presumably, monodomain properties are finally observed in this case. At the same time, the magneto-structural transition is strongly affected. In particular, the second-order-like structural transition is shifted to higher T and increasingly smeared out by the applied stress. It is marked by a broadened minimum of the Young modulus at the highest stress. However, the first-order magnetic transition is only slightly broadened, and T_N remains well-defined. The discontinuous increase at $T < T_N$, which is visible when the domain wall contribution is suppressed, clearly arises from this first-order transition.

Similar effects can be observed in the orthorhombic order parameter under varying $\sigma_{[110]}$. This is done by measuring the thermal expansion of a sample with rectangular shape along the [110] direction using different capacitor gap values. As shown above (section 4.2.3), the gap value is directly related to the uniaxial force to which the sample is subjected along the measured direction. The "orthorhombic order parameter" can be obtained by comparing to a measurement in the twinned state (along [100]) as $\int \left(\alpha_{[100]} - \alpha_{[110]}\right) dT$, see note 4 on page 24. This quantity is shown in Fig. 4.19 for different values of $\sigma_{[110]}$. The sample is detwinned to a significant fraction by a small (uniaxial and approximately homogeneous) pressure of $\sigma_{[110]} = 0.2$ MPa and (nearly) completely detwinned at the highest applied pressure $\sigma_{[110]} = 3.1$ MPa [9]. At the same time, the transition is progressively smeared out and acquires a pronounced high-temperature tail. The thermal-expansion coefficient also reveals a split second-order structural and a first-order magnetic transition. It shows that the structural transition is most affected by $\sigma_{[110]}$, to the extent that T_s cannot be defined at the highest pressure, while the magnetic transition is only slightly broadened and shifted. The behavior

9. The measurement at 3.1 MPa was performed by P. Burger at the Institute of Solid State Physics (IFP) at the Karlsruhe Institute of Technology.

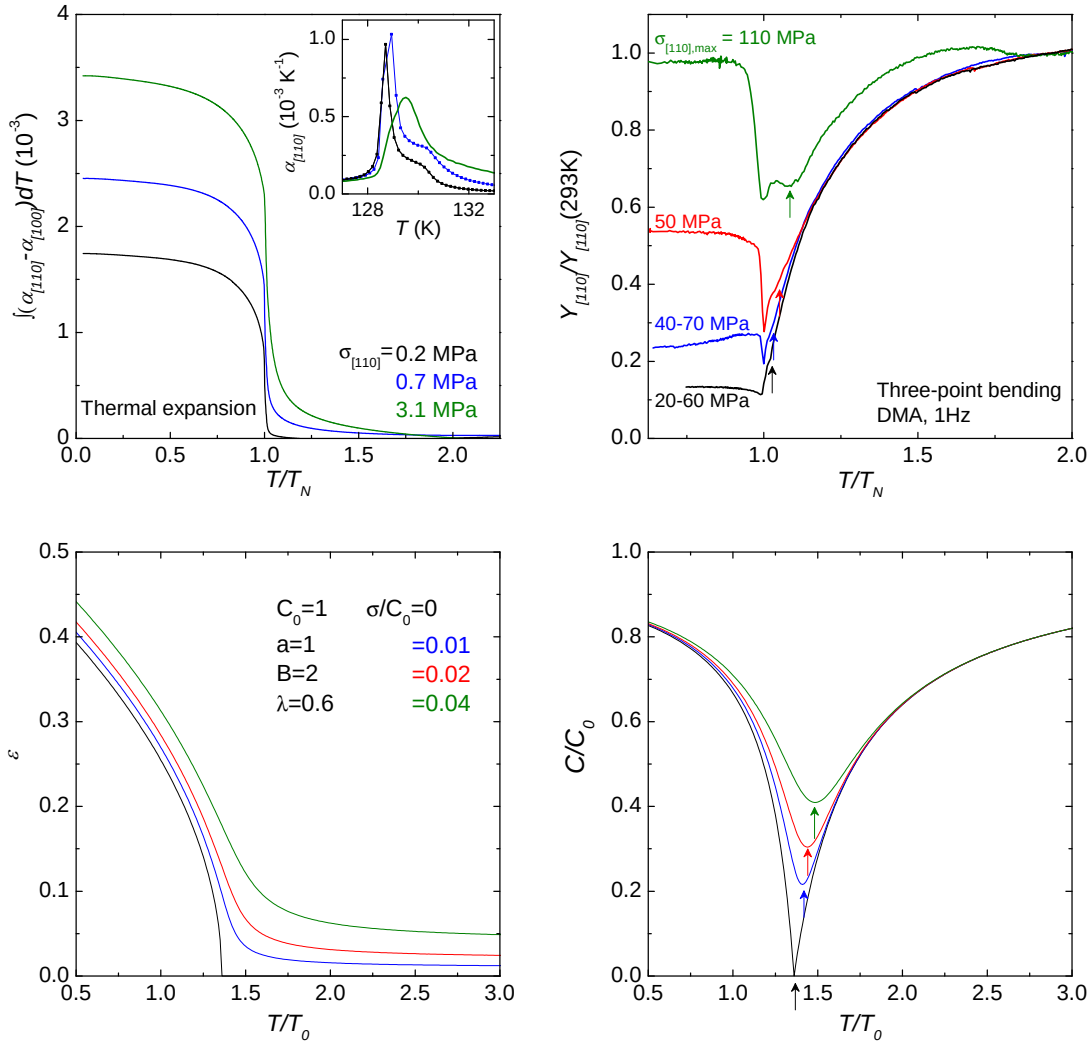

Figure 4.19.: The effect of $\sigma_{[110]}$ on the structural order parameter δ and the shear modulus C_{66} of $BaFe_2As_2$. (a) Experimental data for δ obtained from thermal-expansion measurements under varying the force applied in the dilatometer. (b) data of Fig. 4.13. Solid arrows mark the crossover temperature assigned to the structural transition (minimum in C_{66} in a monodomain state). The experimental data is quite well reproduced by the Landau model of bilinear strain-order parameter coupling eq. 4.30, shown in (c) and (d), but contains additional contributions from domain wall motion (suppressed at high σ) and from a separate first-order transition at $T_N < T_s$.

is fully compatible with the observation of the pressure dependence of the Young modulus in dynamic three-point bending.

Fig. 4.19 also shows the calculation of the order parameter and the corresponding elastic modulus in the Landau model eq. 4.17 with an added conjugate field σ,

$$F = F_0 + a(T - T_0)\varphi^2 + \frac{B}{4}m^4 + \frac{C_0}{2}\varepsilon^2 - \lambda\varepsilon\varphi - \varepsilon\sigma, \tag{4.30}$$

$$C = C_0 - \frac{\lambda^2}{a(T - T_0) + 3B\varphi^2}. \tag{4.31}$$

Note that this describes only the structural transition, and a separate magnetic transition is not included. For simplicity, we search for the minimum of 4.30 as a function of φ numerically, and insert the solution into 4.31. Results are presented in Fig. 4.19. At $\sigma = 0$, the $(T - T_s)/(T - T_0)$-law for the elastic modulus is of course recovered. With increasing σ, the minimum of C around the transition becomes broader, more shallow, and shifts to slightly higher temperatures. Moreover, deviations from the $(T - T_s)/(T - T_0)$-law appear at higher T. The model reproduces the experimental data above T_N quite well, except for the domain wall contributions. The additional first order transition, not included in the model, induces the abrupt hardening below T_N.

4.4.3. Temperature and doping dependence of the nematic susceptibility

The determination of the nematic susceptibility χ_φ at $T > T_s$ is based on equation 4.25, $C_{66} = C_{66,0} - \lambda^2\chi_\varphi$. In real systems, the bare elastic constant C_0 is temperature dependent because of phonon anharmonicity. A hardening by a few % on cooling between room temperature and zero temperature is a typical behavior [109]. In order to remove this background contribution and to extract the effect of coupling between ε_6 and φ on the elastic constant we make the approximation

$$\frac{Y_{[110]}}{Y_0} \approx \frac{C_{66}}{C_{66,0}} \tag{4.32}$$

where Y_0 is the non-critical contribution to the Young modulus. The 33% Co substituted sample was previously shown to provide a good approximation for the phonon contribution to the thermal expansion [11]. On this basis, we assume that it provides also an adequate background for the Young modulus, which we further assume to be doping independent. Note that Yoshizawa et al. [98] use C_{66} of a 24.5% Co-substituted sample as background for the $Ba(Fe,Co)_2As_2$ system.

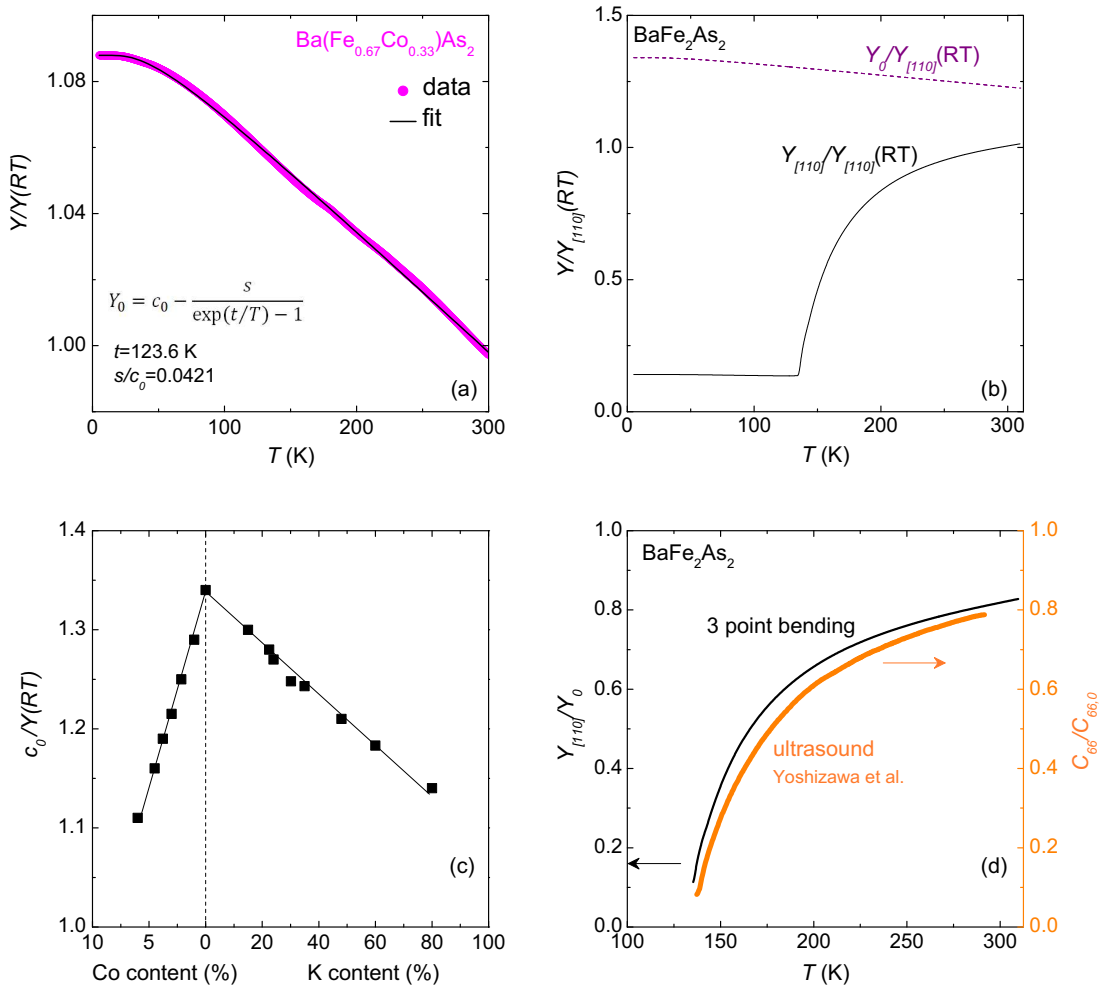

Figure 4.20.: (a) Fit of the Young modulus of $Ba(Fe_{0.67}Co_{0.33})_2As_2$ to the Varshni-formula $Y_0 = c_0 - \frac{s}{\exp(t/T)-1}$, taken as a phonon background. (b) $Y_{[110]}$ of undoped $BaFe_2As_2$ (solid line) and the background contribution Y_0 (dashed line), both normalized by the room temperature value $Y_{[110]}(RT)$ of $BaFe_2As_2$. (c) Doping dependence of the parameter $Y_0(0)/Y(RT)$ needed for determining the phonon background. Lines are a guide to the eye. (d) Softening $Y_{[110]}/Y_0 \approx C_{66}/C_{66,0}$ of $BaFe_2As_2$ used in the subsequent analysis and discussion. Good agreement between three-point bending (black line) and ultrasound (orange circles) techniques is demonstrated.

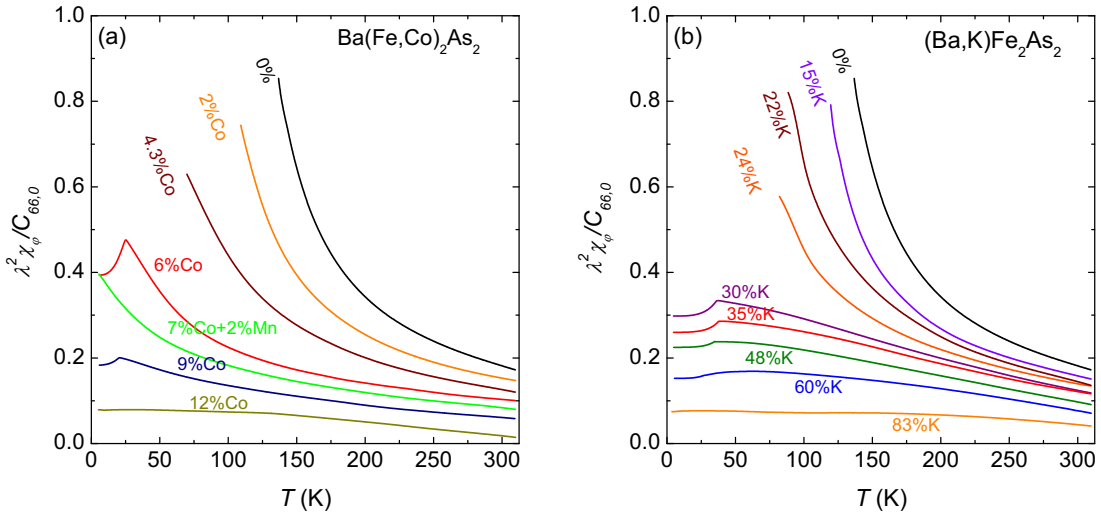

Figure 4.21.: Nematic susceptibility in units of $\lambda^2/C_{66,0}$ of (a) Co- and (b) K-doped $BaFe_2As_2$ obtained from the present data as $\lambda^2\chi_\varphi/C_{66,0} = 1 - Y_{[110]}/Y_0$.

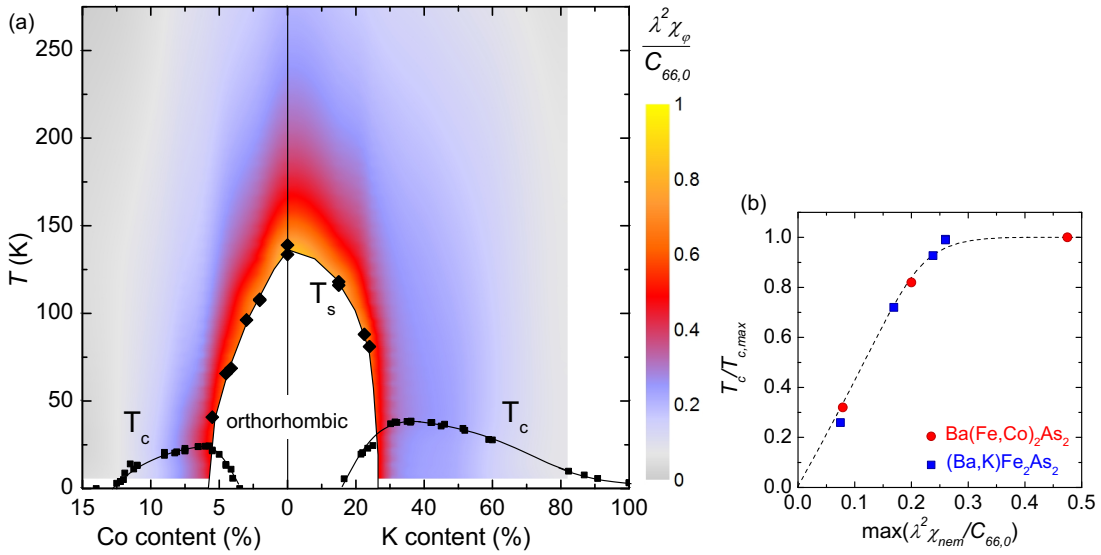

Figure 4.22.: (a) The nematic susceptibility as a color-coded map in the temperature-composition phase diagram of $Ba(Fe,Co)_2As_2$ and $(Ba,K)Fe_2As_2$. (b) Relationship between maximum value of the nematic susceptibility and the ratio $T_c/T_{c,max}$ for overdoped samples of the two systems. $T_{c,max} = 25$ K (38 K) for $Ba(Fe,Co)_2As_2$ ($(Ba,K)Fe_2As_2$). The dashed line is a guide to the eye.

The empirical Varshni formula

$$C_0 = c_0 - \frac{s}{\exp(t/T) - 1} \tag{4.33}$$

is widely used and has been shown to describe well the temperature dependence of elastic constants dominated by phonon anharmonicity [109]. Indeed, it describes very well also the Young modulus of the 33% Co substituted sample (Fig. 4.20). A complication arises because absolute values of the Young modulus cannot be reliably obtained from our three-point bending setup. Thus, from fitting equation 4.33 to the $Ba(Fe_{0.67}Co_{0.33})_2As_2$ data, only the parameter $t = 123.6$ K and the ratio $s/c_0 = 0.0421$ can be extracted. By referring to the Young modulus normalized at room temperature, the relation

$$\frac{C_{66}}{C_{66,0}} \approx \frac{Y_{[110]}}{Y_0} = \frac{Y_{[110]}}{c_0 - \frac{s}{(\exp(t/T)-1)}} = \frac{Y_{[110]}/Y_{[110]}(RT)}{\frac{c_0}{Y_{[110]}(RT)} - \frac{c_0}{Y_{[110]}(RT)}\frac{s/c_0}{\exp(t/T)-1}} \tag{4.34}$$

is found. It contains one free parameter per composition, $\frac{c_0}{Y_{[110]}(RT)}$. The parameter $\frac{c_0}{Y_{[110]}(RT)} = \frac{Y_0(0)}{Y_{[110]}(RT)}$ is adjusted to obtain good agreement with equation 4.27 for compounds which actually undergo the structural transition, and it is then linearly extrapolated to higher doping levels (see Fig. 4.20). The results are comparable to the ultrasound data [98]. For example, we find $\frac{c_0}{Y(RT)} = 1.34$ for undoped $BaFe_2As_2$, while $\frac{c_0}{C_{66}(RT)} = 1.36$ is the equivalent quantity from Ref. [98]. By use of equation 4.25 the nematic susceptibility (in units of λ^2/C_0) may be obtained from the present data as $1 - Y/Y_0$. It is plotted in Fig. 4.21 and shown in Fig. 4.22 as a color-coded map in the composition-temperature phase diagram of $Ba(Fe,Co)_2As_2$ and $(Ba,K)Fe_2As_2$.

χ_φ is significantly enhanced in a broad band around T_s, as expected. It reaches its largest values for the undoped compound right above T_s and decreases smoothly upon substitution. This is at variance with results of Ref. [88] who find a maximum of the nematic susceptibility around optimal doping from measurements of the strain-derivative of the resistivity anisotropy in $Ba(Fe,Co)_2As_2$ (Fig. 4.1). However, the magnitude of the resistivity anisotropy has been shown to be very sensitive to impurity scattering and, thus, the Co content [83, 84]. This means that resistivity anisotropy and nematic susceptibility are not simply proportional over the whole phase diagram, which presumably explains the discrepancy between Ref. [88] and the present data. Indeed, $\lambda^2\chi_\varphi/C_{66,0}$ is expected to be equal to 1 (equivalent to $C_{66} = 0$) at the structural transition for all compositions, but our results show that it does not quite reach this value. Note that C_{66} does not reach zero in the ultrasound study either [98]. Why this is the case

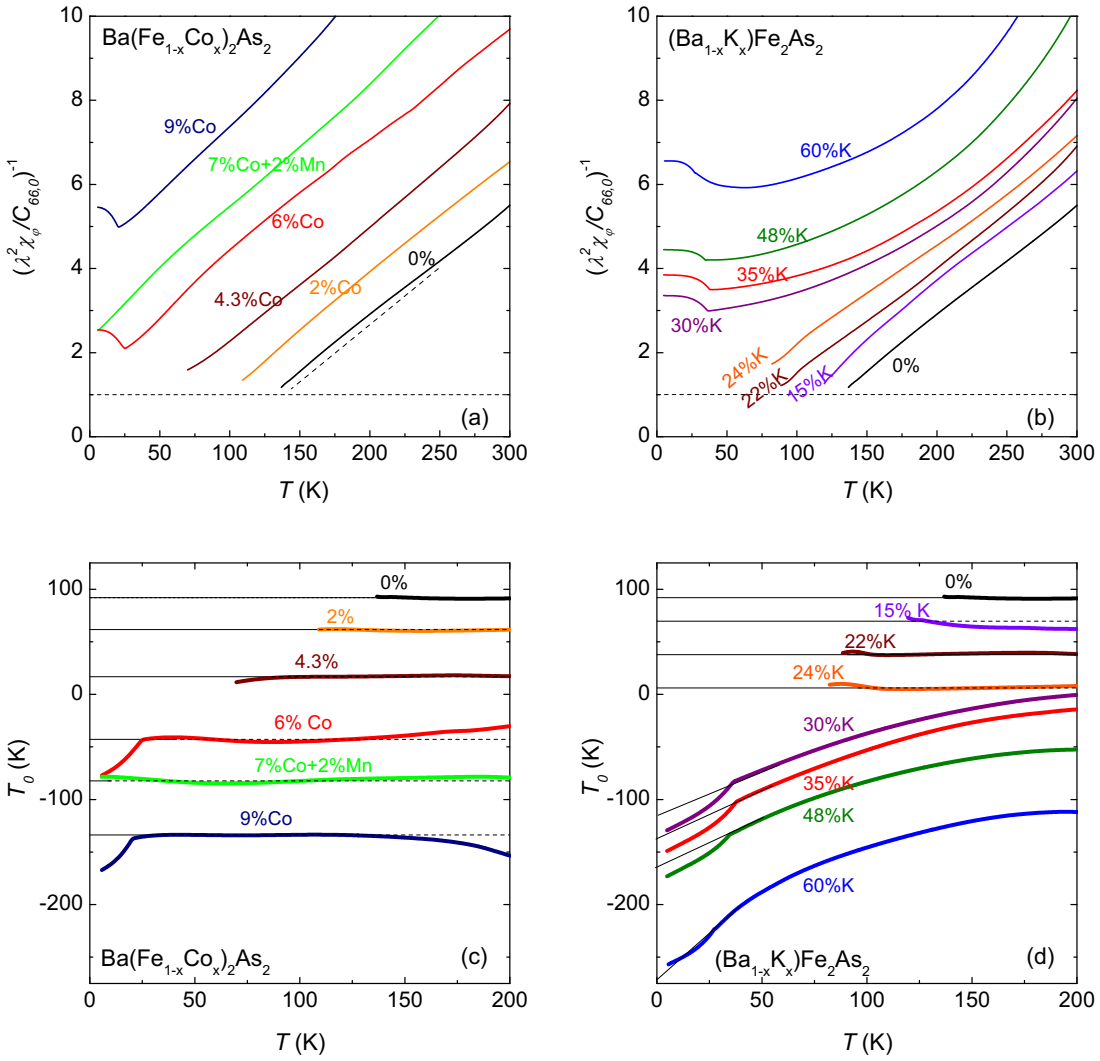

Figure 4.23.: (a), (b) Inverse of the nematic susceptibility $\left(\lambda^2\chi_\varphi/C_{66,0}\right)^{-1}$ of $Ba(Fe,Co)_2As_2$ and $(Ba,K)Fe_2As_2$, respectively. If χ_φ follows the Curie-Weiss law eq. 4.27, data fall on a straight line, whose slope is given by $\lambda^2/AC_{66,0}$ and intercept with 0 by T_0. (c), (d) The parameter $T_0(T)$ for $Ba(Fe,Co)_2As_2$ and $(Ba,K)Fe_2As_2$, respectively, given by $T_0(T) = T - \left(\frac{\lambda^2}{AC_{66,0}}\right)\left(\frac{\lambda^2\chi_\varphi}{C_{66,0}}\right)^{-1}$. For samples with K content $\geq 30\%$, $\frac{\lambda^2}{AC_{66,0}} = 40$ K is used, see Fig. 4.24.

remains an open question. Nevertheless, the large enhancement of the χ_φ close to T_s naturally explains the high sensitivity of the compounds to uniaxial stress.

Interestingly, χ_φ still reaches quite significant values for overdoped samples of $Ba(Fe,Co)_2As_2$ and $(Ba,K)Fe_2As_2$, which do not undergo any structural transition. Indeed, there appears to be a universal relationship between the decrease of T_c with respect to its maximal value in the system, $T_c/T_{c,max}$, and the maximum value of χ_φ on the overdoped side of the phase diagram (Fig.4.22). This finding suggests a close tie between the emergence of superconductivity and the nematic susceptibility. Namely, if the enhancement of χ_φ is taken as a measure for the strength of nematic fluctuations, its correlation with the T_c value in both systems suggests that these fluctuations play an important role in superconducting pairing.

Figure 4.23 details the temperature dependence of χ_φ. Plotting the inverse χ_φ^{-1} in Fig. 4.23 (a), (b) demonstrates that the Curie-Weiss law 4.27

$$\chi_\varphi^{-1} = A(T - T_0)$$

is indeed followed by most samples. Namely, data of $Ba(Fe,Co)_2As_2$ up to 9% Co content and $(Ba,K)Fe_2As_2$ up to 24% K content fall on a straight line. For these samples, the parameters T_s^{CW} and $\lambda^2/AC_{66,0}$ are extracted and shown in Fig. 4.24. The coupling energy $T_s^{\mathrm{CW}} - T_0 = \lambda^2/AC_{66,0} \sim 30 - 40$ K is practically doping independent. In the electron-doped system, the Curie-Weiss temperature T_s^{CW} changes smoothly from positive to negative values, a behavior which has been associated with a quantum critical point at optimal doping [98].

Hole-doped $(Ba,K)Fe_2As_2$ with $\geq$ 30% K content clearly deviates from the Curie-Weiss law, however. These deviations can be parameterized by ascribing them to a temperature dependence the parameter T_0 (eq. 4.27). $T_0(T)$ is obtained from the data in Fig. 4.23, assuming that no other parameter is temperature dependent, and that $\lambda^2/AC_{66,0} = 40$ K for $(Ba,K)Fe_2As_2$ with $\geq$ 30% K content (dashed line in Fig. 4.24(b)). Results are plotted in Fig. 4.23 and demonstrate that $T_0(T)$ is temperature independent for Co contents up to 9% and K contents up to 24%, confirming again that the nematic susceptibility of these compounds obeys the Curie-Weiss law. The behavior changes abruptly between $24 - 30$% K-content, and $T_0(T)$ becomes strongly temperature dependent above this level. It decreases with decreasing temperature below 200 K, which shows that the tendency towards nematic ordering is weakened as the temperature is lowered for these compounds. Fig. 4.24 presents the parameter T_0 at different temperatures as a function of doping. Especially at low temperatures, a step-like anomaly of T_0 as a function of doping occurs, which is suggestive of a first order transition between orthorhombic-magnetic and tetragonal ground states on increasing K content.

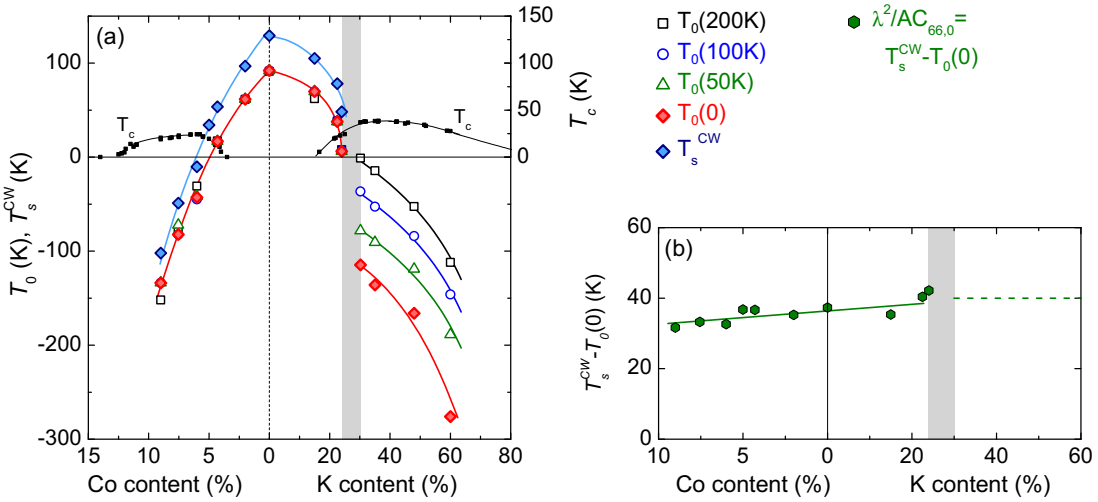

Figure 4.24.: Parameters describing the temperature dependence of χ_φ as $\lambda^2\chi_\varphi/C_{66,0} = \frac{\lambda^2/(AC_{66,0})}{T-T_0(T)}$ in a composition-temperature phase diagram of $Ba(Fe,Co)_2As_2$ and $(Ba,K)Fe_2As_2$. T_0 is temperature independent, equivalent to the fact that χ_φ follows a Curie-Weiss law, for Co content up to 9% and K content up to 24%. An abrupt change of behavior occurs in the shaded region and T_0 is no longer constant above 30% K content. Panel (b) shows the Curie constant $\lambda^2/(AC_{66,0})$, the dashed line representing the extrapolation into the high K-content region. $T_s^{\mathrm{CW}} = T_0 + \lambda^2/(AC_{66,0})$ is the temperature at which C_{66} vanishes and the structural transition is expected. The superconducting domes are indicated for clarity. Lines are a guide to the eye.

Another characteristic temperature is the inflection point of $\chi_\varphi(T)$, T^*. T^* is determined from the maximum of the derivative of $\chi_\varphi(T)$ (see Fig. 4.25). Thus, it either coincides with the structural transition or is somewhat higher, in which case it specifies a lower temperature limit for Curie-Weiss behavior. Fig. 4.26 shows T^* as a function of Co and K substitution. It first decreases on increasing Co or K content, closely following T_s, and then increases upon further doping. However, T^* reaches near zero values (in agreement with a quantum critical scenario) only in the electron-doped $Ba(Fe,Co)_2As_2$ case. Note that, in order to "look beneath" the superconducting dome, we used a non-superconducting 7%Co+2%Mn-codoped sample, because Mn substitution strongly suppresses T_c, but affects T_s only slightly [10]. In contrast, the values of T^* for the hole-doped

10. Specifically, 2% Mn content was found to correspond to 0.7% Co content as far as the magneto-structural transition is concerned [110]. So the sample (composition from EDX: 6.9% Co content and 1.9% Mn content) is most accurately associated with 7.6% Co doping.

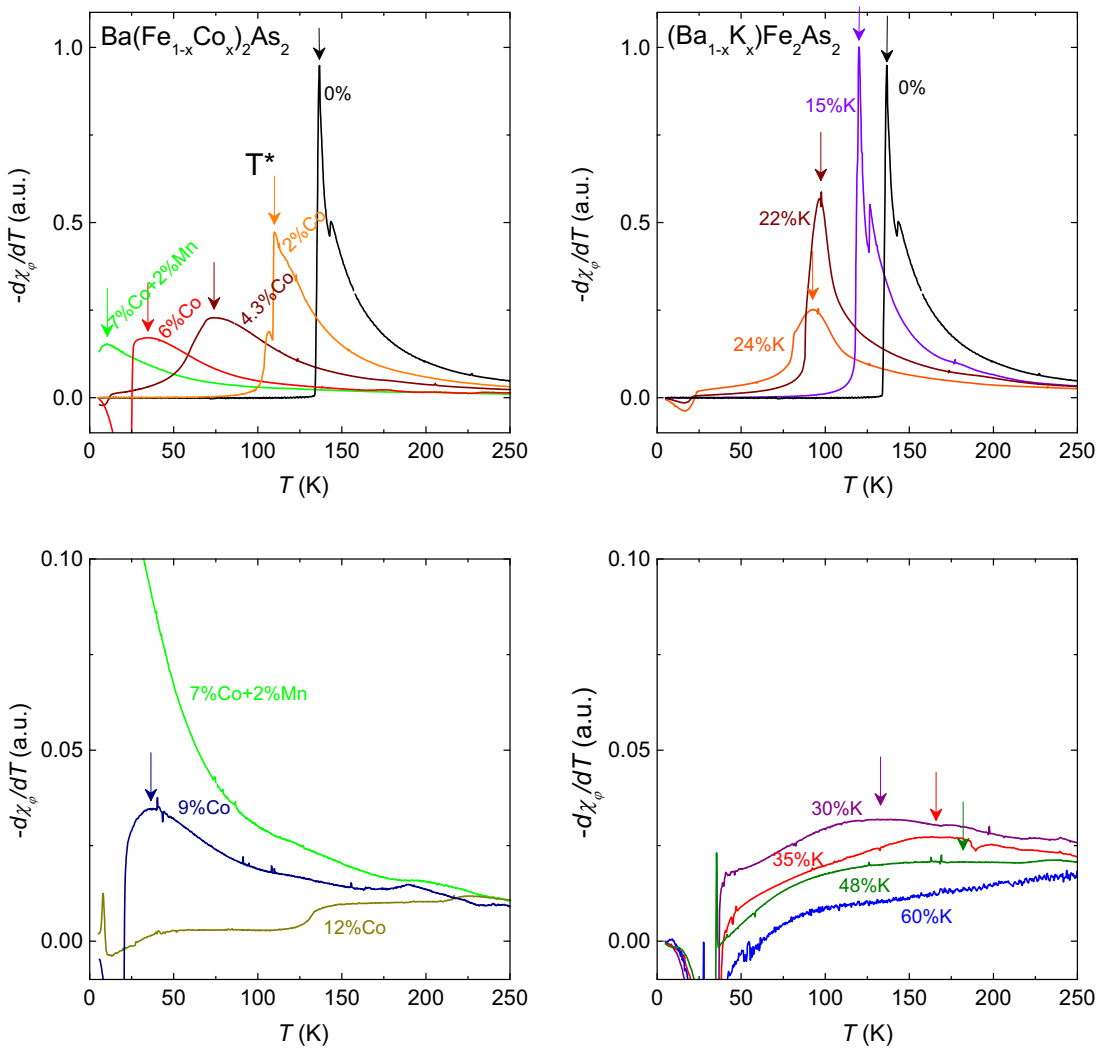

Figure 4.25.: Negative temperature derivative of the nematic susceptibility. Its maximum, T^*, corresponds to the inflection point of $\chi_\varphi(T)$ and is a lower temperature limit for the regime in which the Curie-Weiss law holds.

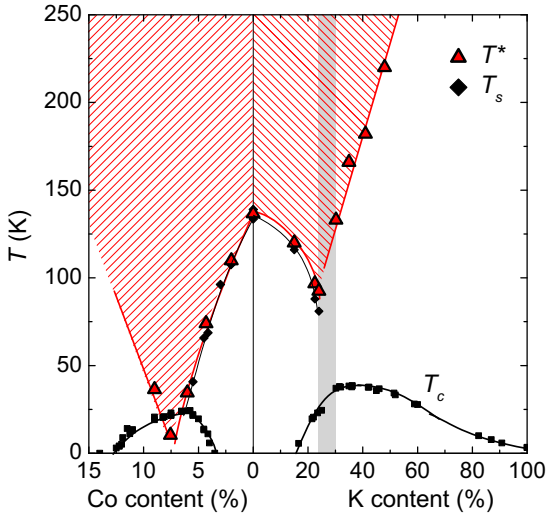

Figure 4.26.: Inflection point of $\chi_\varphi(T)$, T^* (red triangles), determined as the minimum of its temperature derivative, as a function of Co and K substitution. Also shown are T_s (small diamonds) and T_c (small squares). A change of behavior of the nematic susceptibility occurs in the shaded region and T^* does not reach low temperatures in (Ba,K)Fe_2As_2.

system clearly do not go below $\sim$ 75 K, which is incompatible with a quantum critical point (QCP) in this system. For example, optimally doped (Ba,K)Fe_2As_2, which incidentally has a higher T_c than optimally doped $Ba(Fe,Co)_2As_2$, shows the prominent inflection point instead of Curie-Weiss-like critical divergence of the nematic susceptibility.

Finally, we consider the interplay between nematic susceptibility and superconductivity. Fig. 4.27 shows a magnified view of the Young modulus around T_c. The onset of superconductivity produces two effects. The largest effect for intermediate doping levels is an abrupt hardening of the shear modulus below T_c. Note that, however, the 60 % K sample exhibits also a broad hardening of $Y_{[110]}$ starting at $\sim$ 60 K (inset in Fig. 4.27 (a)), which is clearly unrelated to the superconducting transition. The second effect is a small step-like softening at higher doping levels, which can be discerned thanks to the high resolution of our data. This step-like softening of $Y(T)$ at T_c is actually the usual behavior expected from thermodynamics at a second order phase transition and is related to the stress derivative of T_c, i.e., the normal coupling between superconductivity and the lattice [111] (see equation 2.9). The hardening, on the other hand, directly reflects the competition between superconductivity and the nematic order

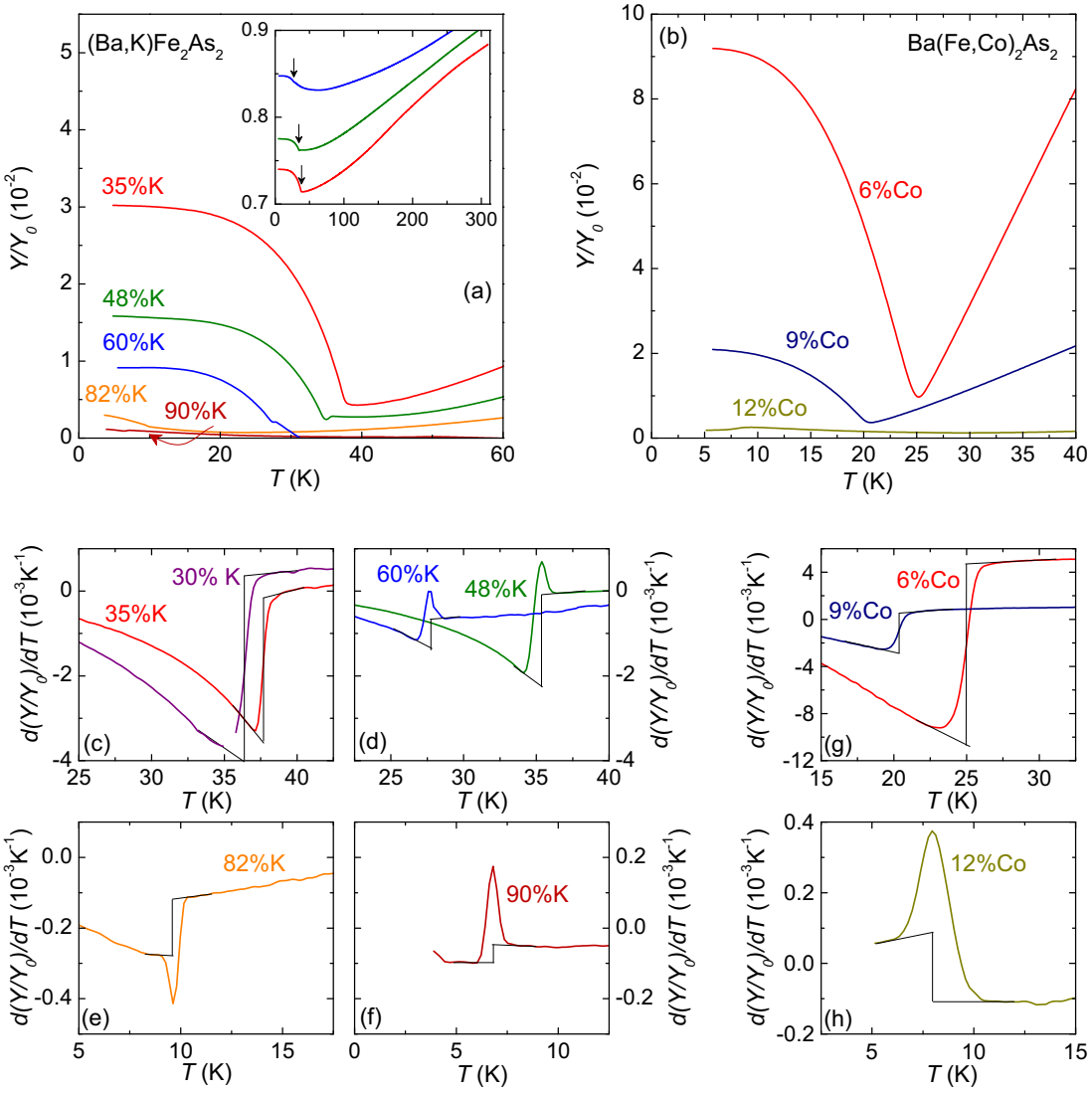

Figure 4.27.: Hardening of the Young modulus, corresponding to a decrease of the nematic susceptibility, below T_c. (a), (b) show a magnified view of the $Y_{[110]}/Y_0 \approx 1 - \lambda^2\chi_\varphi/C_{66,0}$ around T_c of overdoped $(Ba,K)Fe_2As_2$ and $Ba(Fe,Co)_2As_2$, respectively. Data have been offset by arbitrary values for clarity. An abrupt hardening sets in at T_c; also a tiny step-like softening is observed for most samples. The inset in (a) reveals an additional broad hardening, unrelated to superconductivity, setting in at ~ 60 K for $Ba_{0.4}K_{0.6}Fe_2As_2$. Arrows mark T_c. (c)-(h) Derivative of the Young modulus ($= -d\chi_\varphi/dT$) around T_c of $(Ba,K)Fe_2As_2$ and $Ba(Fe,Co)_2As_2$. Lines show how the slope change $\Delta dY/dT$ at T_c, quantifying the impact of superconductivity on the nematic susceptibility, is determined.

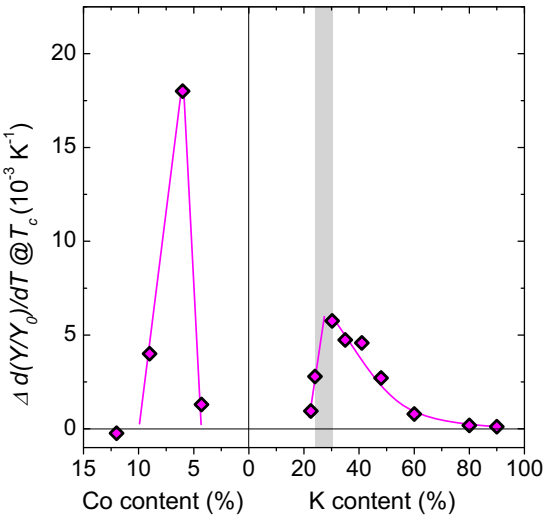

Figure 4.28.: Slope change $\Delta dY/dT$ at T_c, quantifying the effect of superconductivity on the nematic susceptibility, as a function of substitution. The by far largest effect occurs at optimal doping in $Ba(Fe,Co)_2As_2$. Lines are a guide to the eye. The shaded region is the same as in Figures 4.24 and 4.26.

parameter φ affecting the lattice via equation 4.25. In order to quantify the effect of competition between nematic order and superconductivity, we consider the temperature derivative $dY/dT = -d\chi_\varphi/dT$ (Fig. 4.27 (c)-(h)). A peak of dY/dT signals the small step-like softening, while the hardening is mirrored by a step-like decrease $\Delta\,(dY/dT)$ upon cooling through T_c. The size of $\Delta\,(dY/dT)$ is taken as a measure for the coupling between nematic susceptibility and superconductivity. Fig. 4.28 shows that it is largest near optimal doping for both $Ba(Fe,Co)_2As_2$ and $(Ba,K)Fe_2As_2$ and decreases strongly for overdoped samples with a weak tail extending up to at least 82% K on the hole-doped side. The maximum value is, however, three times smaller for $(Ba,K)Fe_2As_2$ than for $Ba(Fe,Co)_2As_2$, suggesting that the competition between nematic order and superconductivity is significantly weaker in this system.

The above results are surprising in a scenario in which superconductivity arises due to the fluctuations surrounding a QCP, because here the system with the higher maximum T_c ($(Ba,K)Fe_2As_2$) exhibits "weaker" critical behavior. Interestingly, a change of the topology of the Fermi-surface on decreasing T, from strongly nesting circular hole pockets to 'propeller'-shaped hole pockets with expected weaker nesting has been found to occur in optimally doped $(Ba,K)Fe_2As_2$ [112]. Such a temperature-induced change of topology of the Fermi-surface could

explain why the nematic susceptibility does not follow a simple Curie-Weiss law for these samples.

The pronounced inflection point of $\chi_\varphi(T)$ in (Ba,K)Fe_2As_2 is especially striking. As a note, it was claimed to be explained in a recent calculation within the orbital scenario [113]. In particular, the temperature dependence

$$\frac{C_{66}}{C_{66,0}} = \frac{T - (T_0 + hT^a)}{T - T_0}, \tag{4.35}$$

with $a \approx 0.5$, and T_0 and h being parameters, has been proposed. Note that this equation describes an inflection point and differs from the above discussed mean-field temperature dependence of C_{66} (Eq. 4.28), which is recovered at $a = 0$. In Ref. [113], all the experimental shear-modulus data of Fig. 4.21 could be reproduced by using $a = 0.5$, $h = 2.67$ and varying T_0 for samples with Co content up to 9% and K content up to 24%. For samples with $\geq 30\%$ K content an abrupt change of parameters to $a = 0.58$, $h = 4.98$ had to be assumed. This would be consistent with a Lifshitz transition in this region of the phase diagram, for which we found indications in section 3.3.2.

4.4.4. On the origin of the structural phase transition

Turning towards a possible determination of the microscopic nature of the nematic order parameter φ in the above Landau model, it is shown that the nematic susceptibility can be related to the nuclear magnetic resonance (NMR) spin-lattice relaxation rate in the spin-nematic model [99]. In this scenario, the electronic nematic order represents the anisotropy of spin fluctuations (see section 4.1). The corresponding "spin-nematic" susceptibility has been calculated in Ref. [10] to

$$\chi_{spin-nem} = \frac{\sum_q \chi^2}{1 - g_0 \sum_q \chi^2}. \tag{4.36}$$

χ is the "dynamic spin susceptibility properly renormalized by magnetic fluctuations" [93]. The magnetic transition occurs when $\sum_q \chi^2$ diverges, while it is sufficient for $\sum_q \chi^2$ to reach a finite threshold value to induce the nematic transition. This is the explanation why T_s can be higher than T_N in this scenario even though both transitions be driven by magnetic fluctuations. It is important to note that g_0 is the bare coupling constant of the two magnetic sublattices (see Fig. 4.4), and has not been renormalized by magneto-elastic coupling. Note that in Refs. [10, 93, 99], on the other hand, the renormalization of g_0 by the coupling λ to the lattice has been taken into account and an effective coupling $g = g_0 + \lambda^2/C_{66,0}$ is used. This is not done here, because in the formalism of

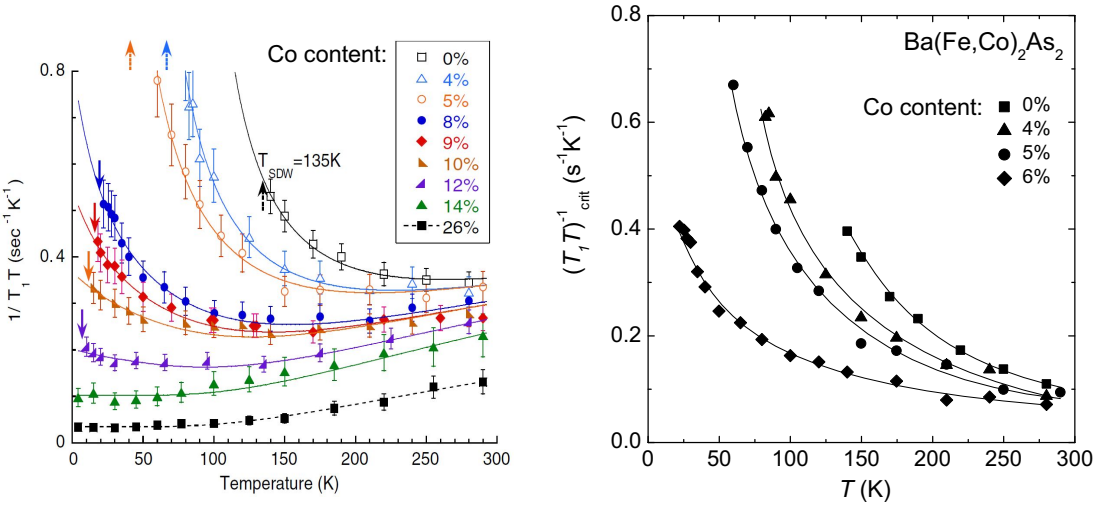

Figure 4.29.: (a) Spin-lattice relaxation rate divided by temperature $1/T_1T$ of $Ba(Fe,Co)_2As_2$, from Ning et al. [114] (b) Critical part of $1/T_1T$ obtained by subtracting the data of strongly overdoped $Ba(Fe_{0.86}Co_{0.14})_2As_2$ from the data in (a).

section 4.4.1 the bare susceptibility χ_φ (with g_0), instead of the renormalized $\tilde{\chi}_\varphi$ (with g instead of g_0) enters the equations.

On the other hand, the spin-lattice relaxation rate divided by temperature, as measured in NMR experiments (see section 5.3), also contains the spin susceptibility χ:

$$\frac{1}{T_1T} = \gamma_g^2 \lim_{\omega\to 0} \sum_{\mathbf{k}} F^2(\mathbf{k}) \frac{\mathrm{Im}\,\chi(\mathbf{k},\omega)}{\omega} \tag{4.37}$$

Here, $F(\mathbf{k})$ is a momentum dependent form factor which peaks at the ordering wave vectors $Q = (0, \pi)$ when the magnetic field is applied parallel to the ab plane [115]. As shown in detail in Ref. [99], the spin-lattice relaxation rate divided by temperature is indeed proportional to $\sum_q \chi^2(q)$

$$\frac{1}{T_1T} = A_{T_1}^{-1} \sum_q \chi^2(q) \tag{4.38}$$

under certain approximations. A_{T_1} is a proportionality constant. This means that the spin-nematic susceptibility can be expressed in terms of T_1T as

$$\chi_{spin-nem} = \frac{A_{T_1}(T_1T)^{-1}}{1 - g_0 A_{T_1}(T_1T)^{-1}}. \tag{4.39}$$

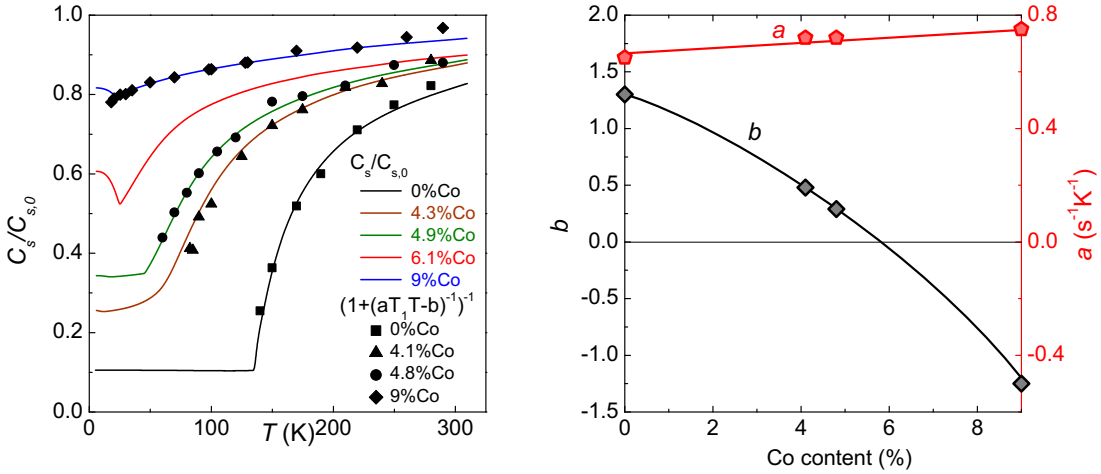

Figure 4.30.: (a) Scaling of spin-lattice relaxation rate and shear modulus softening of $Ba(Fe,Co)_2As_2$ as $C/C_0 = \left(1 + (aT_1T - b)^{-1}\right)^{-1}$. (b) Doping dependence of the scaling parameters a and b. No NMR data is available for 6% Co content.

Finally, if the above nematic susceptibility is indeed responsible for the elastic softening and the ensuing structural phase transition, one would find equation 4.25, $C_{66} = C_{66,0} - \lambda^2 \chi_{spin-nem}$, which in terms of T_1T means

$$\frac{C_{66}}{C_{66,0}} = \frac{1}{1 + \left[\frac{C_{66,0}}{A_{T_1}\lambda^2} T_1T - \left(\frac{g_0 C_{66,0}}{\lambda^2} + 1\right)\right]^{-1}}. \tag{4.40}$$

This scaling relation is verified in the following by comparing T_1 and C_{66} data of $Ba(Fe,Co)_2As_2$.

The spin-lattice relaxation rate $1/T_1$ of $Ba(Fe,Co)_2As_2$ has been reported by Ning et al. [114] (Fig. 4.29). It is used to complement our shear modulus data. First, a non-critical background has to be subtracted from the spin-lattice relaxation rate (see section 5.3), for which data of overdoped $Ba(Fe_{0.86}Co_{0.14})_2As_2$ are used following Ref. [114]. The data are scaled onto the elastic data according to equation 4.40 and the result is shown in Fig. 4.30. It can be seen that the scaling works indeed very well for all Co content levels. This strongly supports that, indeed, the spin-nematic susceptibility $\chi_{spin-nem}$ is responsible for the elastic softening. Note that a similar scaling between the "nematic charge susceptibility", measured by electronic Raman scattering, and the elastic modulus fails [116]. A simpler, linear, scaling between C_{66} and $1/T_1T$, was proposed in Ref. [117] and gives less perfect agreement.

The scaling parameter $a = \frac{C_{66,0}}{A_{T_1}\lambda^2}$ is found to be roughly constant with doping, while $b = \frac{g_0 C_{66,0}}{\lambda^2} + 1$ decreases upon Co substitution and approaches zero around optimal doping. The physical significance of the two parameters can be illuminated in the framework of section 4.4.1 using a mean-field temperature dependence. Indeed, the spin-lattice relaxation rate was experimentally found to follow the Curie-Weiss law

$$(T_1 T)^{-1} = \frac{C_{T_1}}{T - T_{T_1}} \tag{4.41}$$

which means that, according to equation 4.39,

$$\chi_{spin-nem} = \frac{C_{T_1}}{T - (T_{T_1} + g_0)} \tag{4.42}$$

Also, the temperature dependence

$$\frac{C_{66}}{C_{66,0}} = 1 - \frac{\epsilon}{T - T_0} = \frac{T - T_s^{CW}}{T - T_0} \tag{4.43}$$

of the shear modulus was confirmed experimentally. Recall that $\epsilon = \lambda^2 / A C_{66,0} = T_s^{\mathrm{CW}} - T_0$ is an energy characteristic of the coupling λ between nematic order parameter and lattice. Equation 4.40 is consistent with the above if the relationships

$$a = \frac{C_{T_1}}{\epsilon} \tag{4.44}$$

$$b = 1 + \frac{g_0 C_{66,0}}{\lambda^2} = 1 + \frac{T_0 - T_{T_1}}{\epsilon} = \frac{T_s^{CW} - T_{T_1}}{\epsilon} \tag{4.45}$$

are satisfied. a is the ratio between the Curie constant of $1/T_1T$ and the energy characteristic of the electron-lattice coupling, while b is a measure of the coupling strength of the two magnetic sublattices of Fig. 4.4, which gives rise to the spin-nematic order in the first place. If b is greater (smaller) than 1, the bare sublattice coupling g_0 is positive (negative) and the magnetic transition temperature T_{T_1} is lower (higher) than the bare nematic transition temperature T_0. In the latter case, the coupling λ dominates and ensures that, even if $T_{T_1} > T_0$, T_{T_1} will not be larger than the structural transition temperature $T_{T_1} < T_s^{\mathrm{CW}}$. Negative values of b make no sense in this picture, since they would mean that the magnetic transition *precedes* the structural one. In fact, a negative b means that the system has no tendency towards a stripe-type magnetic phase [118], something which might be realized for example in $Ba(Fe,Mn)_2As_2$ [118].

The fact that b decreases upon doping is, hence, a consequence of the fact that T_s^{CW} (the temperature at which $C_{66} \to 0$) and T_{T_1} (where $(T_1T) \to 0$) approach each other. The apparent sign change of b around optimal doping implies that both temperatures tend to a common quantum critical point. Note that, however, the relation between T_1T and $\chi_{spin-nem}$ established above, needs not to be valid around the quantum critical region, because not all approximations which lead to eq. 4.40 can be justified there [99]. It is nevertheless an interesting idea that the system may really tend less towards a stripe-type magnetic state as the Co content is increased. Whether and how the Co-doping dependence of ε and b can be explained by a microscopic model is unclear at the present stage. It would also be interesting to compare spin-lattice relaxation rate and shear modulus of the (Ba,K)Fe_2As_2 system. However, $1/T_1T$ of (Ba,K)Fe_2As_2 shows a complex temperature and doping dependence [119] and it is unclear how the spin-fluctuation contribution can be extracted from it.

In summary, the fact that the spin-nematic susceptibility, obtained from NMR data using the model of Ref. [93], can explain the softening of the shear modulus in Ba(Fe,Co)$_2$As$_2$ is evidence that, indeed, spin fluctuations are the driving force for the structural phase transition and that the paramagnetic-orthorhombic phase of Ba(Fe,Co)$_2$As$_2$ really is a spin-nematic phase.

4.5. Summary

In this chapter, the elastic shear modulus of Co- and K-substituted $BaFe_2As_2$ over a wide doping range has been studied. Measurements were performed using a novel three-point bending setup in our capacitance dilatometer. A method for quantitative analysis was developed and the calibration of the dilatometer for the new technique was presented. The softening of the elastic shear modulus was experimentally obtained and shown to be determined by the nematic susceptibility χ_φ in a Landau model.

The analysis of χ_φ is summarized in Fig. 4.31, which shows the parameters describing its temperature dependence as a function of Co and K content again. The inflection point of $\chi_\varphi(T)$, T^*, has a minimum around optimal doping in both systems. However, the region of possible critical softening, $T > T^*$, clearly reaches near zero temperatures only in the electron-doped compound, consistent with a QCP in this system. In contrast, T^* does not go below 75 K on the hole-doped side, which suggests the absence of such a point in (Ba,K)Fe_2As_2. Fig. 4.31(b) shows the parameter T_0, which describes the tendency towards nematic ordering. T_0 is temperature independent for most samples, equivalent with the fact that χ_φ follows a Curie-Weiss law. However, it there is an abrupt change of behavior

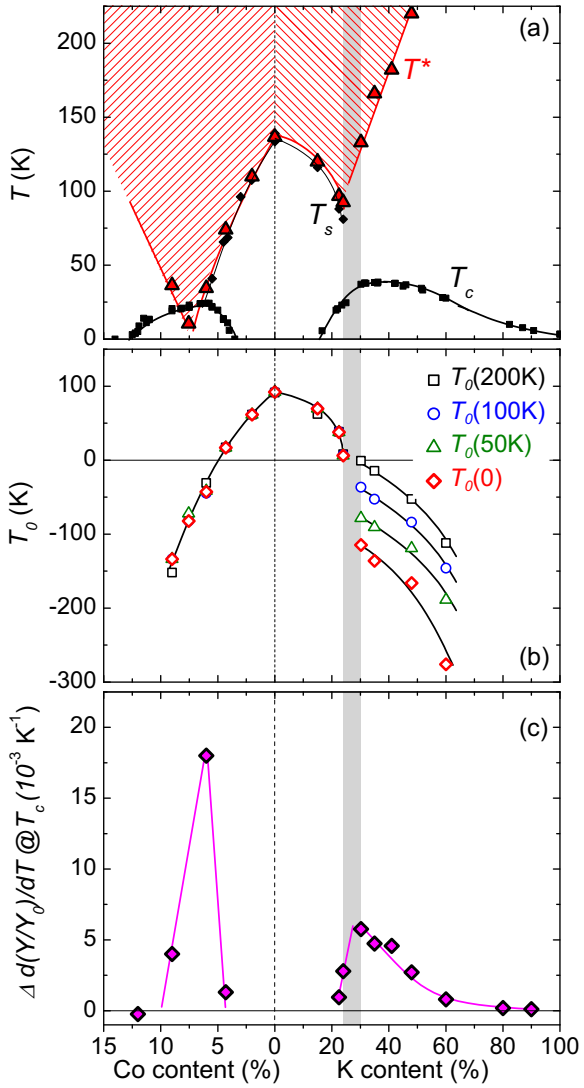

Figure 4.31.: Summary of the phase diagram of $Ba(Fe,Co)_2As_2$ and $(Ba,K)Fe_2As_2$ obtained from analysis of the nematic susceptibility. (a) The inflection point of χ_φ, T^*, showing the absence of critical softening, and a QCP, at optimal doping in $(Ba,K)Fe_2As_2$. (b) The parameter T_0 of the Curie-Weiss law $\chi_\varphi = 1/A(T - T_0)$ at fixed temperatures. It displays an anomaly between 24-30% K content (shaded region) above which T_0 becomes temperature dependent. (c) The slope change of χ_φ at T_c as a measure of the strength of competition between nematicity and superconductivity. Note that it is much weaker in $(Ba,K)Fe_2As_2$, the system with the higher T_c. The results are consistent with a QCP around optimal Co content, but suggest a first-order transition between different ground states as a function of K content.

between 24% and 30% K content, above which T_0 becomes temperature dependent and $\chi_\varphi(T)$ clearly deviates from Curie-Weiss behavior. Especially at low T, T_0 shows a step-like decrease as a function of K substitution, which is suggestive of a first order transition between orthorhombic-magnetic and tetragonal ground states. It is in this transition region that the "new phase" of chapter 3 is found. Finally, Fig. 4.31(c) shows the slope change of $\chi_\varphi(T)$ caused by the onset of superconductivity. The maximum value is three times smaller for $(Ba,K)Fe_2As_2$ than for $Ba(Fe,Co)_2As_2$, suggesting that the coupling between the nematic order and superconductivity is stronger in the latter system, even though it has the lower T_c.

The Landau analysis is independent of the nature (spin or orbital) of the nematic order. In order to gain information on the origin of the structural phase transition, we have shown that in a scenario in which χ_φ emerges from spin correlations, the nematic susceptibility is related to the spin-lattice relaxation rate in NMR measurements [99]. A scaling analysis of $1/T_1T$ and our shear modulus data for $Ba(Fe,Co)_2As_2$, shows that the "spin-nematic susceptibility" from NMR agrees with the nematic susceptibility that causes the shear-modulus softening. This finding is evidence that the structural transition in $Ba(Fe,Co)_2As_2$ is magnetically driven.

Fig. 4.32 gives a final summary of the relevant characteristic temperatures and energy scales for the magnetic, nematic and structural transitions. The coupling energy between nematic order and lattice, ϵ, indicating the difference between T_s^{CW} ($C_{66} \to 0$) and T_0 ($(\chi_\varphi)^{-1} \to 0$), is practically doping independent. On the other hand, the difference between T_s^{CW} and T_{T_1} ($(T_1T) \to 0$), given by $b\epsilon$, decreases strongly upon Co substitution. Its apparent sign change around optimal doping suggests that T_s^{CW} and T_{T_1} both tend to a common quantum critical point. Finally, we note that the magnetic transition should occur at T_{T_1}, i.e., at the point where $1/T_1T$ is expected to diverge from extrapolation of the high-temperature data. However, the real magnetic transition temperature T_N is increased with respect to this value because the preceding structural transition facilitates the magnetic one. Why the real T_s is up to 20 K higher than T_s^{CW} remains to be explained.

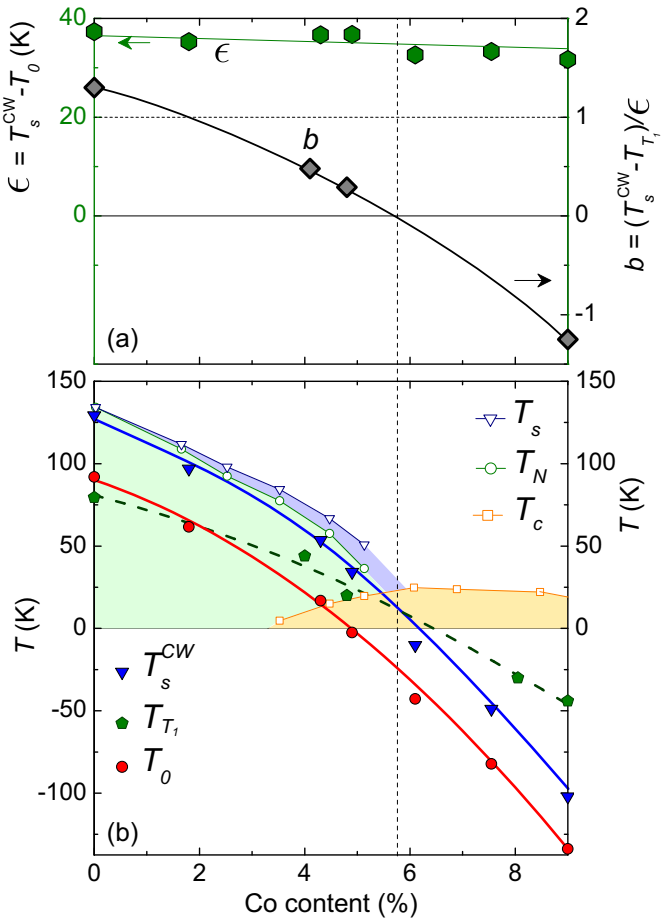

Figure 4.32.: (a) Doping dependence of coupling energies/constants ϵ (coupling between nematic order parameter φ and lattice ε_6) and b (coupling between magnetic sublattices which leads to nematic order in the spin-nematic model). Only b is strongly doping dependent. (b) Phase diagram of $Ba(Fe,Co)_2As_2$ showing the temperatures at which C_{66}, T_1T and $(\chi_\varphi)^{-1}$ extrapolate to zero, respectively, i.e., T_{T_1}, T_s^{CW} and T_0. Relations between coupling energies and temperatures are indicated. 'Real' transition temperatures T_s, T_N, and T_c [80] are shown for orientation. Lines are a guide to the eye.

5. The curious interplay of structure, magnetism and superconductivity in FeSe

FeSe is the structurally simplest iron-based superconductor, but has an uncommon pressure-temperature phase diagram. One of the most interesting features is a huge rise of $T_c = 8$ K to ≈ 37 K under pressure [120–123]. A record-high T_c of up to 70 K has been reported in single-layer thin films [124]. FeSe has been less widely studied than the 122 systems because of difficulties in single-crystal growth. Here, we study uniaxial pressure effects and the interplay of orthorhombic distortion, magnetic fluctuations and superconductivity FeSe single crystals grown by vapor transport [44]. The chapter is organized as follows. A short introduction gives an overview of the pressure-temperature phase diagram of FeSe, as it is known so far, which motivates the present studies. A detailed characterization of our samples is given in the following. Results and discussion are divided into two parts. In the first one, uniaxial thermal-expansion coefficients and shear modulus of FeSe are presented. We discuss uniaxial pressure effects of T_c and the coupling between a possible electronic nematic order parameter, orthorhombic distortion and superconductivity. The second part presents experimental results on the nuclear magnetic resonance (NMR) Knight shift and the spin-lattice relaxation rate. The temperature dependence of magnetic fluctuations is tentatively extracted from the NMR data and the possibility of a spin-nematic phase in FeSe is discussed by comparing shear modulus and spin-lattice relaxation rate. All these results are compared with other iron-based superconductors. Finally, the main results and important open questions are recapitulated in the conclusion.

5.1. Introduction and motivation

FeSe has the simplest crystallographic structure among the iron-based superconductors, lacking the otherwise typical spacer layers between Fe-As(Se) planes. All the same, many of its physical properties are highly atypical for iron-based superconductors. Namely, FeSe undergoes a tetragonal-to-orthorhombic phase

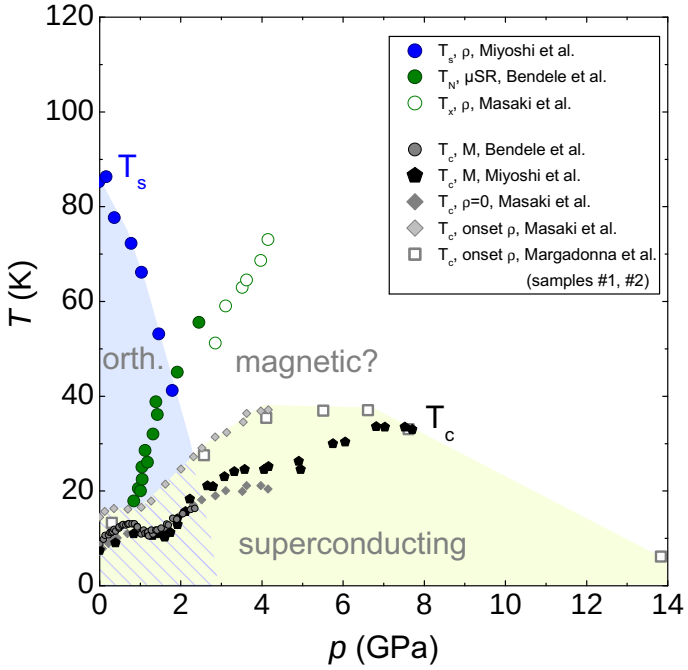

Figure 5.1.: The pressure-temperature phase diagram of superconducting FeSe compiled from various sources. T_s is determined from a shallow minimum in resistivity [127]. T_N at low pressures is determined by μSR [128]. An anomaly in resistivity labeled "T_x" [129] seems also to mark T_N, when it becomes high enough under applied pressure. The resistive superconducting transition becomes very broad under high pressure, which results in a large difference of T_c as determined by the onset and by zero resistivity [129]; the latter one agrees well with T_c determined by magnetization. Altogether, the phase diagram is highly unusual for Fe-based superconductors (see 2.1), especially concerning the reported T_N which evolves similar to T_c and opposite to T_s under pressure.

transition at $T_s \approx 90$ K [122, 125], which is analogous to that of the parent compounds of the 1111 and 122 systems and with similar magnitude of the orthorhombic distortion. Yet, whereas this transition always occurs in proximity to stripe-type antiferromagnetic order in the latter systems, no static magnetism was found in FeSe at ambient pressure [125]. However, enhanced spin fluctuations were found at low temperatures by NMR [126]. FeSe is superconducting below a modest $T_c \approx 8$ K [14].

Further, FeSe is also an extremely pressure sensitive material with a rich temperature-pressure phase diagram. A compilation of available data is shown in

Fig. 5.1. Remarkably, the total increase of T_c under the application of pressure amounts to nearly 30 K. T_c increases initially at a rate of $6-7$ K/GPa and reaches a plateau, possibly a local maximum, at ~ 0.8 GPa [127, 128]. Low-temperature spin fluctuations are also enhanced in this pressure range [126]. Above ~ 0.8 GPa, static magnetic order reportedly sets in at $T_N > T_c$ and its competition with superconductivity has been reported [128, 130]. The nature of the magnetic order remains unknown to date [128]. Another study reports the suppression of the structural transition around 2 GPa [127]. Note that this compilation has to be taken with care because the signatures of T_s and T_N in resistivity are very weak and no study has reported both of them. At higher pressures, T_c and T_N are found to increase with pressure and the onset of T_c reaches surprising 37 K [120–123] at ~ 7 GPa. Superconductivity ultimately disappears at even higher pressures, $\gtrsim 10$ GPa, when the crystallographic structure changes from tetragonal/orthorhombic to hexagonal [121].

The, for iron-based superconductors, uncommon temperature-pressure phase diagram of FeSe, even though it may not be accurately known to date, suggests an atypical interplay of magnetism, structure and superconductivity. In particular, the large paramagnetic, orthorhombic region at low pressures makes FeSe an interesting test case to study the applicability of the spin-nematic and the orbital scenario of the phase transitions in iron-based superconductors [9]. In the spin-nematic scenario, which seems to describe well, e.g., $Ba(Fe,Co)_2As_2$, magnetic fluctuations are assumed to drive all transitions [99]. In the orbital scenario, magnetism is a secondary effect and the structural transition is induced by orbital order while superconductivity is mediated by orbital fluctuations [73].

The study of uniaxial pressure effects is a necessary complement to hydrostatic-pressure studies in any non-cubic material. We have investigated uniaxial pressure effects using thermal-expansion and shear-modulus measurements. These measurements yield the response of the material to infinitesimal uniaxial pressure and do not suffer from the problems of high-pressure experiments. Our data are complemented by NMR measurements of the Knight shift and the spin-lattice relaxation rate $1/T_1$. We study how the orthorhombic phase, superconductivity and magnetic fluctuations interact at ambient pressure and compare with underdoped $Ba(Fe,Co)_2As_2$ and LaFeAsO. In particular, we consider the question whether FeSe is simply a case of extreme separation of structural and magnetic phase transition, which would mean that the orthorhombic, paramagnetic phase is the same nematic phase as in underdoped $Ba(Fe,Co)_2As_2$ (see chapter 4).

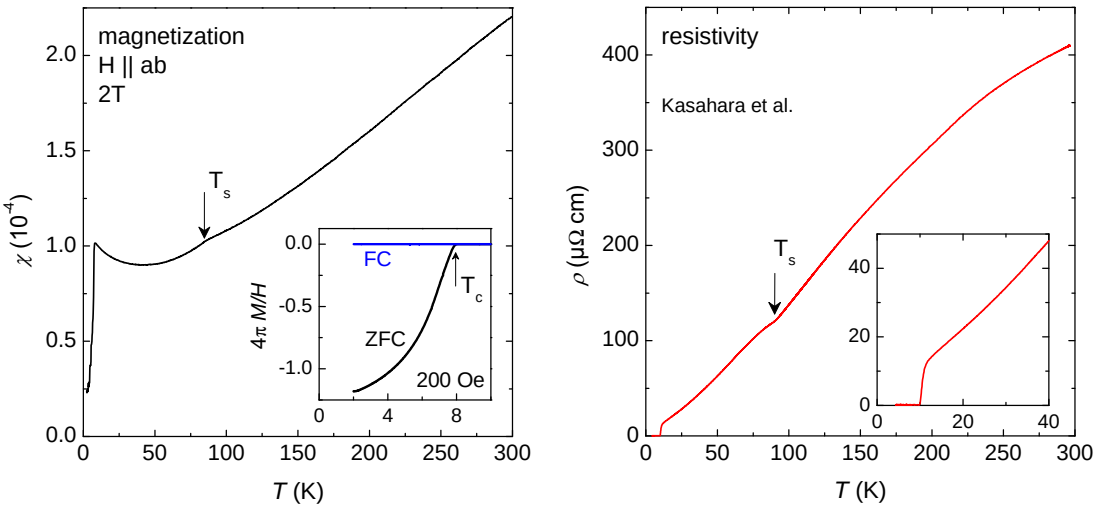

Figure 5.2.: (a) Magnetic susceptibility χ [44] and (b) resistivity ρ [131] of our FeSe single crystals. χ was measured in a field of 2 T parallel to the ab plane. The inset shows the low-temperature data in a field of 20 mT measured under field cooled (FC) and zero-field cooled (ZFC) conditions. The screening is larger than -1 because of the demagnetization effect.

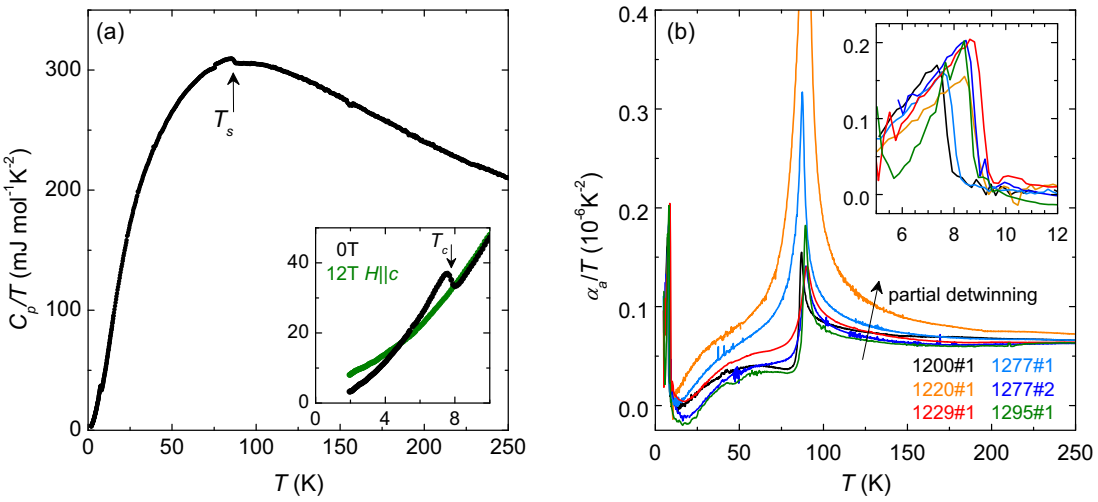

Figure 5.3.: (a) Specific heat C_p/T of an FeSe single crystal. The inset shows a close view of the superconducting transition at $T_c = 7.7$ (0.5 K broad). (b) Sample dependence of T_s and T_c seen in the in-plane thermal expansion coefficient divided by T. The arrow indicates the effect of slight partial detwinning.

5.1.1. Sample characterization

The results presented here were obtained on low-temperature vapor-grown single-crystals (see section 2.4). The growth below 300°C is a necessary condition to obtain phase pure, tetragonal FeSe. Fig. 5.2 shows the temperature dependence of the resistivity [11] and the magnetic susceptibility and Fig. 5.3(a) the specific heat of such an FeSe single crystal. The magnetization was measured in a vibrating sample magnetometer with a field of 2 T applied parallel to the *ab* plane. A small but sharp kink, associated with the structural transition, is observed in magnetization and resistivity and a step in the specific heat. T_s varies between 87 K and 90 K for different samples. The resistivity $\rho(T)$ varies approximately linearly with T below T_s. The lower limit of the residual resistivity ratio $RRR = \rho(300\text{ K})/\rho(T \gtrsim T_c) \sim 40$ is quite high, especially compared to previous reports on samples grown by solid-state reaction with $RRR \sim 4 - 6$ [120, 121, 132]. The superconducting transition in the magnetic susceptibility has a sharp onset and is broadened by the relatively high applied field. The specific-heat discontinuity at T_c is, though pronounced, ~ 0.5 K broad. The bulk T_c, as measured by thermal expansion was found to vary between $7.7 - 9$ K for different samples, even within one batch (Fig. 5.3 (b)).

5.2. Superconductivity and orthorhombic distortion

In this chapter, experimental results on the uniaxial thermal-expansion coefficients and the [110]-Young modulus of single-crystalline FeSe are presented. The structural phase transition is studied in detail and shown to be second order and mean-field like. The shear modulus and the orthorhombic distortion are further shown to be very similar to their counterpart in underdoped 122 pnictides. Then, we discuss uniaxial pressure effects and show that T_c couples only very weakly, if at all, to the orthorhombic distortion, in stark contrast to underdoped 122 pnictides.

5.2.1. Experimental results on uniaxial thermal expansion and shear modulus softening

High-resolution thermal expansion was measured in our capacitance dilatometer (see section 2.3). By detwinning samples *in situ* in the dilatometer, the thermal expansion of the *a* and *b* axis and the orthorhombic distortion δ is obtained, similar to underdoped 122 systems (see 3.1). Note that, following conventions, we call the

11. Resistivity data are a courtesy of S. Kasahara, Kyoto University.

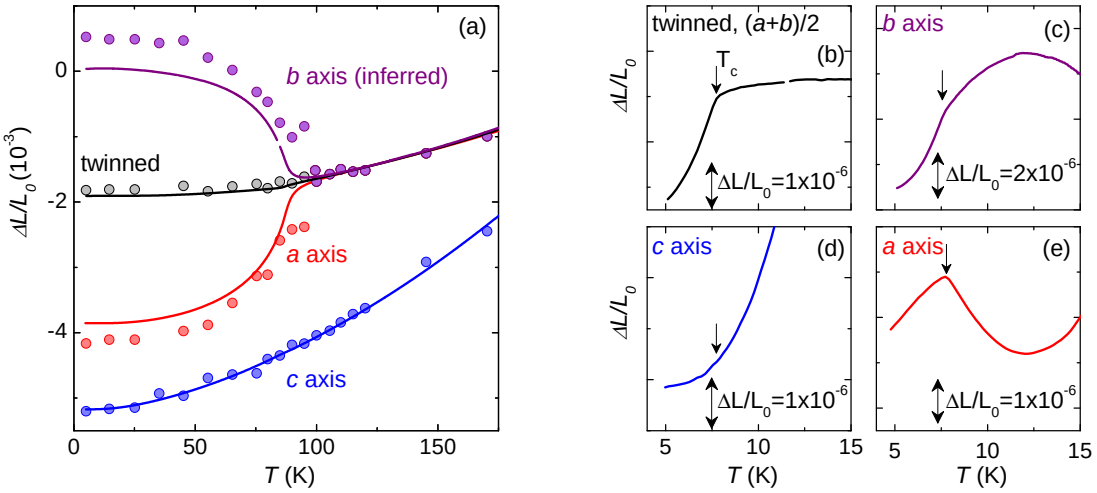

Figure 5.4.: (a) Relative length change of the lattice parameters of FeSe from thermal-expansion measurements (continuous lines). The b-axis data was inferred from measurements of a detwinned (a axis) and a twinned (average of a and b) sample. Comparison with neutron powder diffraction data (circles) [133] shows good agreement. (b)-(e) show the data close to T_c on a magnified scale. Measurements were performed on 3 different samples of batch TWOX1200.

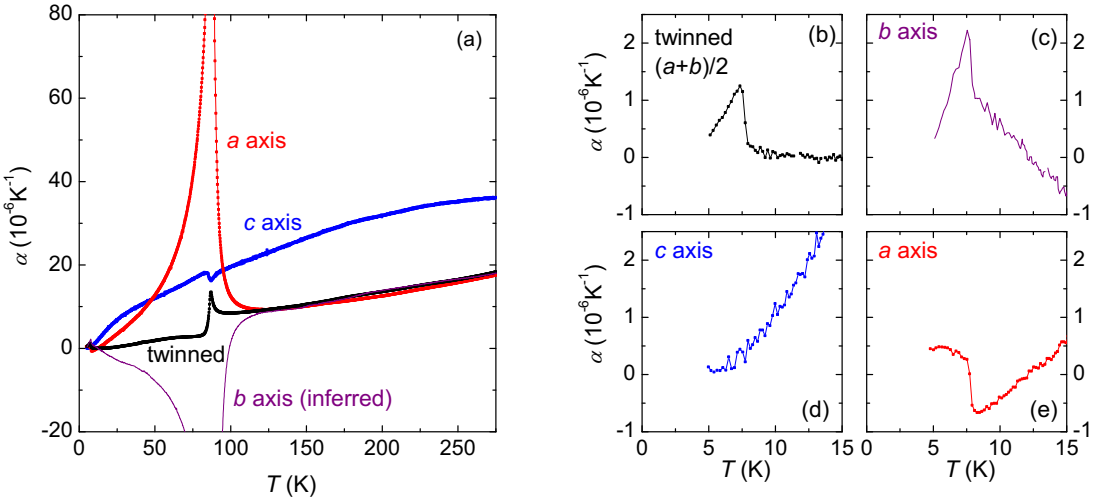

Figure 5.5.: (a) Uniaxial thermal-expansion coefficients of FeSe. The b-axis data was inferred from measurements of a detwinned (a axis) and a twinned (average of a and b) sample. (b)-(e) show the data close to T_c on a magnified scale.

shorter orthorhombic in-plane axis of FeSe a, opposed to the prevailing custom in 122-pnictides used in the previous chapters. Fig. 5.4 shows the thus obtained relative sample-length changes $\frac{\Delta L_i}{L_i} = \frac{L_i(T)-L_i(T_0)}{L_i(T_0)}$ where i stands for the direction. The $\frac{\Delta L_i}{L_i}$ data are in good agreement with previous neutron powder diffraction studies [133], which confirms reliable detwinning. The data clearly show the second-order tetragonal-to-orthorhombic phase transition at $T_s = 87$ K. At the superconducting transition, the in-plane lattice constants show a characteristic discontinuous change of slope.

More detailed information is obtained from the uniaxial thermal-expansion coefficients $\alpha_i = \frac{1}{L_i}\frac{dL_i}{dT}$ (Fig. 5.5). The structural phase transition at $T_s = 87$ K is evident by the sharp peak whose magnitude is largest along [110], very similar to underdoped 122 systems (see section 3.1). No distinct second, potentially magnetic, phase transition is observed below T_s. The c-axis anomaly at T_s is unusually small when compared to underdoped $Ba(Fe,Co)_2As_2$ [11] or $BaFe_2(As,P)_2$ [12]. At $T_c = 7.75$ K, the jump of the in-plane thermal-expansion coefficients $\Delta\alpha_i$ (corresponding to the kink in $\Delta L_i(T)$) clearly confirms a relatively sharp, bulk superconducting transition. However, no such anomaly was observed in the c-axis thermal expansion.

The Young modulus of FeSe was measured using the three-point bending setup in the capacitance dilatometer, described in section 4.2. A previous ultrasound study [134] on single crystals shows that C_{66} (in tetragonal notation) is the soft mode also of FeSe, which is of course consistent with the symmetry of the lattice distortion. Figure 5.6 shows the measured $Y_{[110]}$, which is dominated by C_{66} when C_{66} is small (see section 4.2). Indeed, $Y_{[110]}$ softens significantly on cooling towards T_s. On a much enhanced vertical scale, a tiny anomaly at T_c is also observed. The measured Young modulus of FeSe is analyzed in the same way as the data of the 122 systems. Namely, we approximate $C_{66}/C_{66,0} \approx Y_{[110]}/Y_0$, where Y_0 ($C_{66,0}$) stands for the temperature dependent background from anharmonic phonons. As an approximation, we use the data on $Ba(Fe_{0.67}Co_{0.33})_2As_2$ to estimate the temperature dependence of Y_0 (see section 4.4.3). All data are normalized at room temperature RT, because we do not have access to absolute values of Y. Therefore, one parameter remains free and is taken as $Y_0(0)/Y(RT) = 1.3$, which is very similar to the value for undoped $BaFe_2As_2$, $Y_0(T = 0)/Y(RT) = 1.32$ (see Fig. 4.20).

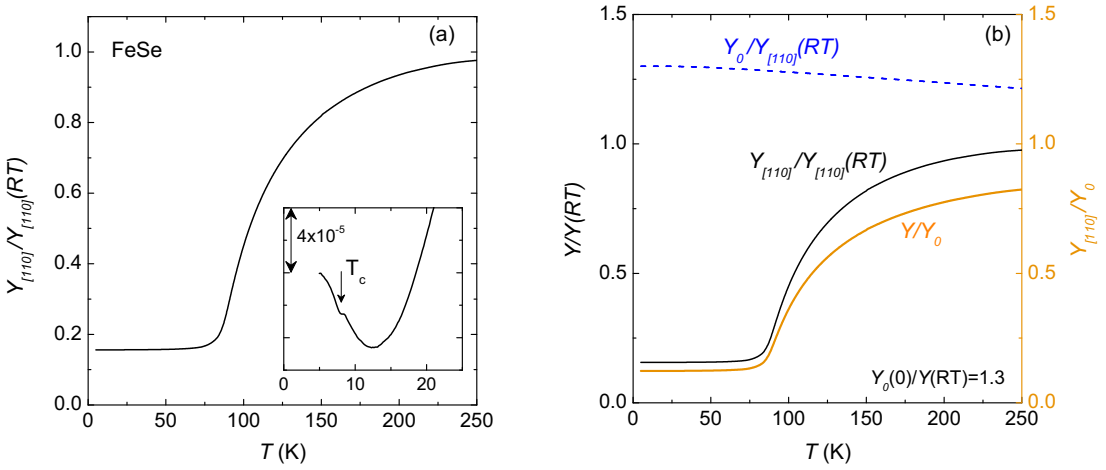

Figure 5.6.: (a) Young's modulus along the tetragonal [110] direction of FeSe, measured using a three-point bending setup in our capacitance dilatometer (section 4.2), normalized at room temperature RT. The inset shows data close to T_c on a greatly magnified vertical scale. (b) Raw data (same as in panel (a), black continous line) and phonon background Y_0 (blue dashed line), both normalized by the room temperature value $Y_{[110]}(RT)$ of FeSe (left scale), and approximated softening of the shear modulus $C_{66}/C_{66,0} \approx Y_{[110]}/Y_0$ (right scale, orange line), analogous to Fig. 4.20 (b),(d). The background Y_0 is taken similar to that of $BaFe_2As_2$.

5.2.2. Pressure effects and lack of coupling between orthorhombic distortion and superconductivity

The structural transition in FeSe is, naturally, clearly seen in the thermal expansion of detwinned samples (Fig. 5.5). In other measurements such as specific heat, resistivity, magnetization or Knight shift (see below), it manifests itself as a tiny jump or kink. Fig. 5.7 details our data on this transition. Panel (a) shows the orthorhombic order parameter, computed from data in Fig. 5.4, which shows a clear second-order like rise below T_s. A small tail can be ascribed to the finite conjugate stress applied for detwinning. The inset shows the critical part of the structural susceptibility $S_{crit} = (C_{66,0}/C_{66} - 1)$ [98], which displays a mean-field-like divergence $\sim 1/(T - T_s)$ above T_s. The mean-field character of the transition is further demonstrated by the sharp jump in the specific heat C_p/T, and in the T-derivative of the magnetic susceptibility $d(\chi T)/dT$ and the resistivity $d\rho/dT$. The volume thermal expansion shows a step-like negative anomaly in addition to a small positive peak. Similarly, the c-axis expansion anomaly also consists of a small (positive) step and a small (negative) peak. From the Grüneisen relation,

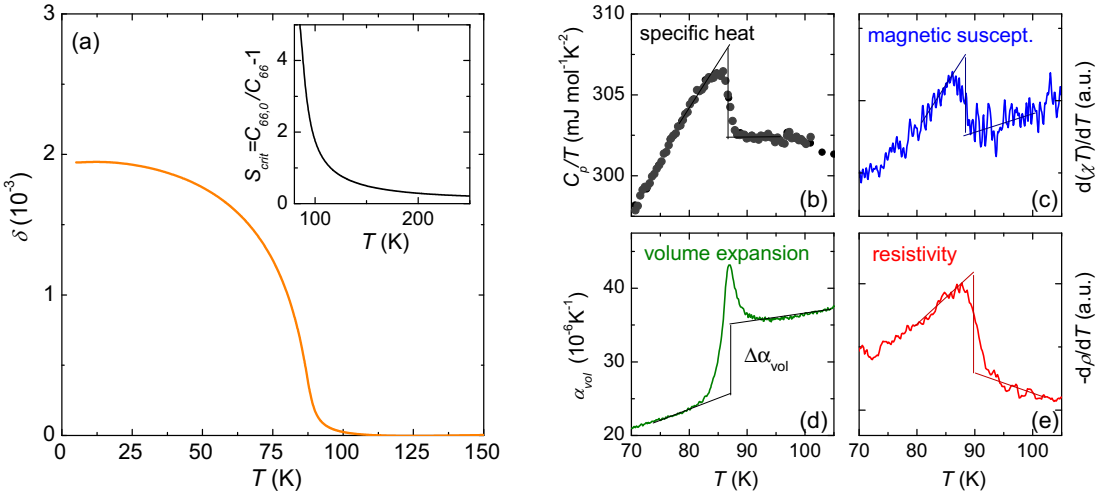

Figure 5.7.: (a) The orthorhombic order parameter of FeSe computed from thermal-expansion measurements. The inset shows the structural susceptibility $S = C_{66,0}/C_{66} - 1$, which follows a near perfect mean-field-like divergence $\sim 1/(T - T_s)$. (b)-(e) The structural transition in specific heat, volume thermal-expansion coefficient, derivative of magnetic susceptibility and resistivity, respectively. A jump-like anomaly is seen in all of these probes, however, the expansion also shows an additional peak. Lines indicate ideal second-order phase transitions.

one would expect only the step-like anomaly and it is hard to explain the origin of the peak. It might arise from the lattice softening around T_s in conjunction with the finite stress applied during the measurement. The pressure derivative of T_s can be estimated via the Ehrenfest relation, eq. 2.8

$$\frac{dT_s}{dp_{vol}} = \frac{V_m \Delta\alpha_{vol}}{\Delta C_p/T_s}$$

from the ratio of the step-like anomaly $\Delta\alpha_{vol}$ to the anomaly in C_p/T. $V_m = 23.34$ cm^3/mol is the molar volume and we find $\Delta C_p/T_c = 5.6$ mJ mol^{-1} K^{-2} and $\Delta\alpha_{vol} = -9.5 \times 10^{-6}$ K^{-1}. This yields $dT_s/dp_{vol} \approx -40$ K/GPa, which is about twice as large as the slope in the phase diagram 5.1 obtained from direct measurements [127] and much larger than the value in $BaFe_2As_2$.

The structural transition of FeSe resembles very closely the structural transition of underdoped $Ba(Fe,Co)_2As_2$, as shown in Fig. 5.8. Here, the orthorhombic order parameter as a function of temperature is plotted. Although no magnetic transition is found, the value $\delta(0)$ is of similar magnitude in FeSe and in the 122 sample having comparable T_s. The high-temperature tail of $\delta(T)$ is more

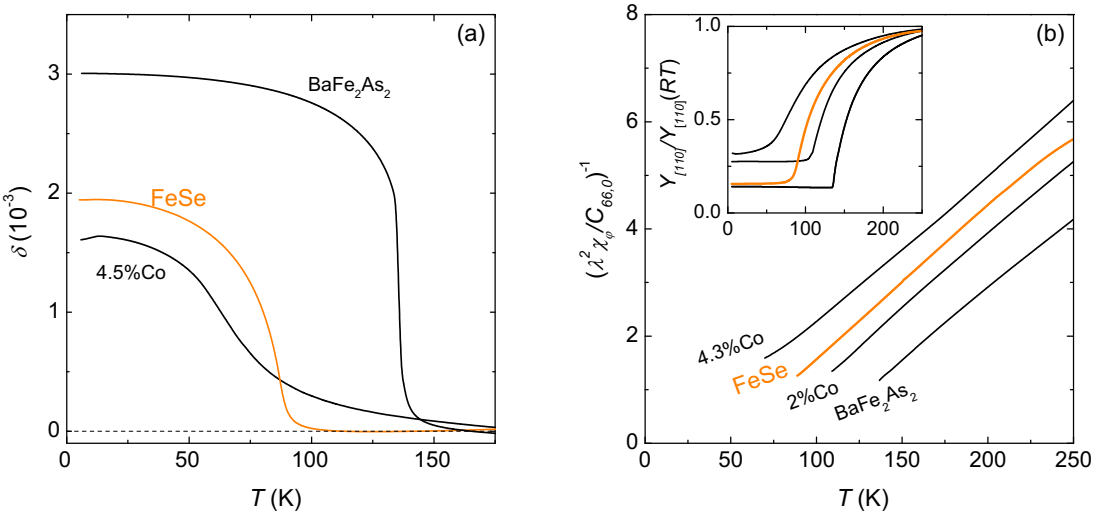

Figure 5.8.: (a) Orthorhombic order parameter $\delta = (a-b)/(a+b)$ of FeSe and underdoped $Ba(Fe,Co)_2As_2$. (b) Inverse of the nematic susceptibility χ_φ in units of the electron-lattice coupling $\lambda^2/C_{66,0}$. The inset shows the Young modulus $Y_{[110]}$ from which χ_φ was extracted. Remarkably, the behavior of FeSe is very similar to underdoped $Ba(Fe,Co)_2As_2$.

pronounced in $Ba(Fe,Co)_2As_2$ than in FeSe, possibly because measurements of FeSe were performed on a sample with a larger cross section and thus under less pressure. Also, the structural transition might be broadened in the "dirty" 4.5% Co-doped $BaFe_2As_2$ or the sample might exhibit a distribution of T_s.

Figure 5.8 also shows the normalized Young modulus $Y_{[110]}/Y_{[110]}(RT)$. Its temperature dependence is very similar for FeSe and underdoped $Ba(Fe,Co)_2As_2$. We apply the Landau theory of section 4.4.1 (eq. 4.17),

$$F = F_0 + \frac{1}{2}C_{66,0}\varepsilon_6^2 - \lambda\varepsilon_6\varphi + \frac{1}{2}\left(\chi_\varphi\right)^{-1}\varphi^2 + \frac{B}{4}\varphi^4,$$

of bilinear coupling between the lattice and a putative electronic nematic order parameter φ which drives the transition, in order to obtain the nematic susceptibility χ_φ of FeSe. Actually, the quantity obtained is $\lambda^2\chi_\varphi/C_{66,0}$, normalized by the electron-lattice coupling constant λ and the bare shear modulus $C_{66,0}$ (see section 4.4.1). The temperature dependence of χ_φ is seen more clearly in a plot of its inverse, which is shown in Fig. 5.8(b) together with data on $Ba(Fe,Co)_2As_2$. Surprisingly, FeSe fits very well into the series of underdoped $Ba(Fe,Co)_2As_2$ and is presumably nearly identical to a sample with 3% Co content. This suggests that χ_φ and the coupling $\lambda^2/C_{66,0}$ have the same value in FeSe and underdoped

$Ba(Fe,Co)_2As_2$. This is a remarkable observation, considering the differences of the two systems, and needs to be explained.

In the following, we consider the uniaxial pressure derivatives of T_c, obtained via the Ehrenfest relation, eq. 2.8, from the data in Fig. 5.5. The specific heat jump at T_c is $\Delta C_p/T_c = 9.6(3)$ mJ mol^{-1}K^{-2} (Fig. 5.3). This yields $\frac{dT_c}{dp_{ab}} = 3.0(5)$ K/GPa for the in-plane average, $\frac{dT_c}{dp_b} = 3.5(1.4)$ K/GPa, $\frac{dT_c}{dp_a} = 2.6(5)$ K/GPa and $\frac{dT_c}{dp_c} = 0(0.5)$K/GPa. These values are much smaller, and have opposite sign as compared to underdoped $Ba(Fe,Co)_2As_2$ [135]. In particular, $\frac{dT_c}{dp_i}$ displays only a very weak in-plane anisotropy and is very small along the c axis.

The hydrostatic pressure derivative of T_c is simply given by the sum of the uniaxial components $\frac{dT_c}{dp_{vol}} = \frac{dT_c}{dp_a} + \frac{dT_c}{dp_b} + \frac{dT_c}{dp_c} = 6.0(1.5)$ K/GPa which is in good agreement with the initial slope of direct measurements, which yield $\frac{dT_c}{dp_v} = 6 - 7$ K/GPa [128, 129]. It is clear from our results that the comparatively large $\frac{dT_c}{dp_{vol}}$ in FeSe arises not from particularly large uniaxial components but from a lack of their cancellation. For example, the in-plane derivatives are comparable in size to slightly overdoped $Ba(Fe,Co)_2As_2$ [43, 135]. However, in $Ba(Fe,Co)_2As_2$, in-plane and c-axis pressure derivatives have opposite signs and largely cancel in the hydrostatic average [11, 43, 135], while the p_c derivative is approximately zero in FeSe. As established in chapter 3, the structural tuning parameter of the 122-systems is the c/a ratio. In contrast, for FeSe the in-plane distance alone appears to be the tuning parameter, which couples more strongly to hydrostatic pressure.

Basically the same picture emerges when considering the uniaxial strain derivatives of T_c, $\frac{dT_c}{d\varepsilon_j} = \sum_i c_{ij} \frac{dT_c}{dp_i}$, which can be calculated if the set of elastic constants c_{ij}, $\{i,j\} \in \{1;2;3\}$, is known. For tetragonal FeSe, these constants have been calculated using DFT [136]: $c_{11} = 95.2$ GPa, $c_{12} = 48.8$ GPa, $c_{13} = 13.9$ GPa and $c_{33} = 39.5$ GPa.[12] Using these c_{ij} values (allowing for an error of 10%) we find $\frac{dT_c}{d\varepsilon_a} = -416(161)$ K, $\frac{dT_c}{d\varepsilon_b} = -459(207)$ K and $\frac{dT_c}{d\varepsilon_c} = -84(53)$ K. It is evident that T_c depends sensitively on the in-plane lengths. Indeed, the corresponding uniaxial Grüneisen parameter, $\frac{d\ln T_c}{d\varepsilon_{ab}} = -56(15)$, shows that shrinking $(a+b)/2$ by 1% increases T_c by $\sim 50\%$. We note that a and b decrease by $\sim 1.5\%$ between ambient pressure and 7 GPa, where the highest T_c is reached [122]. T_c is five times less sensitive to changes of the c-axis length ($\frac{d\ln T_c}{d\varepsilon_c} = -9(6)$). It is striking that

12. c_{33} agrees within 8% with the experimental low-temperature value of 42.7 GPa [137] reported from a measurement on thin films. Using the calculated c_{ij} values, the linear compressibilites $K_a = -\frac{1}{a}\frac{da}{dp} = K_b = 4.8 \times 10^{-3}$ GPa^{-1} and $K_c = 17.1 \times 10^{-3}$ GPa^{-1} are obtained, which are also in relatively good agreement with the experiment ($K_a = 6.3 \times 10^{-3}$ GPa^{-1}, $K_b = 6.9 \times 10^{-3}$ GPa^{-1} and $K_c = 17.6 \times 10^{-3}$ GPa^{-1} [138]). Additionally, the elastic properties show relatively little ab-plane anisotropy, which is why we use the tetragonal c_{ij}.

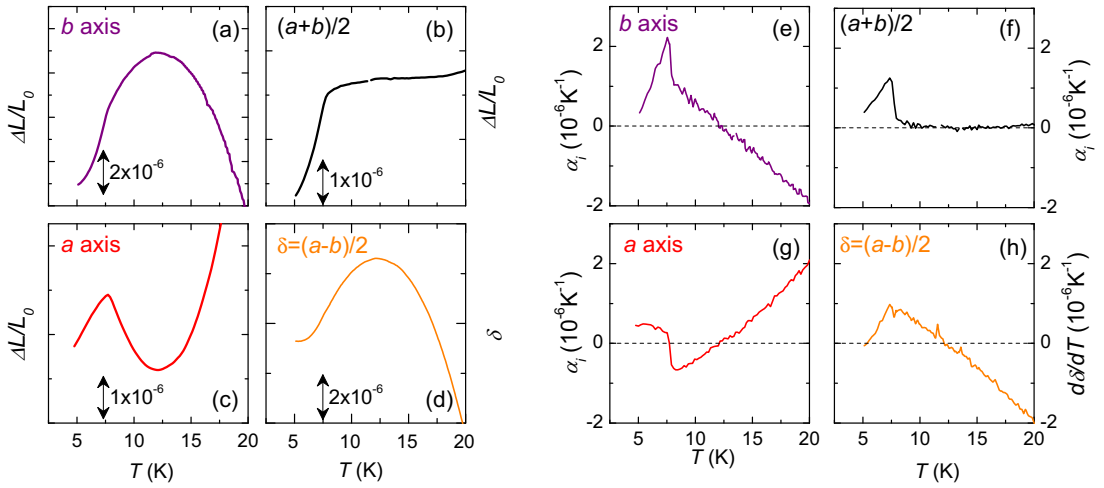

Figure 5.9.: (a)-(d) Length changes of the orthorhombic a and b axis, of their average and their difference, respectively. The latter corresponds to the orthorhombic order parameter. (e)-(h) show the corresponding thermal-expansion coefficients.

the c-axis length has such a small effect on T_c, especially since the Se height (i.e. the c-axis length times the internal z-parameter) was found to correlate closely with T_c [139]. The z parameter however, may depend in a complicated manner both on in-plane and c-axis lengths.

In the following, we discuss the coupling between T_c and the orthorhombic distortion $\delta = (a - b)/(a + b)$, which is very strong in underdoped 122 systems (sections 3.1 and 3.3.1, and Ref. [30]). Fig. 5.9 shows an expanded view of the in-plane lengths changes and thermal-expansion coefficients. Also shown are their average and their difference, the latter being proportional to the orthorhombic order parameter. A jump in α at T_c is observed only for the average and not for the difference of the a- and b-axis expansion. In contrast, the normal-state thermal expansion is nearly zero for the average, while the difference is strongly temperature dependent. The sign change in $\alpha_a - \alpha_b$ corresponds to the weak maximum of δ at 12 K $> T_c$.

Fig. 5.10 contrasts the low-temperature behavior of δ and $Y_{[110]}$ of FeSe with that of underdoped $Ba(Fe,Co)_2As_2$. The data on underdoped $Ba(Fe,Co)_2As_2$, obtained from thermal-expansion and Young's modulus measurements, show familiar behavior [10, 30], namely reduction of δ and hardening of C_{66} below T_c. In contrast, FeSe shows a weak maximum of δ and a slight hardening of $Y_{[110]}$ below $\sim$ 12 K $> T_c$. The competition between magnetic/structural and superconducting order parameters in $Ba(Fe,Co)_2As_2$ results in a step-like increase of

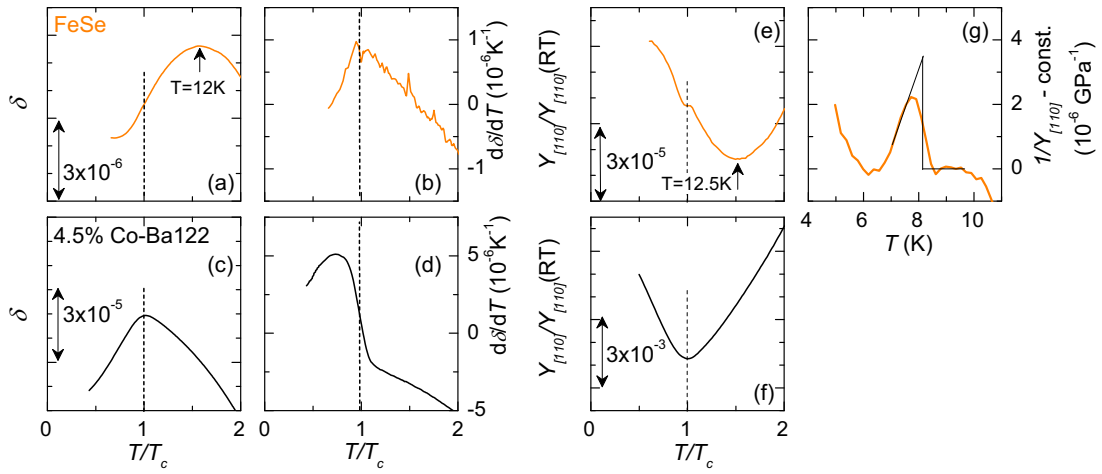

Figure 5.10.: (a), (c) Low-temperature orthorhombic order parameter δ and (b), (d) its temperature derivative for FeSe and underdoped $Ba(Fe,Co)_2As_2$, respectively. A distinct slope change of $\delta(T)$ at T_c, corresponding to a jump in the derivative, is seen only in $Ba(Fe,Co)_2As_2$. $\delta(T)$ in FeSe shows only a change of curvature at T_c and weak maximum at higher temperature. (e), (f) Low-temperature Young's modulus of $Ba(Fe,Co)_2As_2$ and FeSe, showing a hardening at T_c in $Ba(Fe,Co)_2As_2$ and a shallow minimum above T_c in FeSe. An additional step-like softening is seen at T_c in FeSe. (g) shows this step-like anomaly, which is similar to the specific-heat anomaly, in the elastic compliance $1/Y$ (see text). A linear background has been subtracted in (g).

$d\delta/dT$ on cooling through T_c. In FeSe, however, $d\delta/dT$ only shows a kink at T_c, which is such that δ will have a tendency to be somewhat larger in the superconducting state than in the normal state. This kink presumably arises from anisotropic pressure derivatives of the density of states that results in different $\frac{d\gamma}{dp_a}$- and $\frac{d\gamma}{dp_b}$-contributions (type-II contribution of section 2.2) to the thermal expansion. From the experimental resolution, we estimate that any jump $\Delta(\alpha_a - \alpha_b) < 0.1 \times 10^{-6}$ K^{-1}. This implies that the pressure derivative of T_c, $dT_c/dp_a - dT_c/dp_b < 0.23$ K/GPa. Using the aforementioned elastic constants, we estimate that the difference in strain derivatives is very small

$$\frac{1}{T_c}\left(\frac{dT_c}{d\varepsilon_a} - \frac{dT_c}{d\varepsilon_b}\right) < 0.0043. \tag{5.1}$$

This value shows that, if the a axis is expanded by 0.1% and the b axis shrunk by 0.1% (which implies that δ changes from ~ 0.002 to ~ 0.001), then T_c increases at most by 0.43% (assuming linear pressure dependencies). For comparison, a similar estimate in 4.3% Co-doped $BaFe_2As_2$ indicates that T_c would rise by $\approx 67\%$ under

the same conditions. In orthorhombic $YBa_2Cu_3O_{7-\delta}$ ($T_c = 90.9$ K), on the other hand, $(1/T_c)\,(dT_c/d\varepsilon_a - dT_c/d\varepsilon_b) \approx 0.005$ [140], which means that T_c would only increase by 0.5% in the above example.

The giant coupling between δ and T_c in $Ba(Fe,Co)_2As_2$ is remarkable. In the spin-nematic scenario, it is proposed to arise, ultimately, from the competition between magnetism and superconductivity [30]. In short, spin fluctuations, which give rise to spin-nematic order that, in turn, induces an orthorhombic distortion (via magneto-elastic coupling), are weakened by the onset of superconductivity. It is a fundamental question which part of this scenario is not valid for FeSe. Our experimental results suggest that either superconductivity does not interact strongly with spin fluctuations or that the structural transition has a non-magnetic origin. As will be detailed below, results of NMR measurements support the latter possibility.

Furthermore, no hardening of C_{66} is observed at T_c in FeSe, consistent with the observed lack of coupling between δ and T_c (Fig. 5.10). Instead, there is a tiny, step-like softening of $Y_{[110]}$ at T_c. Such an anomaly is expected to arise from the longitudinal components of $Y_{[110]}$ [111]. Its size[13] is proportional to the pressure derivative of T_c.

Curiously, even if there is no coupling between $\delta(T)$ and T_c in FeSe, δ still shows a maximum ($Y_{[110]}$ a minimum) around 12 K, reminiscent of the response of these quantities at T_c in $Ba(Fe,Co)_2As_2$. However, these anomalies are one, respectively two, orders of magnitude smaller in FeSe than in $Ba(Fe,Co)_2As_2$. The plot of $\frac{\alpha_{a,b}}{T}$ (Fig. 5.10) shows that the maximum in $\delta(T)$ arises from an additional low-temperature contribution to the in-plane thermal expansion, emerging below $\sim$ 30 K, which causes a sign change of both $\alpha_a(T)$ and $\alpha_b(T)$ at $\sim$ 12 K. For a Fermi-liquid, one expects a constant $\frac{\alpha}{T}$ term at low temperatures, which is directly related to the uniaxial pressure derivative of the Sommerfeld coefficient, as seen for underdoped 122 systems. The non-Fermi-liquid character of the thermal-expansion of FeSe becomes apparent in this comparison. It seems that a, possibly new, energy scale with a negative (positive) contribution to $\frac{\alpha_a}{T}$ ($\frac{\alpha_b}{T}$) (but which does not couple to the volume) emerges below $\sim$ 30 K and causes these coefficients to diverge. The nature of this energy scale is unclear. It has been suggested that FeSe is close to a BCS-BEC crossover [131], in which case superconducting fluctuations would be expected above T_c. In that case the above results would imply that only the superconducting fluctuations, and not the transition tem-

13. Using the ultrasound results of Ref. [134], we estimate that $Y_{[110]}(RT) \approx 80$ GPa. Then, the absolute value of the step-like discontinuity in the elastic compliance can be estimated to $\Delta\left(1/Y_{[110]}\right) \approx 3.4 \times 10^{-6}$ GPa^{-1}. Using the appropriate Ehrenfest relation 2.9, this yields $dT_c/dp_{ab} = \Delta\left(1/Y_{[110]}\right)/\Delta\alpha_{ab} = 2.7$ K/GPa. Considering the approximations, this is in excellent agreement with the result from α and C_p, $dT_c/dp_{ab} = 3$ K/GPa.

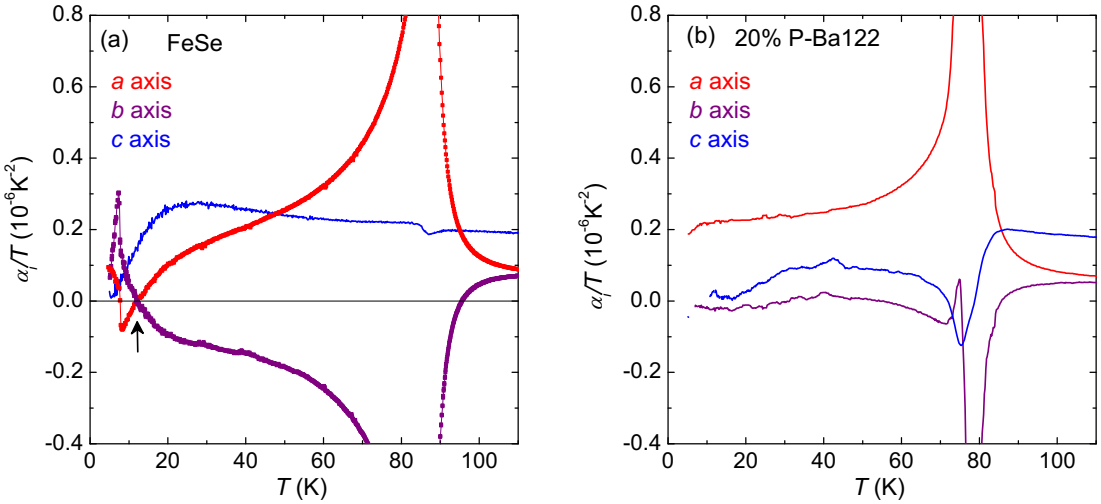

Figure 5.11.: (a) Uniaxial thermal-expansion coefficients divided by temperature of FeSe, revealing non-Fermi-liquid behavior of the in-plane coefficients. Their crossing at $\sim$ 12 K causes the maximum of the orthorhombic distortion. (b) The thermal expansion of 20% P-substituted $BaFe_2As_2$ [12], which does exhibit Fermi-liquid-like thermal expansion below T_s, for comparison.

perature, couple to the orthorhombic distortion in a similar way as T_c does in $Ba(Fe,Co)_2As_2$. On the other hand, as shown below, magnetic fluctuations also become strong in this temperature range.

5.3. Magnetic fluctuations and shear-modulus softening

The above analysis of the thermal expansion is complemented by NMR measurements. NMR measures the size of the Zeeman splitting of the energy levels of a nuclear spin in an external magnetic field. Here, this is the ^{77}Se nuclear spin with $I = 1/2$ in a field of 9 T. Using a radio-frequency perturbation, its resonance energy is revealed as a sharp line in the NMR spectrum (see Fig. 5.12). The aim is to deduce the magnetic properties of the electrons via the magnetic hyperfine interaction between nuclear and electronic spins. Specifically, one measures the internal magnetic field H_{int} at the site of the nucleus, given by the sum of the magnetic moments m of the surrounding ions times a hyperfine coupling tensor A_{hf}. H_{int} adds to the external field and hence shifts the resonance line of

the NMR spectrum, an effect called Knight shift K. For example, the external magnetic field induces a paramagnetic moment $m = \chi H_{ext}$, where χ is the magnetic susceptibility. This moment gives rise to an internal field, and hence to a contribution to the Knight shift proportional to χ.

A second effect of the hyperfine interaction is to allow transitions between different Zeeman levels. This determines the so-called spin-lattice relaxation rate $1/T_1$, i.e., the rate with which nuclear spins return to their equilibrium population after a pulse has taken them to a higher energy level. For a Fermi liquid, this effect gives rise to a contribution to $1/T_1$ proportional to the square of the orbital Knight-shift times T, which corresponds to the so-called Korringa relation [141],

$$\left(\frac{1}{T_1 T}\right)^{1/2} \propto K + \text{const.} \tag{5.2}$$

In the presence of fluctuating magnetic fields perpendicular to the external field, another contribution to $1/T_1$ arises. It is given by a convolution of the imaginary part of the ω- and $\mathbf{k}$-dependent magnetic susceptibility $\chi(\mathbf{k}, \omega)$ with an anisotropic form factor $F(\mathbf{k})$ that is related to the hyperfine coupling tensor as [115]

$$\frac{1}{T_1 T} = \gamma_g^2 \lim_{\omega \to 0} \sum_{\mathbf{k}} F^2(\mathbf{k}) \frac{\Im\chi(\mathbf{k}, \omega)}{\omega}. \tag{5.3}$$

$F(\mathbf{k})$ depends on the direction of the applied magnetic field and γ_g is the gyromagnetic ratio of the nucleus.

In the following section, experimental data of the Knight shift and the spin-lattice relaxation rate, obtained in collaboration with the group of K. Ishida of Kyoto university, are shown. In the discussion, we consider how the strength of magnetic fluctuations can be obtained from $1/T_1$. We further discuss the anisotropy of $1/T_1$ with respect to the applied field and show that it differs from LaFeAsO. Finally, we consider the relationship between shear-modulus softening and enhancement of $1/T_1T$ in FeSe, which seems to differ quite significantly from $Ba(Fe,Co)_2As_2$.

5.3.1. Results of nuclear magnetic resonance experiments

Fig. 5.12 (a) and (b) shows a selection of NMR spectra of a collection of ~ 10 oriented FeSe single crystals with the field applied parallel and perpendicular to the *ab* plane, respectively. The NMR resonance lines are very sharp. The full width at half maximum is only ≈ 4 kHz around 200 K and increases only slightly to $\approx 6-8$ kHz on cooling. For $H||ab$, an ≈ 8 kHz splitting of the resonance line is observed below T_s. NMR is a local probe, hence we attribute the two peaks to two

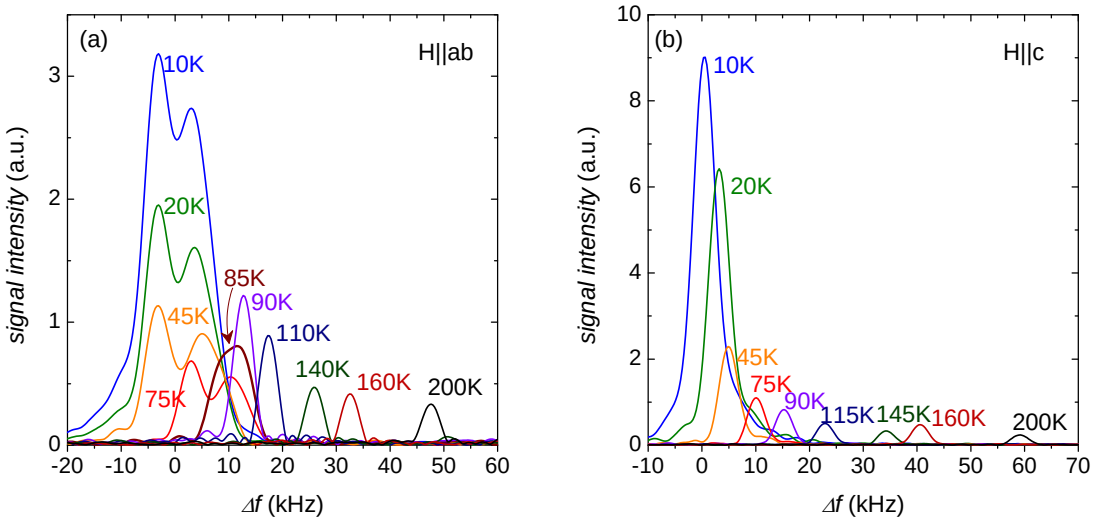

Figure 5.12.: NMR spectra of a collection of ~ 10 FeSe single crystals in a field of 9 T applied parallel to the ab plane and along the c axis, respectively. Extremely sharp resonance lines are observed, which split for in-plane field below T_s.

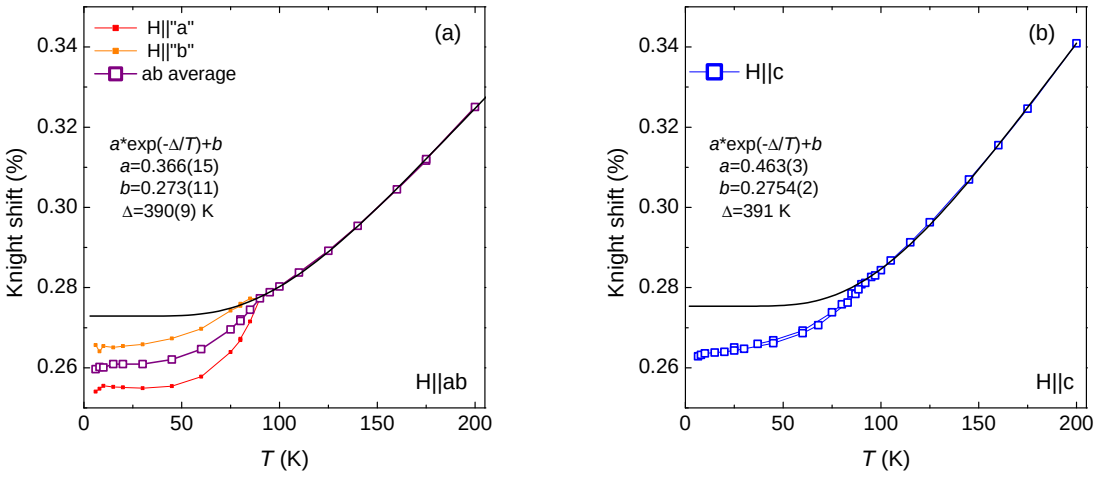

Figure 5.13.: (a),(b) Knight shift of FeSe in field applied parallel to the ab plane and along the c axis, respectively. The Knight shift of domains aligned with their orthorhombic a or b axis parallel to the applied field differs significantly. The attribution of the smaller Knight shift to the a axis is arbitrary. The arithmetic ab average is also shown. Black lines show a fit to an activated type temperature dependence $K = a\exp(-\Delta/T) + b$ above T_s.

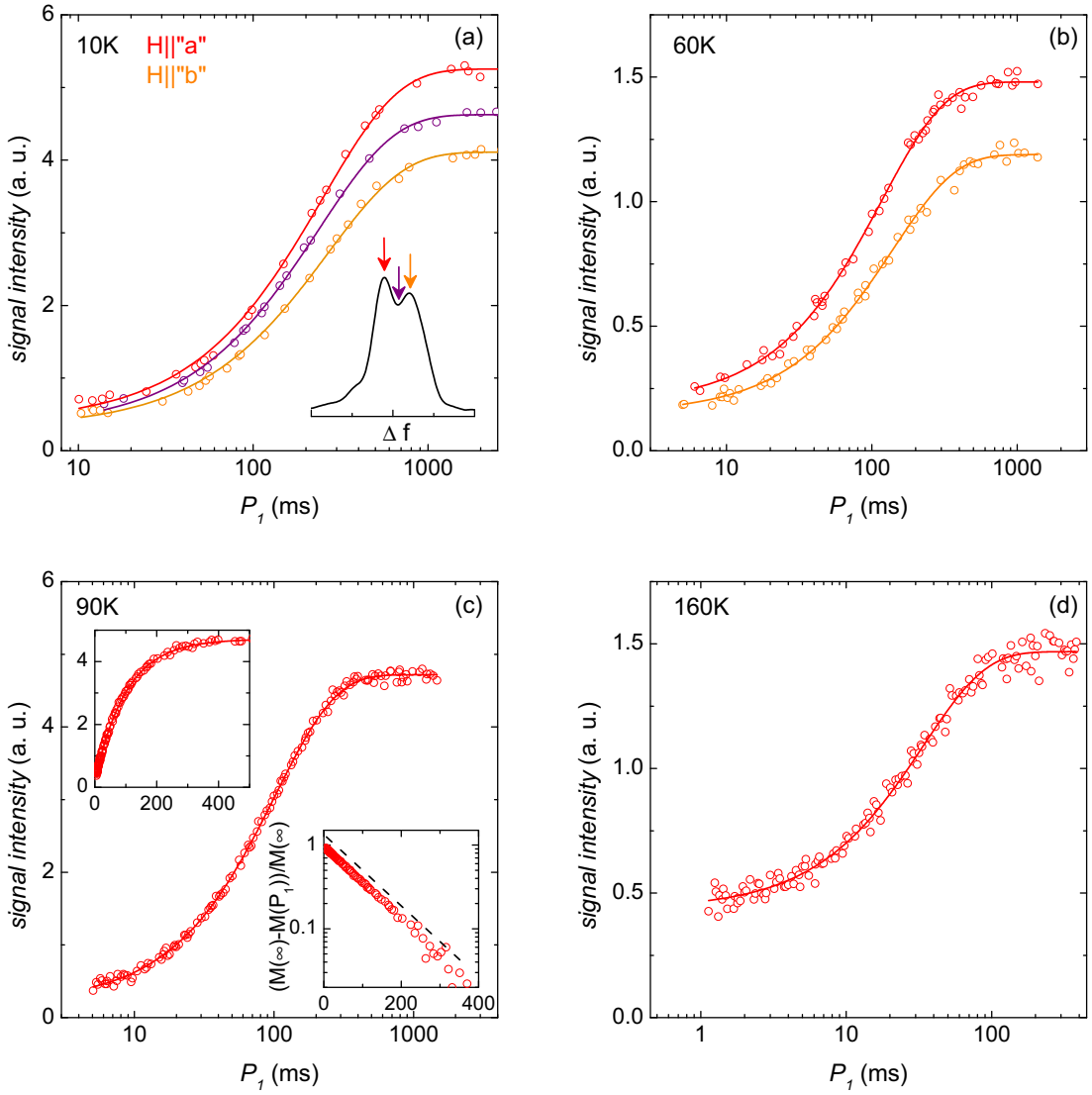

Figure 5.14.: Nuclear magnetization of FeSe at a time P_1 after application of a resonance pulse (see inset in (a)) at different temperatures. Solid lines show a single-exponential decay fit. The insets in (c) illustrate the exponential dependence.

kinds of domains, in which the field is aligned parallel to either the orthorhombic a axis or the b axis. Since we cannot determine which line arises from which kind of domains, we arbitrarily assign the left peak to the a axis ("a") and the right peak to the b axis ("b").

All resonance lines shift monotonically to higher frequency with temperature. Fig. 5.13 shows this temperature-dependent Knight shift K determined as the difference of the resonance frequency f with respect to the resonance frequency f_0 of an isolated ^{77}Se nucleus, $f_0 = \gamma H$, with $\gamma = 8.13$ MHz/T the gyromagnetic ratio of ^{77}Se. K shows a relatively strong temperature dependence, which is very similar to the uniform magnetic susceptibility (Fig. 5.2). Above T_s, the Knight shift follows well a phenomenological activated-type behavior $K = a\exp(-\Delta/T) + b$ [114] with a "gap" $\Delta \approx 390$ K. At T_s, it shows a distinct negative kink, similar to the magnetic susceptibility.

In order to determine the spin-lattice relaxation time T_1, a resonance pulse is applied to the sample at $t = 0$ and the fraction of nuclear spins that have returned into equilibrium position after a time $t = P_1$, the "magnetization" $M(P_1)$, is measured. Fig. 5.14 shows examples of such recovery curves for in-plane applied field. Below T_s, the recovery was measured at both resonance peaks, corresponding to field aligned either along the "a" or the "b" axis. Data are shown as M vs. $\log(P_1)$ plots with a single-exponential decay fit $M(P_1) = M(\infty) - A\exp(-P_1/T_1)$. The very good fit and the saturation at long P_1 is evident. As an illustration, insets in (c) shows the exponential recovery on a linear scale and $\log\left(M(\infty) - M(P_1)\right)/M(\infty)$ vs. P_1, demonstrating the perfect exponential decay.

Fig. 5.15 presents the extracted spin-lattice relaxation rate $1/T_1$ and $1/T_1T$ for $H||ab$ and $H||c$. $1/T_1T$ decreases on decreasing T in the high-temperature regime, similarly to the Knight-shift, and shows a marked upturn below ~ 80 K. The anisotropy with respect to the applied field is moderate. For example, the a-b anisotropy amounts to only $\sim 10\%$. In most of the following, we will compare ab-average with c-axis values.

5.3.2. Temperature dependence and anisotropy of magnetic fluctuations

The spin-lattice relaxation rate divided by temperature $1/T_1T$ is expected to be constant for a degenerate Fermi-liquid. It does, however, show a strong temperature dependence in FeSe. $1/T_1T$ of FeSe qualitatively resembles over-doped $Ba(Fe,Co)_2As_2$, as remarked previously [126]. Namely, $1/T_1T$ decreases on cooling at high temperature and increases again at lower temperature (see Fig.

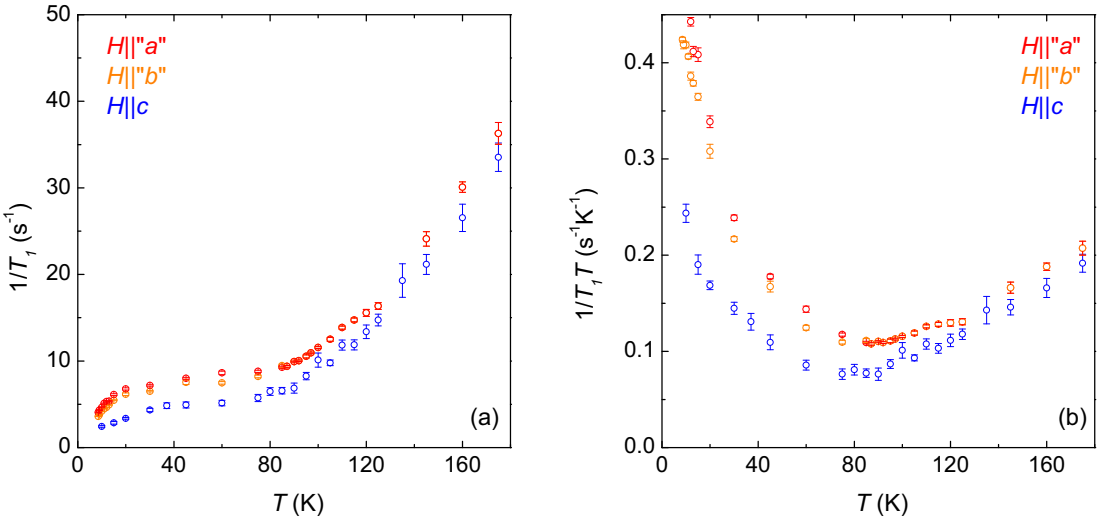

Figure 5.15.: (a) Spin-lattice relaxation rate $1/T_1$ and (b) spin-lattice relaxation rate divided by temperature $1/T_1T$ of FeSe for different directions of the applied field. $1/T_1T$ shows a pronounced temperature dependence, with a decrease on cooling at higher temperature and an upturn below ~ 80 K. The field anisotropy is moderate.

5.15). The high-temperature part closely resembles the Knight shift K, whose strong temperature dependence likely arises from small Fermi-surface pockets [131]. In other words, FeSe cannot be described as a degenerate Fermi-liquid. K follows indeed well a phenomenological activated-type temperature dependence $K = a\exp(-\Delta/T) + b$, with $\Delta \approx 390$ K. Similar behavior, with $\Delta \approx 450$ K, has been reported previously in $Ba(Fe,Co)_2As_2$ [114]. Within the Fermi-liquid picture, T_1 and K are expected to be related via the Korringa relation eq. 5.2. This behavior is tested in Fig. 5.16 where the square root of $1/T_1T$ is plotted versus the Knight shift with temperature as an implicit parameter. The Korringa relation is indeed well satisfied down to ~ 90 K $\sim T_s$. In conclusion, the temperature dependence of $1/T_1T$ above T_s can be attributed to bandstructure effects, without the presence of spin fluctuations.

The strong upturn at low temperature is a clear sign of an additional contribution to $1/T_1T$ from spin fluctuations. In order to extract the spin-fluctuation contribution to the spin-lattice relaxation rate, a background has to be subtracted. Ref. [114] proposed a phenomenological two-component model

$$\frac{1}{T_1T} = \left(\frac{1}{T_1T}\right)_{intra} + \left(\frac{1}{T_1T}\right)_{inter} \tag{5.4}$$

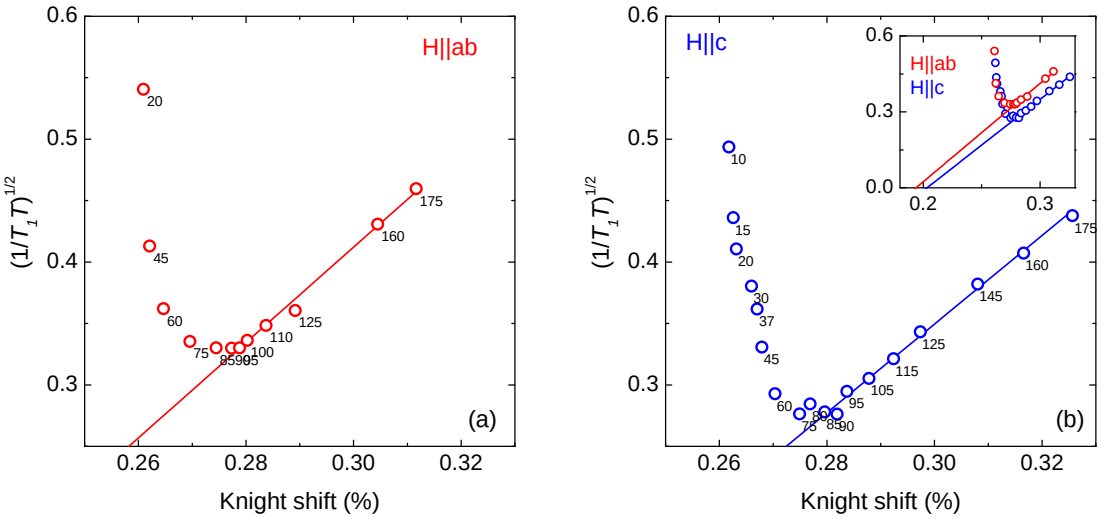

Figure 5.16.: (a), (b) Plot of $(1/T_1T)^{1/2}$ vs. Knight shift of FeSe for field parallel to the ab plane and along the c axis, respectively. Points are labeled with temperature (in K) as an implicit parameter. Data above $\sim$ 90 K fall on a straight line, consistent with the Korringa relation, eq. 5.2. The inset shows the data on a larger scale.

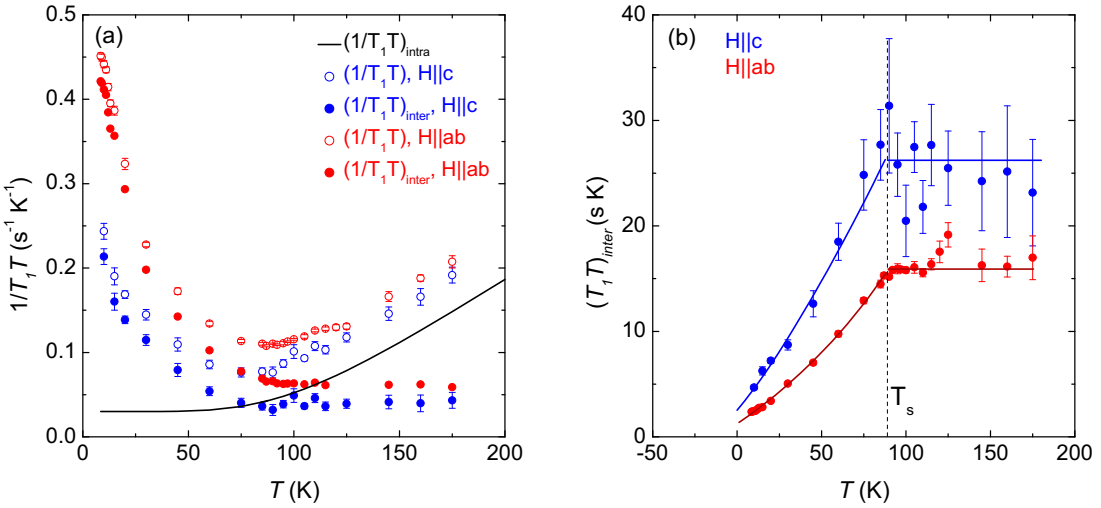

Figure 5.17.: (a) Two-component analysis $1/T_1T = (1/T_1T)_{intra} + (1/T_1T)_{inter}$ for $1/T_1T$ (open symbols) of FeSe. The solid line indicates the intraband contribution, model 5.5, related to the Knight shift, and full symbols show the extracted interband contribution, associated with spin-fluctuations. (b) shows the inverse, $(T_1T)_{inter}$ revealing a kink at T_s and the proximity of FeSe to a magnetic instability.

where the intraband contribution $(1/T_1T)_{intra}$ satisfies the Korringa relation and the interband contribution $(1/T_1T)_{inter}$ arises from spin-fluctuations. It is not clear how the $(1/T_1T)_{intra}$ can best be modeled for FeSe. In a first approximation, we choose a simple activated-type law

$$(1/T_1T)_{intra}\,[\mathrm{s^{-1}K^{-1}}] = 1.1\exp(-390\ \mathrm{K}/T) + 0.03, \tag{5.5}$$

isotropic with respect to the applied field. Fig. 5.17 shows the deduced spin-fluctuation contribution $(1/T_1T)_{inter}$, which strongly increases below ~ 90 K. Its temperature dependence is seen more clearly in a plot of the inverse, $(T_1T)_{inter}$. In fact, $(T_1T)_{inter}$ is nearly constant at high temperature and starts to decrease around, if not exactly, at T_s. Very small values are reached at the lowest temperature, 10 K $> T_c$. An extrapolation suggests that $(T_1T)_{inter}$ would reach zero around -10 K. This clearly indicates that orthorhombic FeSe is close to a magnetic instability, although it does not order magnetically at ambient pressure. Note that magnetic order was indeed found above an external pressure of 0.8 GPa [130]. It should be cautioned, however, that the high-temperature part of the obtained $(T_1T)_{inter}$ depends sensitively on the model for the intraband contribution.

It proved instructive to study the anisotropy of $1/T_1T$ with respect to the applied field in many iron-based superconductors [142]. The *ac*-anisotropy ratio

$$R_{ac} = \frac{\left[(1/T_1)_{H||a} + (1/T_1)_{H||b}\right]/2}{(1/T_1)_{H||c}} \tag{5.6}$$

was found to equal $\sim$ 1.5 in many of them [119, 142]. From an analysis of the symmetry of the As environment (which is identical to the symmetry of Se in FeSe), this value has been suggested to indicate stripe-type spin correlations [142]. Note that the analysis only considers $(1/T_1)_{inter}$. In Fig. 5.18 we compare FeSe to LaFeAsO, a system where T_s and T_N are well split. There, R_{ac} is ~ 1.5 only in the tetragonal state and increases strongly below T_s [142], where the symmetry of the As environment is of course changed. In strong contrast to this, $R_{ac} \sim 1.5-2$ in orthorhombic FeSe at low temperatures, where the intraband contribution is small. Furthermore, R_{ac} does not seem to change significantly across T_s. The high temperature values depend of course extremely sensitively on the model for the intraband contribution.

The comparison of $1/T_1$ measured at the resonance frequencies of the two peaks in the in-plane-field NMR spectrum of FeSe below T_s (Fig. 5.12), shows that the in-plane anisotropy of T_1 is rather small. The ratio

$$R_{ab} = \frac{(1/T_1)_{H||\text{“}a\text{”}}}{(1/T_1)_{H||\text{“}b\text{”}}} \approx 1.1 \tag{5.7}$$

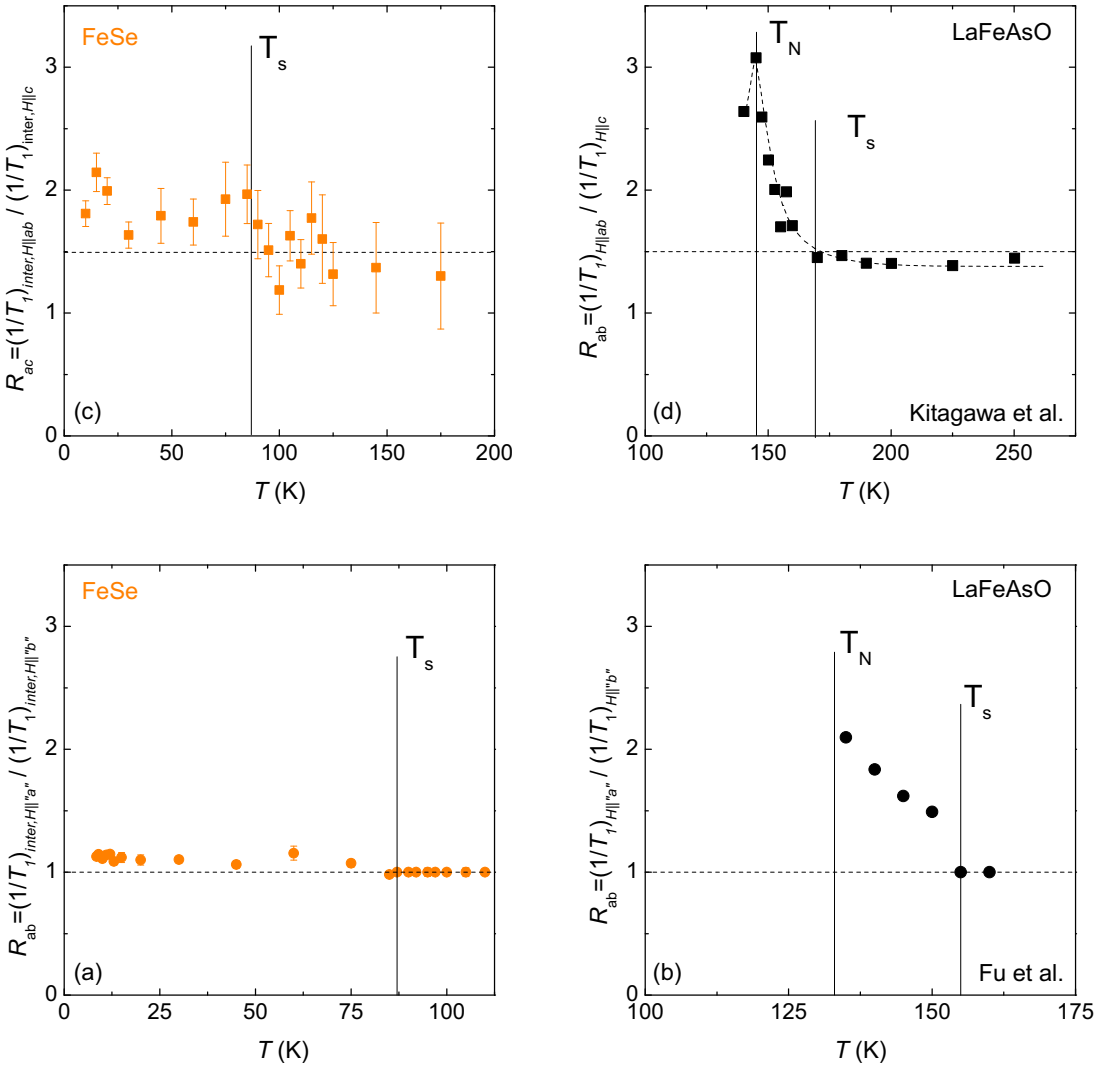

Figure 5.18.: Anisotropy of $1/T_1$ with respect to the applied field for FeSe and LaFeAsO. (a),(b) a-c anisotropy ratio $R_{ac} = \frac{[(1/T_1)_{H||inter,a}+(1/T_1)_{H||inter,b}]/2}{(1/T_1)_{H||c}}$, comparing in-plane average of the interband contribution to $1/T_1T$ with the c-axis values. In both systems, the a-c anisotropy is ~ 1.5, however it increases strongly below T_s only in LaFeAsO. (c),(d) In-plane anisotropy ratio $R_{ab} = (1/T_1)_{H||inter,\text{“}a\text{”}} / (1/T_1)_{H||inter,\text{“}b\text{”}}$, which increases strongly below T_s only in the LaFeAsO.

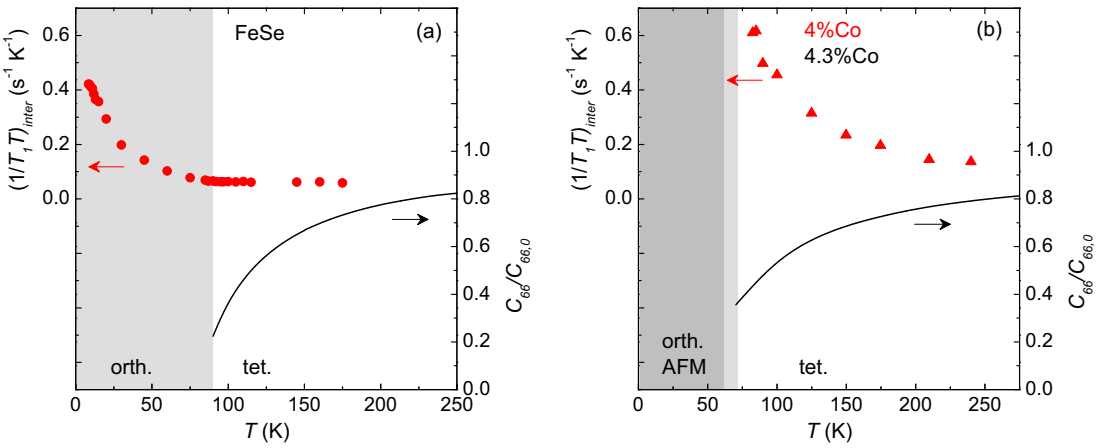

Figure 5.19.: Shear-modulus softening $C_{66}/C_{66,0}$ and spin-fluctuation contribution $(1/T_1T)_{inter}$ of (a) FeSe (b) and underdoped $Ba(Fe,Co)_2As_2$, respectively. A relation between enhancement of $1/T_1T$ and softening of C_{66} is only evident in $Ba(Fe,Co)_2As_2$. The gray shadings indicate the orthorhombic, and the orthorhombic-magnetic phase, respectively.

is furthermore independent of temperature. In LaFeAsO, in contrast, R_{ab} grows strongly on cooling below T_s and exceeds 2 only 20 K below T_s [86]. However, it might be desirable to confirm the FeSe results in future experiments on only one single crystal. In summary, while the temperature dependence of $1/T_1T$ of FeSe qualitatively resembles other iron-based superconductors, its anisotropy with respect to the applied field is quite different.

In section 4.4.4, a relation between the spin-fluctuation contribution $(1/T_1T)_{inter}$ and the softening of the shear modulus $C_{66}/C_{66,0}$ was put forward on the basis of the spin-nematic scenario (eq. 4.40) [99],

$$\frac{C_{66}}{C_{66,0}} = \frac{1}{1 + [aT_1T - b]^{-1}}.$$

It was found to be well satisfied in $Ba(Fe,Co)_2As_2$, providing evidence that the structural transition is magnetically driven. Fig. 5.19 shows a similar attempt for FeSe. The strong difference of the two systems is evident. The enhancement of $1/T_1T$ is very strong in $Ba(Fe,Co)_2As_2$ even above T_s, but it is either very weak or absent in FeSe. Nevertheless, the shear-modulus softening of the two systems is very similar. Hence, a similar scaling of $1/T_1T$ and C_{66} is not likely to work in FeSe, despite of the uncertainty in the choice of the background for $1/T_1T$. It is clear that the magnetic transition is much closer to T_s in $Ba(Fe,Co)_2As_2$

than in FeSe. The latter system is simply close to a magnetic instability but does not exhibit static magnetic order at finite temperature. In this case, the scaling does not need to work even within the spin-nematic theory because the approximations that lead to eq. 4.40 are not satisfied [99]. However, one might nevertheless expect some enhancement of $1/T_1T$ above T_s if it were related to the softening.

In the orbital scenario [73], magnetic order is a secondary effect and is made possible by the structural transition. Indeed the enhancement of $(1/T_1T)_{inter}$, i.e., of spin fluctuations, in FeSe seems to set at the structural transition (Fig. 5.17), which suggests that the orbital scenario is a good description of FeSe. However, an increase of spin fluctuations at T_s is naturally also expected in the spin-nematic scenario. For a definite conclusion, one would need to have certainty of the background $(1/T_1T)_{intra}$ contribution. Nevertheless, the direct comparison of underdoped $Ba(Fe,Co)_2As_2$ and FeSe suggests the qualitative difference of the two systems.

5.4. Conclusions

FeSe has several, for iron-based superconductors, unique properties. One of these is that the structural tuning parameter is the in-plane area and not the c/a ratio. This results in a high initial sensitivity of T_c to hydrostatic pressure.

Even more fascinating is the highly unusual phase interplay of orthorhombic distortion, superconductivity and magnetic fluctuations. The obtained results and their comparison with underdoped $Ba(Fe,Co)_2As_2$ are summarized in Fig. 5.20. First, the temperature dependence of the soft elastic mode C_{66} is found to be practically identical in FeSe and underdoped $Ba(Fe,Co)_2As_2$ of the same T_s. In a Landau model, this implies that the coupling between the lattice and a putative electronic nematic order parameter that drives the softening has the same value in the two systems. Second, the coupling between orthorhombic distortion and the superconducting transition is at least two orders of magnitude smaller in FeSe than in $Ba(Fe,Co)_2As_2$ with comparable T_c and T_s values. Finally, there is no clear signature of magnetic fluctuations above T_s in FeSe, and T_1 follows the Korringa relation, which is in strong contrast to $Ba(Fe,Co)_2As_2$. Hence, magnetic fluctuations are an unlikely driving force for the orthorhombic distortion in FeSe. It might be suggested that the orthorhombic transition is a condition for their development, instead.

The clear differences with respect to underdoped $Ba(Fe,Co)_2As_2$ certainly put the applicability of the spin-nematic scenario to magnetic fluctuations, orthorhombic distortion and superconductivity in FeSe into question. However, whether the

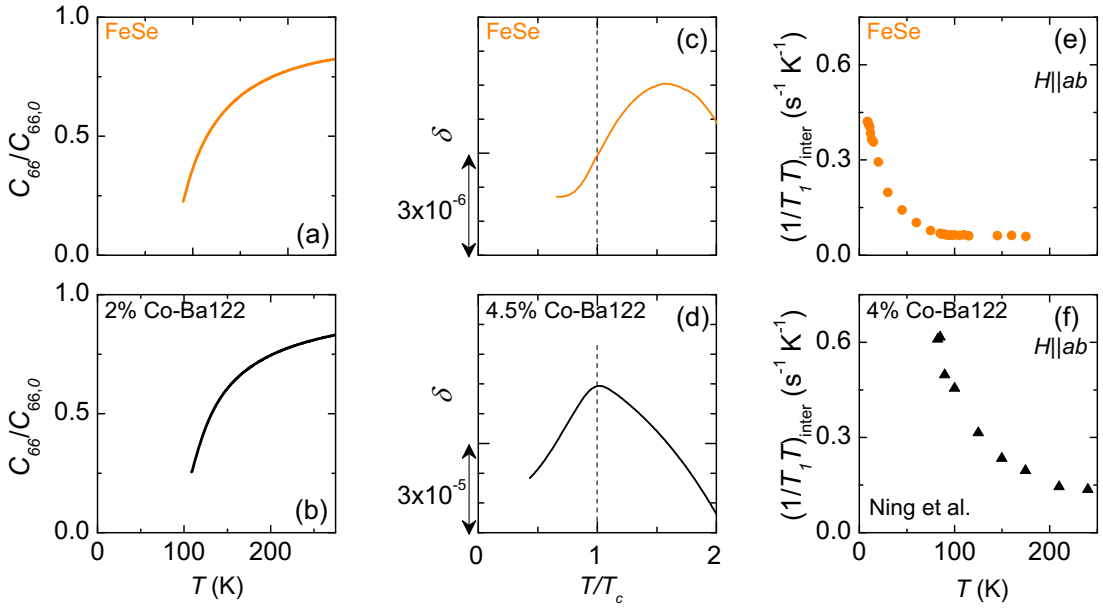

Figure 5.20.: (a), (b) Shear modulus softening $C_{66}/C_{66,0}$, (c),(d) response of the orthorhombic distortion δ at T_c and (e),(f) spin-fluctuation contribution $(1/T_1T)_{inter}$ in FeSe and underdoped $Ba(Fe,Co)_2As_2$, respectively. While the temperature dependence of C_{66} is very similar in the two systems, the reduction of δ below T_c as well as the spin-fluctuation contribution to $1/T_1$ above T_s are only pronounced in $Ba(Fe,Co)_2As_2$.

orbital scenario is applicable to FeSe also remains to be established. The question why the structural soft mode behaves identically in FeSe and underdoped $Ba(Fe,Co)_2As_2$ needs to be answered. Furthermore, it is puzzling why the orthorhombic distortion does not compete with superconductivity in FeSe in the same manner as it does in the 122 systems, if the same electrons are responsible for structural distortion and superconductivity. Further studies are necessary to address these questions.

6. Summary and conclusions

This thesis has presented an in-depth study of competing phases in iron-based superconductors based on thermodynamic measurements. The interplay of structural distortion, nematicity, magnetic order, magnetic fluctuations and, last but not least, superconductivity in substituted $BaFe_2As_2$ and in FeSe has been investigated using high-resolution thermal-expansion and shear-modulus measurements.

A detailed investigation of the phase diagram of single-crystalline $(Ba,K)Fe_2As_2$ revealed a tiny pocket of a previously unknown, presumably tetragonal, phase very close to the point where the stripe-type magnetic state is suppressed by K substitution. Strong competition between this stripe-type magnetic state and superconductivity has been demonstrated by the significant reduction of the orthorhombic order parameter below T_c. Detailed information about pressure effects in the superconducting state could be obtained by an analysis of the thermal-expansion data in a two-band alpha-model, which was conducted in this work for the first time. We compared different chemical substitutions which tune these phases starting from the parent compound $BaFe_2As_2$, namely Co, Ni, P, and K substitution, with uniaxial pressure. This motivated us to draw a phase diagram that exhibits two superconducting domes, with K substitution on one side and P, Co, and Ni substitution on the other side. Then, roughly, the application of uniaxial pressure corresponds to a shift of the whole phase diagram, the c/a ratio being an important structural parameter. Looking more closely, however, K substitution is found to be qualitatively different from uniaxial pressure. In particular, uniaxial pressure not only shifts the superconducting dome of $(Ba,K)Fe_2As_2$, but also changes the maximum T_c. Further, K substitution and uniaxial pressure are found to have opposite effects on the Sommerfeld coefficient γ of the highly correlated state at $60\% - 100\%$ K content. In contrast, Co substitution and uniaxial pressure were shown to be very much equivalent concerning their effects on T_c and γ.

Having emphasized that K and Co substitution in $BaFe_2As_2$ are quite different, we studied the structurally distorted phase and its soft mode, the elastic shear modulus C_{66}, in $Ba(Fe,Co)_2As_2$ and $(Ba,K)Fe_2As_2$ in the second part of this work. Conventional ultrasound measurements cannot be performed for the $(Ba,K)Fe_2As_2$ system because sufficiently large and perfect single crystals are not available. Instead, we have used the novel technique of high-resolution three-

point bending in a capacitance dilatometer, which yields the Young modulus of the material under study. A method for quantitative analysis of the bending data has been developed and necessary calibration measurements have been performed. Comparing results on $Ba(Fe,Co)_2As_2$ with a previous ultrasound study shows that, in the correct sample orientation, the temperature dependence of the obtained Young modulus is given by the temperature dependence of C_{66}. Hence, the temperature dependence of C_{66} of $(Ba,K)Fe_2As_2$ could be obtained for the first time. Using a Landau formalism in which an electronic order parameter, necessarily "nematic" (i.e., it breaks the four-fold rotational symmetry), drives the structural transition, the nematic susceptibility is obtained from shear-modulus data. An analysis of its doping and temperature dependence suggests quantum critical behavior only for the $Ba(Fe,Co)_2As_2$ system, while possibly a first-order transition between orthorhombic-magnetic and tetragonal ground states on increasing K content preempts quantum criticality in $(Ba,K)Fe_2As_2$. Curiously, the latter system has the higher T_c, indicating that quantum criticality is not a necessary condition for high-temperature superconductivity in the iron-based materials. A relation between the T_c value and the maximum of the nematic susceptibility is suggested for overdoped samples of both $(Ba,K)Fe_2As_2$ and $Ba(Fe,Co)_2As_2$. Finally, using the spin-nematic model, in which the nematic order parameter represents the anisotropy of spin fluctuations, we compared spin-lattice relaxation rate and shear-modulus softening of $Ba(Fe,Co)_2As_2$. A priori, these two quantities probe different properties—magnetic fluctuations versus elastic stiffness—but we found that the predicted relation between them is well satisfied. This finding represents strong evidence that the structural transition of $Ba(Fe,Co)_2As_2$ is driven by magnetic fluctuations.

In the final chapter, we investigated FeSe, the iron-based superconductor with the simplest crystallographic structure, and with the arguably the largest pressure effects. In the context of the above, FeSe is of great interest because it exhibits a large region of an orthorhombic-paramagnetic, i.e., potentially nematic, phase and does, in fact, not order magnetically at ambient pressure. Thermal-expansion measurements revealed that superconductivity and orthorhombic distortion do not compete in FeSe the way they do in $(Ba,K)Fe_2As_2$ or $Ba(Fe,Co)_2As_2$. This suggests already a major difference between the two systems. We then proceeded to measure the anisotropic Knight shift and the spin-lattice relaxation rate in FeSe using NMR. The results show that FeSe is in close proximity to a magnetic instability. However, in strong contrast to $Ba(Fe,Co)_2As_2$, no evidence for enhanced spin fluctuations in the tetragonal phase was found in FeSe. Further, the anisotropy of fluctuating magnetic fields in the orthorhombic-paramagnetic phase of FeSe was shown to be different from the orthorhombic-paramagnetic phase of LaFeAsO. This suggests that the "nematic order parameter" of FeSe is

likely not related to spin fluctuations. Intriguingly, the shear-modulus softening and the associated susceptibility in underdoped $Ba(Fe,Co)_2As_2$ and FeSe seems to be identical nevertheless.

This study has highlighted the importance and the benefit of studying and comparing various iron-based systems. Several non-universal properties among these materials have been emphasized. In particular, why do superconductivity and orthorhombic distortion compete in substituted $BaFe_2As_2$, but not in FeSe, and why does the origin of the structural transition in FeSe seem to be different from the other systems? These issues will be interesting questions for future study. On the other hand, we have encountered many common properties of the iron-based materials. All studied systems exhibit a structural distortion, magnetism or magnetic fluctuations, and superconductivity, and are highly sensitive to (uniaxial) pressure. In summary, our high-resolution thermodynamic investigations have contributed to a better understanding of the relationship between different phases and systems of the iron-based materials.

A. Multiband analysis of the thermal expansion of $Ba(Fe,Co)_2As_2$

in this chapter, the thermal-expansion data of superconducting $Ba(Fe,Co)_2As_2$ from Ref. [11] are analyzed using the two-band alpha-model (see section 3.3.3). For the analysis, it is necessary to analyze the specific heat in the same two-band model first. Such a study of the electronic specific heat of $Ba(Fe,Co)_2As_2$ is given in Ref. [49]. Surprisingly, it was found that the C^{el}/T does not extrapolate to zero at low temperature, as would be expected for a regular superconductor. Instead the data suggest, at first sight, that a fraction of the material remains normal at low temperatures. In consequence, a model in which the specific heat is a sum of a contribution from normal quasiparticles plus the contribution from (several) superconducting bands has been applied. However, the residual density of states at low temperature presumably arises from the substituted Co which acts as a pair-breaking impurity. This means that, in principle, the above model is too simple and the residual density of states is really a part of the superconducting bands. As explained in Ref. [46], it may nevertheless give a reasonable description of the $Ba(Fe,Co)_2As_2$ system.

Fig. A.1 summarizes the findings of Ref. [49] from the specific heat of the $Ba(Fe,Co)_2As_2$ series ($0 < x < 15\%$). The total density of states γ_{tot} is peaked at 6% Co content. It is divided into three contributions according to the model outlined above. γ_r is the density of states which remains ungapped at zero temperature. It is highest at the endpoints of the superconducting dome. The remaining γ is divided into the two contributions γ_1 and γ_2, which carry the gaps Δ_1 and Δ_2, respectively. The index 1 corresponds to the smaller gap. The relative weight of band 1 is $\gamma_1/(\gamma_1 + \gamma_2)$ and varies only slightly with doping. The relevant parameters for the five superconducting samples of Ref. [11] are interpolated and also shown in Fig. A.1.

According to the model explained in section 3.3.3, the thermal expansion of such a superconductor is determined by the following six parameters: γ_1, γ_2, γ_r,

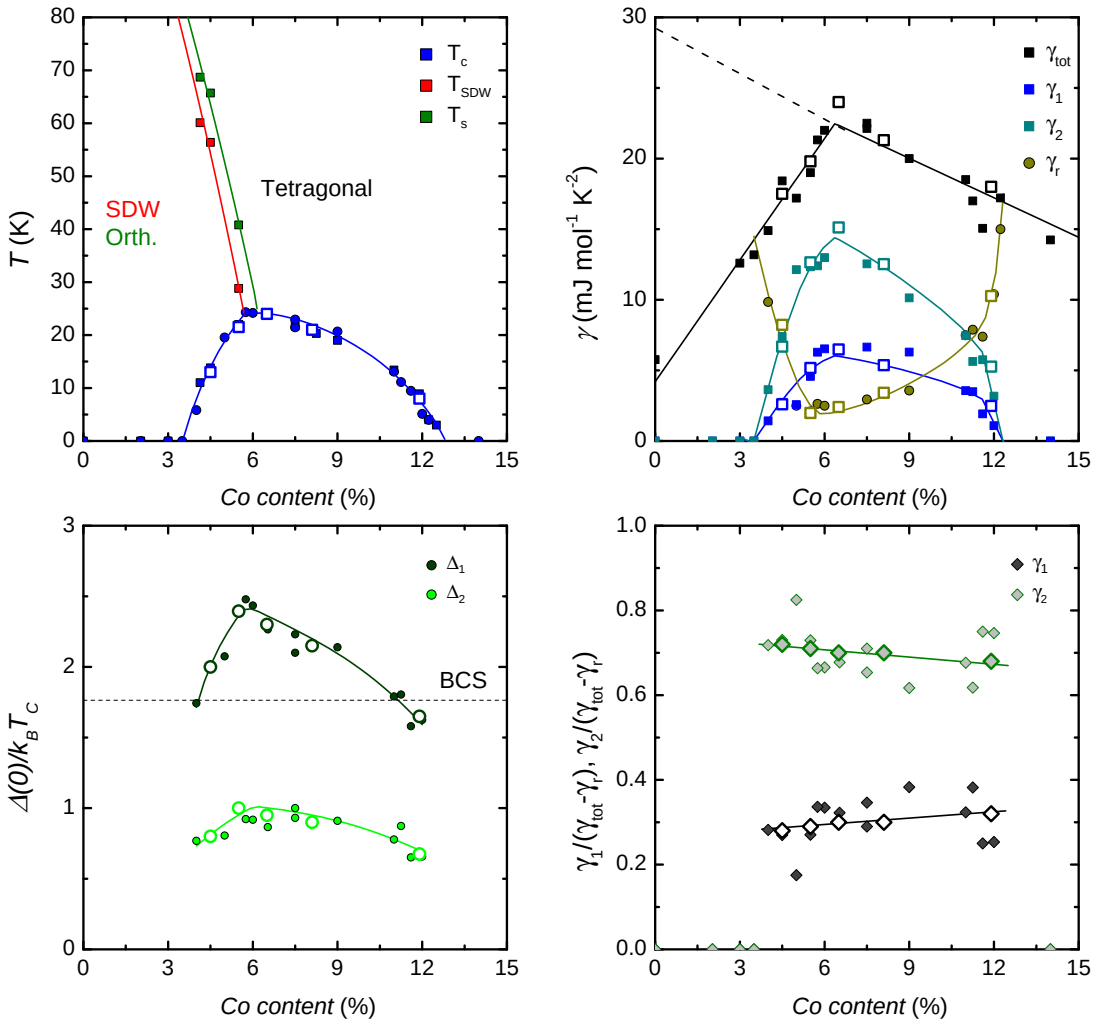

Figure A.1.: Parameters from two-band analysis of the specific heat of $Ba(Fe,Co)_2As_2$ [49]. (a) shows the transition temperatures, (b) the density of states and its division into three contributions, (c) the size of the superconducting gaps and (d) the relative weight of the superconducting bands. Values for the five samples whose thermal expansion is analyzed here, are interpolated and shown as open symbols. Lines are a guide to the eye. Their derivative with respect to Co substitution is shown in Fig. 3.27.

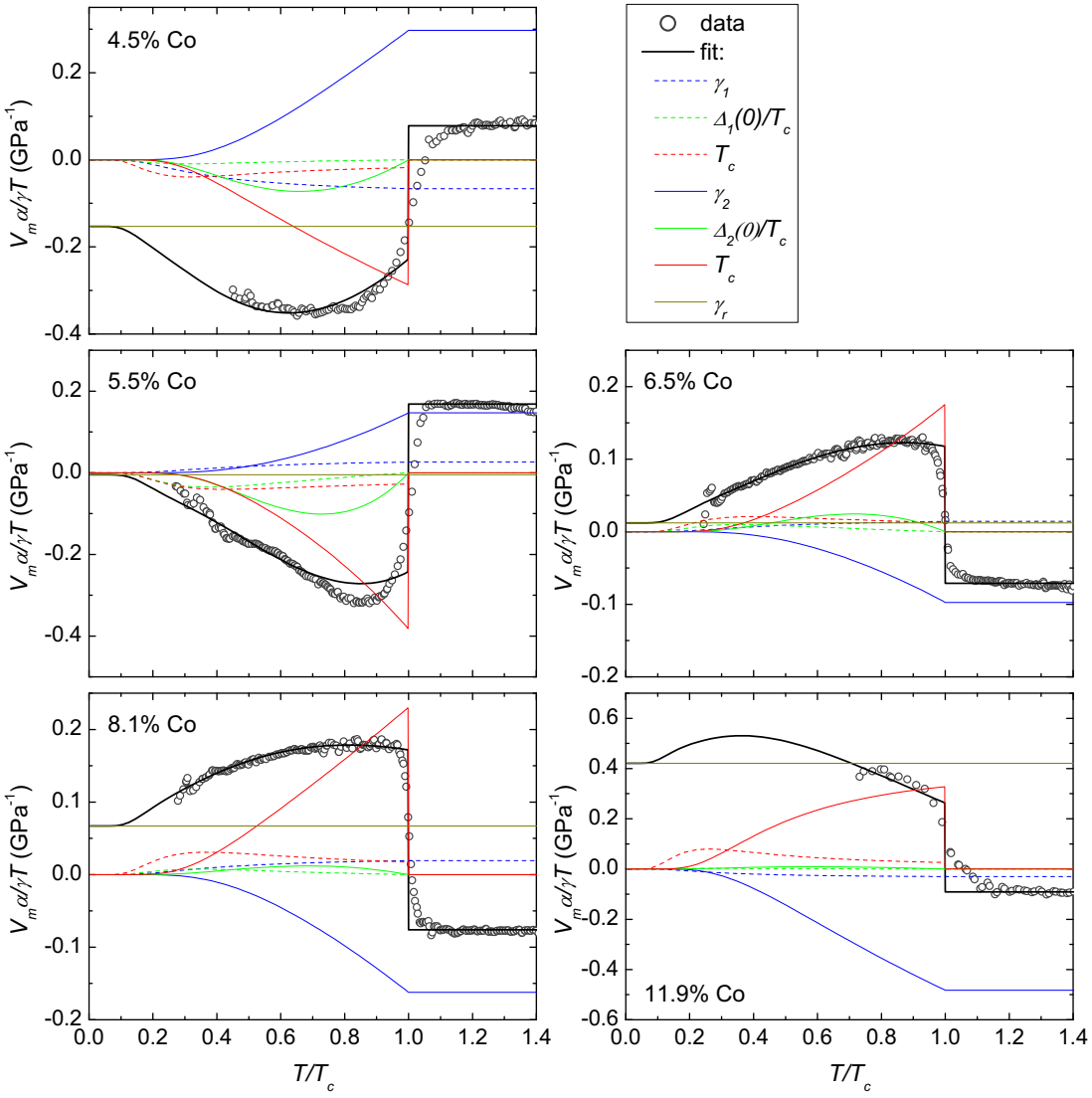

Figure A.2.: Two-band analysis of the thermal-expansion coefficients of superconducting $Ba(Fe,Co)_2As_2$. Data are taken from Ref. [11] and the parameters T_c, γ_1, γ_2, γ_r, $\Delta_1(0)/T_c$, $\Delta_2(0)/T_c$ are taken from Fig. A.1. Their logarithmic pressure derivatives are proportional to the calculated contributions shown as colored lines (labeled as in Fig. 3.18) and were adjusted. They are shown in Fig. A.3.

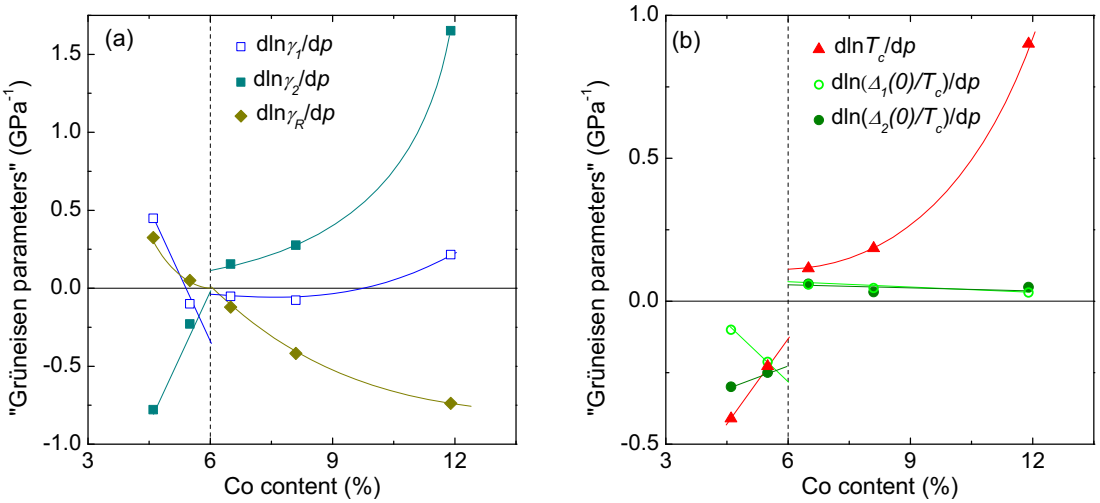

Figure A.3.: Logarithmic uniaxial-pressure derivative, which is the Grüneisen parameter except for a compressibility factor, of (a) γ_1, γ_2 and γ_r and (b) T_c, $\Delta_1(0)/T_c$ and $\Delta_2(0)/T_c$ of $Ba(Fe,Co)_2As_2$. Lines are a guide to the eye.

$\Delta_1(0)/T_c$, $\Delta_2(0)/T_c$ and T_c (taken from Fig. A.1) and their pressure derivative. The condition

$$\frac{d\gamma_1}{dp} + \frac{d\gamma_2}{dp} + \frac{d\gamma_r}{dp} = \frac{d\gamma_{tot}}{dp} = \frac{V_m \alpha_N^{el}}{\gamma_{tot} T} \tag{A.1}$$

on the normal-state value of the electronic thermal expansion α_N^{el} adds one constraint. One may caution that the coexistence with the spin-density-wave in the underdoped side of the phase diagram has been neglected. In principle, it will add more contributions to the pressure dependence of the entropy. However, since the main effect effect of the SDW is to reduce the density of state, we assume that its effect will be approximately included in the $d\gamma_i/dp$-terms.

The electronic thermal expansion of $Ba(Fe,Co)_2As_2$, obtained from subtracting data of the $Ba(Fe_{0.67}Co_{0.33})_2As_2$ sample as a phonon background, was presented in Ref. [11]. The data was normalized by γ_{tot}/V_m and the curves were adjusted in a least-squares fit using 5 parameters (Fig. A.3). Since the curves have less features in $Ba(Fe,Co)_2As_2$ than in $(Ba,K)Fe_2As_2$, several sets of parameters yield satisfactory fits for some of the compositions. $d\ln\gamma_r/dp$ is uniquely determined by the low-temperature limit of α^{el}, where data at sufficiently low temperature is available. dT_c/dp can also be determined relatively reliably because it determines exclusively the discontinuity of α at T_c. However, especially in the underdoped samples, the size of this discontinuity cannot be clearly read off the curves. This

is because of the most prominent feature of the curves, namely their 'rounded' shape, which is particularly pronounced on the underdoped side. It indicates that the pressure derivative of the coupling strength $d(\Delta_2(0)/T_c)/dp$ is quite large.

Fig. A.2 shows the data with the adjusted curves. For the presentation, the thermal expansion is split into seven contributions, in analogy to Fig. 3.22. The term proportional to $d\ln\gamma_r/dp$ is temperature independent within the model because it represents the thermal expansion of Fermi-liquid-like normal electrons. It is largest at very low and very high Co content. The thermal-expansion of the overdoped samples is dominated by the $d\ln T_c/dp$ term and the contribution from $d\ln\gamma_2/dp$, which grows at higher Co content. Further, the derivatives of $\Delta_1(0)/T_c$ and $\Delta_2(0)/T_c$ are also important to reproduce the data. The fit is less satisfactory for the sample with 5.5% Co content, which may be because T_N is only slightly higher than T_c and the spin-density-wave gap presumably contributes to the thermal expansion in a more complicated way than simply by changing $d\gamma/dp$. Fig. A.3 summarizes the obtained parameters. Fig. 3.27 in the main text shows a comparison of the obtained logarithmic pressure derivatives with the corresponding doping derivatives.

B. Elements of elasticity theory

Elastic strain describes the deformation of a body with respect to a reference state. Mathematically, a transformation from the reference state to the deformed state can be described by $\vec{r'} = \vec{r} + \vec{u}\,(\vec{r})$, where $\vec{u}$ is a deplacement vector (Fig. B.1(a)). This corresponds to a strain

$$\varepsilon_{ij} = \frac{1}{2}\left(\frac{du_i}{dr_j} + \frac{du_j}{dr_i}\right). \tag{B.1}$$

ε is a tensor of the second order. Only small transformations in an orthogonal coordinate system will be considered here. The thermodynamically conjugate variable to strain is stress,

$$\sigma_{ij} = \frac{dF}{d\varepsilon_{ij}}, \tag{B.2}$$

with F the free energy. The component σ_{ij} of the stress tensor indicates the density of (internal) contact forces directed along direction i, acting on a surface element of normal direction j (see Fig. B.1(b)). Its sign is such that traction normal to a surface is positive and therefore opposite to uniaxial pressure. The stiffness tensor C is a forth-rank tensor and relates stress and strain

$$\sigma_{ij} = C_{ijkl}\varepsilon_{kl}. \tag{B.3}$$

The inverse of the stiffness tensor is the elastic compliance $S = C^{-1}$. Since strain and stress are thermodynamically conjugate variables, it follows from the B.3 that

$$C_{ijkl} = \frac{d^2F}{d\varepsilon_{ij}d\varepsilon_{kl}} \tag{B.4}$$

and $C_{ijkl} = (d\varepsilon_{kl}/d\sigma_{ij})^{-1}$ is an inverse susceptibility.

ε is symmetric by definition and σ has to be symmetric in order to guarantee the balance of torque moments (Cauchy's second theorem). Therefore, both have

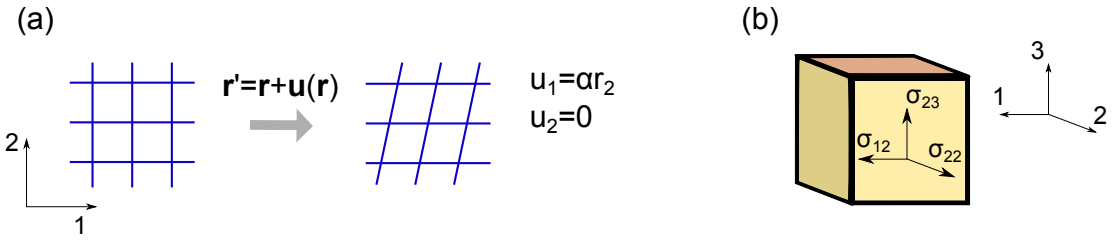

Figure B.1.: (a) A shear transformation as an example for a deformation. Only the strain component $\varepsilon_{12} = \alpha/2$ (ε_6 in the Voigt notation) is non-zero in this case. (b) Components of the stress tensor, acting on the surface with normal direction '2'.

six independent elements which can arranged into a kind of vector according to the following rule (Voigt notation)

$$\begin{aligned} 11 &\to 1 \\ 22 &\to 2 \\ 33 &\to 3 \\ 23 &\to 4 \\ 13 &\to 5 \\ 12 &\to 6 \end{aligned} \tag{B.5}$$

In this representation, the C is a symmetric 6×6-matrix with 21 independent components. These components are called elastic constants. Crystal symmetry imposes further constraints, so that, e.g., for an orthorhombic system, only nine independent elastic constants are possible [14]

$$\begin{pmatrix} \sigma_1 \\ \sigma_2 \\ \sigma_3 \\ \sigma_4 \\ \sigma_5 \\ \sigma_6 \end{pmatrix} = \begin{pmatrix} C_{11} & C_{12} & C_{13} & 0 & 0 & 0 \\ C_{12} & C_{22} & C_{23} & 0 & 0 & 0 \\ C_{13} & C_{23} & C_{33} & 0 & 0 & 0 \\ 0 & 0 & 0 & C_{44} & 0 & 0 \\ 0 & 0 & 0 & 0 & C_{55} & 0 \\ 0 & 0 & 0 & 0 & 0 & C_{66} \end{pmatrix} \begin{pmatrix} \varepsilon_1 \\ \varepsilon_2 \\ \varepsilon_3 \\ \varepsilon_4 \\ \varepsilon_5 \\ \varepsilon_6 \end{pmatrix}. \tag{B.6}$$

14. To show one example, we consider the mirror operation perpendicular to the '3' axis: The '4' and '5' component of ε and σ change sign under this operation while the other components are unaffected. Writing out $\sigma_1 = C_{11}\varepsilon_1 + C_{12}\varepsilon_2 + C_{13}\varepsilon_3 + C_{14}\varepsilon_4 + C_{15}\varepsilon_5 + C_{16}\varepsilon_6$, which changes under the mirror operation to $\sigma_1 = C_{11}\varepsilon_1 + C_{12}\varepsilon_2 + C_{13}\varepsilon_3 - C_{14}\varepsilon_4 - C_{15}\varepsilon_5 + C_{16}\varepsilon_6$, shows that $C_{14} = C_{15} = 0$ if the system contains such a mirror plane. The presence of this symmetry plane actually imposes $C_{i,4} = C_{i,5} = 0$ for $i \neq 4, 5$.

The Young's modulus Y is defined as the ratio between the amount of applied uniaxial stress and induced strain along the same direction, i.e., the elastic modulus for uniaxial tension. The definition makes it clear that Y corresponds to a component of the compliance matrix $Y_i = (S_{ii})^{-1}$. It is the material property which determines, e.g., the stiffness of a compression spring.

C. List of samples

C.1. (Ba,K)Fe_2As_2

Table C.1.: List of measured samples of $Ba_{1-x}K_xFe_2As_2$. The columns indicate the batch name, the K content in the starting composition of the growth (nominal $x = 0 - 1$), the sample name, the K content x of the sample and the method with which the K content was determined (4-circle=structural refinement of 4-circle x-ray diffraction data; EDX=energy dispersive x-ray spectroscopy; phase diag (T_c, T_s)=estimated from comparing the transition temperatures T_c or T_s to the phase diagram Fig. 3.11). Further, the measurements performed on the sample (α_i=thermal expansion along i, 3PB=Young's modulus measurement using three-point bending, C_p=specific heat, χ=magnetic susceptibility; bold symbols indicate results presented in this work) are given. In the comment, the symbols $\oplus$, $\odot$, $\ominus$ indicate a rating of the quality of the sample (sharp vs. broad transitions, whether transition temperatures fit well into the phase diagram and whether the shape of thermal-expansion curve fits into the systematic evolution with K substitution). Samples rated $\oplus$ or $\odot$ were included in the phase diagram Fig. 3.11, if their K content was determined independently.

batch	nominal x	sample	x	method	measurements	comment
TWOX950	0.35	TW950#1			α_a	$\ominus$ FeAs impurity phase
		TW950#3	0.362(12)	4-circle	α_a	$\oplus$
		TW950#4			α_a, C_p, α_c	$\ominus$ slight double transition
TWOX956	0.29	TW956#1	0.33(1)	EDX	α_a	$\ominus$ unusual transition shape
		TW956#2	0.386(3)	4-circle	α_a	$\ominus$ T_c too low, unusual shape
TWOX964	0.40	TW964#1			α_a	$\ominus$ unusual transition
		TW964#2	0.42(1)	EDX	α_a	$\oplus$
		TW964#3	0.514(2)	4-circle	$\boldsymbol{\alpha_a}$, α_c, $\mathbf{C_p}$,...	$\oplus$ sample of Ref. [41]

TWOX979	0.16		0.32	4-circle	$\alpha_a, ...$	$\ominus$ T_s, T_s far too low, 6 samples checked
TWOX987	0.65	TW987#1	0.46(1)	EDX	α_a	$\oplus$
		TW987#2	0.519(4)	EDX	$\boldsymbol{\alpha_a}$	$\ominus$ slight double transition
TWOX1000	0.087	TW1000#1			α_b	$\oplus$
TWOX1005	0.8	TW1005#1				$\ominus$ very strange shape
TWOX1015	0.14	TW1015#1			α_b	$\ominus$ broad transition
		TW1015#2	0.165(4)	4-circle	α_b	$\oplus$
		TW1015#3			α_c	$\ominus$
		TW1015#4			α_{ab}	$\ominus$ shape of elastic anomaly
TWOX1021	0.18	TW1021#1	0.223(4)	4-circle	α_{ab}	$\oplus$
		TW1021#2			α_c	$\oplus$
		TW1021#2B	0.250(5)	4-circle	$\boldsymbol{\alpha_{ab}}$, $\boldsymbol{\alpha_b}$	$\oplus$ piece of #2
		TW1021#3	0.252(4)	4-circle	α_{ab},	$\ominus$ no T_c!
		TW1021#4	0.215(10)	phase diag (T_s, T_c)	$\boldsymbol{\alpha_c}$	$\oplus$
		TW1021#5	0.2(1)	phase diag (T_c)	**3PB**	$\oplus$
TWOX1034	0.24	TW1034#1	0.303(4)	4-circle	$\boldsymbol{\alpha_a}$, **3PB**,$\mathbf{C_p}$	$\oplus$
		TW1034#2	0.315(10)	EDX	T_c (ac-suscept)	$\oplus$
		TW1034#3	0.35(1)	phase diag (T_c)	**3PB**, α_a	$\oplus$
TWOX1040	0.2	TW1040#1			α_b	$\ominus$ strange transitions
TWOX1040	0.2	TW1040#2			α_b	$\ominus$ strange transitions
TWOX1058	0.26	TW1058#1	0.444(3)	4-circle	α_a	$\oplus$
TWOX1074	0.4	TW1074#1	0.361(5)	4-circle	$\boldsymbol{\alpha_c}$	$\oplus$
		TW1074#2	0.35(1)	EDX	$\boldsymbol{\alpha_a}$	$\oplus$
		TW1074#3	0.35(1)	phase diag (T_c)	3PB,α_a, $\mathbf{C_p}$	$\oplus$
TWOX1075	0.16	TW1075#1	0.215(1)	EDX	$\boldsymbol{\alpha_b}$	$\oplus$
		TW1075#2			α_c	$\oplus$
		TW1075#3	0.225(5)	phase diag (T_s, T_c)	$\boldsymbol{\alpha_{ab}}$, $\mathbf{C_p}$	$\oplus$
		TW1075_3M	0.22(1)	phase diag (T_c)	**3PB**	$\oplus$
		TW1075#4	0.22(1)	phase diag (T_c)	$\boldsymbol{\alpha_{ab}}$	$\oplus$
TWOX1081	0.5	TW1081#1				$\ominus$ very strange shape
TWOX1083	0.6	TW1083#1	0.48(2)	EDX	$\boldsymbol{\alpha_a}$, **3PB**	$\oplus$
TWOX1088	0.7	TW1088#1	0.42(10)	EDX	$\boldsymbol{\alpha_a}$,$\mathbf{C_p}$	$\oplus$
		TW1088#2	0.626	4-circle	α_a	$\ominus$ very broad T_c

TWOX1091	0.8	TW1091#2	0.627(2)	4-circle	α_a	$\ominus$ very broad T_c
		TW1091#3	0.589(3)	4-circle	α_a, $\mathbf{C_p}$	$\oplus$
		TW1091#3	0.60(1)	phase diag (T_c)	$\boldsymbol{\alpha_a}$, **3PB**, C_p	$\oplus$
TWOX1094	0.12	TW1094#1	0.166(6)	4-circle	$\boldsymbol{\alpha_b}$, $\mathbf{C_p}$	$\oplus$
		TW1094#2	0.155(10)	EDX	**3PB**	$\oplus$
TWOX1049	1				α_a, α_c, C_p, ...	$\oplus$ pure K122
TWOX1130	1	TW1130#5			α_c, C_p, ...	$\oplus$ pure K122
TWOX1165	0.95	TW1165#1	0.765(4)	4-circle	α_a	$\ominus$ very broad transition
		TW1165#2			α_a	$\ominus$ very broad transition
TWOX1181	0.98	TW1181#1	0.908(3)	4-circle	$\boldsymbol{\alpha_a}$, C_p	$\oplus$
TWOX1196	0.2	TW1196#1			α_{ab}	$\ominus$
TWOX1199	0.95	TW1199#1			α_a	$\oplus$
		TW1199#2			α_a	$\ominus$ broad transition
		TW1199#2A	0.827(2)	4-circle	$\boldsymbol{\alpha_a}$, **3PB**, $\mathbf{C_p}$	$\oplus$ piece of #2
		TW1199#2B	0.827(2)	phase diag (T_c)	$\boldsymbol{\alpha_c}$, 3PB	$\odot$ piece of #2, T_c a bit broader
		TW1199#3			3PB	$\oplus$
		TW1199_0.6mg	0.876(4)	4-circle	χ	
		TW1199_5.4mg	0.919(3)	4-circle	χ	
TWOX1214	0.2	TW1214#1			α_a	$\ominus$ strange double transitions
TWOX1232	0.75	TW1232#1	0.60(1)	phase diag (T_c)	$\boldsymbol{\alpha_c}$	$\odot$ $T_c \sim 3$ K broad
		TW1232#2	0.633(2)	4-circle	α_c	$\odot$ $T_c \sim 2.5$ K broad
TWOX1285	0.21	TW1285#1			α_{ab}	$\odot$ shows T_s,T_1, T_2
		TW1285#2			α_{ab}	$\ominus$ presumably two-phase sample
TWOX1307	0.22	TW1307#1			α_a	$\ominus$ broad T_c
		TW1307#2			α_{ab}	$\odot$ shows T_s,T_1, T_2
		TW1307#3	0.282(3)	4-circle	$\boldsymbol{\alpha_a}$	$\oplus$ tetragonal ground state
		TW1307#6	0.262(3)	4-circle	$\boldsymbol{\alpha_{ab}}$, $\boldsymbol{\alpha_b}$, $\mathbf{C_p}$, $\boldsymbol{\chi}$	$\oplus$
		TW1307#7	0.276(3)	4-circle	α_{ab}, $\boldsymbol{\alpha_b}$, χ	$\oplus$
		TW1307#9			α_b	$\odot$ shows T_s,T_1, T_2
		TW1307#13			α_b	$\odot$ somewhat broad T_s,T_1, T_2
		TW1307#15-I			α_{ab}, α_c, C_p	$\oplus$
TWOX1321	0.215	TWOX1321#1			α_b	$\oplus$

C.2. TM-substituted $BaFe_2As_2$ (TM=Co, Mn, Ni)

Table C.2.: List of transition-metal substituted $BaFe_2As_2$ samples, mainly used for three-point bending measurements. The columns indicate the batch name, the Co content, the method with which is was determined (EDX=energy-dispersive x-ray spectroscopy; distribution coefficient=from the composition of the starting materials together with the known distribution coefficient; phase diagram=from the transition temperatures in comparison with the phase diagram), the measurements which were performed on the samples and a comment.

batch	TM content	method	measurements	comment
TWOX879	0%		3PB,α_a,α_c	batch of Ref. [11]
TWOX800	2%Co	distribution coefficient	3PB,α_{ab}	batch of Ref. [11]
TWOX1128	4.3%	distribution coefficient	3PB,α_{ab}	
TWOX864	5%	EDX+phase diagram	3PB,α_{ab}, α_b	
TWOX1025	6%	phase diagram	3PB,α_a, α_b	
TWOX856	9%	distribution coefficient	3PB, α_a	
TWOX841	11.9%	distribution coefficient	3PB,α_a	batch of Ref. [11]
TWOX1057	6.9%Co+1.9%Mn	EDX	3PB,α_a,α_c, C_p	
TWOX1126	2.7%Ni	EDX	α_a	
TWOX1131	5%Ni	EDX	α_a	

C.3. FeSe

Table C.3.: List of studied FeSe samples. The columns indicate the batch name, the sample name, the composition and structural parameters a, c and z, determined from 4-circle x-ray refinement, the measurements performed and a comment. Structural refinement could not done on the same samples on which the measurements were performed because the material is very easily deformed.

batch	sample	composition	a (Å)	c (Å)	z	measurements	comment
TWOX1200		$Fe_{0.995(4)}Se_1$	3.7727(13)	5.523(2)	0.26668(9)	α, χ	batch of Ref. [44]
TWOX1200	TW1200#1					α_{ab}	
TWOX1200	TW1200#2					α_b	
TWOX1200	TW1200#3					α_c	
TWOX1220		$Fe_{0.994(5)}Se_1$	3.7725(30)	5.5204(30)	0.26683(10)		
TWOX1220	TW1220#1					α_{ab}, α_b	
TWOX1229						K, T_1	batch used for NMR
TWOX1229	TW1229#1					α_{ab}	
TWOX1277	TW1277#1					α_{ab}	
TWOX1277	TW1277#2					α_{ab}, C_p	mass=4.11 mg
TWOX1295		$Fe_{0.9933(40)}Se_1$	3.7728(14)	5.526(6)	0.26691(9)		
TWOX1295	TW1295#1					α_{ab}	
TWOX1295	TW1295#2					3PB	

List of Figures

Bibliography

[1] Y. Kamihara, T. Watanabe, M. Hirano, and H. Hosono, "Iron-based layered superconductor La[$O_{1-x}F_x$]FeAs ($x = 0.05-0.12$) with $T_c = 26$ K," Journal of the American Chemical Society **130**, 3296–3297 (2008).

[2] M. Putti, I. Pallecchi, E. Bellingeri, M. R. Cimberle, M. Tropeano, C. Ferdeghini, A. Palenzona, C. Tarantini, A. Yamamoto, J. Jiang, J. Jaroszynski, F. Kametani, D. Abraimov, A. Polyanskii, J. D. Weiss, E. E. Hellstrom, A. Gurevich, D. C. Larbalestier, R. Jin, B. C. Sales, A. S. Sefat, M. A. McGuire, D. Mandrus, P. Cheng, Y. Jia, H. H. Wen, S. Lee, and C. B. Eom, "New Fe-based superconductors: properties relevant for applications," Superconductor Science and Technology **23**, 034003 (2010).

[3] K. Tanabe and H. Hosono, "Frontiers of research on iron-based superconductors toward their application," Japanese Journal of Applied Physics **51**, 010005 (2012).

[4] J. ichi Shimoyama, "Potentials of iron-based superconductors for practical future materials," Superconductor Science and Technology **27**, 044002 (2014).

[5] J. Paglione and R. L. Greene, "High-temperature superconductivity in iron-based materials," Nature Physics **6**, 645–658 (2010).

[6] D. C. Johnston, "The puzzle of high temperature superconductivity in layered iron pnictides and chalcogenides," Advances in Physics **59**, 803–1061 (2010).

[7] G. R. Stewart, "Superconductivity in iron compounds," Rev. Mod. Phys. **83**, 1589–1652 (2011).

[8] Y. J. Uemura, "Superconductivity: Commonalities in phase and mode," Nat Mater , 253–255 (2009).

[9] R. M. Fernandes, A. V. Chubukov, and J. Schmalian, "What drives nematic order in iron-based superconductors?" Nature Physics **10**, 97–104 (2014).

[10] R. M. Fernandes, L. H. VanBebber, S. Bhattacharya, P. Chandra, V. Keppens, D. Mandrus, M. A. McGuire, B. C. Sales, A. S. Sefat, and J. Schmalian, "Effects of nematic fluctuations on the elastic properties of iron arsenide superconductors," Phys. Rev. Lett. **105**, 157003 (2010).

[11] C. Meingast, F. Hardy, R. Heid, P. Adelmann, A. Böhmer, P. Burger, D. Ernst, R. Fromknecht, P. Schweiss, and T. Wolf, "Thermal expansion and Grüneisen parameters of $Ba(Fe_{1-x}Co_x)_2As_2$ - a thermodynamic quest for quantum criticality," Phys. Rev. Lett. **108**, 177004 (2012).

[12] A. E. Böhmer, P. Burger, F. Hardy, T. Wolf, P. Schweiss, R. Fromknecht, H. v. Löhneysen, C. Meingast, H. K. Mak, R. Lortz, S. Kasahara, T. Terashima, T. Shibauchi, and Y. Matsuda, "Thermodynamic phase diagram, phase competition, and uniaxial pressure effects in $BaFe_2(As_{1-x}P_x)_2$ studied by thermal expansion," Phys. Rev. B **86**, 094521 (2012).

[13] F. Bouquet, Y. Wang, R. A. Fisher, D. G. Hinks, J. D. Jorgensen, A. Junod, and N. E. Phillips, "Phenomenological two-gap model for the specific heat of MgB_2," EPL (Europhysics Letters) **56**, 856 (2001).

[14] F.-C. Hsu, J.-Y. Luo, K.-W. Yeh, T.-K. Chen, T.-W. Huang, P. M. Wu, Y.-C. Lee, Y.-L. Huang, Y.-Y. Chu, D.-C. Yan, and M.-K. Wu, "Superconductivity in the PbO-type structure α-FeSe," Proceedings of the National Academy of Sciences **105**, 14262–14264 (2008).

[15] X. Wang, Q. Liu, Y. Lv, W. Gao, L. Yang, R. Yu, F. Li, and C. Jin, "The superconductivity at 18 K in LiFeAs system," Solid State Communications **1480**, 538 – 540 (2008).

[16] M. Rotter, M. Tegel, and D. Johrendt, "Superconductivity at 38 K in the iron arsenide $Ba_{1-x}K_xFe_2As_2$," Phys. Rev. Lett. **101**, 107006 (2008).

[17] C. Löhnert, T. Stürzer, M. Tegel, R. Frankovsky, G. Friederichs, and D. Johrendt, "Superconductivity up to 35 K in the iron platinum arsenides $(CaFe_{1-x}Pt_xAs)_{10}Pt_{4-y}As_8$ with layered structures," Angewandte Chemie International Edition **50**, 9195–9199 (2011).

[18] H. Ogino, Y. Shimizu, K. Ushiyama, N. Kawaguchi, K. Kishio, and J. ichi Shimoyama, "Superconductivity above 40 K observed in a new iron arsenide oxide $(Fe_2As_2)(Ca_4(Mg,Ti)_3O_y)$," Applied Physics Express **3**, 063103 (2010).

[19] H. Wadati, I. Elfimov, and G. A. Sawatzky, "Where are the extra d electrons in transition-metal-substituted iron pnictides?" Phys. Rev. Lett. **105**, 157004 (2010).

[20] A. S. Sefat, R. Jin, M. A. McGuire, B. C. Sales, D. J. Singh, and D. Mandrus, "Superconductivity at 22 K in Co-doped $BaFe_2As_2$ crystals," Phys. Rev. Lett. **101**, 117004 (2008).

[21] L. J. Li, Y. K. Luo, Q. B. Wang, H. Chen, Z. Ren, Q. Tao, Y. K. Li, X. Lin, M. He, Z. W. Zhu, G. H. Cao, and Z. A. Xu, "Superconductivity induced by Ni doping in $BaFe_2As_2$ single crystals," New Journal of Physics **11**, 025008 (2009).

[22] S. Sharma, A. Bharathi, S. Chandra, V. R. Reddy, S. Paulraj, A. T. Satya, V. S. Sastry, A. Gupta, and C. S. Sundar, "Superconductivity in Ru-substituted polycrystalline $BaFe_{2-x}Ru_xAs2$," Phys. Rev. B **81**, 174512 (2010).

[23] S. Jiang, H. Xing, G. Xuan, C. Wang, Z. Ren, C. Feng, J. Dai, Z. Xu, and G. Cao, "Superconductivity up to 30 K in the vicinity of the quantum critical point in $BaFe_2(As_{1-x}P_x)_2$," Journal of Physics: Condensed Matter **21**, 382203 (2009).

[24] D. Johrendt, "Structure-property relationships of iron arsenide superconductors," J. Mater. Chem. **21**, 13726–13736 (2011).

[25] C. de la Cruz, Q. Huang, J. W. Lynn, J. Li, W. R. II, J. L. Zarestky, H. A. Mook, G. F. Chen, J. L. Luo, N. L. Wang, and P. Dai, "Magnetic order close to superconductivity in the iron-based layered $LaO_{1-x}F_xFeAs$ systems," Nature **453**, 899–902 (2008).

[26] A. Cano, M. Civelli, I. Eremin, and I. Paul, "Interplay of magnetic and structural transitions in iron-based pnictide superconductors," Phys. Rev. B **82**, 020408 (2010).

[27] M. G. Kim, R. M. Fernandes, A. Kreyssig, J. W. Kim, A. Thaler, S. L. Bud'ko, P. C. Canfield, R. J. McQueeney, J. Schmalian, and A. I. Goldman, "Character of the structural and magnetic phase transitions in the parent and electron-doped $BaFe_2As_2$ compounds," Phys. Rev. B **83**, 134522 (2011).

[28] J.-H. Chu, J. G. Analytis, C. Kucharczyk, and I. R. Fisher, "Determination of the phase diagram of the electron-doped superconductor $Ba(Fe_{1-x}Co_x)_2As_2$," Phys. Rev. B **79**, 014506 (2009).

[29] D. K. Pratt, W. Tian, A. Kreyssig, J. L. Zarestky, S. Nandi, N. Ni, S. L. Bud'ko, P. C. Canfield, A. I. Goldman, and R. J. McQueeney, "Coexistence of competing antiferromagnetic and superconducting phases in the underdoped $Ba(Fe_{0.953}Co_{0.047})_2As_2$ compound using x-ray and neutron scattering techniques," Phys. Rev. Lett. **103**, 087001 (2009).

[30] S. Nandi, M. G. Kim, A. Kreyssig, R. M. Fernandes, D. K. Pratt, A. Thaler, N. Ni, S. L. Bud'ko, P. C. Canfield, J. Schmalian, R. J. McQueeney, and A. I. Goldman, "Anomalous suppression of the orthorhombic lattice distortion in superconducting $Ba(Fe_{1-x}Co_x)_2As_2$ single crystals," Phys. Rev. Lett. **104**, 057006 (2010).

[31] H. Padamsee, J. Neighbor, and C. Shiffman, "Quasiparticle phenomenology for thermodynamics of strong-coupling superconductors," Journal of Low Temperature Physics **12**, 387–411 (1973).

[32] P. G. de Gennes, *Superconductivity in metals and alloys*, edited by D. Pines (W. A. Benjamin, 1966).

[33] M. A. Simpson and T. F. Smith, "Thermal expansion in the superconducting state," Journal of Low Temperature Physics **32**, 57–65 (1978).

[34] H. R. Ott, "The volume change at the superconducting transition of lead and aluminum," Journal of Low Temperature Physics **9**, 331–343 (1972).

[35] R. Pott and R. Schefzyk, "Apparatus for measuring the thermal expansion of solids between 1.5 and 380K," Journal of Physics E: Scientific Instruments **16**, 444 (1983).

[36] C. Meingast, B. Blank, H. Bürkle, B. Obst, T. Wolf, H. Wühl, V. Selvamanickam, and K. Salama, "Anisotropic pressure dependence of T_c in single crystal $YBa_2Cu_3O_7$ via thermal expansion," Phys. Rev. B **41**, 11299–11304 (1990).

[37] P. Nagel, *Planung und Aufbau eines Hochtemperatur-Dilatometers sowie Messungen an 'normalem' und 'polymerem' C_{60}*, Diplomarbeit, Forschungszentrum Karlsruhe (1996).

[38] F. R. Kroeger and C. A. Swenson, "Absolute linear thermal-expansion measurements on copper and aluminum from 5 to 320 K," Journal of Applied Physics **48**, 853–864 (1977).

[39] M. A. Tanatar, A. Kreyssig, S. Nandi, N. Ni, S. L. Bud'ko, P. C. Canfield, A. I. Goldman, and R. Prozorov, "Direct imaging of the structural domains in the iron pnictides $A\mathrm{Fe_2As_2}$ (A=Ca,Sr,Ba)," Phys. Rev. B **79**, 180508 (2009).

[40] I. R. Fisher, L. Degiorgi, and Z. X. Shen, "In-plane electronic anisotropy of underdoped '122' Fe-arsenide superconductors revealed by measurements of detwinned single crystals," Reports on Progress in Physics **74**, 124506 (2011).

[41] H. K. Mak, P. Burger, L. Cevey, T. Wolf, C. Meingast, and R. Lortz, "Thermodynamic observation of a vortex melting transition in the Fe-based superconductor $\mathrm{Ba_{0.5}K_{0.5}Fe_2As_2}$," Phys. Rev. B **87**, 214523 (2013).

[42] P. Burger, F. Hardy, D. Aoki, A. E. Böhmer, R. Eder, R. Heid, T. Wolf, P. Schweiss, R. Fromknecht, M. J. Jackson, C. Paulsen, and C. Meingast, "Strong Pauli-limiting behavior of H_{c2} and uniaxial pressure dependencies in $\mathrm{KFe_2As_2}$," Phys. Rev. B **88**, 014517 (2013).

[43] F. Hardy, P. Adelmann, T. Wolf, H. v. Löhneysen, and C. Meingast, "Large anisotropy uniaxial pressure dependencies of T_c in single crystalline $\mathrm{Ba(Fe_{0.92}Co_{0.08})_2As_2}$," Phys. Rev. Lett. **102**, 187004 (2009).

[44] A. E. Böhmer, F. Hardy, F. Eilers, D. Ernst, P. Adelmann, P. Schweiss, T. Wolf, and C. Meingast, "Lack of coupling between superconductivity and orthorhombic distortion in stoichiometric single-crystalline FeSe," Phys. Rev. B **87**, 180505 (2013).

[45] H. Okamoto, "The Fe-Se (iron-selenium) system," Journal of Phase Equilibria **12**, 383–389 (1991).

[46] F. Hardy, T. Wolf, R. A. Fisher, R. Eder, P. Schweiss, P. Adelmann, H. v. Löhneysen, and C. Meingast, "Calorimetric evidence of multiband superconductivity in $\mathrm{Ba(Fe_{0.925}Co_{0.075})_2As_2}$ single crystals," Phys. Rev. B **81**, 060501 (2010).

[47] S. Drotziger, P. Schweiss, K. Grube, T. Wolf, P. Adelmann, C. Meingast, and H. v. Löhneysen, "Pressure versus concentration tuning of the superconductivity in $\mathrm{Ba(Fe_{1-x}Co_x)_2As_2}$," Journal of the Physical Society of Japan **79**, 124705 (2010).

[48] A. E. Böhmer, P. Burger, F. Hardy, T. Wolf, P. Schweiss, R. Fromknecht, H. von Löhneysen, C. Meingast, S. Kasahara, T. Terashima, T. Shibauchi,

and Y. Matsuda, "High-resolution thermal expansion of isovalently substituted $BaFe_2(As_{1-x}P_x)_2$," Journal of Physics: Conference Series **391**, 012122 (2012).

[49] F. Hardy, P. Burger, T. Wolf, R. A. Fisher, P. Schweiss, P. Adelmann, R. Heid, R. Fromknecht, R. Eder, D. Ernst, H. v. Löhneysen, and C. Meingast, "Doping evolution of superconducting gaps and electronic densities of states in $Ba(Fe_{1-x}Co_x)_2As_2$ iron pnictides," EPL (Europhysics Letters) **91**, 47008 (2010).

[50] C. Meingast, (unpublished).

[51] S. Avci, O. Chmaissem, E. A. Goremychkin, S. Rosenkranz, J.-P. Castellan, D. Y. Chung, I. S. Todorov, J. A. Schlueter, H. Claus, M. G. Kanatzidis, A. Daoud-Aladine, D. Khalyavin, and R. Osborn, "Magnetoelastic coupling in the phase diagram of $Ba_{1-x}K_xFe_2As_2$ as seen via neutron diffraction," Phys. Rev. B **83**, 172503 (2011).

[52] D. A. Zocco, K. Grube, F. Eilers, T. Wolf, and H. v. Löhneysen, "Pauli-limited multiband superconductivity in KFe_2As_2," Phys. Rev. Lett. **111**, 057007 (2013).

[53] S. A. J. Kimber, A. Kreyssig, Y.-Z. Zhang, H. O. Jeschke, R. Valentí, F. Yokaichiya, E. Colombier, J. Yan, T. C. Hansen, T. Chatterji, R. J. McQueeney, P. C. Canfield, A. I. Goldman, and D. N. Argyriou, "Similarities between structural distortions under pressure and chemical doping in superconducting $BaFe_2As_2$," Nature Materials **8**, 471–475 (2009).

[54] E. Wiesenmayer, H. Luetkens, G. Pascua, R. Khasanov, A. Amato, H. Potts, B. Banusch, H.-H. Klauss, and D. Johrendt, "Microscopic coexistence of superconductivity and magnetism in $Ba_{1-x}K_xFe_2As_2$," Phys. Rev. Lett. **107**, 237001 (2011).

[55] R. M. Fernandes and J. Schmalian, "Competing order and nature of the pairing state in the iron pnictides," Phys. Rev. B **82**, 014521 (2010).

[56] E. Hassinger, G. Gredat, F. Valade, S. R. de Cotret, A. Juneau-Fecteau, J.-P. Reid, H. Kim, M. A. Tanatar, R. Prozorov, B. Shen, H.-H. Wen, N. Doiron-Leyraud, and L. Taillefer, "Pressure-induced Fermi-surface reconstruction in the iron-arsenide superconductor $Ba_{1-x}K_xFe_2As_2$: Evidence of a phase transition inside the antiferromagnetic phase," Phys. Rev. B **86**, 140502 (2012).

[57] S. Avci, , O. Chmaissem, J. Allred, S. Rosenkranz, I. Eremin, A. Chubukov, D. Bugaris, D. Chung, M. Kanatzidis, J.-P. Castellan, J. Schlueter, H. Claus, D. Khalyavin, P. Manuel, A. Daoud-Aladine, and R. Osborn, "Magnetically driven suppression of nematic order in an iron-based superconductor," Nat Commun **5**, 3845.

[58] F. Waßer, A. Schneidewind, Y. Sidis, S. Aswartham, S. Wurmehl, B. Büchner, and M. Braden, "Spin reorientation in Na-doped $BaFe_2As_2$ studied by neutron diffraction," ArXiv e-prints , 1407.1417 (2014).

[59] S. Avci, O. Chmaissem, D. Y. Chung, S. Rosenkranz, E. A. Goremychkin, J. P. Castellan, I. S. Todorov, J. A. Schlueter, H. Claus, A. Daoud-Aladine, D. D. Khalyavin, M. G. Kanatzidis, and R. Osborn, "Phase diagram of $Ba_{1-x}K_xFe_2As_2$," Phys. Rev. B **85**, 184507 (2012).

[60] F. Hardy, A. E. Böhmer, D. Aoki, P. Burger, T. Wolf, P. Schweiss, R. Heid, P. Adelmann, Y. X. Yao, G. Kotliar, J. Schmalian, and C. Meingast, "Evidence of strong correlations and coherence-incoherence crossover in the iron pnictide superconductor KFe_2As_2," Phys. Rev. Lett. **111**, 027002 (2013).

[61] F. Hardy and *et al.*, (in preparation).

[62] L. de' Medici, G. Giovannetti, and M. Capone, "Selective Mott physics as a key to iron superconductors," Phys. Rev. Lett. **112**, 177001 (2014).

[63] Z. Zhang, A. F. Wang, X. C. Hong, J. Zhang, B. Y. Pan, J. Pan, Y. Xu, X. G. Luo, X. H. Chen, and S. Y. Li, "Heat transport in $RbFe_2As_2$ single crystal: evidence for nodal superconducting gap," ArXiv e-prints , 1403.0191 (2014).

[64] F. Hardy, R. Eder, M. Jackson, D. Aoki, C. Paulsen, T. Wolf, P. Burger, A. Böhmer, P. Schweiss, P. Adelmann, R. A. Fisher, and C. Meingast, "Multiband superconductivity in KFe_2As_2: Evidence for one isotropic and several lilliputian energy gaps," Journal of the Physical Society of Japan **83**, 014711 (2014).

[65] H. Suhl, B. T. Matthias, and L. R. Walker, "Bardeen-Cooper-Schrieffer theory of superconductivity in the case of overlapping bands," Phys. Rev. Lett. **3**, 552–554 (1959).

[66] M. Merz, P. Schweiss, P. Nagel, T. Wolf, H. v. Loehneysen, and S. Schuppler, "To dope or not to dope: Electronic structure of Ba-site and Fe-site substituted single-crystalline $BaFe_2As_2$," ArXiv e-prints , 1306.4222 (2013).

[67] J. Zhao, Q. Huang, C. de la Cruz, S. Li, J. W. Lynn, Y. Chen, M. A. Green, G. F. Chen, G. Li, Z. Li, J. L. Luo, N. L. Wang, and P. Dai, "Structural and magnetic phase diagram of $CeFeAsO_{1-x}F_x$ and its relation to high-temperature superconductivity," Nature Materials **7**, 953–959 (2008).

[68] C.-H. Lee, A. Iyo, H. Eisaki, H. Kito, M. Teresa Fernandez-Diaz, T. Ito, K. Kihou, H. Matsuhata, M. Braden, and K. Yamada, "Effect of structural parameters on superconductivity in fluorine-free $LnFeAsO_{1-y}$ (Ln=La, Nd)," Journal of the Physical Society of Japan **77**, 083704 (2008).

[69] S. L. Bud'ko, M. Sturza, D. Y. Chung, M. G. Kanatzidis, and P. C. Canfield, "Heat capacity jump at T_c and pressure derivatives of superconducting transition temperature in the $Ba_{1-x}K_xFe_2As_2$ ($0.2 \leq x \leq 1$) series," Phys. Rev. B **87**, 100509 (2013).

[70] V. Zinth, T. Dellmann, H.-H. Klauss, and D. Johrendt, "Recovery of a parentlike state in $Ba_{1-x}K_xFe_{1.86}Co_{0.14}As_2$," Angewandte Chemie International Edition **50**, 7919–7923 (2011).

[71] N. Ni, A. Thaler, J. Q. Yan, A. Kracher, E. Colombier, S. L. Bud'ko, P. C. Canfield, and S. T. Hannahs, "Temperature versus doping phase diagrams for $Ba(Fe_{1-x}TM_x)_2As_2$ (TM=Ni,Cu,Cu/Co) single crystals," Phys. Rev. B **82**, 024519 (2010).

[72] M. Nakajima, S. Ishida, T. Tanaka, K. Kihou, Y. Tomioka, T. Saito, C. H. Lee, H. Fukazawa, Y. Kohori, T. Kakeshita, A. Iyo, T. Ito, H. Eisaki, and S. Uchida, "Normal-state charge dynamics in doped $BaFe_2As_2$: Roles of doping and necessary ingredients for superconductivity," ArXiv e-prints , 1308.6133 (2013).

[73] H. Kontani, T. Saito, and S. Onari, "Origin of orthorhombic transition, magnetic transition, and shear-modulus softening in iron pnictide superconductors: Analysis based on the orbital fluctuations theory," Phys. Rev. B **84**, 024528 (2011).

[74] R. M. Fernandes, A. V. Chubukov, J. Knolle, I. Eremin, and J. Schmalian, "Preemptive nematic order, pseudogap, and orbital order in the iron pnictides," Phys. Rev. B **85**, 024534 (2012).

[75] N. Ni, M. E. Tillman, J.-Q. Yan, A. Kracher, S. T. Hannahs, S. L. Bud'ko, and P. C. Canfield, "Effects of Co substitution on thermodynamic and transport properties and anisotropic H_{c2} in $Ba(Fe_{1-x}Co_x)_2As_2$ single crystals," Phys. Rev. B **78**, 214515 (2008).

[76] C. Lester, J.-H. Chu, J. G. Analytis, S. C. Capelli, A. S. Erickson, C. L. Condron, M. F. Toney, I. R. Fisher, and S. M. Hayden, "Neutron scattering study of the interplay between structure and magnetism in $Ba(Fe_{1-x}Co_x)_2As_2$," Phys. Rev. B **79**, 144523 (2009).

[77] A. Kreyssig, M. G. Kim, S. Nandi, D. K. Pratt, W. Tian, J. L. Zarestky, N. Ni, A. Thaler, S. L. Bud'ko, P. C. Canfield, R. J. McQueeney, and A. I. Goldman, "Suppression of antiferromagnetic order and orthorhombic distortion in superconducting $Ba(Fe_{0.0.961}Rh_{0.039})_2As_2$," Phys. Rev. B **81**, 134512 (2010).

[78] H. Luetkens, H.-H. Klauss, M. Kraken, F. J. Litterst, T. Dellmann, R. Klingeler, C. Hess, R. Khasanov, A. Amato, C. Baines, M. Kosmala, O. J. Schumann, M. Braden, J. Hamann-Borrero, N. Leps, A. Kondrat, G. Behr, J. Werner, and B. Büchner, "The electronic phase diagram of the $La(O_{1-x}F_x)FeAs$ superconductor," Nat. Mater. **8**, 305–309 (2009).

[79] D. R. Parker, M. J. P. Smith, T. Lancaster, A. J. Steele, I. Franke, P. J. Baker, F. L. Pratt, M. J. Pitcher, S. J. Blundell, and S. J. Clarke, "Control of the competition between a magnetic phase and a superconducting phase in cobalt-doped and nickel-doped NaFeAs using electron count," Phys. Rev. Lett. **104**, 057007 (2010).

[80] J.-H. Chu, J. G. Analytis, K. De Greve, P. L. McMahon, Z. Islam, Y. Yamamoto, and I. R. Fisher, "In-plane resistivity anisotropy in an underdoped iron arsenide superconductor," Science **329**, 824–826 (2010).

[81] M. Yi, D. Lu, J.-H. Chu, J. G. Analytis, A. P. Sorini, A. F. Kemper, B. Moritz, S.-K. Mo, R. G. Moore, M. Hashimoto, W.-S. Lee, Z. Hussain, T. P. Devereaux, I. R. Fisher, and Z.-X. Shen, "Symmetry-breaking orbital anisotropy observed for detwinned $Ba(Fe_{1-x}Co_x)_2As_2$ above the spin density wave transition," Proceedings of the National Academy of Sciences **108**, 6878–6883 (2011).

[82] J. J. Ying, X. F. Wang, T. Wu, Z. J. Xiang, R. H. Liu, Y. J. Yan, A. F. Wang, M. Zhang, G. J. Ye, P. Cheng, J. P. Hu, and X. H. Chen, "Measurements of the anisotropic in-plane resistivity of underdoped FeAs-based pnictide superconductors," Phys. Rev. Lett. **107**, 067001 (2011).

[83] M. Nakajima, S. Ishida, Y. Tomioka, K. Kihou, C. H. Lee, A. Iyo, T. Ito, T. Kakeshita, H. Eisaki, and S. Uchida, "Effect of co doping on the in-plane

anisotropy in the optical spectrum of underdoped $Ba(Fe_{1-x}Co_x)_2As_2$," Phys. Rev. Lett. **109**, 217003 (2012).

[84] S. Ishida, M. Nakajima, T. Liang, K. Kihou, C. H. Lee, A. Iyo, H. Eisaki, T. Kakeshita, Y. Tomioka, T. Ito, and S. Uchida, "Anisotropy of the in-plane resistivity of underdoped $Ba(Fe_{1-x}Co_x)_2As_2$ superconductors induced by impurity scattering in the antiferromagnetic orthorhombic phase," Phys. Rev. Lett. **110**, 207001 (2013).

[85] A. Dusza, A. Lucarelli, F. Pfuner, J.-H. Chu, I. R. Fisher, and L. Degiorgi, "Anisotropic charge dynamics in detwinned $Ba(Fe_{1-x}Co_x)_2As_2$," EPL (Europhysics Letters) **93**, 37002 (2011).

[86] M. Fu, D. A. Torchetti, T. Imai, F. L. Ning, J.-Q. Yan, and A. S. Sefat, "Nmr search for the spin nematic state in a LaFeAsO single crystal," Phys. Rev. Lett. **109**, 247001 (2012).

[87] L. W. Harriger, H. Q. Luo, M. S. Liu, C. Frost, J. P. Hu, M. R. Norman, and P. Dai, "Nematic spin fluid in the tetragonal phase of $BaFe_2As_2$," Phys. Rev. B **84**, 054544 (2011).

[88] J.-H. Chu, H.-H. Kuo, J. G. Analytis, and I. R. Fisher, "Divergent nematic susceptibility in an iron arsenide superconductor," Science **337**, 710–712 (2012).

[89] E. C. Blomberg, A. Kreyssig, M. A. Tanatar, R. M. Fernandes, M. G. Kim, A. Thaler, J. Schmalian, S. L. Bud'ko, P. C. Canfield, A. I. Goldman, and R. Prozorov, "Effect of tensile stress on the in-plane resistivity anisotropy in $BaFe_2As_2$," Phys. Rev. B **85**, 144509 (2012).

[90] C. Dhital, Z. Yamani, W. Tian, J. Zeretsky, A. S. Sefat, Z. Wang, R. J. Birgeneau, and S. D. Wilson, "Effect of uniaxial strain on the structural and magnetic phase transitions in $BaFe_2As_2$," Phys. Rev. Lett. **108**, 087001 (2012).

[91] J. Hu, C. Setty, and S. Kivelson, "Pressure effects on magnetically driven electronic nematic states in iron pnictide superconductors," Phys. Rev. B **85**, 100507 (2012).

[92] M. Yoshizawa and S. Simayi, "Anomalous elastic behavior and its correlation with superconductivity in iron-based superconductor $Ba(Fe_{1-x}Co_x)_2As_2$," Modern Physics Letters B **26**, 1230011 (2012).

[93] R. M. Fernandes and J. Schmalian, "Manifestations of nematic degrees of freedom in the magnetic, elastic, and superconducting properties of the iron pnictides," Superconductor Science and Technology **25**, 084005 (2012).

[94] I. I. Mazin, D. J. Singh, M. D. Johannes, and M. H. Du, "Unconventional superconductivity with a sign reversal in the order parameter of $LaFeAsO_{1-x}F_x$," Phys. Rev. Lett. **101**, 057003 (2008).

[95] K. Kuroki, S. Onari, R. Arita, H. Usui, Y. Tanaka, H. Kontani, and H. Aoki, "Unconventional pairing originating from the disconnected fermi surfaces of superconducting $LaFeAsO_{1-x}F_x$," Phys. Rev. Lett. **101**, 087004 (2008).

[96] I. Mazin and J. Schmalian, "Pairing symmetry and pairing state in ferropnictides: Theoretical overview," Physica C: Superconductivity **469**, 614 – 627 (2009), Superconductivity in Iron-Pnictides.

[97] H. Kontani and S. Onari, "Orbital-fluctuation-mediated superconductivity in iron pnictides: Analysis of the five-orbital Hubbard-Holstein model," Phys. Rev. Lett. **104**, 157001 (2010).

[98] M. Yoshizawa, D. Kimura, T. Chiba, S. Simayi, Y. Nakanishi, K. Kihou, C.-H. Lee, A. Iyo, H. Eisaki, M. Nakajima, and S.-i. Uchida, "Structural quantum criticality and superconductivity in iron-based superconductor $Ba(Fe_{1-x}Co_x)_2As_2$," Journal of the Physical Society of Japan **81**, 024604 (2012).

[99] R. M. Fernandes, A. E. Böhmer, C. Meingast, and J. Schmalian, "Scaling between magnetic and lattice fluctuations in iron pnictide superconductors," Phys. Rev. Lett. **111**, 137001 (2013).

[100] T. Goto, R. Kurihara, K. Araki, K. Mitsumoto, M. Akatsu, Y. Nemoto, S. Tatematsu, and M. Sato, "Quadrupole effects in layered iron pnictide superconductor $Ba(Fe_{0.9}Co_{0.1})_2As_2$," Journal of the Physical Society of Japan **80**, 073702 (2011).

[101] B. W. Rossiter and R. C. Baetzold, eds., *Determination of elastic and mechanical properties*, Physical methods of chemistry, Vol. 7 (Wiley, New York, N.Y., 1991).

[102] J.-M. Berthelot, *Matériaux composites: Comportement mécanique et analyse des structures*, 5th ed. (Lavoisier, 2012).

[103] H. M. Ledbetter, "Elastic constants of polycrystalline copper at low temperatures. Relationship to single-crystal elastic constants," physica status solidi (a) **66**, 477–484 (1981).

[104] E. K. H. Salje and W. Schranz, "Low amplitude, low frequency elastic measurements using dynamic mechanical analyzer (DMA) spectroscopy," Zeitschrift für Kristallographie Crystalline Materials **226**, 1–17 (2010).

[105] J. P. Benoît, J. Berger, M. Krauzman, and J. L. Godet, "Experimental observation of a soft mode in ammonium hydrogen oxalate hemihydrate by Brillouin scattering," J. Phys. France **47**, 815–819 (198).

[106] A. V. Kityk, V. P. Soprunyuk, A. Fuith, W. Schranz, and H. Warhanek, "Low-frequency elastic properties of the incommensurate ferroelastic $[N(CH_3)_4]_2CuCl_4$," Phys. Rev. B **53**, 6337–6344 (1996).

[107] W. Schranz, H. Kabelka, A. Sarras, and M. Burock, "Giant domain wall response of highly twinned ferroelastic materials," Applied Physics Letters **101**, 141913 (2012).

[108] W. Schranz, H. Kabelka, and A. Tröster, "Superelastic softening of ferroelastic multidomain crystals," Ferroelectrics **426**, 242–250 (2012).

[109] Y. P. Varshni, "Temperature dependence of the elastic constants," Phys. Rev. B **2**, 3952–3958 (1970).

[110] A. E. Böhmer and *et al.*, (unpublished).

[111] L. R. Testardi, "Elastic modulus, thermal expansion, and specific heat at a phase transition," Phys. Rev. B **12**, 3849–3854 (1975).

[112] D. V. Evtushinsky, A. A. Kordyuk, V. B. Zabolotnyy, D. S. Inosov, T. K. Kim, B. Büchner, H. Luo, Z. Wang, H.-H. Wen, G. Sun, C. Lin, and S. V. Borisenko, "Propeller-like low temperature Fermi surface of $Ba_{1-x}K_xFe_2As_2$ from magnetotransport and photoemission measurements," Journal of the Physical Society of Japan **80**, 023710 (2011).

[113] H. Kontani and Y. Yamakawa, "Linear response theory for shear modulus C_{66} and raman quadrupole susceptibility: Evidence for orbital nematic fluctuations in Fe-based superconductors," ArXiv e-prints , 1312.0528 (2013).

[114] F. L. Ning, K. Ahilan, T. Imai, A. S. Sefat, M. A. McGuire, B. C. Sales, D. Mandrus, P. Cheng, B. Shen, and H.-H. Wen, "Contrasting spin dynamics between underdoped and overdoped $Ba(Fe_{1-x}Co_x)_2As_2$," Phys. Rev. Lett. **104**, 037001 (2010).

[115] A. Smerald and N. Shannon, "Angle-resolved NMR: Quantitative theory of ^{75}As T_1 relaxation rate in $BaFe_2As_2$," Phys. Rev. B **84**, 184437 (2011).

[116] Y. Gallais, R. M. Fernandes, I. Paul, L. Chauvière, Y.-X. Yang, M.-A. Méasson, M. Cazayous, A. Sacuto, D. Colson, and A. Forget, "Observation of incipient charge nematicity in $Ba(Fe_{1-x}Co_x)_2As_2$," Phys. Rev. Lett. **111**, 267001 (2013).

[117] Y. Nakai, T. Iye, S. Kitagawa, K. Ishida, S. Kasahara, T. Shibauchi, Y. Matsuda, H. Ikeda, and T. Terashima, "Normal-state spin dynamics in the iron-pnictide superconductors $BaFe_2(As_{1-x}P_x)_2$ and $Ba(Fe_{1-x}Co_x)_2As_2$ probed with NMR measurements," Phys. Rev. B **87**, 174507 (2013).

[118] X. Wang and R. M. Fernandes, "Impact of local-moment fluctuations on the magnetic degeneracy of iron arsenide superconductors," Phys. Rev. B **89**, 144502 (2014).

[119] M. Hirano, Y. Yamada, T. Saito, R. Nagashima, T. Konishi, T. Toriyama, Y. Ohta, H. Fukazawa, Y. Kohori, Y. Furukawa, K. Kihou, C.-H. Lee, A. Iyo, and H. Eisaki, "Potential antiferromagnetic fluctuations in hole-doped iron-pnictide superconductor $Ba_{1-x}K_xFe_2As_2$ studied by ^{75}As nuclear magnetic resonance measurement," Journal of the Physical Society of Japan **81**, 054704 (2012).

[120] Y. Mizuguchi, F. Tomioka, S. Tsuda, T. Yamaguchi, and Y. Takano, "Superconductivity at 27 K in tetragonal FeSe under high pressure," Applied Physics Letters **93**, 152505 (2008).

[121] S. Medvedev, T. M. McQueen, I. A. Troyan, T. Palasyuk, M. I. Eremets, R. J. Cava, S. Naghavi, F. Casper, V. Ksenofontov, G. Wortmann, and C. Felser, "Electronic and magnetic phase diagram of β-$Fe_{1.01}$ with superconductivity at 36.7 K under pressure," Nature Mat. **8**, 630–633 (2009).

[122] S. Margadonna, Y. Takabayashi, Y. Ohishi, Y. Mizuguchi, Y. Takano, T. Kagayama, T. Nakagawa, M. Takata, and K. Prassides, "Pressure evolution of the low-temperature crystal structure and bonding of the superconductor FeSe ($T_c = 37$ K)," Phys. Rev. B **80**, 064506 (2009).

[123] G. Garbarino, A. Sow, P. Lejay, A. Sulpice, P. Toulemonde, M. Mezouar, and M. Núñez-Regueiro, "High-temperature superconductivity (T_c onset at 34 K) in the high-pressure orthorhombic phase of FeSe," EPL (Europhysics Letters) **86**, 27001 (2009).

[124] R. Peng, X. P. Shen, X. Xie, H. C. Xu, S. Y. Tan, M. Xia, T. Zhang, H. Y. Cao, X. G. Gong, J. P. Hu, B. P. Xie, and D. L. Feng, "Measurement of an enhanced superconducting phase and a pronounced anisotropy of the energy gap of a strained FeSe single layer in FeSe/Nb : $SrTiO_3/KTaO_3$ heterostructures using photoemission spectroscopy," Phys. Rev. Lett. **112**, 107001 (2014).

[125] T. M. McQueen, A. J. Williams, P. W. Stephens, J. Tao, Y. Zhu, V. Ksenofontov, F. Casper, C. Felser, and R. J. Cava, "Tetragonal-to-orthorhombic structural phase transition at 90 K in the superconductor $Fe_{1.01}Se$," Phys. Rev. Lett. **103**, 057002 (2009).

[126] T. Imai, K. Ahilan, F. L. Ning, T. M. McQueen, and R. J. Cava, "Why does undoped FeSe become a high-T_c superconductor under pressure?" Phys. Rev. Lett. **102**, 177005 (2009).

[127] K. Miyoshi, K. Morishita, E. Mutou, M. Kondo, O. Seida, K. Fujiwara, J. Takeuchi, and S. Nishigori, "Enhanced superconductivity on the tetragonal lattice in FeSe under hydrostatic pressure," Journal of the Physical Society of Japan **83**, 013702 (2014).

[128] M. Bendele, A. Ichsanow, Y. Pashkevich, L. Keller, T. Strässle, A. Gusev, E. Pomjakushina, K. Conder, R. Khasanov, and H. Keller, "Coexistence of superconductivity and magnetism in $FeSe_{1-x}$ under pressure," Phys. Rev. B **85**, 064517 (2012).

[129] S. Masaki, H. Kotegawa, Y. Hara, H. Tou, K. Murata, Y. Mizuguchi, and Y. Takano, "Precise pressure dependence of the superconducting transition temperature of FeSe: Resistivity and ^{77}Se-NMR study," Journal of the Physical Society of Japan **78**, 063704 (2009).

[130] M. Bendele, A. Amato, K. Conder, M. Elender, H. Keller, H.-H. Klauss, H. Luetkens, E. Pomjakushina, A. Raselli, and R. Khasanov, "Pressure induced static magnetic order in superconducting $FeSe_{1-x}$," Phys. Rev. Lett. **104**, 087003 (2010).

[131] S. Kasahara and et al., (submitted).

[132] D. Braithwaite, B. Salce, G. Lapertot, F. Bourdarot, C. Marin, D. Aoki, and M. Hanfland, "Superconducting and normal phases of FeSe single crystals at high pressure," Journal of Physics: Condensed Matter **21**, 232202 (2009).

[133] R. Khasanov, M. Bendele, K. Conder, H. Keller, E. Pomjakushina, and V. Pomjakushin, "Iron isotope effect on the superconducting transition temperature and the crystal structure of $FeSe_{1-x}$," New Journal of Physics **12**, 073024 (2010).

[134] G. A. Zvyagina, T. N. Gaydamak, K. R. Zhekov, I. V. Bilich, V. D. Fil, D. A. Chareev, and A. N. Vasiliev, "Acoustic characteristics of FeSe single crystals," EPL (Europhysics Letters) **101**, 56005 (2013).

[135] S. L. Bud'ko, N. Ni, S. Nandi, G. M. Schmiedeshoff, and P. C. Canfield, "Thermal expansion and anisotropic pressure derivatives of T_c in $Ba(Fe_{1-x}Co_x)_2As_2$ single crystals," Phys. Rev. B **79**, 054525 (2009).

[136] S. Chandra and A. K. M. A. Islam, "Elastic properties of mono- and polycrystalline PbO-type $_{1-x}Te_x$ (x = 0–1.0): A first-principles study," Physica C: Superconductivity **470**, 2072–2075 (2010).

[137] Y.-C. Wen, Y.-C. Liao, H.-H. Chang, B.-H. Mok, Y.-C. Lee, T.-W. Huang, K.-W. Yeh, J.-Y. Luo, M.-J. Wang, C.-K. Sun, and M.-K. Wu, "Elastic stiffness of single-crystalline FeSe measured by picosecond ultrasonics," Journal of Applied Physics **110**, 073505 (2011).

[138] J. N. Millican, D. Phelan, E. L. Thomas, J. B. Leão, and E. Carpenter, "Pressure-induced effects on the structure of the FeSe superconductor," Solid State Communications **149**, 707–710 (2009).

[139] Y. Mizuguchi, Y. Hara, K. Deguchi, S. Tsuda, T. Yamaguchi, K. Takeda, H. Kotegawa, H. Tou, and Y. Takano, "Anion height dependence of T_c for the Fe-based superconductor," Superconductor Science and Technology **23**, 054013 (2010).

[140] C. Meingast, O. Kraut, T. Wolf, H. Wühl, A. Erb, and G. Müller-Vogt, "Large *a*-*b* anisotropy of the expansivity anomaly at t_c in untwinned $yba_2cu_3o_{7-\delta}$," Phys. Rev. Lett. **67**, 1634–1637 (1991).

[141] J. Korringa, "Nuclear magnetic relaxation and resonance line shift in metals," Physica **16**, 601 – 610 (1950).

[142] S. Kitagawa, Y. Nakai, T. Iye, K. Ishida, Y. Kamihara, M. Hirano, and H. Hosono, "Stripe antiferromagnetic correlations in $LaFeAsO_{1-x}F_x$ probed by ^{75}As NMR," Phys. Rev. B **81**, 212502 (2010).

Acknowledgements

Many people have contributed to this work, and I would like to thank all of them.

Zunächst möchte ich Hilbert von Löhneysen danken, für das Ermöglichen dieser Arbeit, das Lesen des Manuskripts und den Ausbau der Kollaboration mit Kyoto.

Bei Jörg Schmalian möchte ich mich für die fortwährende theoretische Unterstützung, das Diskutieren über zahlreiche experimentelle Ergebnisse und für die Übernahme des Korreferats bedanken.

Mein ganz besonderer Dank gilt meinem Betreuer, Christoph Meingast, der mich die letzten Jahre in jedweder Hinsicht unterstützt hat: mit täglichen Gesprächen bei der Interpretation der vielen Messergebnisse, mit Reparaturen am Dilatometer, beim Schreiben von Veröffentlichungen, bei Konferenzteilnahmen und mit wertvollem Rat in allen Lebenslagen.

Un grand merci à Frédéric Hardy, avec lequel j'ai partagé le labo, le bureau, les échantillons, les résultats et les modèles. Merci pour les maths, pour la relecture du manuscript, et pour les nombreuses discussions, scientifiques et autres.

Bei Peter Schweiss möchte ich mich für die sehr zahlreichen 4-Kreis Diffraktometriemessungen an meinen Kristallen bedanken, ohne die es kein Phasendiagram gäbe. Vielen Dank auch an Rainer Fromknecht für die EDX Messungen.

Ein ganz großes Dankeschön gilt Doris Ernst, Peter Adelmann und Thomas Wolf für die Probenpräparation. Danke für hunderte Chargen, viele davon „auf Bestellung", ohne die diese Arbeit niemals so zustande gekommen wäre, und von denen ich leider nur einen Bruchteil zeigen konnte. Danke, Thomas, auch für die offene Tür und die vertrauensvollen Gespräche.

Allen Mitgliedern des IFP, insbesondere auch meinen Mitdoktoranden Philipp Burger, Sebastian Zaum, Felix Eilers, Sven Krannich, Michael Maschek, Alexander Herbig und Andreas Kapuvari, möchte ich danken für die sehr angenehme und freundschaftliche Atmosphäre.

Vielen Dank auch allen Mitgliedern der Werkstatt für das schnelle Ausführen von Aufträgen und Reparaturen und für die Versorgung mit Helium.

I would like to thank Rafael Fernandes for the discussions and for always listening to my concerns.

Bei Marius Reinecker und Wilfried Schranz möchte ich mich für die Gastfreundschaft in Wien bedanken. Danke, Marius, für die Woche gemeinsames Messen und,

Wilfried, für die sehr hilfreichen Gespräche über Drei-Punkt-Biegen, Landautheorie und für deinen ansteckenden Enthusiasmus.

Bei Rolf Lortz möchte ich mich für die Einladung nach Hong Kong und die Gastfreundschaft bedanken. Thanks to all the group of Rolf Lortz for the friendly welcome.

It was a great pleasure to visit Kyoto again, and I would like to thank Kenji Ishida for the hospitality and welcome in the lab. A great thanks to Takeshi Arai, Taisuke Hattori, Tetsuya Iye and Kenji Ishida for the NMR measurements we did together during long days and long nights. Finally, I would like to thank all the Ishida group, and Yuji Matsuda, Takasada Shibauchi, Shigeru Karahara and all the others in Matsuda lab for their repeated hospitality and warm welcome in Kyoto.

Schließlich möchte ich mich bei meinem Mann, Felix, und bei meiner Familie für die unentwegte Unterstützung bedanken.